The University of Nottingham

UNITED KINGDOM · CHINA · MALAYSIA

Decoration of Graphene - Carbon Nanotube Nanostructures: Synthesis and Applications

Chenxi Hu, MSc

Thesis submitted to the University of Nottingham for the degree of

Doctor of Philosophy

Supervisors: Dr. Fang Xu, Prof. David Grant & Dr. Xianghui Hou

Jan 2021

Abstract

Nanomaterials have played increasingly important roles in our lives with the development of modern science and technology. The design and synthesis of advanced nanomaterials have become the priorities to keep pace with the increasing demands of modern society. Carbon materials, which are made up of a broad array of allotropes, have played unique roles in numerous fields, especially the 1D carbon nanotubes (CNTs) and 2D graphene. Since the discovery of CNTs and graphene, an increasing number of experiments have been carried out on nanostructured CNTs, graphene and their roles as fillers in composites. CNTs and graphene have been regarded as promising materials, exhibiting exceptional mechanical, electrical and thermal properties, and have become a popular research topic.

In this research, the major aim is to prepare well-dispersed CNT - graphene oxide (GO) based nanostructures to utilise the properties of CNT and GO. To achieve this aim, different strategies, including the freeze-drying and molecular-level-mixing (MLM) methods, have been investigated. The obtained samples were then explored for potential applications (such as thermal management and dye removal materials).

In the first stage, a freeze-drying approach is introduced to prepare the well-dispersed 3D GO-CNTs (GNT) hybrid nanostructures. After that, metal nanoparticles (Cu, Ag and Ni) have been decorated on the GNT hybrid nanostructures through the molecular-level-mixing (MLM) method and subsequent reduction process. By adjusting the preparation parameters (i.e., reduction temperatures, durations and atmosphere), the results showed that metal nanoparticles were uniformly decorated on the GNT nanostructures. Meanwhile, the decorated metal nanoparticles could act as the spacers in reducing the agglomeration of graphene or CNTs.

The Ag and Ni nanoparticle decorated GNT nanostructures were explored as fillers in the poly(ether ether ketone) (PEEK) and epoxy matrix, respectively. The freeze-dried Ag-GNT (FGAg) nanostructures were dispersed in the PEEK matrix, and the obtained composites exhibited enhanced thermal conductivity (ca. 1.62 times compared to pure PEEK) and significantly improved electrical conductivity (from 10^{-10} Ω m^{-1} of pure PEEK to 10^{-1} Ω m^{-1} of FGAg-PEEK composite) and better thermal durability even above the melting temperature of PEEK. The improvements can be ascribed to the 3D network generated by the FGAg nanostructures in the PEEK matrix. Similarly, the Ni-GNT (FGNi) nanostructures formed 3D aligned pathways in the epoxy matrix with the assistance of a magnetic field, which effectively enhanced the thermal (from 0.137 W $m^{-1}K^{-1}$ to the highest 0.462 W $m^{-1}K^{-1}$) and electrical (from around 10^{10} to 4.6×10^{5} Ω m^{-1}) conduction. The additional benefit was to prevent the thermal expansion of the epoxy matrix. The freeze-dried Cu-GNT (FGCu) nanostructures were explored as fillers in a Cu matrix. The FGCu-Cu pellet obtained through the spark plasma sintering demonstrated that the graphene-layer structure of FGCu samples became horizontally distributed in the matrix. However, the measured thermal conductivity of the FGCu-Cu pellet, which was in the vertical direction, was lower than pure Cu pellets (237.78 W m^{-1} K^{-1} to 360 W m^{-1} K^{-1}). It can be predicted that there is a great potential for thermal conduction performance in the horizontal direction.

The dye removal performances of the GNT based products were then investigated. The well-dispersed 3D GNT nanostructures acted as the absorbents to react with both cationic (RhB) and anionic (MO) dyes. The results showed that both RhB and MO dyes could be adsorbed, and the best adsorption capacity was found to be 248.48 mg g^{-1} for RhB and 66.96 mg g^{-1} for MO. The FGNi nanostructures exhibited excellent dye removal performance through a synergistic effect of physical adsorption and photodegradation under UV irradiation. The FGNi samples displayed a removal capacity of 41.5 mg g^{-1} in 5 ppm RhB solution, which outperformed the

most reported Ni/C products. Meanwhile, the FGNi samples were easily collected after the reaction through magnetic separation technology.

The well-dispersed GNT nanostructures and their metal nanoparticle (Ag, Ni And Cu) decorated nanostructures have been prepared via the freeze-drying method with subsequent MLM and reduction processes. The obtained products have demonstrated enhanced performances not only acting as fillers in different matrices but also applying as dye removal materials. Therefore, this research work has displayed several positive results, and such products with unique structures have shown great potential as candidates in numerous fields.

Publications

1. **C. Hu**, T. Liu, N. Neate, M. Fay, X, Hou, D. Grant & F. Xu,. Magnetic alignment of Ni nanoparticles decorated GO-CNT nanostructures reinforced epoxy composites with superior anisotropic thermal conductivity. (In preparation)
2. **C. Hu**, T. Liu, N. Neate, M. Fay, X, Hou, D. Grant & F. Xu,. Uniformly Ag nanoparticles decorated GO-CNT nanocomposites nanostructures reinforced poly (ether ether ketone) composites with enhanced thermal and electrical properties. (*Composites part A: Applied Science and Manufacturin*g, in submission)
3. **C. Hu**, A. Thi, S. Pung, L, Stevens, N. Neate, X, Hou, D. Grant & F. Xu,. Efficient dye-removal via Ni nanoparticles decorated graphene oxide - carbon nanotube composites. (*Materials Chemistry and Physics*, accepted)
4. **C. Hu**, F. Xu, X, Hou, D. Grant,. High Rhodamine B and Methyl orange removal performance of graphene oxide/carbon nanotube nanocomposites. (*Materials Today: Proceedings*, in press)
5. K. Thummavichai, N. Wang, L. Lem, M. Phillips, C. Ton-That, H. Chang, **C. Hu**, et al. Lanthanide-doped $W_{18}O_{49}$ nanowires: Synthesis, structure and optical properties. *Materials Letters*, 2018 214, 232-235.
6. N. Wang, Z. Yang, K. Thummavichai, F. Xu, **C. Hu**, et al. Novel graphitic carbon coated IF-WS_2 reinforced poly (ether ether ketone) nanocomposites. *RSC Advances*, 2017 7(56), 35265-35273

Acknowledgments

I would like to express my deepest thanks to Dr. Fang Xu, Dr. Xianghu Hou and Prof. David Grant for their invaluable support, advice and encouragement during my doctoral research period. Without them, this research and subsequent thesis would not have existed. Their attitude, enthusiasm and insight in the research are appreciable and be the source of inspiration and motivation. It has been a life-changing experience for me.

I also wish to give thanks to the technical staff in Advanced Materials Group, especially to Mr. Rory Sceaton, Mr. Jason Greaves and Dr. Nigel Neate, for their constant help and expertise on equipment. Thanks to Mr. Martin Roe and Dr. Michael Fay from the Nanoscale and Microscale Research Centre (NMRC) for their help on SEM and TEM. Thanks to Dr. Lee Stevens from the Low Carbon Energy and Resources Technologies Research Group for the BET measurements. I appreciate the friendship and technical help from group members Dr. Junpeng Liu, Dr. Barun Ghosh, Dr. Bo Song, Dr. Tianhui Liu, Mr. Jie Wang, Mr. Peifeng Li, Miss Hongnan Zhang and many others. I am grateful to Prof. Yanqiu Zhu and his group from the University of Exeter, and Dr. Swee Yong Pung and his group from the Universiti Sains Malaysia, Malaysia, for their collaborative assistance.

Heartiest thanks to the China Scholarship Council and the University of Nottingham for the scholarship support.

Finally, my honest gratitude goes to my wife, my parents and my family for their love, caring, understanding and support. I will always love them and try to make them proud of who I am.

Table of Contents

List of Figures and Tables

List of Abbreviations

1D	One-dimensional
2D	Two-dimensional
3D	Three-dimensional
AC	Alternating current
BET	Brunauer-Emmett-Teller theory
BQ	P-benzoquinone
BSE	Back-scattered electrons
CL	Characteristic X-rays and light
CNT	Carbon nanotube
CTE	Coefficient of thermal expansion
CVD/PVD	Chemical/physical vapor deposition method
DC	Direct current
DMF	N,N-dimethylformamide
DSC	Differential scanning calorimetry
DSSCs	Dye-sensitized cells
EFAS	Electric field assisted sintering
FGAg	Silver nanoparticles decorated GNT nanostructures
FGCu	Copper nanoparticles decorated GNT nanostructures
FGNi	Nickel nanoparticles decorated GNT nanostructures
GnPs	Graphene flakes
GNS	Graphene nanosheets
GNT	GO-CNT nanostructures
GO	Graphene oxide
HP	Hot pressing
JCPDS	Joint Committee on Powder Diffraction Standards
LN	liquid N_2

MLM	Molecular level mixing
MO	Methyl orange
MWCNTs	Multi-walled carbon nanotubes
NR	Natural rubber
PAS	Plasma assisted sintering
PCS	Particles composite system
PECS	Pulsed electric current sintering
PEEK	Poly (ether ether ketone)
PI	Potassium iodide
PVA	Polyvinyl alcohol
PVP	Polyvinyl pyrrolidone
RhB	Rhodamine B
SE	Secondary electrons
SEM	Scanning electron microscope
SPS	Spark plasma sintering
SWCNTs	Single-walled carbon nanotubes
TC	Thermal conductivity
TEM	Transmission electron microscopy
TGA	Thermogravimetric analysis
UFAs	Carbon ultra-flyweight aerogels
XRD	X-ray powder diffraction
XPS	X-ray photoelectron spectroscopy

1 Introduction

1.1 Background

Since the discovery of CNTs by Ijima in 1991 and graphene by Novoselvo in 2004 [1, 2], the one-dimensional (1D) CNTs and 2-dimensional (2D) graphene materials have attracted significant attention not only in theoretical investigations but also in application explorations. As shown in Table *1-1*, various useful properties have been predicted or exhibited because of the unique structure of CNTs and graphene, such as high theoretical surface area and Young's and elastic modulus, good tensile strength as well as outstanding thermal and electrical conductivities [3-11]. Specifically, the thermal conductivities of these CNT or graphene materials can reach above 1500 W $m^{-1}K^{-1}$ either from experimental data or theoretical prediction [6]. Therefore, an increasing number of investigations have been made not only on the preparation of pristine CNTs and graphene materials but also on exploring their potential in composites. However, because of the π-π interactions and/or Van der Waals forces between each carbon atom layer, an agglomeration is prevalent. A good dispersion strategy must be adopted with the application of these carbon materials.

Table 1-1 Properties of CNT and graphene. [3-11]

Sample	Specific surface area (m^2 g^{-1})	Tensile strength (GPa)	Young's modulus (GPa)	Thermal conductivity (W $m^{-1}K^{-1}$)	Electrical conductivity (S m^{-1})
CNT	100 - 1000	11 - 63	270-950	1500 - 3500	~10^2
Graphene	2630	130	1000	1500 - 2500	~10^2

Pure Cu has been widely applied as thermal management material due to its high theoretic thermal conductivity (~ 400 W $m^{-1}K^{-1}$). However, there is great potential utilising the excellent

thermal properties of CNT and graphene materials to enhance the metal materials further and offer alternatives with the polymer-based materials in the thermal management applications, for example, the electronic packaging system (such as die-attach, thermally conductive adhesives, thermal interface materials and encapsulations) [12]. Two issues have been outlined as the main challenges in preparing carbon materials - based composites: one is the uniform dispersion of carbon materials in the matrix; the other is the interface between carbon materials and matrix. However, the reported results of such composites are not as good as the predictions. For example, in polymers, whose thermal conductivity of around 0.3 W $m^{-1}K^{-1}$, the increases in thermal conductivity after reinforcement were only around 1 W $m^{-1}K^{-1}$ [13], far lower than the predicted in tens or hundreds of W $m^{-1}K^{-1}$. This can be ascribed to the high resistance of heat transfer at the carbon filler - polymer boundary. Therefore, it has become a critical issue to take advantage of the excellent thermal performances of CNT and graphene in such metal and polymer matrices.

Another potential application for the CNT and graphene-based materials is the organic dye removal application. The coloured pollutants, which are normally hard to decompose due to their chemical stability, are mostly toxic and potentially carcinogenic. Therefore, developing economic and efficient dye removal approaches has become an important target for humanity. Carbon-based materials, which show large surface areas, are regarded as ideal candidates not only because of the physical adsorption due to the electrostatic interactions, hydrogen bond, and π-π interaction and/or hydrophobic interactions but also as the carriers for the photo-degradation of the dyes. Uniformly dispersed carbon-based composite is also critical for applying as the dye removal materials.

1.2 Aims and objectives

The aim of this research is to prepare the CNT and/or GO based nanostructures with well-dispersed structures to optimise the properties of CNT and GO. Different strategies (including the freeze-drying and molecular-level-mixing method) have been explored to achieve this aim, and the obtained samples were then investigated for potential applications, such as thermal management and dye removal materials. The specific objectives of the research were:

- To prepare 3D GO-CNTs (GNT) hybrid nanostructures ultilising a freeze-drying approach during the mixing of CNT and graphene materials to prevent agglomeration.
- To introduce metal (Cu, Ag and Ni) nanoparticles in the GNT hybrid nanostructures, using the molecular-level-mixing (MLM) methods to optimise decoration of GNTs.
- To explore the effects of metal nanoparticle decorated GNT nanostructures in different matrices (polymer and metal) and characterise the thermal and electrical performances of the composites.
- To study the dye removal performances of GNT and Ni decorated GNT samples with organic dyes.

1.3 Thesis outline

This thesis has been organised into eight chapters. Chapter 1 gives a brief introduction to the motivation, objectives, and structures of the thesis. Chapter 2 presents a review of the literature about the CNT and/or graphene - based composites as well as their applications in thermal management and dye removal fields. Chapter 3 provides information about the methodology, experimental equipment, and materials utilised in this thesis. Chapter 4 presents the fabrication of GNT nanostructures and the Cu, Ni, and Ag nanoparticles decorated nanostructures, and discusses the effects of different preparation parameters on the final morphology and

composition of the samples. Chapter 5 investigates the utilisation of Ni and Ag nanoparticles decorated GO-CNT nanostructures to enhance the polymer matrix (PEEK and epoxy resin) and their applications for thermal management materials. Chapter 6 describes the roles of pure GO-CNT and Ni decorated GO-CNT products on the organic dyes (RhB and MO) removal performances and proposes the removal mechanism under different conditions. Chapter 7 assesses the different pressing methods (such as manual pressing and sintering and spark plasma sintering) in preparing dense Cu pellets for thermal management applications. Finally, the conclusions of this thesis and some future investigation suggestions are summarised in chapter 8.

2 Literature review

This chapter focuses on the review of the literature about two-dimensional (2D) layer graphene, one-dimensional (1D) carbon nanotubes (CNTs) materials and composites based on them. Section 2.1 focuses on the introduction of graphene and/or CNT materials, while section 2.2 explains the reinforced composites based on graphene and/or CNT, especially the metal and polymer-based composites. Section 2.3 gives application examples of these composites.

2.1 Graphene, carbon nanotube and their hybrid nanostructures

2.1.1 Graphene materials and their properties

Graphene is a 2D material based on a layer of hexagonally arranged carbon atoms and can be exfoliated directly from graphite. In contrast to pristine graphite, this 2D layer material has exhibited exceptional physical properties since it was first isolated by Novoselov and co-workers in 2004 [1], such as its large theoretical surface area of around 2630 m^2 g^{-1} [3], high Young's modulus of ~1.0 TPa [4], good thermal (1500-2000 W $m^{-1}K^{-1}$) and electrical (ca. 10^2 S m^{-1}) conductivity.

The thermal performances of different kinds of graphene materials obtained through various preparation methods have been carefully studied. Balandin et al. investigated the thermal properties (especially thermal conductivity) of the graphene materials with different layers [5, 14, 15]. The measurement was carried out through a method called Raman optothermal process, which is based on the confocal micro-Raman spectroscopy [14]. Specifically, the graphene prepared through the exfoliated process was suspended in the middle of Si/SiO_2 substrates. As shown in the schematic (Figure *2-1*), the depth of the trench is around 300 nm, and the width is varied from 2 to 5 μm. The few-layer graphene (FLG) materials exhibit the thermal

conductivity decreasing from around 2800 to 1300 W $m^{-1}K^{-1}$ at room temperature when the number of atomic planes in FLG increases from 2 to 4 [5]. Measurement of single-layer graphene exhibited thermal conductivity in the range of ~ 3080 - 5300 W $m^{-1}K^{-1}$ [14, 15]. The increase of layers in graphene materials is not beneficial for thermal conduction.

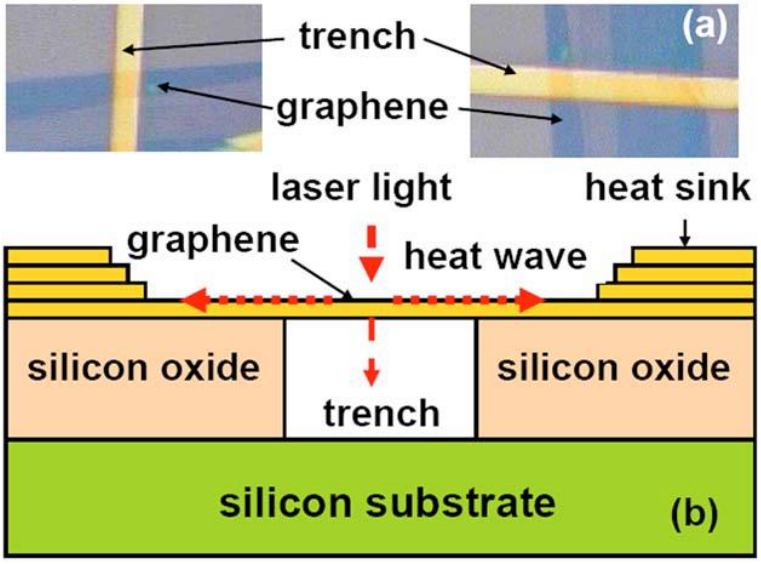

Figure 2-1 (a) High-resolution scanning electron microscopy image of the suspended graphene flakes. (b) Schematic of the experimental setup for measuring the thermal conductivity of graphene. [5]

Graphene materials tend to agglomerate due to π-π interactions and/or Van der Waals forces between each carbon atom layer even after dispersion, resulting in unsatisfied composites properties compared to prediction. Therefore, to effectively increase the dispersity of the graphene materials among the matrix, a popular wet chemical exfoliation method was adapted to obtain exfoliated graphene oxides (GOs) [12]. The functionalised groups (i.e., carboxylic acid and phenolic hydroxyl groups) [16] attached onto the surfaces of the obtained products improve their dispersion in water, making them an ideal filler for composites. Figure *2-2* shows the schematic of obtained well-dispersed GOs through the oxidation process followed by a sonication approach [16]. The electrostatic repulsion between each layer reduces the agglomeration trend.

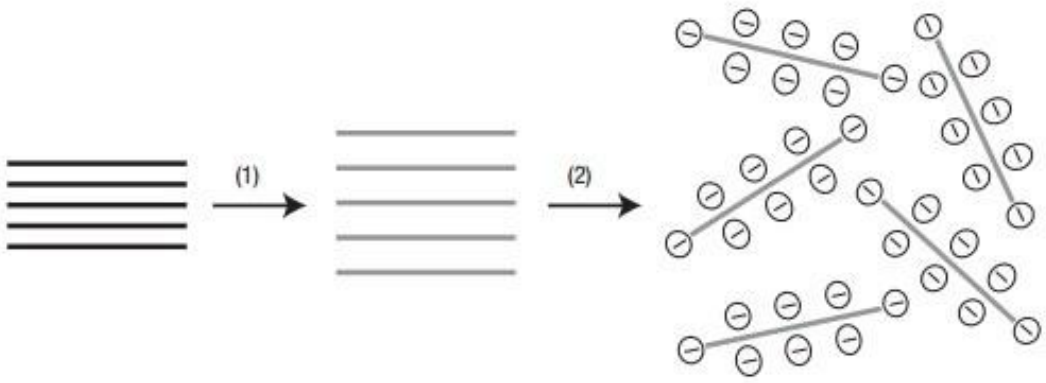

Figure 2-2 Schematic of obtained well-dispersed GOs through the wet chemical exfoliation method. [16]

2.1.2 Carbon nanotubes: properties and dispersity

Carbon nanotubes (CNTs), which were first discovered by Ijima in 1991 [2], show the cylindrical and extended-fullerene structures and can also be considered as a rolled carbon sheet. Based on the number of the side-walls, there are several different types of carbon nanotube: the single-walled carbon nanotubes (SWCNTs) are just made up of one graphene sheet, while double and multi-walled carbon nanotubes (MWCNTs) are made of two to series concentric layers. The experimentally estimated tensile strength for the outermost layer of the CNTs ranges from 11 to 63 GPa, and the elastic modulus ranges from 270-950 GPa [6]. In addition, CNTs also exhibit excellent thermal performance. For example, an isolated SWCNT's thermal conductivity at room temperature was predicted as high as 6000 W $m^{-1}K^{-1}$, while the measured value for an individual MWCNT is 3000 W $m^{-1}K^{-1}$. The thermal properties of a suspended metallic SWCNT are extracted by the Joule self-heating [7]. As shown in Figure *2-3*, a typical SWCNT, which is around 2.6 μm in length and 1.7 nm in diameter, was suspended over a trench, and the obtained thermal conductivity is found to be 3500 W $m^{-1}K^{-1}$. The thermal conductivity of the MWCNT was investigated by McEuen et al.. The MWCNT, which was suspended between two silicon nitride membranes, exhibited the thermal conductivity of more than 3000 W $m^{-1}K^{-1}$[17].

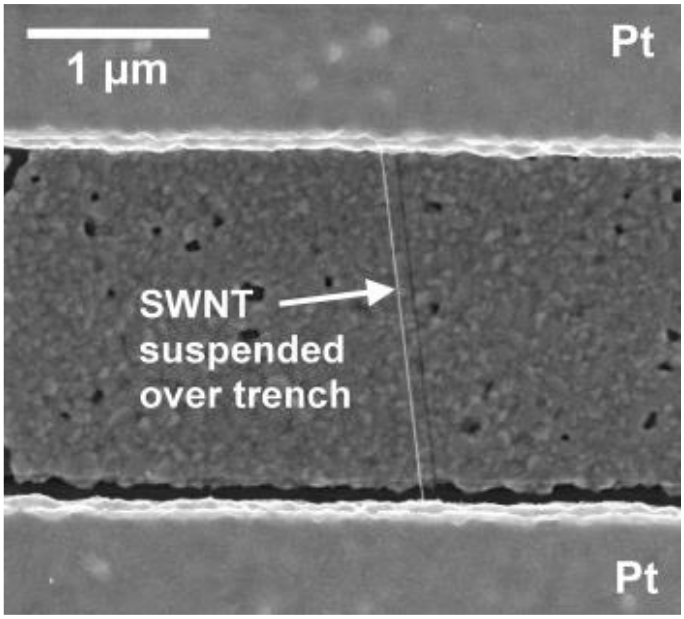

Figure 2-3 Scanning electron microscope (SEM) image of a typical SWCNT freely suspended across a 2 μm trench. [7]

Like graphene materials, CNTs also show an agglomeration trend after dispersion in solutions. To deal with the strong Van der Waals interactions between each tube and their high aspect ratio [18-20], researchers have studied various methods to prepare CNTs with better dispersity. Strategies included ball milling to shorten CNTs [21, 22], covalent and non-covalent strategy (including acid treatment) [23, 24], adopting surfactants in the solvent [23, 25], stirring [25, 26] and sonication [22, 24]. Among them, covalent and non-covalent surface modification strategies are the most common methods to optimise the dispersity. Figure *2-4* shows the schematic of the covalent and non-covalent functionalisation process with CNTs [27]. The covalent functionalisation contains chemical methods to obtain functionalised groups (i.e., carboxylic and hydroxyl groups), while the non-covalent functionalisation is a method to attach chemical handles through π-π interactions and/or Van der Waals forces [28]. With non-covalent approaches, surfactants or polymer wrapping could also improve the dispersity of CNTs in water. Surfactant-assisted processing is investigated based on such a non-covalent strategy. Gong et al. exhibit that better dispersion and interfacial bonding were obtained after adding

Polyoxyethylene 8 lauryl ($C_{12}EO_8$) [29]. Figure *2-5* shows the fracture surface SEM images with and without $C_{12}EO_8$. Superior distribution of CNTs was obtained after the addition of $C_{12}EO_8$. Meanwhile, the elastic modulus of the products increased by more than 30% after the addition of $C_{12}EO_8$.

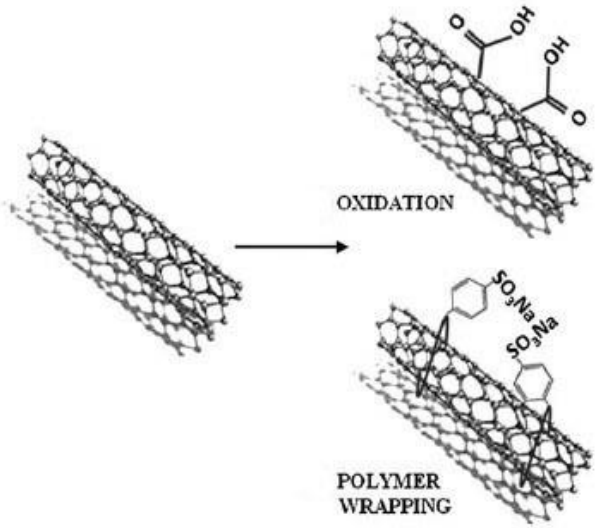

Figure 2-4 Schematic of the covalent (adding functionalized groups) and non-covalent strategy (wrapping polymers) of CNTs. [27]

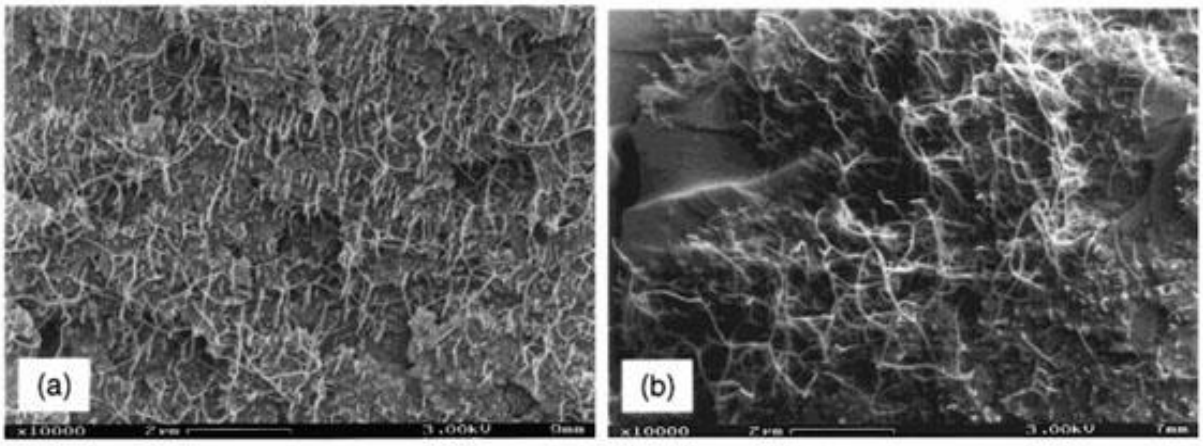

Figure 2-5 SEM images of CNTs on fracture surfaces of the composite samples: (a) with $C_{12}EO_8$ and (b) without $C_{12}EO_8$. [29]

To qualitatively analyse the dispersity of carbon nanomaterials, different methods have been adopted, such as scanning electron microscopy (SEM), transmission electron microscopy (TEM), atomic force microscopy (AFM), optical microscopy, Raman spectroscopy and UV–Vis spectroscopy. Figure *2-6* displays the dispersion results of MWCNTs in epoxy resin through UV-vis spectroscopy by Garg and co-workers [38]. UV-vis spectroscopy uses light in the

visible and adjacent ranges, and it indicates the dispersion quality by analysing the absorption of light. The UV-visible spectra (Figure *2-6*) show the absorbance of different samples after different ultrasonication times (a) and in epoxy with different stirring duration (b). It was found that the 170 min sonication reached a maximum intensity while the maximum absorption was located at ~300 nm (Figure *2-6*a). As shown in Figure *2-6*b, the maximum absorption also appeared at ~300 nm. The absorbance remains constant even after a continuous stirring for 24 h.

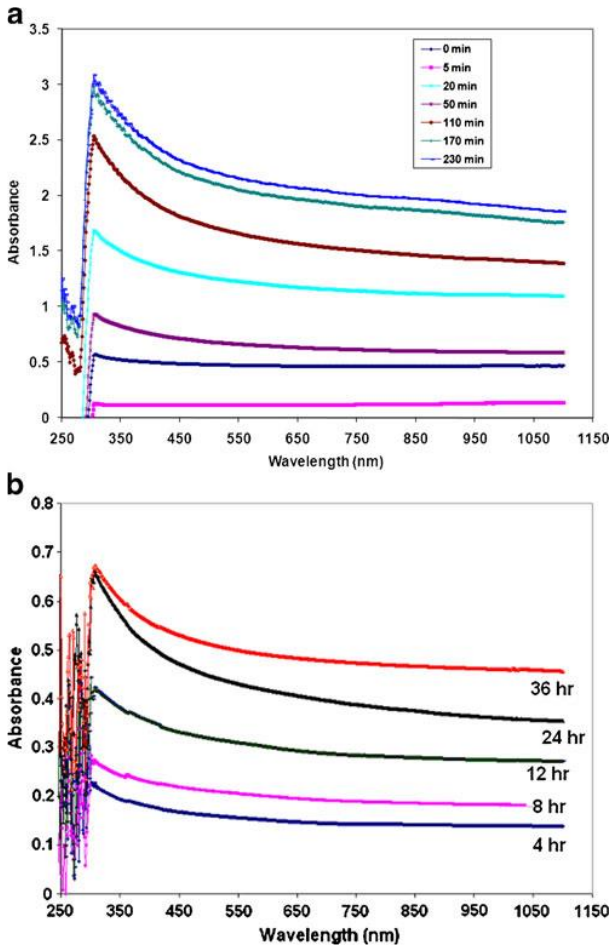

Figure 2-6 UV-visible spectra of MWCNTs in the solvent after different ultrasonication time (a) and in epoxy with different stirring duration. [30]

2.1.3 Graphene and carbon nanotube hybrid nanostructure

Another widely used approach combines CNTs and graphene to generate a 3-dimensional (3D) structure [3]. The introduction of graphene layers into the CNTs could prevent the

agglomeration of CNTs as the graphene layers play the roles of spacers that enter the spaces of CNTs [28, 31]. Because of the π-π interactions between carbon atoms, the CNTs can be attached onto the surface of each graphene layer. In addition, the introduction of functional groups on the surface of both graphene and CNTs could also make them better dispersion in solutions before mixing due to the electrostatic repulsion effects. By mixing the GO and CNTs, the as-prepared 3D GO-CNT nanostructures (GNT) display well-dispersed structures [28]. According to previous research, not only do the GOs act as the spacers, but the CNTs also function as bridges that connect gaps between GO layers, and the combination finally resulted in a subsequent 3D carbon nanostructure [3] [32]. This 3D structure could be applied in numerous fields. Zhang et al. detailed a method to prepare aqueous dispersions of different weight fractions of CNTs and GOs [28]. GOs and CNTs were first dispersed in water by ultrasonication, followed by a centrifugation process to remove un-stabilised CNTs and excess GOs, Figure *2-7*. The CNT-GO suspension (Figure *2-7*c) remained stable even after centrifugation. Besides the traditional preparation methods, the freeze-drying method has become increasingly popular.

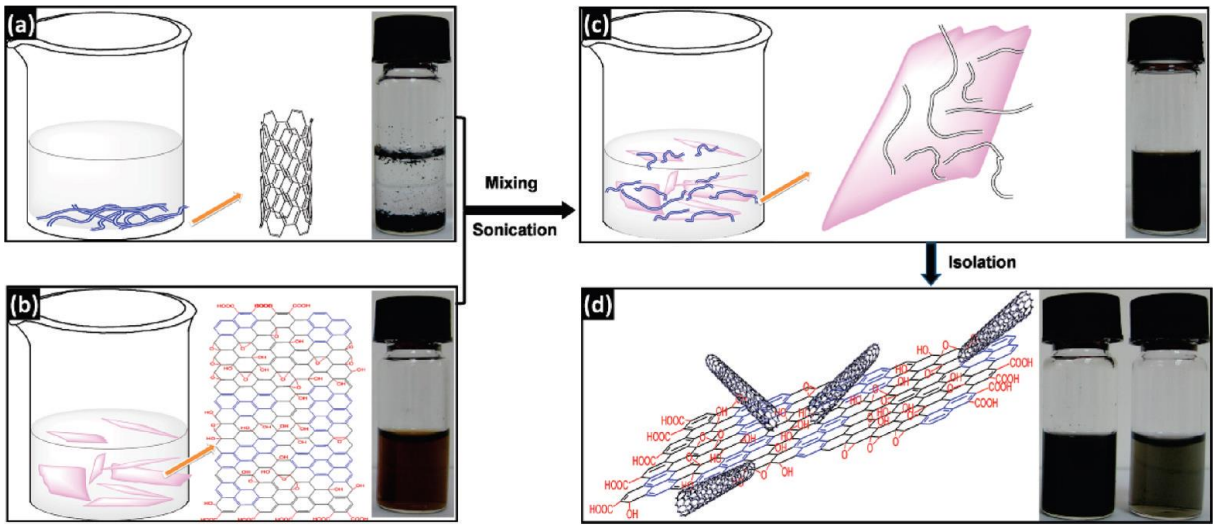

Figure 2-7 The dispersity comparison among CNT (a), GO (b) and CNT-GO (c) and schematic mechanism (d) of preparing CNT-GO complexes. [28]

Freeze-drying method

In recent years, a new method, the freeze-drying method, has been widely applied to prepare

well-dispersed structures, which is mainly based on the sublimation process [33-35]. When the dispersion is uniformly dispersed, the dispersion is then quickly moved into a liquid nitrogen atmosphere which could largely keep the well-dispersed structure [32]. Hui et al. prepared a 3D GO-MWCNT foam as a building unit [33]. Liang et al. reported the Fe_3O_4-GO-CNT foam which was also obtained through the freeze-drying method [34]. The anisotropic graphene aerogel with a highly aligned porous structure was obtained by Liu et al. through freeze-drying [35]. Similarly, the carbon ultra-flyweight aerogels (UFAs) were prepared via freeze-drying CNTs-GOs solutions and reducing them with hydrazine vapour by Sun and et al, and Figure *2-8* details the UFAs products. [32]. The carbon structures were kept well-dispersed in water, and then the water was removed by sublimation (freeze-drying). The carbon aerogels exhibited extremely low density (Figure *2-8*c) and well-dispersed structures (Figure *2-8* d-h), which resulted from the synergistic effect of CNT and graphene. Therefore, a combination of pre-treat CNT and graphene, which contain a large number of functional groups, could be effectively dispersed and stay stable for a long time in solution. The subsequent freeze-drying process could largely keep the well-dispersed structure of this hybrid composite. It becomes an ideal preparation method to prepare a well-dispersed CNT-GO structure.

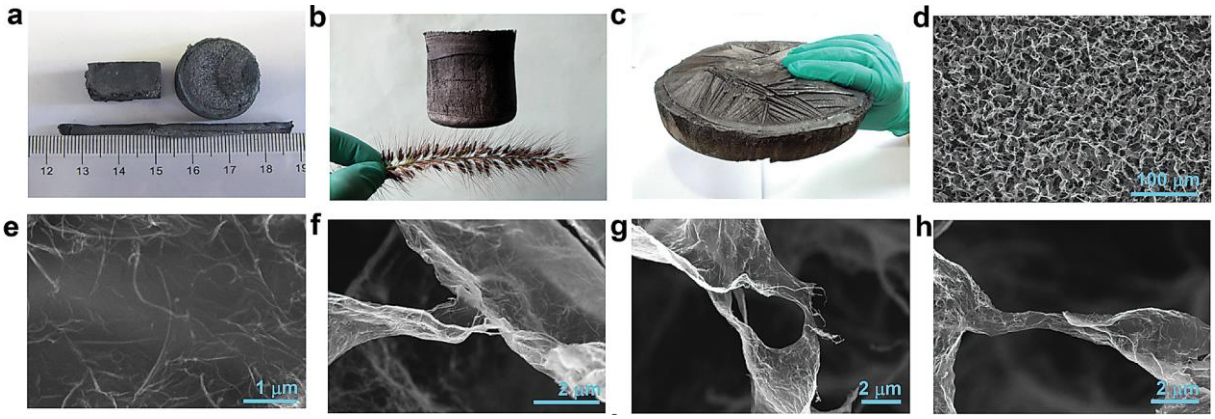

Figure 2-8 Macroscopic and Microscopic structures of UFAs. (a) Digital photograph of UFAs with diverse shapes. (b) A 100 cm^3 UFA cylinder standing on a flower-like dog's tail. (c) A ~ 1000 cm^3 UFA cylinder (21 cm in diameter and 3 cm in thickness). (d-e) Microscopically porous architecture of a UFA at different magnifications, showing CNT-coated graphene cell walls. (f-h) SEM images of different interconnections for CNTs-coated graphene (graphene@CNTs) cell walls: overlapping (f), twisting (g), and wrapping (h). [32]

Since the successful preparation of GNT nanostructures through various approaches, well-dispersed GNTs have been widely applied. For example, Ma et al. has reported a 3D hybrid material comprising graphene and acid-MWCNTs [31]. The results showed that the obtained 3D hybrid material could be applied as a working electrode in dye-sensitized cells (DSSCs). This 3D hybrid material not only provided greater dye adsorption and a lower level of charge recombination when compared with solo MWCNTs or graphene as electrodes but also demonstrated a conversion efficiency of 6.11 % with a TiO_2 matrix, which is 31% higher than that of conventional TiO_2 based devices [31]. The GO-MWCNT hybrids reinforced epoxy composites were investigated by Kim et al. [36]. GO-MWCNT sample was prepared by mixing and vacuum filtration and then mixed with epoxy resin as the matrix. The results showed that the increase of the GO-MWCNT amount (from 10 - 50 wt.%) could effectively enhance the thermal conductivity of the matrix. This enhancement can be ascribed to the formation of 3D heat conduction paths by the addition of MWCNTs [36].

2.2 Preparation of graphene and/or carbon nanotube reinforced composite

In this section, different preparation methods of graphene and/or carbon nanotube reinforced composites (including metal and polymer matrix) are introduced.

2.2.1 Carbon based materials reinforced metal composites

Powder metallurgy routes, including conventional sintering, hot pressing and spark plasma sintering, are introduced in section 2.2.1.1, while chemical and physical vapour deposition and molecular-level-mixing approaches are detailed in section 2.2.1.2.

2.2.1.1. Powder Metallurgy Routes

The powder metallurgy technique is an established sample preparation method that can date back to brick making. It can be described as the fabrication of components from powdered materials. Typically, powders are pressed in a die with the required shape, and pressure is applied under cold or hot compaction. The pressed compact has porosities and thus must be further densified using other processes. A common consolidation method is sintering, in which the pressed compact is heated in a furnace at a certain temperature below the melting point of the material. This relies on mass transport via diffusion. The main advantage of the powder metallurgy technique is that nearly every composition can be synthesised, as powder metallurgy is not dictated by thermodynamics and phase diagrams. It is easy to disperse the two phases in powder forms, and the level of mixing is then governed by the size of the components added. Since no bulk melting occurs, there is less rearrangement in distributing the phases of the final product. For example, the powder metallurgy technique has been used extensively for the fabrication of Al-CNT and Cu-CNT composites. It has also been used for other metal-matrix-CNT composites, such as Mg, Ni, Ti, and Ti-based alloys, intermetallics, and Ag and Sn-alloys [37]. Consolidation methods (including conventional sintering, hot pressing and spark plasma sintering) are introduced for metal matrix-CNT composite processing using powder precursor as the starting material.

Conventional sintering

Conventional sintering is the simplest and most common method for producing carbon nanotube-metal composites. Fabrication of Al-CNT and Cu-CNT composites, as well as the Ag, Mg, and W-Cu composites with CNTs, have been reported [38, 39]. In general, it is advantageous to retain the size of matrix grains of composites in the nanometer region because a significant improvement in hardness, yield strength and wear resistance of composites can be

obtained in the presence of nanosized grains. For example, Zhong et al. attempted to prepare nano-Al/SWCNT composites having a nano-grained matrix [38]. The composites were prepared by mixing Al nano-powders (53 nm) and purified SWCNTs in alcohol ultrasonically. The blended material was dried, cold compacted into disks at room temperature, followed by hot consolidation at 260 - 480°C under the pressure of 1GPa. Excessive grain growth occurred during hot compression of the Al nano-powders. The grain size of the composite matrix grew up to ~800 nm during hot compaction at 480°C. Using this method, the nanotubes have little effect on restricting the grain growth of matrix grains in this example. SWCNTs tended to be dispersed as bundles rather than individual nanotubes in the Al matrix. Gupta and coworkers prepared Mg-MWCNT nanocomposites with low filler loadings (0.06, 0.18 and 0.30 wt%) by sintering and hot extrusion [39]. Clusters of MWCNTs were observed in the 0.3 wt% Mg-MWCNT nanocomposite and limited improvement in ultimate tensile strength as expected. In addition, as shown in Figure *2-9*, the increased amount of CNTs in the matrix led to the porosity in the Mg matrix, which resulted in the worse property.

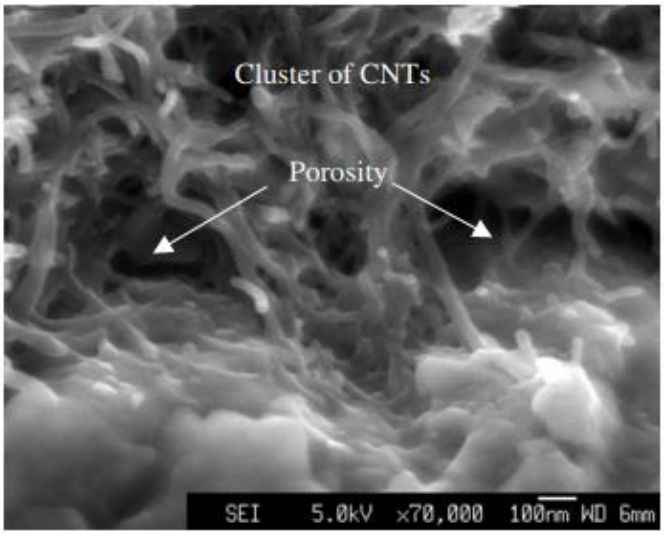

Figure 2-9 Clustering of CNTs leading to an increase in porosity in the Mg matrix. [39]

Hot pressing (HP)

Using pressure during sintering to result in denser compacts has advantages, and hot pressing

can be traced back to the patent in 1933 by George F. Taylor [40]. Wei et al. has reported the Al-CNT composites prepared through hot pressing [41]. The Al powders were hand-mixed with different ratios of CNTs (from 1 - 10 wt.%), and the mixed powders were then hot pressed at 520°C with a pressure of 25 MPa for more than 30 min. Unfortunately, CNT agglomerates were found mainly at the Al grain boundaries, while few single CNTs were found embedded within the matrix. The electrical resistivities at room temperature of the products were investigated. The results showed a slight decrease in electrical resistivities with the volume increase of carbon nanotubes in the Al matrix (from 4.4 to 6.6 μΩcm), which can be ascribed to the CNT clusters in the matrix. Baik et al. used a novel approach that combined the SWCNTs with a copper matrix [42]. In the study, SWCNTs were first coated by Ni through the electroless plating and then mixed with copper powders via mechanical mixing. Figure *2-10*a displays the uniform coating of Ni on the surface of the SWCNTs. Because the density of Ni is close to Cu, the obtained mixed powders can be homogeneously mixed (Figure *2-10*b). As shown in Figure *2-10*c, the hot press process was carried out at 600°C under 45 MPa with a ramping rate of 15°C min^{-1}. The obtained pellet is displayed in the insert figure of Figure *2-10*. Thus, to modified the CNTs with metal component that is close to the matrix material would be competitive approach to overcome the poor interface between CNTs and matrix.

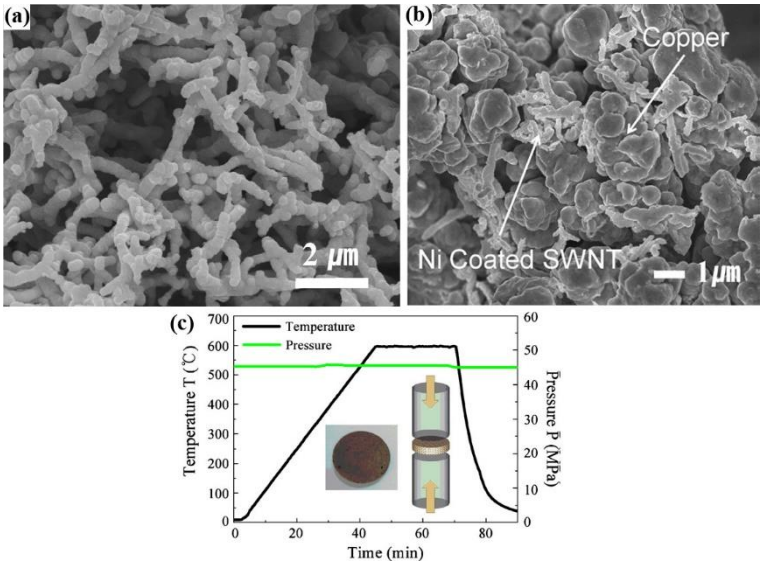

Figure 2-10 (a) SEM image of Nickel-coated single-walled carbon nanotubes, (b) Magnified SEM image of the mixture, (c) Temperature and pressure conditions for the hot-pressing process. The inset images show a disk-shaped specimen and a schematic diagram of the apparatus. [42]

Combined to the CNT reinforced composites, graphene materials have also been reported to enhance the metal matrix by HP. For example, graphene nanosheets (GNS) have been introduced to reinforce pure Cu powders by Yue et al. [43]. The GNSs were first mixed with Cu powders via ball-milling, and the results showed that the uniform dispersion of the GNSs could be obtained after 5 h ball-milling (Figure *2-11*b). The obtained mixed powders were then placed into a hot-press furnace and sintered at 800°C with a pressure of 25 MPa for 1 h under vacuum (Figure *2-11*a). It was found that the increase of GNSs content (over 5 wt.%) would result in aggregation of GNS. He et al. reported Ag nanoparticles on graphene as an enhancement in the Cu matrix [44]. The Ag-GO composites were synthesised through a chemical and thermal reduction process. Specifically, $Ag(NH_3)_2OH$ solution, which was first prepared by drop-wise adding ammonia into the $AgNO_3$ solution, was mixed with GO dispersion in an ultrasound bath for 30 min. Vitamin C solution was then slowly added as the reduction agent and stirred at 95°C for 1 h. After filtration and drying, the obtained powders were calcined under Ar/H_2 atmosphere at 700°C for 2 h, and the obtained relative density of

the pellet is around 96.5%. The morphology of the obtained Ag-GO composites is shown in Figure *2-12*. After ball-milling with Cu powders, the mixed powders were then hot pressed at 700°C for 45 min with a pressure of 50 MPa through the Vacuum Uniaxial Hot-Pressure Sintering Furnace. Thus, to modify the carbon materials with metal particles has become a popular approach to improve the interface between carbon fillers and the matrix.

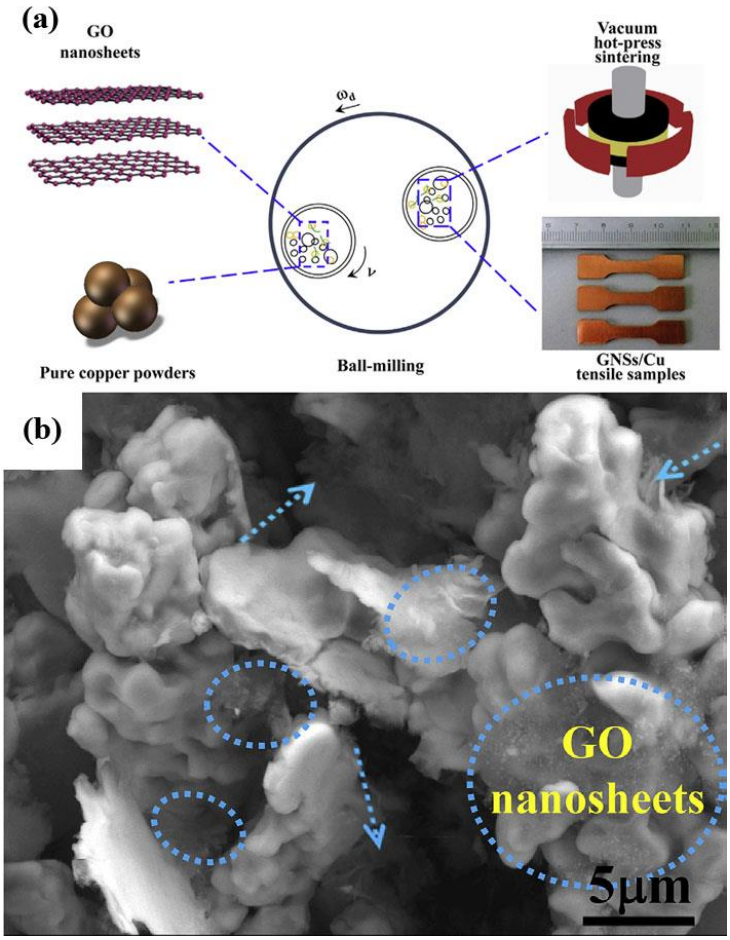

Figure 2-11 (a) Schematic of the preparation of GNSs/Cu composites and (b) SEM image of GO-Cu mixed powders. [43]

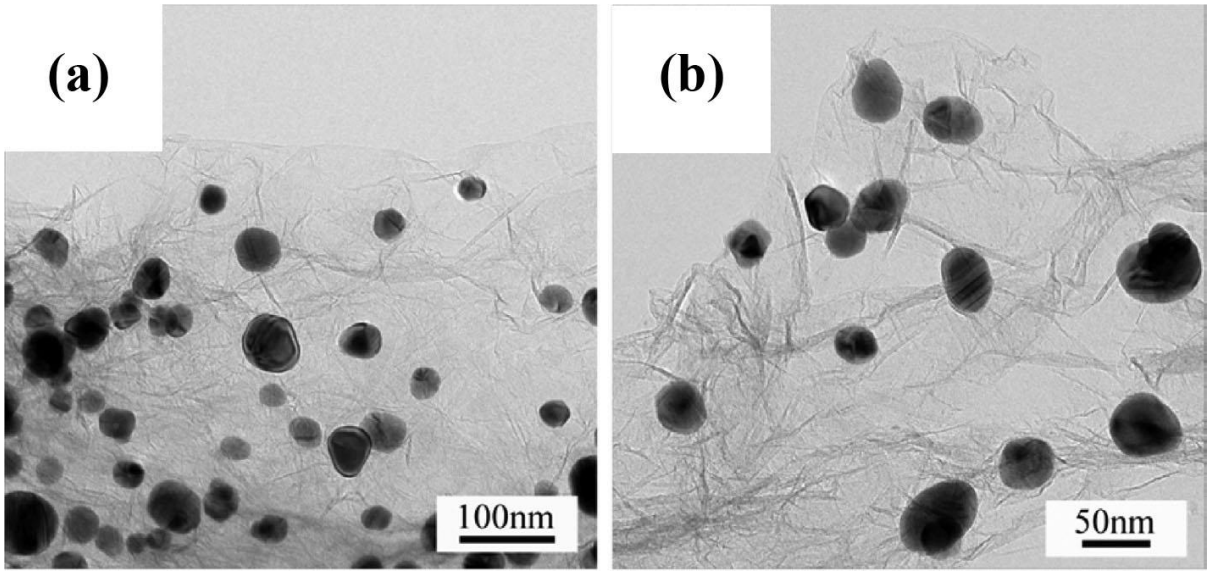

Figure 2-12 TEM images of the Ag-GO composites under different magnification. [44]

Spark plasma sintering (SPS)

Spark plasma sintering (SPS), which is also known as electric field assisted sintering (EFAS), plasma assisted sintering (PAS) or pulsed electric current sintering (PECS), is a variation of hot pressing. The heat source of SPS is a pulsed direct current (DC) passed through the die or the powders (depending on whether the powder is electrically conducting) during consolidation. SPS can achieve much higher consolidation in a shorter time when compared with the traditional techniques (i.e., HP) due to the low voltage spark pulses current. SPS has already been widely reported to fabricate graphene and/or carbon nanotube reinforced composites. For example, in the Cu-CNT composites [49], CNTs were first ultrasonicated in ethanol to separating clusters. After drying, Cu powders of 100 nm and 200 μm size were then mixed with the CNTs to obtain compositions containing 0 to 15 vol.% of CNT. The powder mixtures were ball milled for 24 h. The resulting mixture was consolidated by SPS at 750°C for a hold time of 1 min at a pressure of 40 MPa. Chu et al. developed a different approach of mixing MWCNTs with Cu powders through the particle composite system (PCS) [45]. As shown in Figure *2-13*, it can be found that the powders could be effectively mixed by the blades in the machine. After mixing, the obtained powders were then sintered at 600°C for 5 min under a pressure of 50

MPa with a ramping rate of 100 °C min^{-1}. Wang et al. prepared Al-CNT composites utilising SPS [46]. The MWCNTs, which were first acid-treated, were then mixed with Al powders in ethanol under ultrasonication. After drying, the obtained mixed powders were consolidated by SPS at 580°C for 10 min with a uniaxial pressure of 40 MPa. The obtained relative densities of the products decreased slightly with the increase of the MWCNT contents, but all of them were above 98% from 1-5 wt.%. Although via different mixing approaches, the obtained relative dentisies of these SPS pressed pellets all reached above 98% in shorted duration compared to HP.

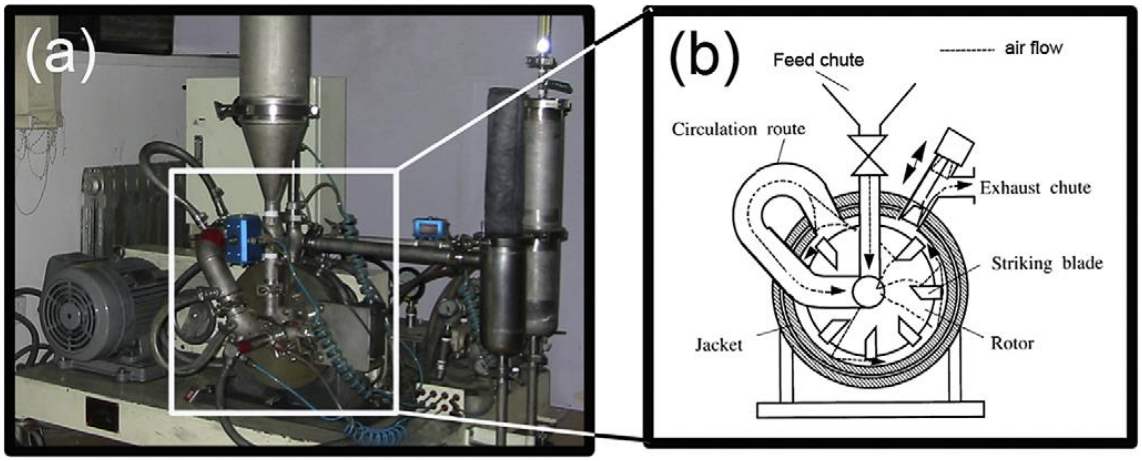

Figure 2-13 Particle composite system (PCS): (a) photograph, and (b) schematic illustration. [45]

Like CNTs, graphene is also widely reported to be fabricated in the metal matrix with the assistance of SPS. Zhou et al. has reported copper–graphene bulk composites with a homogenous graphene dispersion [47]. Polyvinyl pyrrolidone (PVP) was added to graphene dispersion during the stirring, which could improve the dispersity due to the hydrophilicity (Figure *2-14*). Then, polyvinyl alcohol (PVA) was added to the Cu powders dispersion and stirred for 1 h. The PVP modified graphene dispersion was then added drop by drop into the PVA modified Cu slurry. The mixture was then stirred, filtrated, rinsed and dried. After that, the obtained mixed powders were then processed under Ar/H_2 atmosphere at 300°C for 30 min and 700°C for 120 min. SPS was then used to consolidate the graphene-Cu mixed powder at

700°C for 5 min with a pressure of 30 MPa. Similar to CNT enhanced composites, SPS can also be applied to prepare dense pellets of graphene based composites.

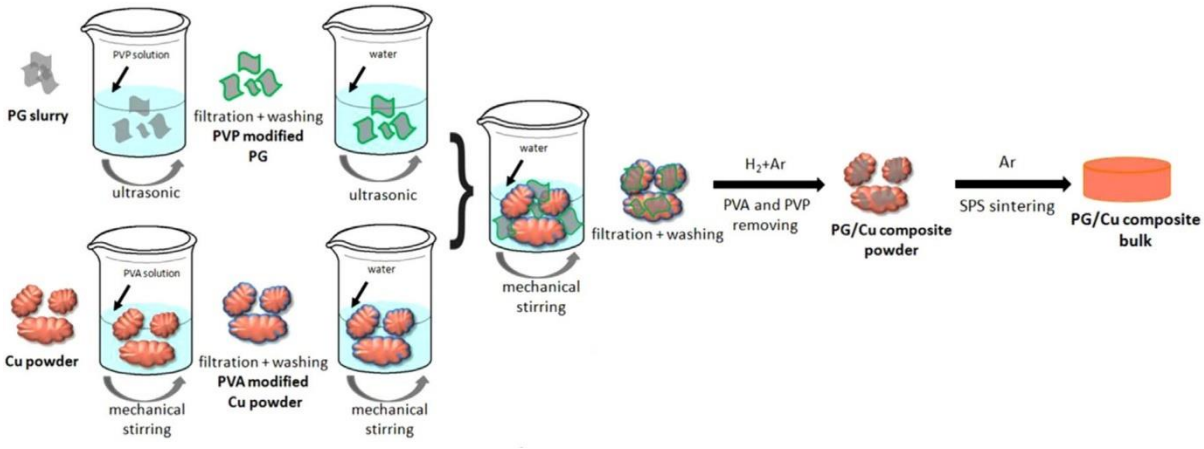

Figure 2-14 Schematic of preparation graphene-Cu composites. [47]

A graphene network enhanced Cu composite was investigated by Chu et al. [48], which demonstrated high alignment of graphene in the matrix. The schematic of the preparation method is displayed in Figure *2-15*. The large-sized graphene nanoplatelets (25 μm in length) were first dispersed in the anhydrous ethanol under sonication for one hour. The Cu powders were then added to the homogeneous graphene suspension, followed by vortex-mixing for another hour. After that, the well-dispersed suspension was vacuum filtrated and dried for 24 h. The obtained mixed powders were then densified using the SPS at 750°C for 5 min under an axial pressure of 50 MPa. The obtained densities of the pellets decreased with the increase of the graphene ratios (from 5-35 vol. %). In this research, it was found that graphene layers tented to be aligned in the X-Y direction, which is perpendicular to the pressing force, during SPS pressing.

Figure 2-15 Schematic illustration of the preparation process of GNP/Cu composites. [48]

Table *2-1* compares the information from all these consolidation processes mentioned above. It can be found that the pressed samples from the conventional sintering process always need a long duration and the whole process is also complicated. The relative densities of these obtained pellets are lower than the others. Meanwhile, the hot-pressed samples show denser pellets, and the consolidation duration is also shorter than the conventional sintering. Meanwhile, the SPS consolidated samples demonstrated the best relative density (above 98%) and the entire process is simple and causes less time (a couple of mins) compared to conventional sintering and HP. Therefore, SPS can be regarded as the optimal consolidation process to prepare graphene and/or CNT reinforced metal composites. In addition, the previous research also demonstrated that the bare carbon materials had a poor interface with the metal matrix even through advanced consolidation approaches. The introduction of metal particle decoration, which is close or same to the matrix material, could be a potential choice to improve the interface between carbon fillers and matrix.

Table 2-1 Consolidation information of different samples via different Powder Metallurgy Routes.

	Components	Parameters	Relative density (%)	Ref.
Conventional sintering	Al-SWCNT	Cold compacted into disks, and then hot consolidated at 260-480°C under 1 GPa	90	[38]
	Mg-MWCNT	Compacted under 723 MPa and sintered at 650°C for 2 h	95	[39]
Hot pressing	Al-CNT	Hot-pressed at 650°C under a pressure of 25 MPa for 30 min	96-97	[41]
	Cu-Ni-SWCNT	Hot-pressed at 45 MPa, the temperature was ramped to 600 °C in 40 min and kept constant for 30 min	96	[42]
	Cu-GNSs	Sintered at 800°C with a pressure of 25 MPa for 1 h under vacuum	95	[43]
	Cu-Ag-GO	Hot pressed at 700°C for 45 min with a pressure of 50 MPa	97	[44]
SPS	Cu-MWCNT	Sintered at 600°C for 5 min under a pressure of 50 MPa with a ramping rate of 100 °C min^{-1}	98	[45]
	Al-CNTs	Consolidated by SPS at 580°C for 10 min with a uniaxial pressure of 40 MPa	98	[46]
	Cu-graphene	consolidate the graphene-Cu mixed powder at 700°C for 5 min with a pressure of 30 MPa	99	[47]
	Cu-graphene	SPS at 750°C for 5 min under an axial pressure of 50 MPa	97	[48]

2.2.1.2. PVD, CVD and MLM approaches

Physical vapour deposition (PVD) routes such as sputtering techniques can be used to deposit metal over carbon materials and produce composites with small dimensions (of the length scale of the CNT). This could also be used for the production of 1D nanostructures and aligned CNT

composites. For example, the vertically aligned MWCNTs were first produced through the xylene-ferrocene chemical vapor deposition (CVD) method [49]. Then, one micrometer thick pure Al was then deposited by magnetic sputtering. Figure *2-16* displays the SEM and XRD results of the as-prepared Al-CNT composites. It can be found that Al was successfully coated on the surface of these CNTs. Sputter-depositing metal nano-particles on SWCNT bundles was shown by Zuo et al. [50], and the results showed that self-organization occurred into evenly spaced clusters. Au, Ag, and Cu were found to form an array of nanocrystals (~10 Å) on the surface of CNTs (Figure *2-16*), whereas Ti, Zr, and Mo formed nanowires at the grooves of the SWCNT bundles (Figure *2-17*). Thus, such PVD approaches can be regarded as promising approaches to prepare metal decorated CNT composites. Combined the previous findings, these decorated CNTs maybe potential candidates that have better interface with metal mtrices.

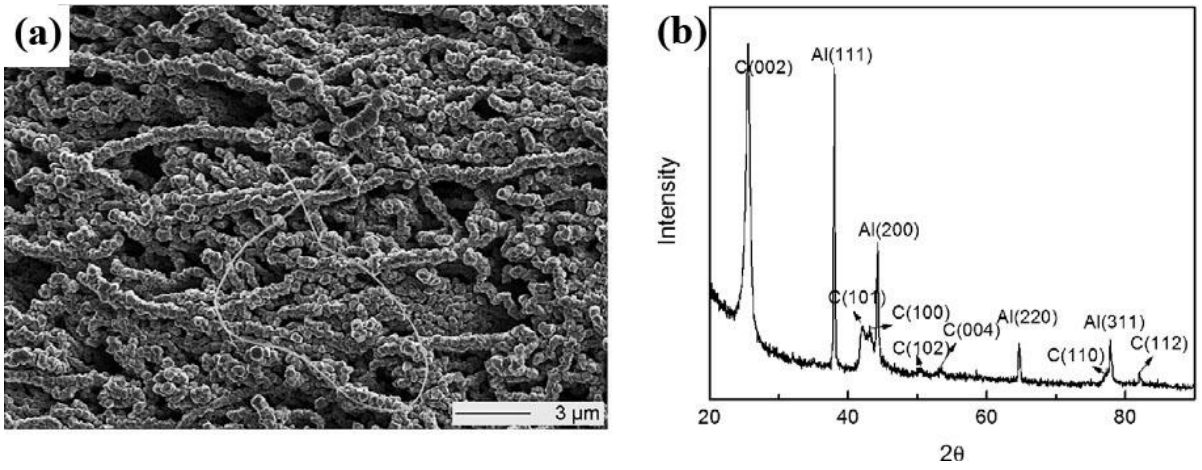

Figure 2-16 (a) SEM image of the as-prepared Al-CNT composites and (b) XRD XRD patterns of the as-deposited Al/CNT composites. [49]

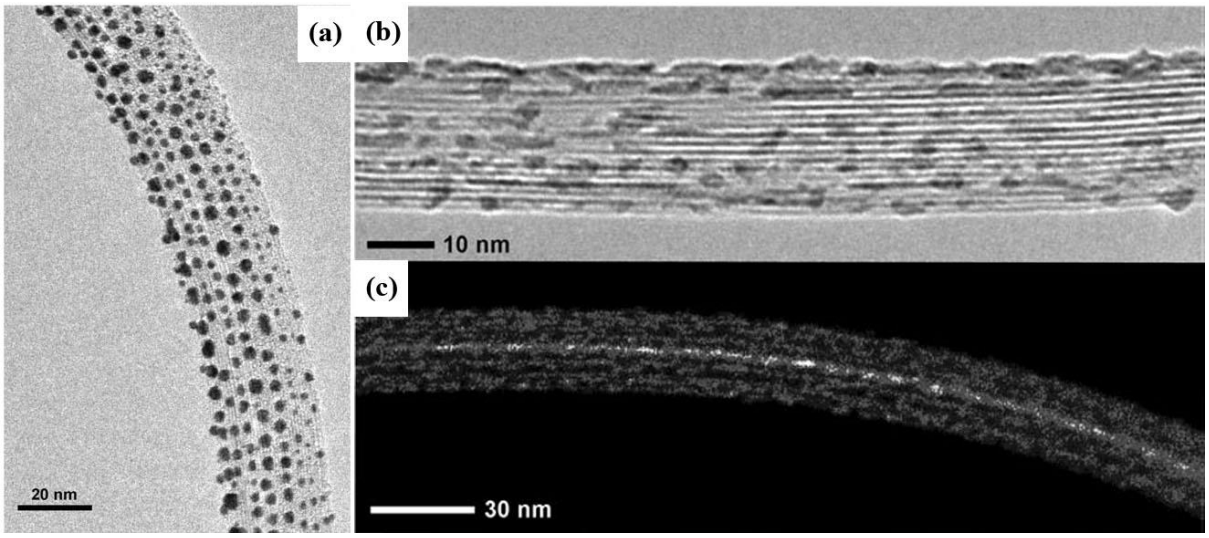

Figure 2-17 (a) TEM micrograph of multiple arrays of Au clusters on an SWCNT, (b) TEM image of a CNT bundle after deposition of Ti and (c) High-angle dark-field STEM image of a continuous ultrafine Ti nanowire formed on a curved CNT bundle. [50]

In addition, CNTs have also been coated with tungsten through a physical vapor deposition (PVD) method provided by Zhu et al. [51]. Specifically, CNTs were put in an alumina crucible, and a W filament at 8 mm distance was heated to 2200°C in H_2 flow of 1200 sccm at 50 Torr. Figure *2-18* shows the obtained W-coated CNTs. Although it can be found that W was coated on the CNTs, there were still un-coated regions. Si-CNT composites, which have been used as an active anode layer in lithium-ion batteries, have been prepared and reported by Li et al. [52]. Si-coated CNTs have been produced by the decomposition of silane (SiH_4) over CNTs to increase the thermal stability of CNTs [53]. The SiH_4 was pumped into the vacuum chamber, the clean MWCNTs were exposed to SiH_4 and the gas could adequately penetrate MWCNTs due to the pressure difference. The SiH_4 was then decomposed under Ar atmosphere. As shown in Figure *2-19*, the well-covered coating of Si of 10 nm thickness could be observed. Therefore, the CVD or PVD based approaches both show great potential to prepare uniform metal decorated CNTs samples, and the decorated metal particles could be found to be uniform and tiny than traditional synthesis methods.

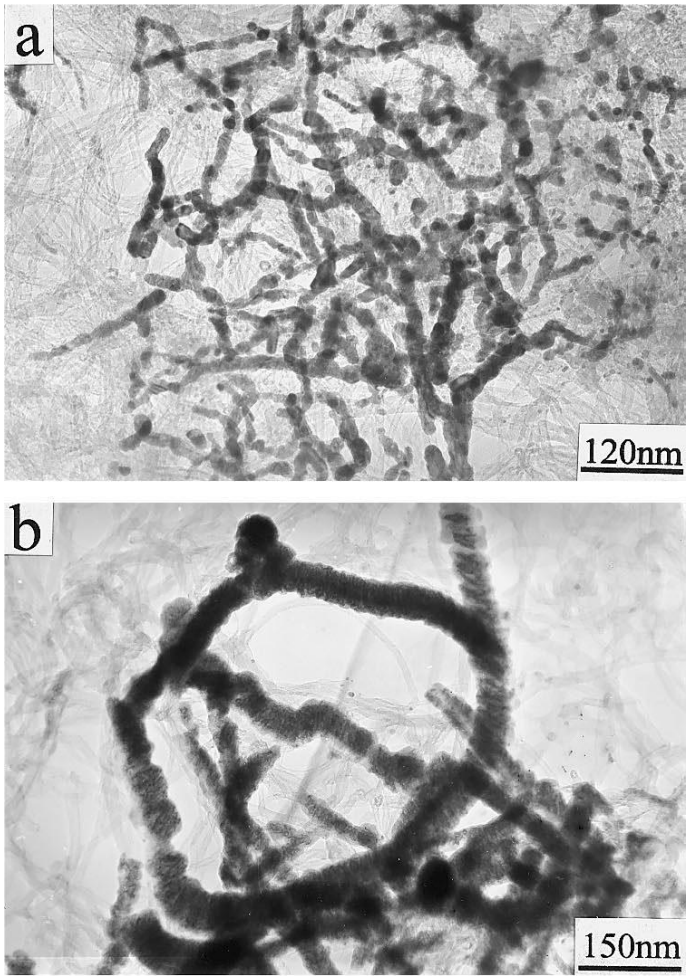

Figure 2-18 the micrograph of composite nanowires based on coating W on CNTs. [51]

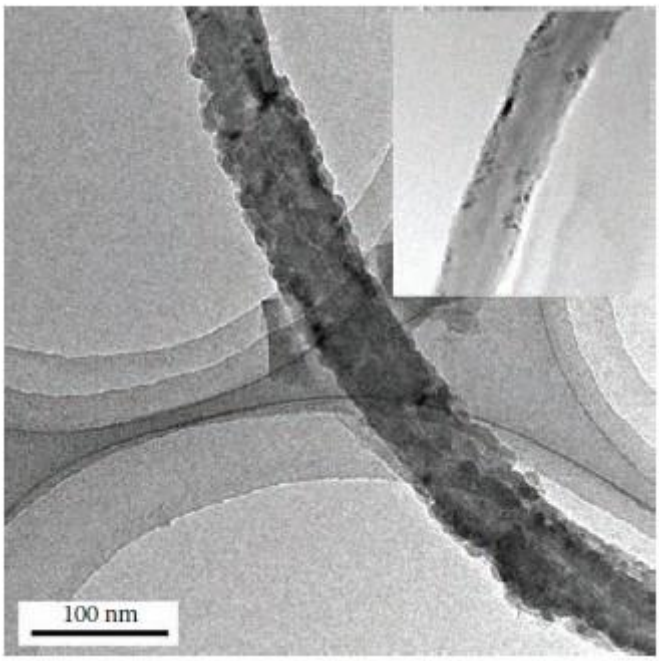

Figure 2-19 TEM image of Si-coated MWNTs using cycled vacuum-feeding CVD. [54]

Molecular-level-mixing (MLM) method is a composite powder preparation technique

developed by Cha and co-workers [55]. As the name suggests, the contact of metal ions with well-dispersed CNTs is achieved on the molecular level by this method. Figure *2-20* shows the schematic of the preparation process of the CNT-Cu nanocomposites. The CNTs were initially acid-treated, and the functional groups were attached onto the surface of them. After that, the Cu^{2+} solution was added into the well-dispersed acid-treated CNTs. The Cu ions were attracted to the functional groups based on the electrostatic attraction as the different charges of Cu ions (positive) and functional groups (negative). Figure *2-20* shows the SEM and TEM micrographs of the resultant Cu/CNT powder. The CNTs can be found uniformly mixed with the Cu particles. Thus, besides PVD and CVD, such an MLM approach also promises in preparing uniform distribution of metal particles with CNTs.

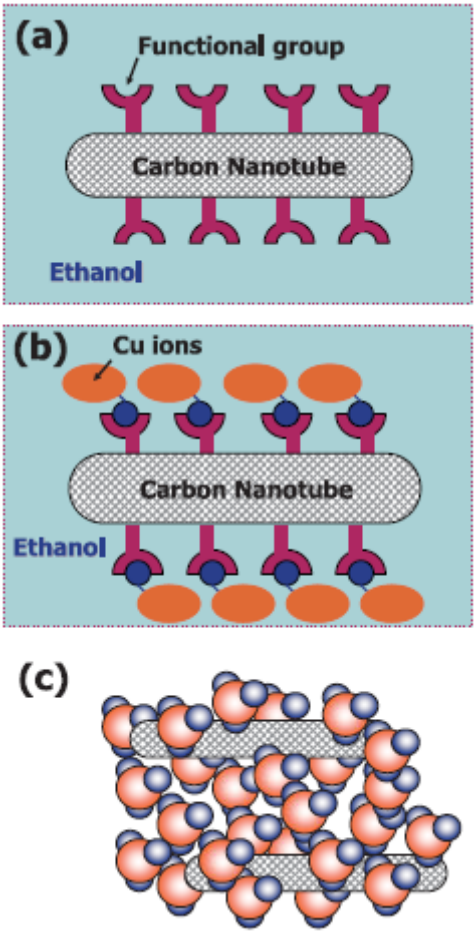

Figure 2-20 Schematic of preparing MLM process to fabricate CNT-Cu composite powders. [40]

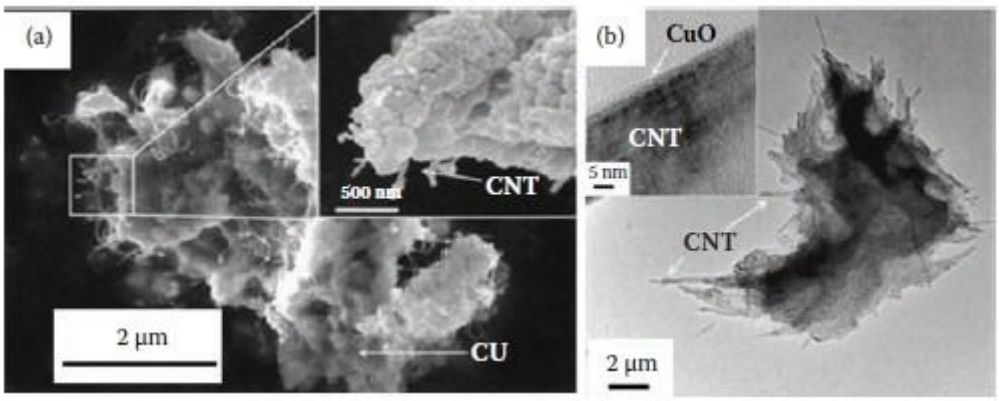

Figure 2-21 (a) SEM and (b) TEM image of the CNT-Cu composite powders. [15]

Similar to the CNT-Cu composites, GOs have also been introduced with Cu via the MLM process by Jeon et al. [56]. Figure *2-22* displays a schematic of the preparation method. GOs were first obtained by Hommer's method. Like the CNT-Cu system, because of the large numbers of functional groups on the surface of GO layers, Cu ions that were added to the GO dispersion became attached to them. The NaOH aqueous solution was then added to obtain CuO, and the GO/CuO nanocomposites were then rinsed and dried. The CuO in the composite powders were then reduced to Cu under hydrogen atmosphere. Figure *2-23* displays the SEM image of the GO-Cu composites, and the Cu nanoparticles can be clearly seen on the surface of the GO layers.

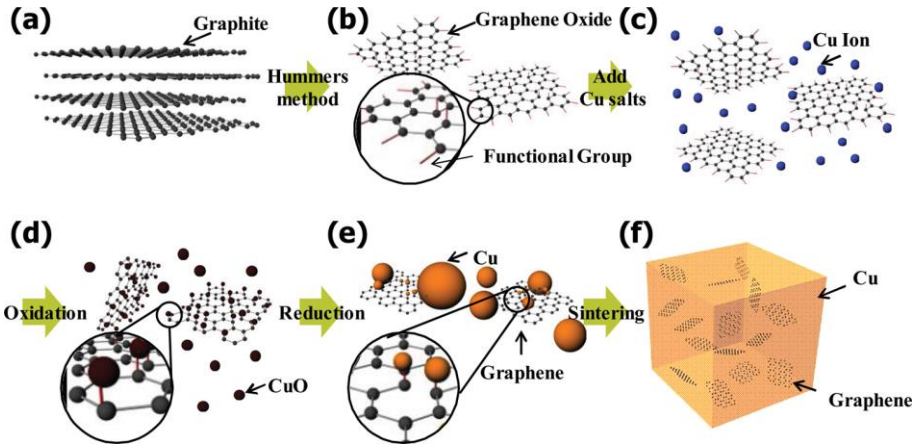

Figure 2-22 Schematic of the fabrication process of GO-Cu nanocomposite through MLM method. [56]

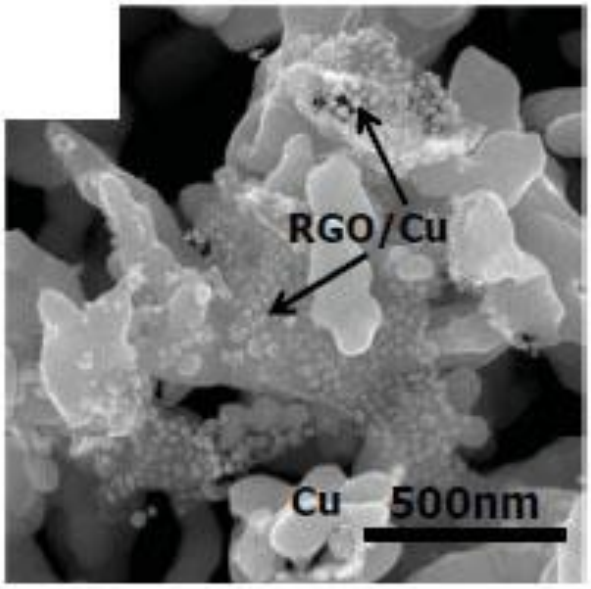

Figure 2-23 SEM image of the GO-Cu composites. [56]

He et al. reported an in-situ space-confined strategy based on the MLM method to construct well-dispersed CNTs embedded in a 3D graphene network hybrid structure, and this structure was then introduced to reinforce the Cu matrix [57]. The MWCNTs suspension was added drop by drop in the mixture of $Cu(NO_3)_2$, NaCl and glucose solutions. After dispersion under intense stirring, the mixed homogeneous suspension was rapidly frozen by liquid nitrogen and then kept at -20°C for 12 h. The frozen water was then removed by freeze-drying technology. The obtained powders were then calcinated at 750°C for 2 h under H_2 atmosphere (200 ml min^{-1}). The as-prepared CNT-GN/Cu composites powders were then added into the $Cu(CH_3COO)_2$ and $NH_3 \cdot H_2O$ solution. After the evaporation of the water, the obtained mixed powders were then dried and calcined at 350°C in 5 h in air, and then reduced at 400°C for 3h under H_2 atmosphere. Although this is a complicated preparation method that a successful 3D CNT-Graphene-Cu structure was obtained, the introduction of freeze-drying method could effectively keep the well-dispersed structure of the samples.

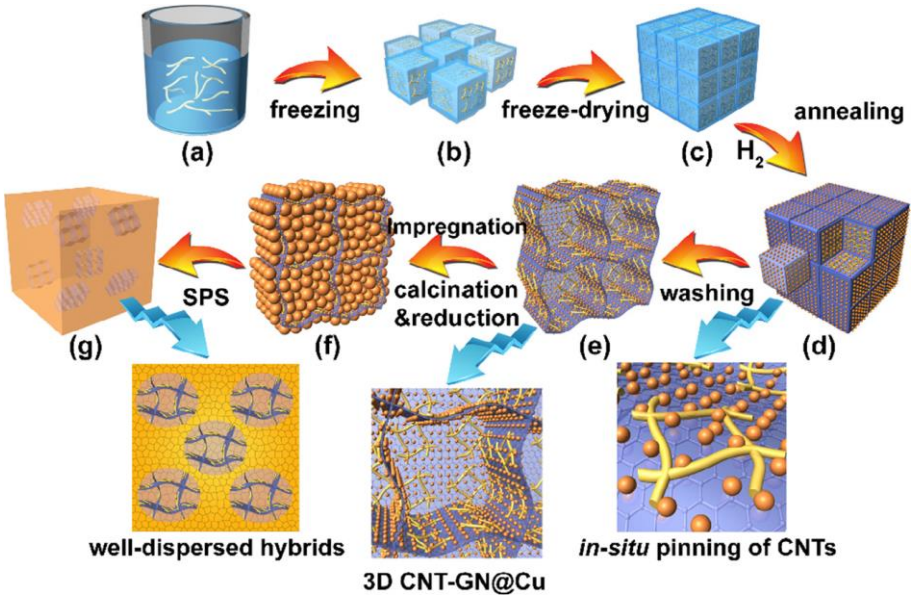

Figure 2-24 Schematic of preparation of 3D CNT-GN/Cu nanocomposites. [57]

As detailed above, various strategies have been developed and reported to prepare CNT and/or graphene based metal composites. As traditional powders metallurgy routes, SPS is regarded as the optimal method that could result in denser products via a much shorter and more convenient process than HP and conventional sintering. However, the interface between bare carbon fillers and matrix in the obtained samples was poor. Several methods were attempted. One is to decorate the carbon materials with metal particles that are close or same to the matrix material. Thus, novel techniques (including PVD, CVD and MLM apporaoches) have been explored. The results showed the products with uniform distribution of metal particles. Combining such novel techniques and SPS could be a promising choice to prepare CNT/graphene - metal composites.

2.2.2 Carbon based materials reinforced polymer composites

Polymer materials, which have been regarded as good electrical insulators in the past, have now attracted increasing attention in numerous applications (such as electronic and mechanical devices) with the advantage of the introduction of fillers [58]. Among these fillers, carbon materials, especially the 1D CNTs and 2D graphene materials, are regarded as ideal candidates.

Because of the unique performances of the CNT and graphene materials discussed above, the CNT and/or graphene enhanced polymer composites have been widely investigated in different platforms, especially as electronics [59]. To prepare advanced carbon-based polymer composites, uniform dispersion of these carbon materials (including CNTs and graphene) is a priority. Solution methods are one of the most widely used processes for carbon materials-polymer dispersion. Three different protocols involve the dispersion of the carbon materials into polymers for the preparation of the polymer composites: (1) dispersion of carbon materials into a monomer followed by polymerisation; (2) dispersion of carbon materials in a liquid that also includes dissolved polymer followed by removal of the solvent; (3) dispersion of carbon materials in dispersed monomer, followed by polymerisation [58].

2.2.2.1. Dispersion-Reaction

The dispersion-reaction process disperses the carbon materials in the monomer via methods such as ultrasonication and high-shear mixing. Then the monomer is polymerised. Both the thermoplastic and thermoset polymers can be prepared via this process. The most commonly used thermoset monomers include epoxy [60, 61], vinyl ester [62, 63] and polyimides [64, 65], while the most commonly used thermoplastics from liquid monomers are polystyrene [66, 67] and acrylates [68-70].

The addition of dispersants has also been investigated in the Dispersion-Reaction process. The research shows that there is a deleterious effect on mechanical properties to the final composites if the dispersant is in the solid state [71]. Functionalisation process of the carbon materials is also an effective way to improve the dispersity of the carbon materials in the polymer. One of the results showed that the functionalisation of the CNTs obviously increased the dispersity of the treated CNTs in epoxy resin and definitely increased the mechanical property of the final products [72]. The covalent MWCNTs were found to have a better dispersion in the epoxy

matrix compared to non-covalent MWCNTs and pristine MWCNTs. Epoxy composites containing covalently modified MWCNTs also showed greater modulus.

Another method is to directly impregnate the polymer into the as-prepared carbon materials. Kim et al. provided a simple preparation method to synthesise GO-CNT/epoxy composite [36]. As shown in Figure *2-25*, the pre-treated CNTs were first mixed with GO in water with the assistance of ultrasonication to obtain a homogeneous suspension. The suspension was then filtered via a vacuum filtration system, and the obtained GO-CNT cake was then peeled off from the membrane and completely dried. The epoxy, which contained the curing agent (with a ratio of 2:1), was then added drop by drop onto the GO-CNT cake. The added epoxy could penetrate into the fabricated cake easily [28].

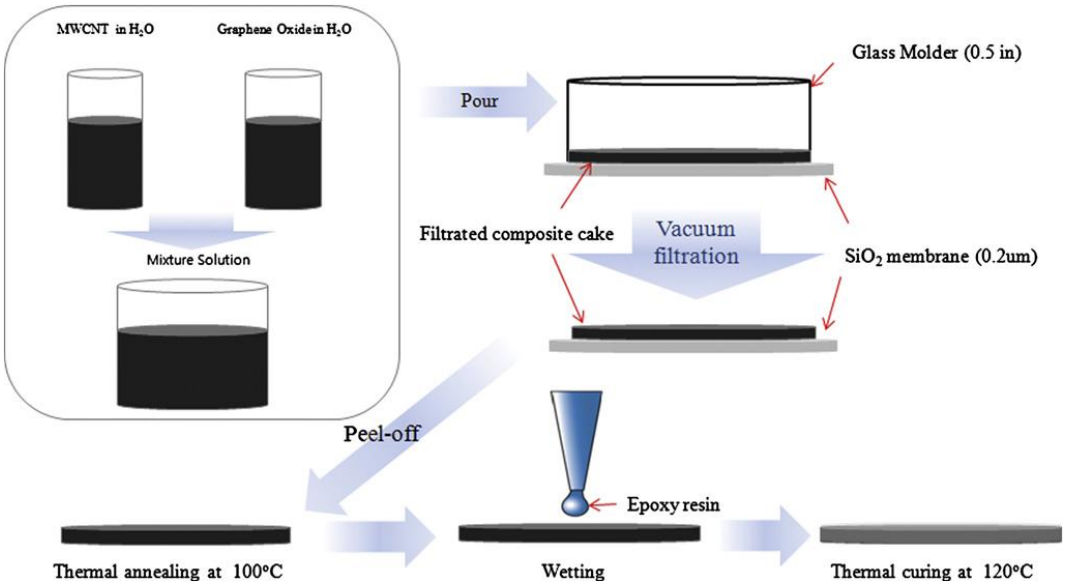

Figure 2-25 Schematic diagram of the fabrication procedure of the GO-MWCNT/epoxy composite. [69]

2.2.2.2. Dissolution–Dispersion–Precipitation

The term dissolution-dispersion-precipitation means that the polymer is dissolved in a certain solvent, which is the same solvent used to disperse the carbon materials. The dispersion of carbon materials must be done separately as the typical method of sonication causes molecular

weight degradation of the polymer [13, 59]. Hence, the dissolution is done separately from dispersion in most cases of the dissolution-dispersion-precipitation method. The two solutions are subsequently mixed. The dissolution-dispersion-precipitation process is also an excellent choice for laboratory production because good dispersion of carbon materials is possible in low viscosity solvents. However, for commercial production, the water-soluble polymers are not suitable for most envisioned applications with carbon materials, as the large volume requirements of the organic solvents for the dispersion of carbon materials [13].

After the dispersion, another critical issue is removing the solvent in the system, in particular, how fast it can be removed from the solvent. As the carbon materials that are well-dispersed in the system would show a trend of reaggregation [73, 74]. One approach is to rapidly add the solvent–polymer–carbon material solution to an excess of liquid that is miscible with the solvent, while the polymer does not dissolve and the carbon materials are not dispersed [75, 76]. After that, the polymer-carbon mixture can be separated from the solvent. Another method, which is slower, is the evaporation method after mixing [77-79]. For example, He et al. has reported MWCNTs-natural rubber (NR) composites, which showed alignment of MWCNTs in the NR matrix with the help of an electrical field [80]. First, the NR, which was divided into small particles, was dissolved in methylbenzene for 48 h, and the pre-treated MWCNTs were also dispersed with methylbenzene. After the additives dispersing in methylbenzene, these three parts were then mixed by mechanical agitation in a flask to obtain stable and uniform latex. The mixture was then poured into a glass container set at a maintained alternating current (AC) field (as shown in Figure *2-26*). The methylbenzene was evaporated, and the MWCNTs could be aligned with the assistance of the AC field in the NR matrix.

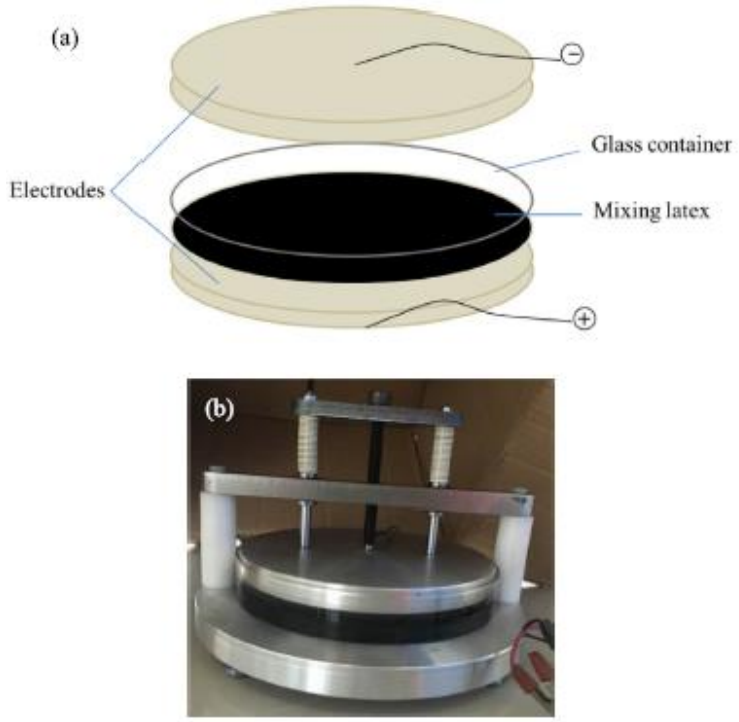

Figure 2-26 An electric-field oriented device for CNTs. (a) Schematic of a device used for electric field induced alignment of CNTs, (b) setting a glass container with latex inside before the device working. [80]

2.2.2.3. Dispersion–Dispersion–Evaporation

Besides the two preparation methods discussed above, another typical process is the dispersion-dispersion-evaporation process so that the polymer is dispersed rather than dissolved. Specifically, both the polymer and carbon materials are dispersed in the liquid (such as water) and then mixed. The liquid in the system is then evaporated [13].

Two approaches are possible: reacting the monomer in a dispersion polymerisation in the presence of nanotubes or mixing a solution of the dispersed polymer with a solution of the dispersed nanotubes. The second approach that involves the mixing the dispersed carbon materials with polymer colloids is more commonly used, such as poly(methacrylate) [81], poly (vinyl acetate) [82], polystyrene [83] and poly (ether ether ketone) (PEEK) [84-86]. Chen et al. prepared MWCNTs-PEEK composites [84]. PEEK powders were separately dispersed in N,N-dimethylformamide (DMF) with the help of sonication for 30 min. The mixed solution was

mixed with pre-treated MWCNTs for another 30 min under sonication and then dried in an aluminium mould at 60°C until a constant weight was achieved. Although agglomeration may occur during the evaporation, this a typical dispersion-dispersion-evaporation process to prepare PEEK-CNT composite. Like CNTs, the PEEK-graphene nanocomposites were prepared by Salavagione et al. [85]. Graphene and PEEK were physically mixed in a small volume of ethanol under ultrasonication for 1 h. The dispersion was then slowly dried at 60°C and then completely dried at 80°C in a vacuum furnace overnight. The pre-mixed powders were then further processed by melt blending in a Haake Minilab extruder operating at 380°C. PEEK with the addition of GO-CNTs as fillers were studied by Kim et al. [86]. As shown in Figure *2-27*, the GO, PEEK and MWCNT were pre-mixed with anhydrous DMF using the ultrasonication at room temperature for 1 h. The pre-mixed GO and MWCNTs were then slowly added into the PEEK mixture, and the mixture was then completely dispersed with ultrasonication followed by continuous stirring at 65°C for 8 h. The obtained slurry was then dried overnight in an oven at 100°C. The hot press method was the introduced at 340°C with a pressure of 15 MPa for 10min to obtain the dense composite pellets. Therefore, it can be found that the CNT and/or GO materials can all be dispersed in polymer through via this method.

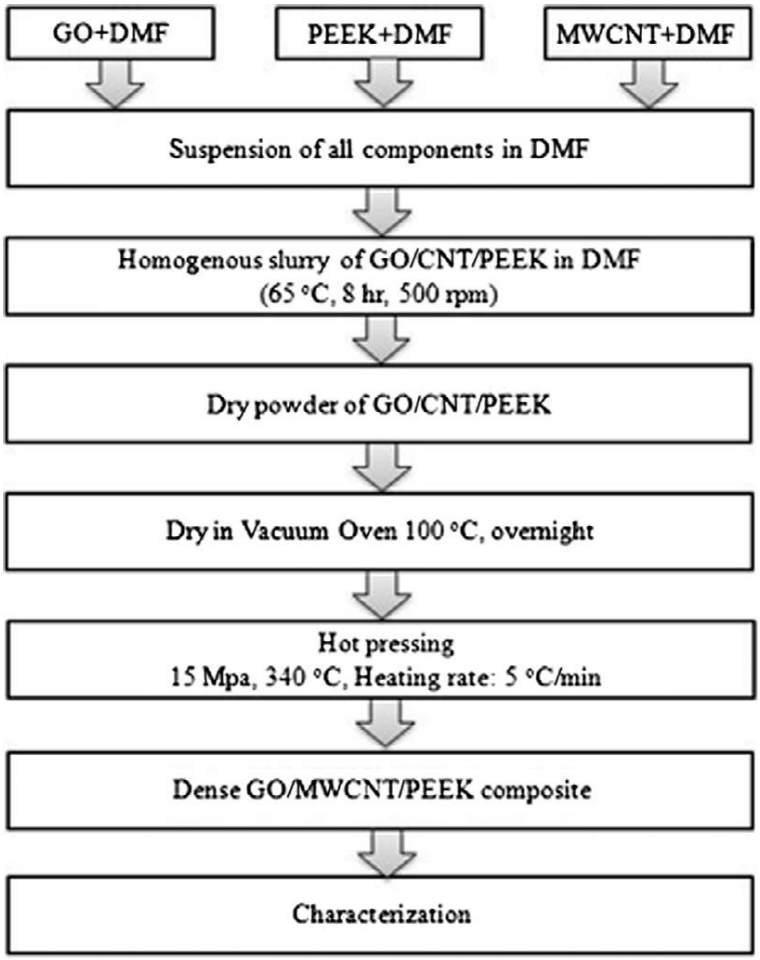

Figure 2-27 Flowchart for preparation of PEEK composites through the dispersion-dispersion-evaporation process. [86]

In the polymer system, three different approaches have been introduced, and Table *2-2* listed the details of each approach. The dispersion-reaction method is the simplest one, but cannot guarantee the dispersity of the fillers. The dissolution-dispersion-precipitation approach results in a better dispersity of carbon fillers as the separated dispersion strategy. However, scale-up production could only be applied to water-soluble polymers, and most polymers could only be dissolved in the organic solvent. The dispersion-dispersion-evaporation method needs separated dispersion rather than desolvation, followed by evaporation, which can be widely applied with most polymers. However, the subsequent evaporation process may need a longer duration and result in the sediment of filler. Although previous research demonstrated that the addition of CNT and/or graphene as reinforcements in the polymer matrix could be a possible

option in enhancing the matrix's properties, it is still a critical point to select a proper preparation approach based on the materials adopted.

Table 2-2 Details of three strategies in preparing polymer-based composites.

Method	Description	Advantages	Disadvantages
Dispersion-reaction	Disperse the fillers in the monomer, and polymerise the monomer	Simple and convenient	Sometimes fillers could not well dispersed in the monomer
Dissolution-dispersion-precipitation	Polymer is dissolved in a solvent, and the fillers are dispersed in the same solvent, then mix together	Better dispersion of fillers	Not suitable for scale-up production if use organic solvent
Dispersion-dispersion-evaporation	Both the polymer and the carbon materials are dispersed in the liquid (such as water) and then mixed. The liquid is then evaporated	Better dispersion of fillers, and suitable for most polymers	The evaporation process takes a long duration and may lead to the sediment of fillers

2.3 Applications of graphene/carbon nanotube reinforced composites

In this section, thermal management and water purification performances of the carbon-based composites reported by literature are discussed.

2.3.1 Thermal management application

Nowadays, electronic devices have played increasingly important roles in our daily lives and in the military and aerospace fields. Since these microelectronic semiconductor devices have been introduced, an increasing number of developments were achieved on these integrated circuit chips. With these increased achievements, the requirements of making devices smaller and more efficient have been put on schedule and led to the miniaturisation and integration processes of these devices. Along with the miniaturisation process and the demands of higher power density for next-generation semiconductor electronic devices, various problems also arrive. The continuous working of these miniature electronic devices will generate a large amount of unwanted heat, leading to a hotter working environment in a tiny space. Recent studies have already connected most failures with temperature-dependent faults. For example, the reliability of the semiconductor devices typically reduces by 50% when the working environment temperature increases by 10°C [87]. A typical Aircraft Versa Module Europa board could produce 250 W over a 15.24 cm × 22.86 cm area in the aviation field, and this number could reach around 500 W in 0.16 cm^2 for high power aircraft electronics [87]. The heat problem not only degrades the performance but also reduces the service life and reliability (causing ca. 55% of device failures). Therefore, the development of advanced thermal management technologies should be adopted during the design of electronic devices.

From a thermal management perspective, typical heat transfer can be divided into three stages. First, the heat that is generated from the semiconductor core part is transferred to the electronic packaging of microelectronics. The heat then transfers from the package to the heat spreader or heat sink. Finally, heat transfers to the ambient environment through these heat dissipaters. Figure 2-28 illustrates the schematic of a typical electronic package assembly [12]. There are different package levels for certain electronic devices, including chip-level, board-level and

system-level [12], which means different requirements and thermal management approaches will be adopted according to different package levels. Based on this single printed circuit board, the trend of increasing power density and frequency leads to a so-called high-level integration process, which results in increased heat density. Accordingly, improved thermal management approaches need to be introduced to maintain the performance and reliability of these electronic systems. Among these possible approaches, novel materials with the enhanced thermal property will always play important roles in dissipating unwanted heat in all these package levels.

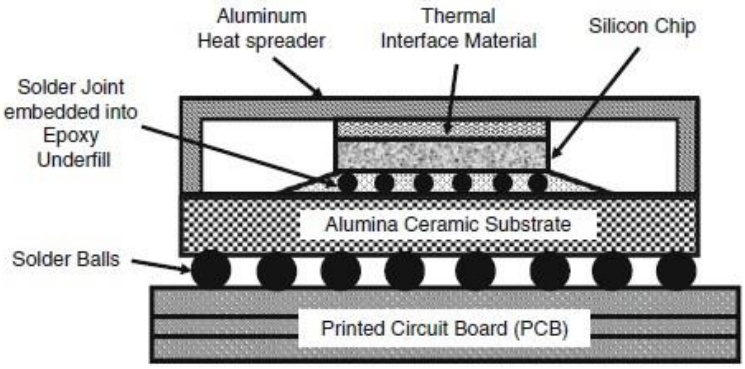

Figure 2-28 Schematic of a typical electronic package assembly. [12]

Theoretically, the thermal conductivity in a certain material is mainly based on its atomic structure. Different structures of material will result in different thermal properties. Sometimes, when the structure of a material is reduced to the nanometer scale, their thermal properties changed accordingly. For carbon materials (Figure 2-29), bulk graphite displays a thermal conductivity of around 2000 W $m^{-1}K^{-1}$. Monocrystalline diamond has been regarded as one of the best thermal conductors whose thermal conductivity ranges from 1000-2200 W $m^{-1}K^{-1}$ because of the stiff sp3 bonds [88, 89]. Single graphene or CNTs materials even exhibit the thermal conductivity of as high as 3000-6000 W $m^{-1}K^{-1}$ [7, 17, 90]. However, it is of great importance to notice that the difference in thermal conductivity between graphene, CNT and other carbon-based materials are largely related to different kinds of measurement methods and

some time is based on a single tube or layer.

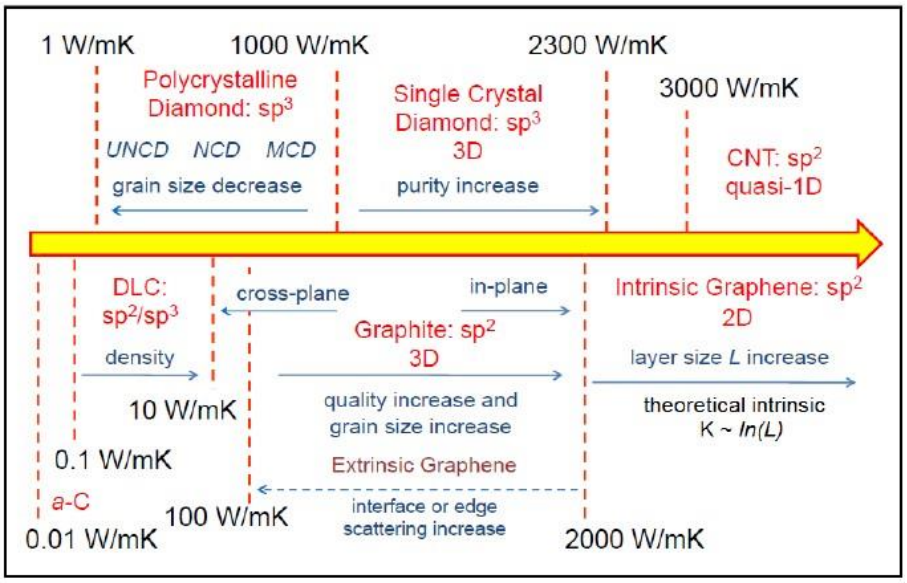

Figure 2-29 Average values of thermal conductivities reported. [91]

Through Fourier's law, the thermal conductivity is generally described as $q = -K\Delta T$, in which q represents the heat flux, K equals the thermal conductivity and ΔT is the temperature gradient. The thermal conductivity is usually regarded as a constant, which is valid for small temperature (T) variations. However, when it comes to a broad temperature range, it becomes a function of the temperature (T). Among solid materials, heat is always carried by acoustic phonons and electrons, so the equation K = Kp + Ke represents the thermal conductivity, where Kp and Ke are the contributions of phonons and electrons [91].

In metals, the Ke plays the most crucial role due to a large number of free carriers. Pure copper displays a room temperature thermal conductivity of around 400 W $m^{-1}K^{-1}$, while the Kp is only about 1-2% of the total. Ke is also an important coefficient in defining the electrical conductivity (σ) through the Wiedemann-Franz law, $Ke/(\sigma T) = \pi^2 kB^2/(3e^2)$, in which kB represents the Boltzmann constant and e is a single electron's charge. In carbon materials, heat conduction is generally dominated by phonons. This strong covalent sp2 bonding between carbon atoms allows heat to transfer by lattice vibrations more efficiently, even for the metal-

like carbon component - graphite [92, 93].

Metal-based composites for the thermal management application

Conventional, bulk materials that were applied for heat spreading and dissipating need to exhibit high thermal conductivities (TC), relatively low coefficient of thermal expansions (CTE), low densities, high strength and stiffness, and low costs. Pure metals [like copper (Cu) and aluminum (Al)] are widely studied as thermal management materials, especially in heat spreaders or sink for a long time [87]. Because of the low cost, easy machining and processing, and most importantly relative high TC (180 - 240 W $m^{-1}K^{-1}$), Al is widely applied, especially since the thermal load is not very high. Cu is another common metal that is easily processed. A higher theoretic TC (~ 400 W $m^{-1}K^{-1}$) of Cu component to Al make Cu a popular candidate not only in scientific research but also in industry. However, Cu and Al both have high CTEs (16.5×10^{-6} K^{-1} in copper and 23×10^{-6} K^{-1} for aluminum [87]), which are both too high to match ceramics and Si chips (3×10^{-6} K^{-1}). A large difference of CTEs between each component in a sealed chip results in a stress in processing. The continuous working of the system leads to an accumulation of this stress and resulting in the premature failure of the device, due to heat sink bending, ceramic substrate wrapping and completely failing or cracking [12]. The TC and CTE of pure metals cannot catch up with the innovation pace of electronic technologies and improved approaches should be adopted. Meanwhile, graphene-based materials have been reported with lower CTE values (around 10^{-6} K^{-1}) which is close to Si chips [94]. Thus, the introduction of carbon-based materials could be a promising approach to enhance the thermal management performances of the metal matrices.

As discussed in section 2.3.2, numerous methods have been investigated in preparing the graphene and/or CNT enhanced metal composites, and the thermal management properties of these products have been carefully studied. Chu et al. investigated the preparation of CNTs-Cu

systems and their thermal conductivities [45, 95]. The MWCNTs reinforced Cu matrix composites were prepared through a simple dispersion with a subsequent consolidation process by SPS [45]. The obtained pellets were then measured using a laser flash method, and the results are shown in Figure 2-30a. Chu found the obtained thermal conductivity of the obtained MWCNT-Cu composites showed a slight decrease from 5 vol.% to 10 vol. % of MWCNTs compounds, when compared with pure pressed Cu (~330 W $m^{-1}K^{-1}$), with a sharp decrease at 15 vol. % of MWCNTs to ca. 240 W $m^{-1}K^{-1}$. The pure pressed Cu also showed lower thermal conductivity than the theoretical value (400 W $m^{-1}K^{-1}$). The authors ascribed this to the grain boundaries and defects in the polycrystals, which always show lower thermal conductivity than their corresponding bulk single-crystals [96]. The decrease of the measured thermal conductivity can be attributed to the increasing numbers of CNTs, which resulted in clusters, porosities, inhomogeneous distribution of CNTs (Figure 2-30b) and the large thermal resistance between the Cu matrix and CNTs. Therefore, an improved method was explored by Chu et al. [95]. In this case, the pre-alloyed Cu-0.85 wt.% Ti powders were mixed with acid-treated CNTs through high-energy ball milling to improve the interface, and the obtained powders were then consolidated by HP at 780°C for 15 min. The results in Figure 2-30c showed that now the measured thermal conductivities increased with the amount of the CNTs added, from 318 $m^{-1}K^{-1}$ of pure pressed Cu to 342 and 366 $m^{-1}K^{-1}$ for 5 and 10 vol. %. of CNT-Cu-Ti composites. The HRTEM image (Figure 2-30d) showed that there was a diffusion TiC reaction layer between CNT and Cu-Ti matrix which can chemically enhance the interfacial bonding, and this also was ascribed to the increase of the thermal performance of the as-prepared pellets. This could further illustrates that the introduction of metal decoration on CNTs is an advanced approach to enhance the interface between CNTs and the matrix and then increases the improve the thermal conduction performance. On th other hand, the measured thermal conductivities of CNT-Cu-Ti cimposites are still lower then the theoretical value of Cu, which can be ascribed

to the relevant low densities obtained by HP.

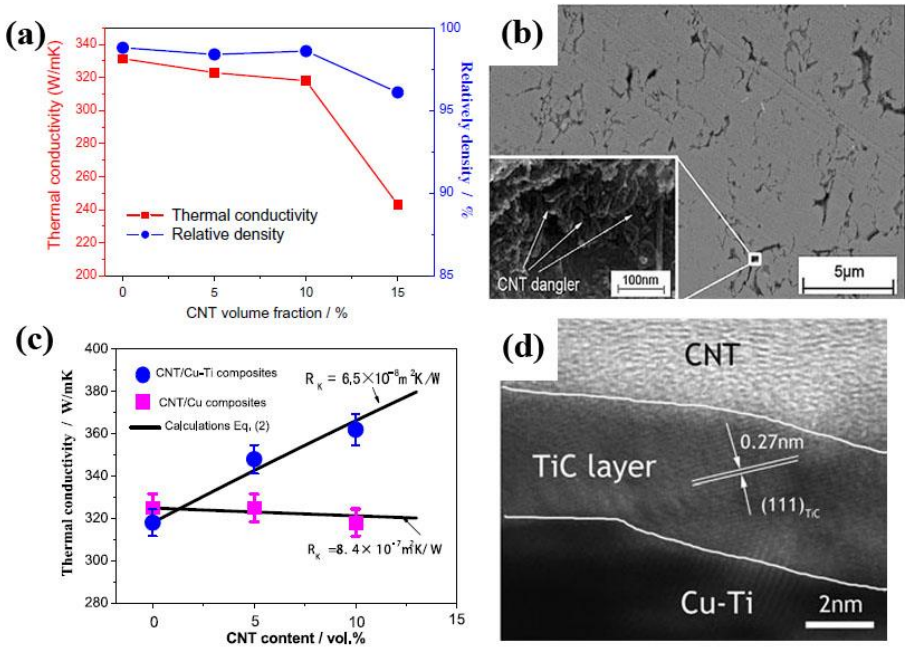

Figure 2-30 The thermal conductivity of CNT-Cu (a) and CNT-CU-Ti (b); morphology of CNT-Cu (c) and CNT-CU-Ti (d). [45, 95]

Thermal management properties of the graphene materials enhanced Cu matrix composites have also been widely investigated [48, 97]. Huang et al. processed GO-Cu composites via the MLM process followed by chemical reduction, and the obtained powders were consolidated through SPS at 700°C for 5 min with a pressure of 50 MPa. As shown in Figure 2-31a, the obtained pressed pellet was cut into two smaller pellets, which were in different directions (vertical and horizontal), and the thermal diffusivities of both pellets were measured. Both directions' thermal diffusivities decreased with the increase of the graphene contents (Figure 2-31b). The decrease of the thermal diffusivity is likely to be ascribed to the following three reasons: a) the mean-free path of heat carriers was reduced due to the decreased matrix grain size and increased dislocation density [98]; b) the interfacial thermal resistance was raised by the large thermal expansion mismatch and poor adherence between copper and graphene [99]; c) voids forming during sintering serving as insulating barriers to the heat flow. The obtained densities displayed in the insert figure of Figure 2-31b also exhibited a decreasing trend with carbon content. Meanwhile, the thermal diffusivity of the horizontal direction decreased slower

than the vertical direction (Figure 2-31b) with the increase of graphene content. From the SEM images of the pressed pellets (Figure 2-31 d and e), the added graphene appeared aligned in the perpendicular direction of consolidation force with the increase of the graphene ratio. It can be found that the advanced consolidation processes, like SPS, could effectively facilitate the distribution of fillers in the matrix with the help of vertical force adopted. In addition, the thermal conductivity of graphene at the in-plane direction is thousands of times higher than that at the through-plane direction, which explains the difference performance between the horizontal and vertical directions in the obtained pellets.

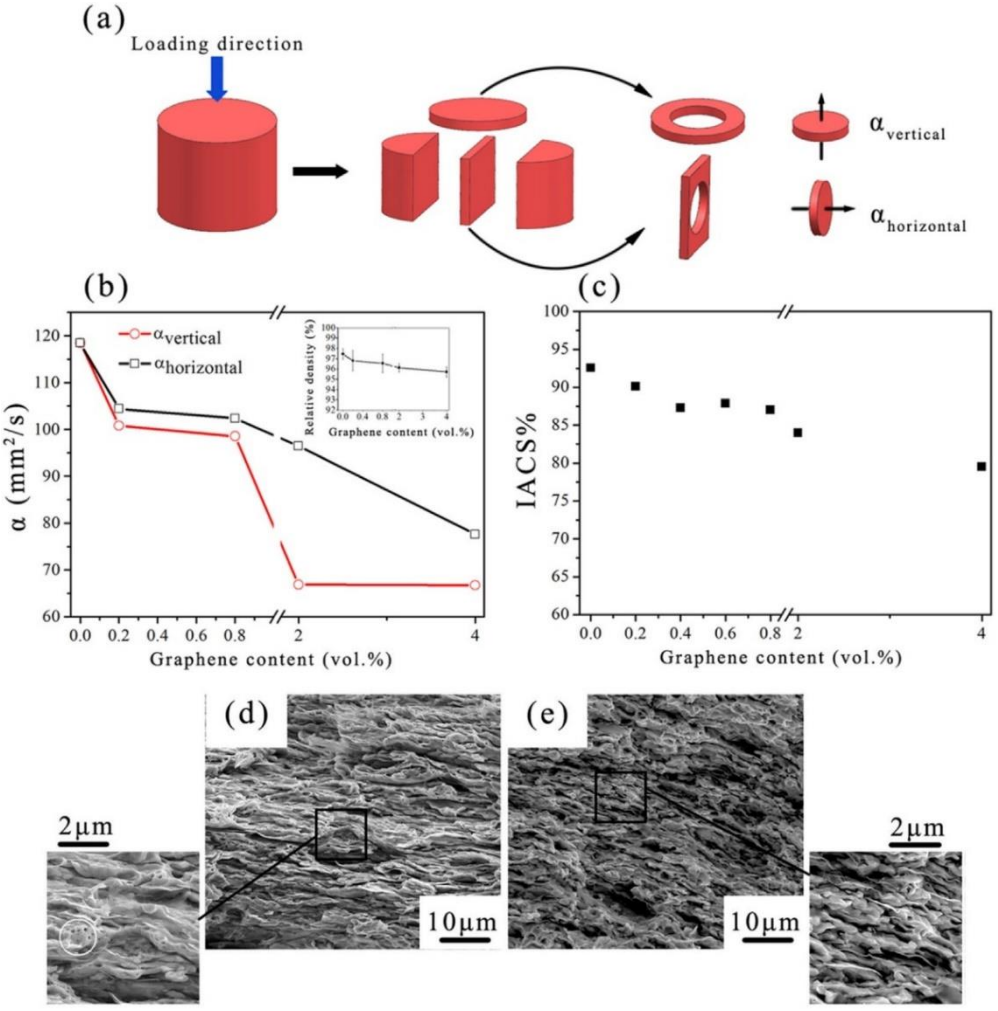

Figure 2-31 (a) Schematic of preparation method for thermal diffusivity test, (b) thermal diffusivity and relative density (insert program) as a function of GNPs content, (c) electrical conductivity of Cu/GNPs composites (IACS indicates the percentage of measured EC compared to initial value), (d) Cu-2.0 vol.% GNPs and (e) Cu-4.0 vol.% GNPs. [97]

An efficient route to prepare the graphene nanoplatelet graphene-Cu composites with highly aligned graphene has been reported by Chu et al. [48] via vacuum filtration followed by spark plasma sintering. The SPS pressed graphene-Cu, which was obtained through a vortex mixed process and the subsequent vacuum filtration method (V-GNT/Cu), exhibited anisotropic structure compared with the non-vacuum filtration samples (NV-GNP/Cu) (Figure 2-32 a, b and e, f). The larger amount of graphene in the composites, the more easily the alignment of graphene layers were observed in the as-pressed pellets. The measured thermal conductivities of both V-GNP/Cu and NV-GNP/Cu pellets are displayed in Figure 2-32 g and h. Here it was found that the V-GNP-Cu sample showed an increasing trend in the measured thermal conductivity of the in-plane direction with the growth of the graphene content, while the thermal conductivities of the NV-GNP-Cu sample decreased. It can be concluded that the alignment of graphene was observed and the thermal conductivity of the in-plane direction of the obtained pellets was further enhanced, which is similar to the research above. Thus, the graphene-based composites exhibited great potentials in improving the thermal performances of metals, especially with the help of vertical pressing during consolidation.

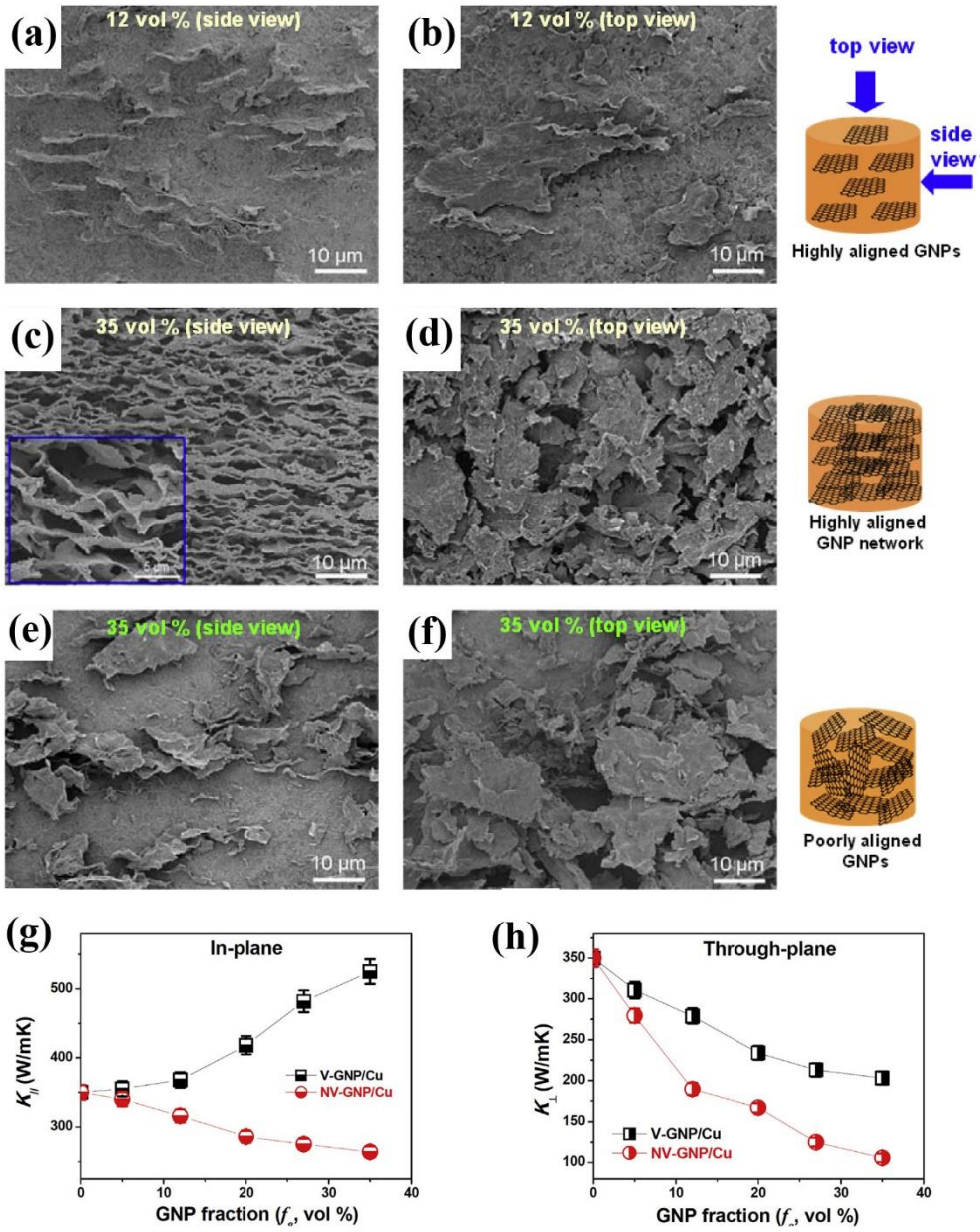

Figure 2-32 SEM images of etched V-GNP/Cu (a, e and d) and NV-GNP/Cu (e and f) composites from the different view directions and corresponding schematic diagrams: (a) 12 vol% V-GNP/Cucomposite (side view). (b) 12 vol% V-GNP/Cu composite (top view). (c) 35 vol% V-GNP/Cu composite (side view). (d) 35 vol% V-GNP/Cu composite (top view). (e) 35 vol% NV-GNP/Cu composite (side view). (f) 35 vol% NV-GNP/Cu composite (top view). (g) in-plane TC and (h) through-plane TC of V-GNP/Cu and NV-GNP/Cu composites at different volume percentages. [48]

Polymer-based composites for the thermal management application

As stated above, carbon materials exhibit excellent thermal performance (over 1500 W $m^{-1}K^{-1}$), the obtained results for polymer composites by previous research were much less than the prediction. Instead of the increase in thermal conductivity being measured in tens or hundreds,

the reported results are typically less than 1 W $m^{-1}K^{-1}$ [13]. Table *2-3* displays some results from previous research. The reason for this behaviour is that the resistance to the transfer of heat at the carbon material - polymer boundary is sufficiently large, and hence the thermal conductivity increase is modest. For example, the thermal conductivity of the PEEK-carbon fibre (CF) laminates enhanced by graphene was studied by Xiao et al. [100]. The PEEK powders were first mixed with graphene in ethanol by sonication followed by the balling method. The obtained powders were then hot-pressed and then manufactured with CF fabric to prepare the laminates (Figure 2-33a). The thermal conductivity results (Figure 2-33b) rose with the increase of graphene content to 53.7% (0.3763 W $m^{-1}K^{-1}$), higher than that of PEEK-CF laminates (0.2449 W $m^{-1}K^{-1}$). As a heat conductive bridge, graphene (GE) can be explained to form a continuously connected network throughout the PEEK matrix. Thus, it was found that the uniform or ordered distribution of the carbon fillers in the polymer matrix could be a potential strategy to further improve the properties.

Table 2-3 Comparison of thermal conduction performances from previous results.

Sample	**Thermal conductivity (W $m^{-1}K^{-1}$)**	**Ref.**
GO in PEEK	0.35	[86]
PEEK/graphene/carbon fibre	0.38	[100]
Carbon fibre-PEEK	0.21	[101]
Ag NPs-PEEK	0.30	[102]

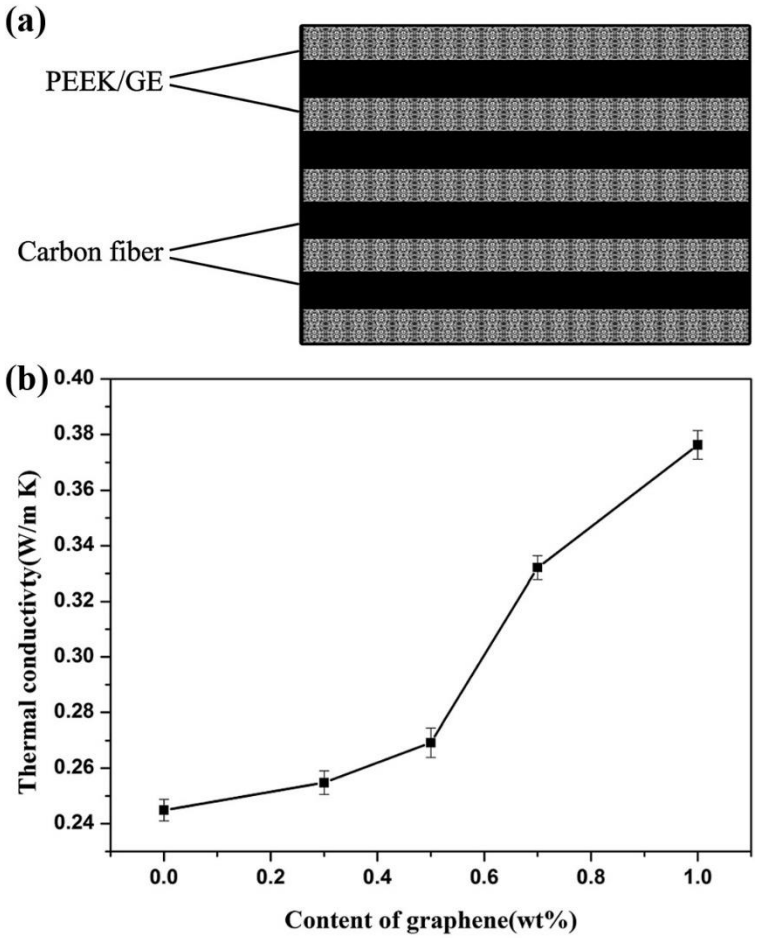

Figure 2-33 (a) Schematic representation of the lay-up stacking sequence of the PEEK/graphene/CF laminate and (b) thermal conductivity of PEEK/GE/CF laminates with different contents of graphene. [100]

Figure 2-34 a and b display the measured thermal conductivities of as-prepared PEEK with the GO-CNTs hybrids composites by Kim [86]. The thermal conductivity was enhanced from 0.18 W $m^{-1}K^{-1}$ (pure PEEK) to 0.36 W $m^{-1}K^{-1}$ for 1 wt. % PEEK-GO composites, which is a 2-fold improvement (Figure 2-34a). Meanwhile, after fixing the weight ratio of GO as 1 wt.%, CNT was added to result in an initial increase of thermal conductivity up to 0.5 wt.% of CNT content. The thermal conductivity then decreased to 1 wt.% carbon content. This was attributed to the PEEK matrix not having enough effective volume to allow MWCNT packing, which resulted in the agglomeration of CNTs to fit into the small packing volume [86]. Thus, to explore the ratios between CNT and GO as fillers is also a critical point to enhance the thermal conduction performance of the polymer matrix.

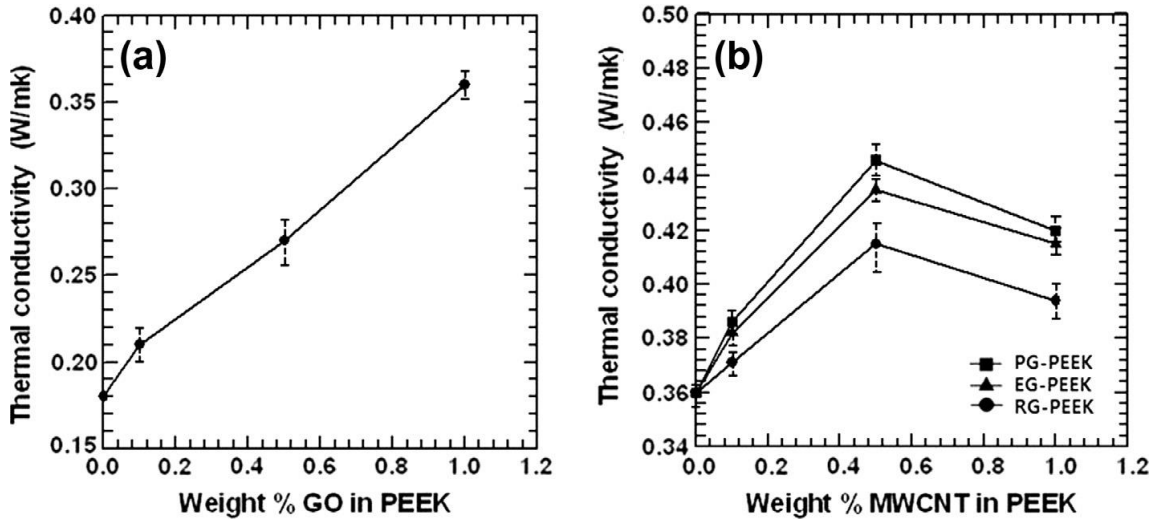

Figure 2-34 Thermal conductivity of PEEK composites as a function of the (a) GO and (b) MWCNT. [53]

The thermal conductivity of aligned CNTs ultilising AC field in epoxy resin has been studied by He et al. [80]. SEM image and schematic (Figure 2-35 a and b) showed the parallel CNTs were obtained through the AC field among the epoxy resin matrix. The measured thermal conductivities displayed in Figure 2-35 g illustrate that the aligned CNTs in the epoxy exhibited better thermal conduction performances when compared with the un-aligned ones, although both composites showed an increasing trend with the growth of CNT contents. As shown in, the 9% higher thermal conductivity in aligned CNT-epoxy composites compared with the random distribution one can be ascribed to the more physical contacts of the filler networks [80]. The thermal conductivity of the composites with 6 vol. % loading of aligned CNTs was 0.392 W $m^{-1}K^{-1}$, which is superior to the 8.3 vol. % conductive black enhanced natural rubber with 0.22 W $m^{-1}K^{-1}$. Wang et al. reported the external electric field aligned multilayer graphene in the epoxy matrix [103]. Figure 2-35 c-f showed the time-lapse images for the epoxy resin containing 0.054 vol. % of graphene. The formation of a chain-like graphene network in the direction of the applied electric field can be found. The thermal conductivity of the aligned graphene in epoxy resin showed the highest value with the increase of the graphene content (Figure 2-35). Thus, to form a 3D network or continuous pathways of the fillers could be a promising method to further enhance the properties of the polymer matrices compared to

random distributed one.

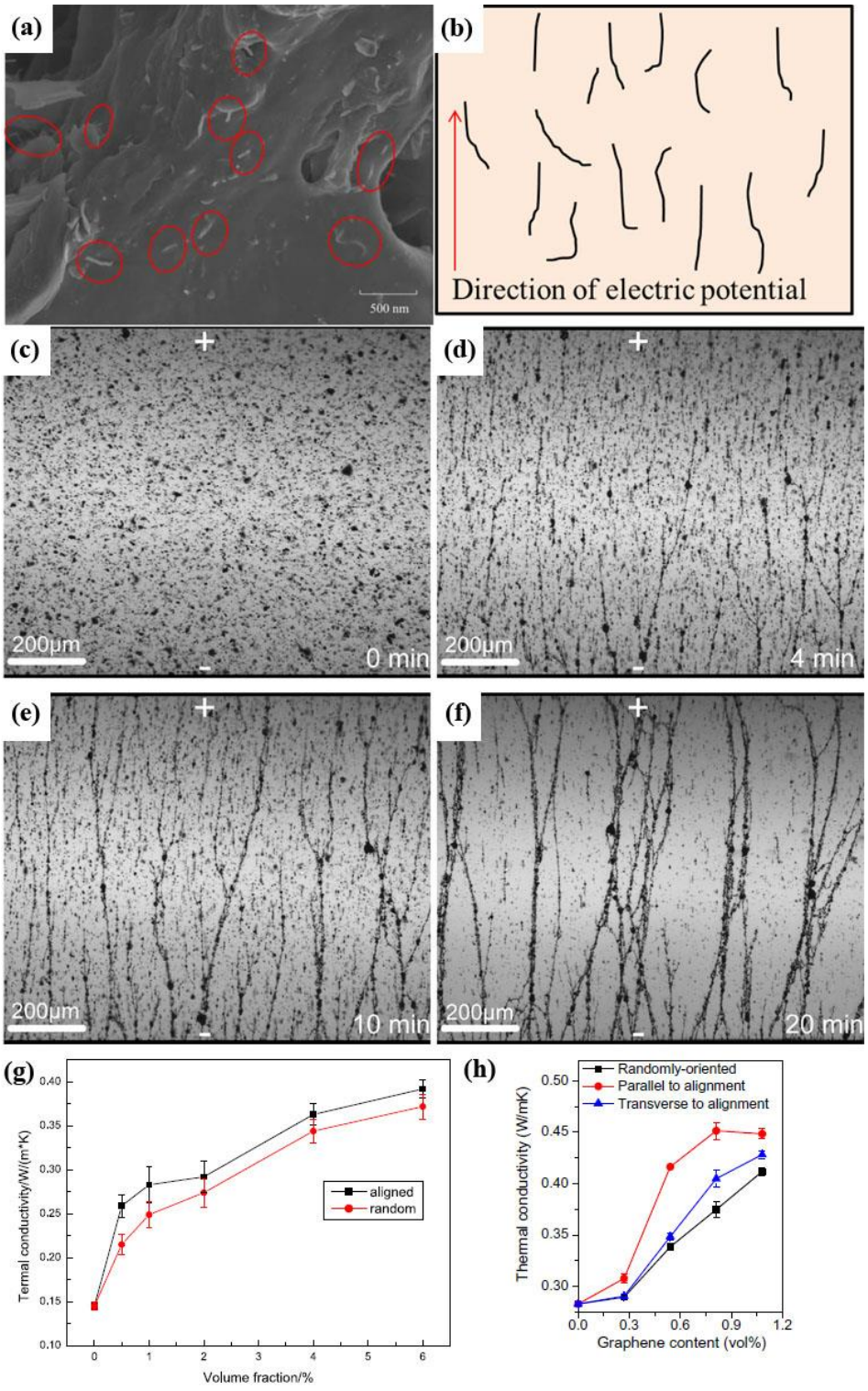

Figure 2-35 SEM and schematics images of nanocomposites (a, b) 2.0 vol% MWCNTs, (c) randomly-oriented graphene before the field was applied; (d), (e), and (f) after the field was applied for 4 min, 10 min, and 20 min, respectively. (g) the thermal conductivity of MWCNTs/NR composites and (h) Effects of the volume content and alignment of the graphene on the thermal conductivities of the epoxy nanocomposites [80, 103].

2.3.2 Dye removal performance of the graphene and/or carbon nanotube-based composites

Water, one of the essential resources to humanities, has many environmental pollution problems. Among pollutants, synthetic organic dyes, which are the common colouring agents, are widely used in the continuous production of modern industries, such as paper, textile, plastics, cosmetics, foods and printing industries [104, 105]. The industrial dyes can be classified through different methods, like chemical structure [105], applications [106] and particle charges in aqueous solution [107, 108]. Because of the different charges on dyes in the aqueous medium, they can be classified as cationic and anionic dyes. Generally, the cationic dyes contain basic dyes with different substituted aromatic groups, depending on a positive ion. In contrast, the anionic dyes depend on a negative ion, which includes compounds from varied classes (i.e., direct, acid or reactive dyes) [108].

These coloured pollutants, which usually are difficult to be decomposed due to their chemical stability, are mostly regarded as toxic and potentially carcinogenic [109]. Thus, efficient approaches to remove dyes from discharged wastewater have become a critical issue and are of great importance to human health. Adsorption and filtration are widely used to remove an extensive range of effluents due to their easy operation; however, this transfers pollutants from water to another phase, which may cause secondary pollutions. Photo-degradation has shown potentials in dealing with effluents. This technique can transform harmful molecules into environment-friendly by-products [110, 111]. Therefore, to adopt suitable methods to deal with the dyes in wastewater has become a critical issue.

Recently, carbon materials, especially the 1D CNTs and 2D graphene, have attracted increasing attention as water purification materials. Generally, the physical adsorption of organic

chemicals by a certain material is mainly through electrostatic interactions, hydrogen bond and π-π interaction and/or hydrophobic interactions [112]. In the CNTs system, due to the highly hydrophobic property from the π electron of SP^2 carbon atoms, adsorption could take place through π-π interaction between the bulk π system of CNTs and C=C or benzene rings in dye molecules [112]. Electrostatic interactions would happen if acid treatments have been introduced to CNTs, and functional groups were attached onto the sidewalls. Like CNTs, π-π and electrostatic interactions are two main ways in graphene systems, especially when graphene oxides (GOs), which contain abundant functional groups, were introduced [113]. Until now, pristine and modified CNTs and graphene materials obtained by different methods have been reported in dealing with wastewater [114-118] (Table 2-4). However, overcoming the strong trend of agglomeration among carbon-based materials has become an important strategy to have better adsorption performance.

Table 2-4 Adsorption capacity of RhB and MO with different carbon-based adsorbents.

Adsorbents	Dye	Adsorption capacity (mg g^{-1})	References
Reduced GO-based hydrogels	RhB	29.44	[114]
Bentonite-CNT nanocomposite	RhB	142.80	[115]
MWCNTs	MO	54.84	[116]
Calcium alginate-MWCNTs	MO	12.50	[117]
Ni embedded graphitic carbon	RhB	168.10	[118]

Traditional semiconductors (i.e. ZnO [119], TiO2 [120], Fe_2O_3 [121], CdS [122] and SnO_2 [123]), the noble metal nanoparticles (e.g. Au [124], Ag [125], [126]) and ferrites ($NiFe_2O_4$, $CoFe_2O_4$ and $MnFe_2O_4$) [127] have been employed as photo-catalysts to remove coloured dyes from water. Among them, noble metal-based composites, especially Ni-based materials, have attracted increasing attention. The Ni nanoparticle shows potential in application due to its

lower cost when comparing with Au or Ag. The ferromagnetism of Ni also made it more convenient to collect after reaction and reuse when compared with traditional semiconductors [128, 129]. In addition, nanoparticles can also play an important role as spacers in reducing the agglomeration of graphene or CNTs when uniformly disperse among them. Therefore, a combination of such materials has become a possible route for preparing advanced materials in dealing with dyes.

Physical adsorption

The term adsorption refers to accumulating a substance at the interface between two phases (liquid-solid interface or gas-solid interface). The substance that accumulates at the interface is called adsorbate and the solid on which adsorption occurs is adsorbent [130]. Two different adsorptions can be classified according to the different bonding types between adsorbate and adsorbent: chemical adsorption and physical adsorption. The chemical adsorption is illustrated by forming strong chemical associations between molecules or ions of adsorbate to the adsorbent surface. In contrast, the physical adsorption is characterised by weak van der Waals intraparticle bonds between the adsorbate and adsorbent, which leads to reversible in most cases [131]. In carbon-based materials, the removal of the organic dyes is always ascribed to physical adsorption. As shown in Figure 2-36, the schematic displays the common adsorption process on the pre-treated CNTs and GOs. It can be found that the electrostatic attraction is the most common mode as the functional groups attached on the carbon materials are always negative charged which could effectively attracted positive charged dyes (i.e., methylene blue in the schematic, Figure 2-36). In addition, other physical bonds, including hydrogen bond and π-π interaction and/or hydrophobic interactions, have also been observed in previous research.

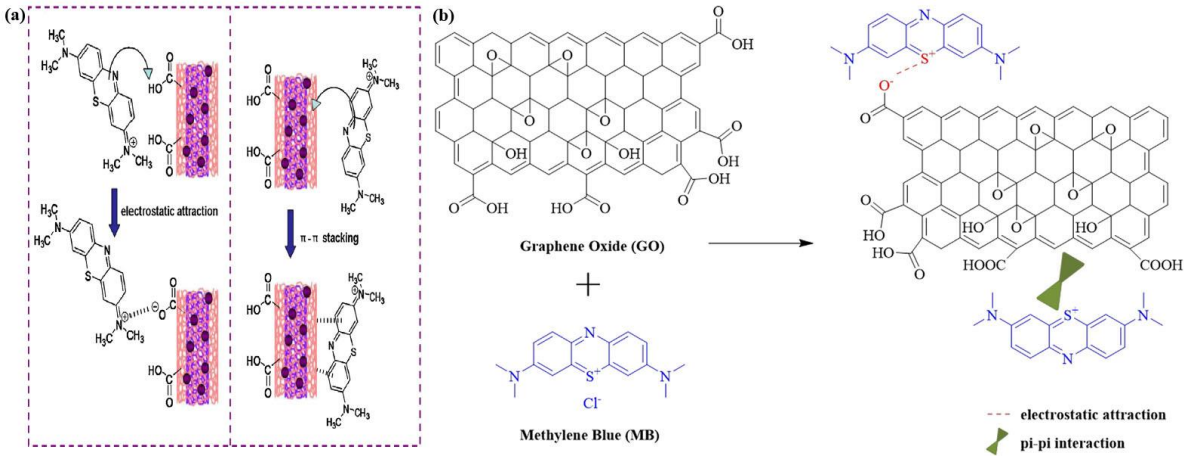

Figure 2-36 Schematic of the physical adsorption process on CNTs (a) and GOs (b). [112, 113]

Although the physical adsorption is affected by various factors, i.e., pH, initial dye concentration, temperature and amount of adsorbent, the controlling mechanisms of adsorption are used to determine kinetic models. The study of the adsorption kinetics illustrates how the solute uptake rate controls the residence time of the adsorbate at the solution interface [104]. The kinetics of anionic and cationic dye onto various adsorbent materials were analysed using different kinetic models, which are presented below.

The pseudo-first-order model could be defined as bimolecular reaction that is made to behave like a first-order reaction and presented as [132]:

$$log(q_e - q_t) = logq_e - \frac{k_1 t}{2.303} \qquad \text{Equation 2-1}$$

where q_e and q_t are the amounts of dye (mg g^{-1}) adsorbed at time t and equilibrium, while k_1 is the rate constant of pseudo-first-order adsorption (min^{-1}).

The pseudo-second-order model is the surface adsorption that involves chemisorption, where the removal from a solution is due to physicochemical interactions between the two phases, and could be presented as [133]:

$$\frac{t}{q_t} = \frac{1}{k_2 q_e{}^2} + \frac{t}{q_e} \quad \text{Equation 2-2}$$

where q_e and q_t are the amounts of dye (mg g^{-1}) adsorbed at time t and equilibrium, while k_2 is the rate constant of pseudo-second-order adsorption (g mg^{-1} min^{-1}).

The intra-particle diffusion model could be presented as [134]:

$$q_t = K_{id} t^{0.5} \quad \text{Equation 2-3}$$

where q_t is the adsorption capacity at time t, $t^{0.5}$ is the half-life time in second (s), and K_{id} (mg g^{-1} $min^{-0.5}$) is the rate constant of intraparticle diffusion.

Generally, the best-fit model can be chosen based on the values of the linear regression correlation coefficient (R_2). One example is the investigation of the methylene blue (MB) adsorption with the self-assembled cylindrical graphene-CNTs hybrids by Ai [105]. Figure 2-37 displayed the adsorption results of the MB and the fitted results with the three models above. In Figure 2-37 a, the adsorption of MB with the self-assembled cylindrical graphene-CNTs hybrids rose with both the increase of time and initial concentration. The adsorption capacity at different initial dye concentration and adsorption time was then taken into the three models, and the obtained plots were illustrated in Figure 2-37 b-d and the insert table. It can be found that the fitted results of the pseudo-second-order model showed the best fitting both in the plots (Figure 2-37 c) and the regression correlation coefficient (R_2). Therefore, the results showed that the adsorption kinetics studies obeyed the pseudo-second-order kinetics.

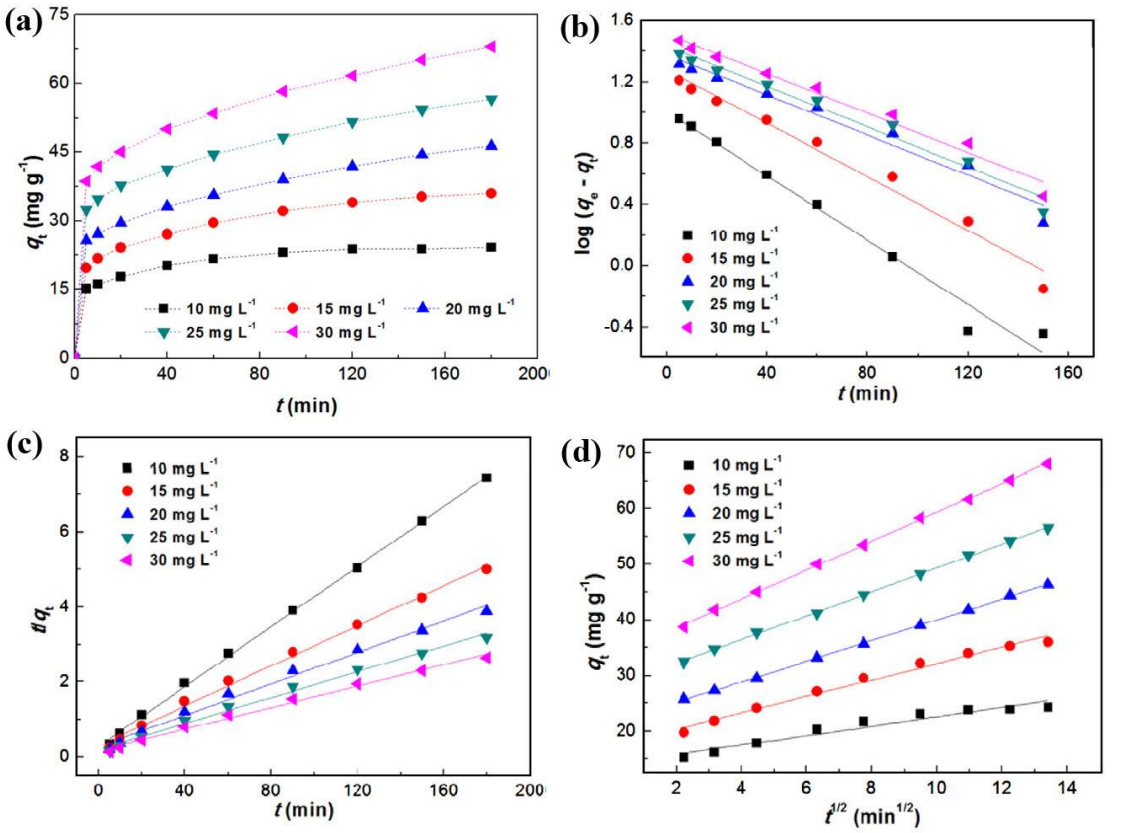

	Pseudo-first-order kinetics				Pseudo-second-order kinetics			Intraparticle diffusion model		
C_0 (mg L^{-1})	k_1 (min^{-1})	$q_{e,exp}$ (mg g^{-1})	$q_{e,cal}$ (mg g^{-1})	R^2	k_2 (g mg^{-1} min^{-1})	$q_{e,cal}$ (mg g^{-1})	R^2	k_i (mg g^{-1} min$^{1/2}$)	C (mg g^{-1})	R^2
10	0.0242	24.20	10.16	0.9763	0.0059	24.96	0.9989	0.8464	14.08	0.9311
15	0.0201	35.97	19.08	0.9767	0.0025	37.37	0.9954	1.4804	17.34	0.9841
20	0.0151	46.36	23.84	0.9655	0.0017	47.64	0.9894	1.8715	21.33	0.9997
25	0.0152	56.50	27.19	0.9738	0.0015	57.87	0.9913	2.1515	27.84	0.9994
30	0.0148	68.02	32.48	0.9752	0.0013	69.54	0.9915	2.5985	33.37	0.9993

Figure 2-37 (a) Effect of contact time on the adsorption capacity of MB onto the G–CNT hybrid at different initial concentrations, Pseudo-first-order (b), pseudo-second-order (c) and intraparticle diffusion (d) kinetics plots of MB adsorption onto the G–CNT hybrid and the Adsorption kinetic parameters for the adsorption of MB onto the G–CNT hybrid (insert table). [105]

The adsorption isotherm is another significant index in the investigation of the dye adsorption to explain how the adsorbent will interact with the adsorbate and give an idea of adsorption capacity. It described the adsorption based on the surface phase, which can be considered as a monolayer or multilayer adsorption. Langmuir [135] and Freundlich [136] models are the most widely used to describe the adsorption isotherm.

$$\frac{C_e}{q_e} = \frac{1}{bq_m} + \frac{C_e}{q_m} \qquad \text{Equation 2-4}$$

$$lnq_e = \frac{1}{n} lnC_e + lnK_f \qquad \text{Equation 2-5}$$

where the C_e (mg L^{-1}) is the initial dye concentration at the different point, q_e (mg g^{-1}) is the obtained adsorption capacity at different concentration (C_e), b (L mg^{-1}) is a constant in Langmuir isotherm, and q_m (mg g^{-1}) is the Langmuir monolayer adsorption capacity which can indicate the maximum adsorption. The 1/n in the Freundlich isotherm model is a constant related to the adsorption intensity and the K_f is a Freundlich constant related to adsorption capacity. The adsorption isotherm study of the self-assembled cylindrical graphene-CNTs hybrids with MB was also analysed [105] and the results were displayed in Figure 2-38. It can be found that the linear regression of the Freundlich model showed a better fit, which demonstrates that a multilayer adsorption process has taken place on the surface of the G–CNT hybrid. The Freundlich constant n is found to be greater than 1, indicating a favorable condition for adsorption. The maximum adsorption capacity for MB is measured to be 81.97 mg g^{-1}.

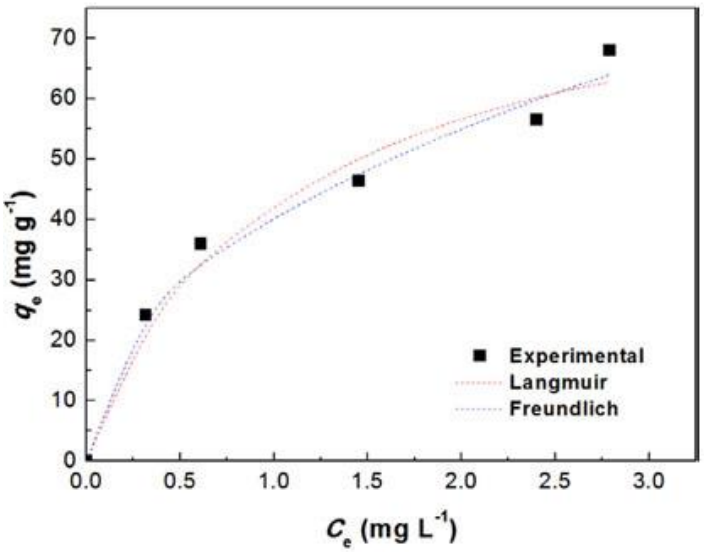

Langmuir			Freundlich		
b (L mg^{-1})	q_m (mg g^{-1})	R^2	K_f	n	R^2
1.17	81.97	0.9415	41.17	2.33	0.9665

Figure 2-38 Adsorption isotherm curves for the adsorption of MB onto the G–CNT hybrid and the insert table is isotherm parameters for the adsorption of MB onto the G–CNT hybrid. [105]

Photo-degradation

An alternative to removing the dyes in wastewater is the advanced oxidation processes (AOPs)

[137]. This has been reported to be effective for the near-ambient degradation of soluble organic contaminants from waters and soils because they can provide an almost total degradation [138-142]. Photolysis is one of the most common processes. Figure 2-39 illustrated the typical photocatalytic dye degradation process. Specifically, when a certain photocatalyst is exposed to UV irradiation, the electrons are promoted from the valence band to the conduction band. As a result, an electron-hole pair is produced [143]

$$photocatalyst + hv \longrightarrow e^-{}_{cb} + h^+{}_{vb} \qquad \text{Reaction 2-1}$$

where, $e^-{}_{cb}$ and $h^+{}_{vb}$ are the electrons in the conduction band and the electron vacancy in the valence band, respectively. Both these entities can migrate to the catalyst surface, entering a redox reaction with other species present on the surface. In most cases, $h^+{}_{vb}$ can easily react with surface bound of H_2O to produce $OH^{\cdot}$ radicals, whereas $e^-{}_{cb}$ can react with O_2 to produce superoxide radical anion of oxygen [144]

$$H_2O + h^+{}_{vb} \longrightarrow OH^{\cdot} + H^+ \qquad \text{Reaction 2-2}$$

$$O_2 + e^-{}_{cb} \longrightarrow O_2{}^{\cdot -} \qquad \text{Reaction 2-3}$$

Both the reactions could prevent the recombination of electrons and holes generated through the UV irradiation, and the obtained radicals ($OH^{\cdot}$ and $O_2{}^{\cdot -}$) could then also react with the dyes to form peroxylated or hydroxylated intermediates and then degraded or mineralized products [145].

$$O_2{}^{\cdot -} + dye \longrightarrow H_2O_2 \qquad \text{Reaction 2-4}$$

$$H_2O_2 \longrightarrow 2OH^{\cdot} \qquad \text{Reaction 2-5}$$

$$OH^{\cdot} + dye \longrightarrow dye_{ox} \qquad \text{Reaction 2-6}$$

$$e^-{}_{cb} + dye \longrightarrow dye_{red} \qquad \text{Reaction 2-7}$$

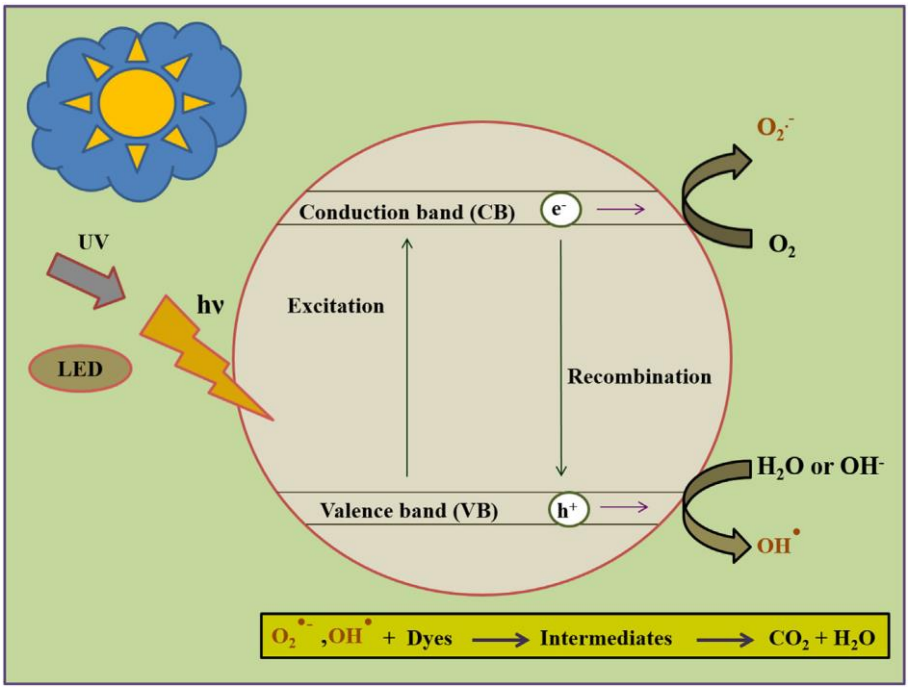

Figure 2-39 Schematic representation of the photocatalytic dye degradation process. [113]

Zhao et al. have reported metal nanoparticle coated graphene nanocomposites for photocatalytic degradation. The results demonstrated a slight difference in the mechanism described above, which is the electrons directly transferred from dyes to the pure metals [146, 147]. In the gold-graphene nanocomposites, the Au nanoparticles were successfully deposited on the surface of reduced GO through a spontaneous chemical reduction of chloroauric acid ($HAuCl_4$) [147]. The photoactivity of the GO-Au sample was carried out with the rhodamine B (RhB). The results showed that the RhB degradation was remarkably enhanced with the presence of GO-Au. The rate constant was calculated to be about 8.7×10^{-3} min^{-1}, which is much higher than GOR and P25 (TiO_2) (Table 2-5). According to the authors (Figure 2-40 a), it can be concluded that the electrons which were exited from RhB due to the irradiation can be transferred to the surface of Au nanoparticles through graphene since the different work function and then reacted with the adsorbed O_2 to form reactive oxidative species (like $OH^{\cdot}$) that can degrade the dyes [147]. Another Ni-CNT-GO system was prepared by pillaring the graphene platelets with the CNTs, and the Ni was kept as the catalyst to produce CNTs [146].

The degradation of RhB was remarkably increased in the presence of the RGOCNT catalysts, especially those with a shorter length of CNTs. The photocatalytic reaction rates of the RGOCNT catalysts were faster than that of commercial photocatalyst P25. Similar to the Au-graphene nanocomposites, the electrons excited from RhB could transfer to Ni nanoparticles through graphene and CNTs due to the differences of work function (-4.42 eV for graphene, -4.8 eV for CNTs 29 and -5.15 eV for Ni). The electrons then reacted with the adsorbed O_2 on the surface of Ni to form reactive oxidative species (Figure 2-40b) [146].

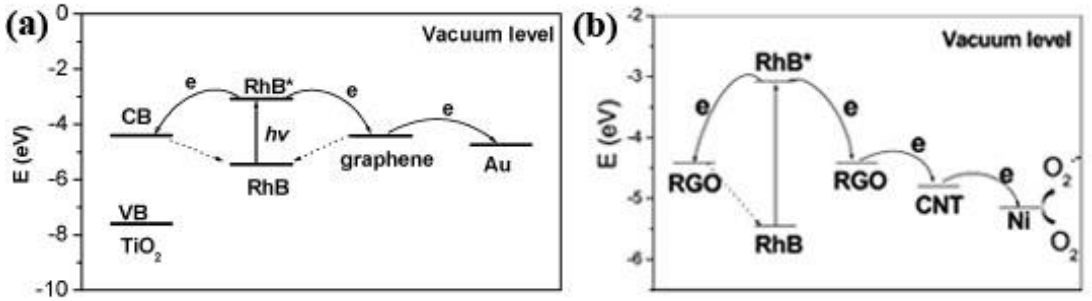

Figure 2-40 (a) The energy diagram of RhB, TiO_2, graphene and Au [147] and (b) Energy diagram showing the proposed mechanism of photosensitized degradation of RhB [146].

Table 2-5 Photocatalytic performances and related properties of samples [146].

samples	Fluorescence lifetime (ns)	Rate constant (min^{-1})
RhB	1.68	-
P25	1.58	4.9×10^{-3}
GOR	1.48	3.9×10^{-4}
Ni-CNT-GO	1.24	6.9×10^{-3}

2.4 Summary

In this chapter, a brief introduction has been made based on the characteristics and properties of 1D CNTs, 2D graphene and composites based on them. Different methods to obtain the uniform dispersions of carbon materials from previous research were discussed. Among these methods, the preparation of 3D graphene-CNTs hybrid structure has become an ideal process

that could prevent further agglomeration of the carbon materials. After that, the graphene and/or CNTs materials have been applied as potential reinforcements in enhancing different matrices (including metals and polymers). However, the results showed that the bare carbon materials could not be uniformly distributed in the composites due to the strong agglomeration trend and the poor interface between carbon material and matrix, resulting in reduced properties. To overcome these problems, introducing metal nanoparticles has become a possible approach. Numerous advanced methods, like powder metallurgy routes, PVD, CVD and MLM are listed. As one of the powder metallurgy routes, SPS has become the optimal choice due to its simple and time-saver characteristics. However, the powder metallurgy routes cannot solve the interface problem. Novel approaches, like PVD, CVD and MLM, have been explored. The advantages and disadvantages of such methods have also been discussed, which also give us ideas on sample preparation in this thesis. Meanwhile, by considering the unique structure and property of the graphene and/or CNTs based materials, potential applications (like thermal management and dye removal properties) have been reviewed. Therefore, according to the detailed discussion of graphene and/or CNTs based materials above, systematic research based on the metal nanoparticles decorated graphene-carbon nanotube nanocomposites were investigated in subsequent chapters. The thermal management and dye removal properties exploration of the obtained products, see aiming and objectives in section 1.2, have also been carefully studied.

3 Methodologies

In this chapter, the details of the facile freeze-drying method to prepare GO/CNT (GNT) nanostructures and the molecular-level-mixing (MLM) with the subsequent reduction procedure to synthesis metal (Cu, Ni, and Ag) nanoparticles decorated GNT samples are introduced. Different parameters for preparing each nanocomposite are carefully explored, and the parameters are optimised. Meanwhile, more detailed technical information associated with specific experimentations will be described in the subsequent chapter. To analyse the obtained products, comprehensive characterisation methods (i.e., XRD, SEM and XPS) are adopted. In addition, the characterisation techniques used in this thesis, the equipment (including their working principles) and result processing methods are all included in this chapter.

3.1 Raw materials and chemicals

Carbon nanotubes (CNTs) were purchased from Carbon Nanotubes Plus, graphene oxide (GO) dispersions were purchased from William Blythe Limited, 98% sulfuric acid (H_2SO_4), copper acetate [$Cu(CH_3COO)_2$], nickel acetate [$Ni(CH_3COO)_2$], silver acetate (CH_3COOAg), rhodamine B (RhB), methyl orange (MO), potassium iodide (PI), p-benzoquinone (BQ), methanol, ethanol, conductive silver paste and acetone were purchased from Sigma-Aldrich, while 70% nitric acid (HNO_3) was purchased from Fisher Scientific. Liquid N_2, pure Ar gas and Ar/H_2 mixed gas (5 % H_2 + 95 % Ar) were supplied by BOC Gas Cylinders. PEEK was purchased from Vicote coatings. The micron copper powders were purchased from Inoxia Ltd. The low viscosity epoxy resin was provided by Aktinium Technologies.

3.2 Preparing graphene-carbon nanotube hybrid nanostructures (GNTs)

3.2.1 Acid treatment of carbon nanotubes

0.5 g as-received CNTs were placed into a reaction flask, and 10 mL HNO_3 (70 %) was gently poured inside, followed by the slow addition of 5 mL H_2SO_4 (98 %) for further modification. The flask was then connected to a reflux system and gradually heated up to 130°C in an oil bath. After boiling for 25 min, the acid-treated CNTs were subject to further filtering and rinsing several times with distilled water and then freeze-dried at -55 °C and 0.024 mBar in the freeze dryer or the vacuum oven at 100°C overnight.

3.2.2 Preparation of graphene oxide - carbon nanotubes nanostructure through freeze-drying method

As shown in Figure 3-1, the CNT and GO nanostructures were prepared by dispersing 20 mg pre-treated CNTs and GO separately with the help of ultrasonication for an hour, then mixing with different ratios at a concentration of 0.4 mg mL^{-1} under sonication for another hour in order to achieve the uniform suspension (100 mL). The CNT and GO mixed suspension was quickly frozen by liquid N_2 (LN) and then frozen dried in a freeze dryer at -55°C and 0.024 mBar. To investigate the effect of the reduction process to the GNT nanostructures, the freeze-dried GNT products were subsequently reduced under H_2/Ar atmosphere at 400°C in a tube furnace for 2 h. The as-prepared samples were named based on different ratios of GO : CNT (i.e., GNT 1-1 refers to 50 wt.% of GO and 50 wt.% of CNT content).

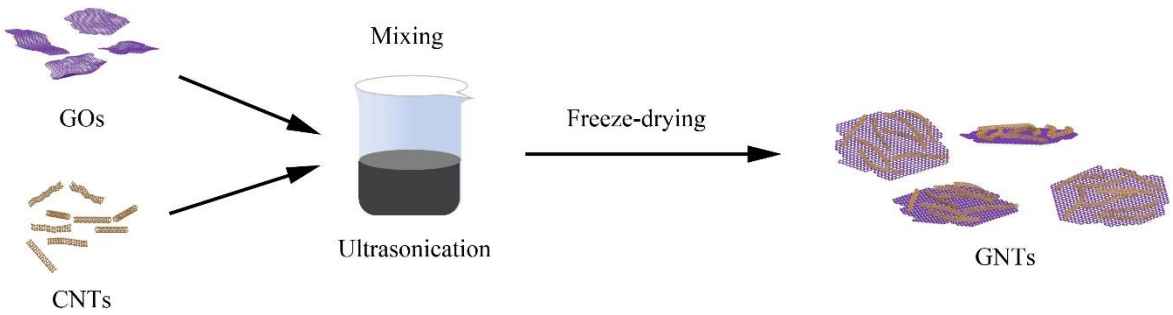

Figure 3-1 Schematic of the preparation of GNT nanostructures through the freeze-drying process.

3.3 Decorating of novel metal particles on GNT hybrids

3.3.1 Fabrication of copper nanoparticles coated GNT nanostructures

Based on the preparation of GNT sample, the copper nanoparticle decorated GNT (FGCu) nanostructures were subsequently obtained through the MLM method. As shown in Figure *3-2*, 2.82 g $Cu(CH_3COO)_2$ was dissolved in 50 mL H_2O, 100 mg CNTs and GOs were dispersed in water with a ratio of 1:1 and ultra-sonicated for half an hour. The MLM method was adapted by pouring the obtained carbon mixture into the copper solution, then stirred with magnetic stirring for another 2 hours with a different weight ratio of Cu : C to 9:1. This step was used to ensure that the contact of Cu ions with the well-dispersed GNTs is achieved at the molecular level. After the mixing, the suspension was quickly transferred into the liquid nitrogen (LN) to freeze. The obtained precursor was then obtained through the freeze-drying approach via the freeze dryer (Labconco FreeZone 76705 freeze dryer) at -55°C and 0.024 mBar and the sample was then reduced under H_2/Ar atmosphere at a set temperature in a tube furnace for up to 3 h. The obtained products were stored in the vacuum bag from further oxidation.

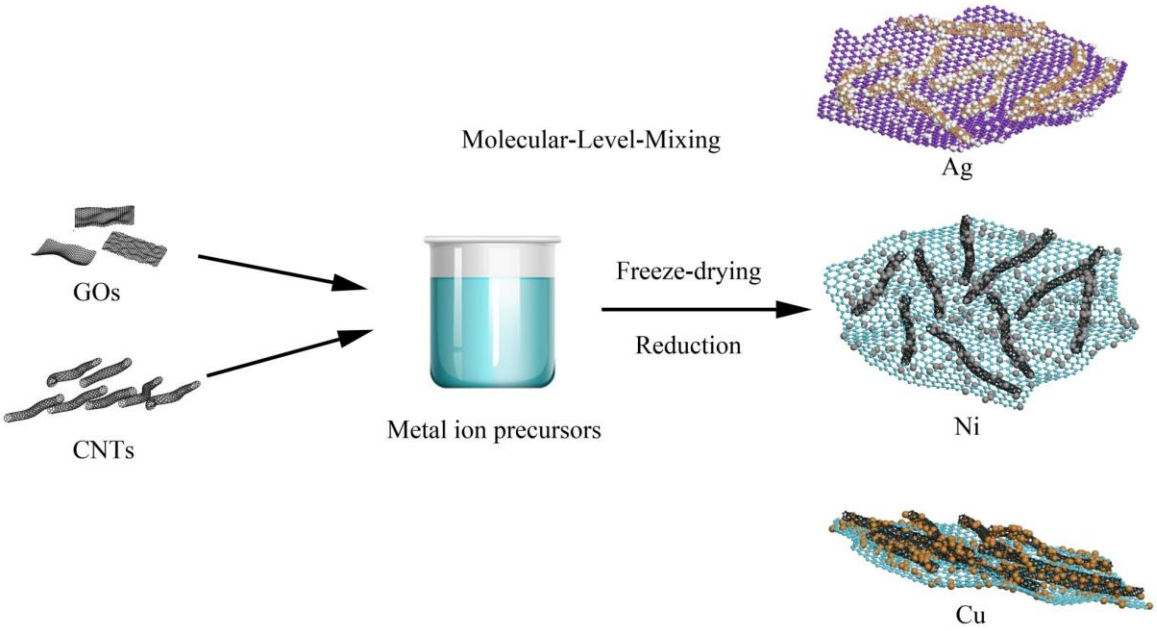

Figure 3-2 Schematic of the preparation of Cu, Ni and Ag nanoparticles decorated GNT nanostructures.

3.3.2 Fabrication of Nickel nanoparticles coated GNT nanostructures

Similar to the procedure of preparing the FGCu nanostructures (Figure *3-2*), the CNT and GO powders (with a weight ratio of 1:1) were firstly dispersed in water with a concentration of 0.4 mg mL^{-1} under sonication for one hour to achieve a homogeneous suspension. Different concentrations of nickel acetate (from 17.5 – 1100 mg) were then dissolved in 50 mL water whilst stirring. The CNT and GO suspension was then added to the well-dissolved nickel acetate solution and magnetically stirred for another 2 h to ensure the Ni ions have good contact with the GNT dispersions. After that, the suspension of Ni/GNTs was quickly frozen by LN and then freeze-dried at -55°C and 0.024 mBar. The obtained Ni/GNT precursors were subsequently reduced under H_2/Ar atmosphere at set temperatures in a tube furnace for 2 h. The as-prepared samples were named based on their calculated carbon ratio from FG10Ni90 to FG70Ni30 as the freeze-dried GNT/Ni samples (i.e., FG10Ni90 refers to 10 wt.% of carbon content and 90 wt.% of Ni content). The pure Ni sample was also prepared as a reference sample following the same method, without the addition of the CNT-GO mixture. The obtained

products were stored in the vacuum bag from further oxidation.

3.3.3 Fabrication of Silver nanoparticles coated GNT nanostructures

The Ag decorated GNT nanostructures were also obtained through the MLM method with a subsequent freeze-drying and reduction process. Figure *3-2* also displays the schematic of the preparation of the FGAg nanostructures. 288 mg of CH_3COOAg was dissolved in 50 mL H_2O. 80 mg CNTs and GOs with a ratio of 1:1 were mixed and dispersed under ultra-sonication which was then poured into the silver solution and stirred with a magnetic stirrer for another 2 h with a weight ratio of Ag : C of 8:2. After that, the suspension was quickly transferred into an LN atmosphere for fast freezing. The precursor was then obtained through a freeze-drying approach at -55 °C and 0.024 mBar and was subsequently reduced under H_2/Ar atmosphere at set temperatures in a tube furnace for up to 3 h. The obtained products were stored in the vacuum bag from further oxidation.

3.4 Densification of as-prepared powders

3.4.1 Manual pressing and sintering

For thermal management measurements, densified pellets were required. Manual pressing was initially introduced with pure micron copper powders (325 mesh, 0.1%> 63μm, 96.1%<45μm). Firstly, the obtained powders were pressed by the Specac Manual Hydraulic Press at 5 tons for 5 min with a 13 mm (equal 376 MPa), and the density of the obtained pellets die was measured. As shown in Figure 3-3, the compacted samples were then placed in an Al_2O_3 crucible and placed in the centre of a vacuum furnace provided by the Elite thermal system Ltd. The pellet was heated to a set temperature (from 550 to 800°C) at a heating rate of 3 °C min^{-1} and held for one hour under a vacuum atmosphere. The obtained pellets were pressed by the Specac Manual Hydraulic Press at 5 tons for 5 min again and the densities were measured again. To obtain the

denser pellets, the procedure was repeated several times, and the densities of the pellets were also measured each time. After that, the thermal management properties of these as-prepared Cu pellets which were obtained from different processes were then investigated.

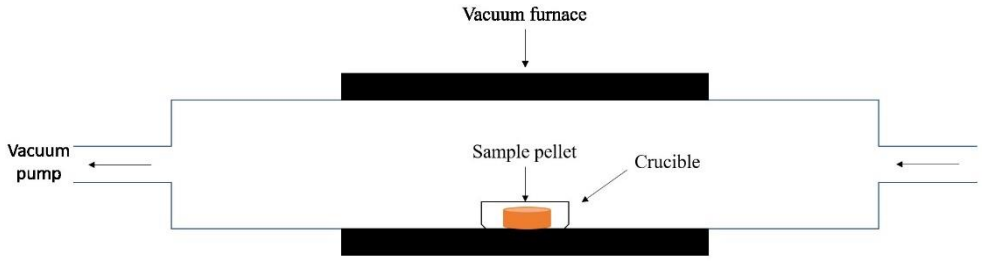

Figure 3-3 Schematic of the manual pressing and sintering process of preparing Gu pellet.

3.4.2 Spark plasma sintering

To prepare denser pellets, an advanced sintering method, spark plasma sintering (SPS), was introduced. The SPS 630 system provided by Kagaku-analys AB company is adopted. Figure 3-4 displays its working principle. The SPS process is based on the electrical spark discharge phenomenon: the spark plasma at high localised temperatures can be momentarily generated by high energy. Low voltage spark pulses current, which may produce up to ten thousand degrees centigrade, was used between the particles which will result in optimum thermal and electrolytic diffusion. This causes vaporization and the melting of the surfaces of the powder particles during the SPS process (however, this is a short period, approximately 5 to 20 min, which includes the rise and holding duration), constricted shapes or “necks” are formed around the contact area between the particles. During SPS, these necks gradually develop, and plastic transformation progresses during sintering, resulting in a sintered compact of over 99% of relative density.

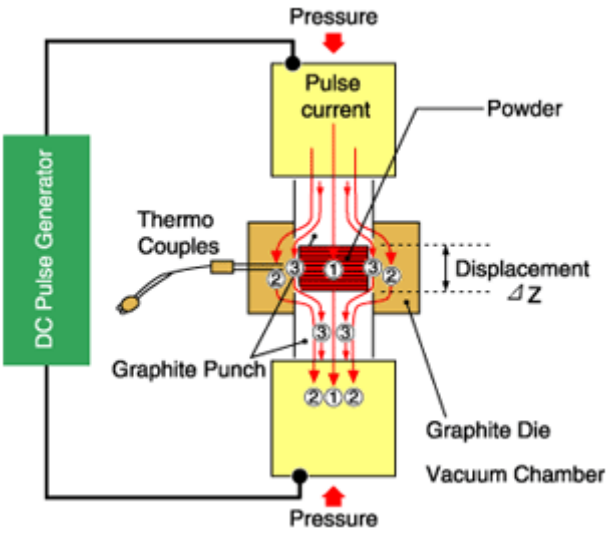

Figure 3-4 Schematic of the SPS apparatus. [48]

For the specific pressing procedure, the obtained powders were firstly placed in the graphite die and between two graphite punches, and then a thermocouple was inserted into the hole located in the middle of the die. The air in the chamber was then pumped out, and a high vacuum atmosphere (*ca.* 10^{-4} Pa) was obtained via a diffusion pump. The powders were then consolidated by the SPS 630 at a set temperature (from 600 - 900°C) for 5 min with a heating rate of 100 °C min^{-1} and an applied pressure of 60 MPa. The as-prepared pellets were then collected for the subsequent measurement, and densities of them were obtained utilising the Archimedes principle.

3.5 Preparation of polymer matrix composites

3.5.1 Preparation of FGAg-PEEK composites

To prepare the PEEK based composites, the as-prepared FGAg nanostructures were initially mixed with PEEK powders. Firstly, the FGAg samples and PEEK powders were separately dispersed in ethanol with the help of sonication and mixed with a weight ratio of 30:70 (FGAg : PEEK) and stirred by a magnetic follower for 1 h, the calculated volume ratio of Ag and C in the AGGNT-PEEK composites are 3.9 vol.% for Ag and 5 vol.% for C. Secondly, the well-

mixed solution was then continuously stirred and heated at 90°C to remove all the solvent. After that, the obtained mixed powders were transferred into an oven and completely dried at 120°C overnight. Finally, 0.5 g mixed powders were pre-pressed into pallets with a diameter of 13 mm using the Specac Manual Hydraulic Press at 5 tons for 5 min and then heated at 370°C for 2 h in a furnace. Meanwhile, pure GNT and pure Ag samples were separately mixed with PEEK as the reference sample with the ratios of 6 wt.% for GNT and 24 wt.% for Ag. As the ratio of Ag : C in FGAg is 8 : 2 and the weight percentage of FGAg in FGAg-PEEK composite is 30 wt.%, the ratio is 6 wt. % of GNT in GNT-PEEK composites and 24 wt.% of Ag in Ag-PEEK composites. In addition, the obtained pellets were prepared the same as FGAg-PEEK composites.

3.5.2 Preparation of FGNi-Epoxy composites with the assistance of magnetic field

After the preparation of the FGNi nanostructures, the obtained powders were applied as fillers with the epoxy resin; Figure 3-5 illustrates the diagram of the relevant apparatus. Firstly, 200 mg FGNi powders and 533 mg epoxy resin part A were dissolved in acetone separately. The two solutions were then mixed and stirred under mechanical string for 1 h to obtain a uniform dispersion. After thorough mixing of FGNi and epoxy A, 266 mg epoxy part B was added dropwise in the mixture with a weight ratio of epoxy A : B (2 : 1). The mixture was then stirred for another 15 min and poured into a mould (with the sample size of 10 mm × 10 mm). The mould was placed in the middle of a parallel magnetic field with a magnetic field strength of around 500 mT, and the magnetic field applied here is designed to align the FGNi fillers in the epoxy resin matrix. After one hour in the magnetic field, the mould was transferred into an oven at 60°C for 1 h and 90°C for another 1 h for the curing of the epoxy-based samples. For the reference FGNi-epoxy sample, a similar procedure was adopted just without the assistance

of the magnetic field, the pure epoxy sample was prepared without the addition of FGNi nanostructures and the assistance of the Magnetic field. The ratio of FGNi fillers was ranging from 10 to 30 wt.%.

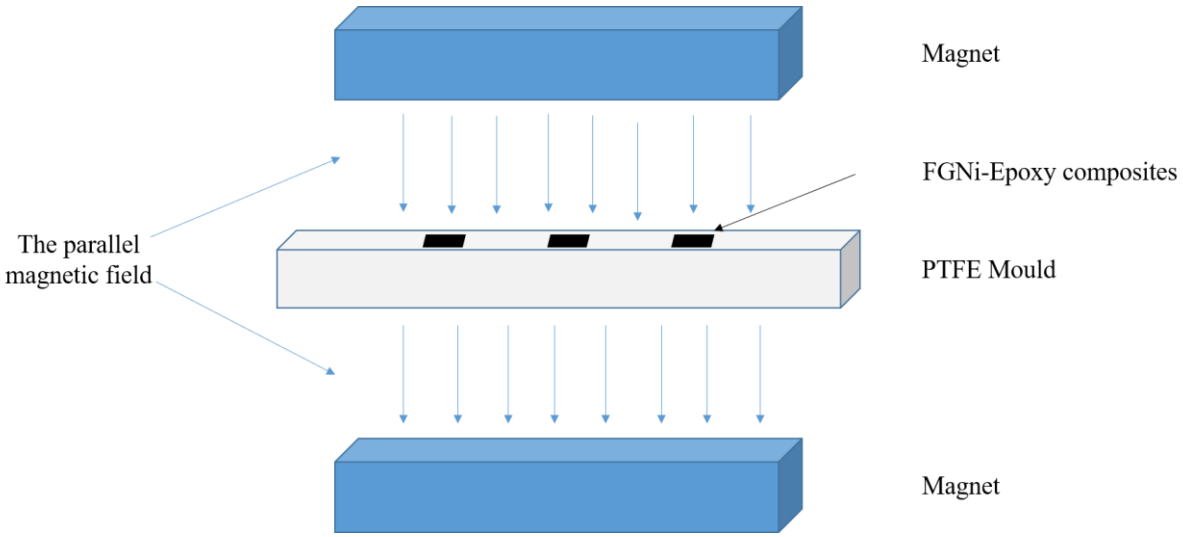

Figure 3-5 Apparatus of preparing FGNi-epoxy composite.

3.6 Characterisation techniques

3.6.1 Structure characterisation methods

3.6.1.1. X-ray powder diffraction

The X-ray powder diffraction (XRD) is a widely used characterisation method that is focused on investigating the phase composition of different materials. XRD works with the following principle and a schematic is displayed in Figure 3-6.

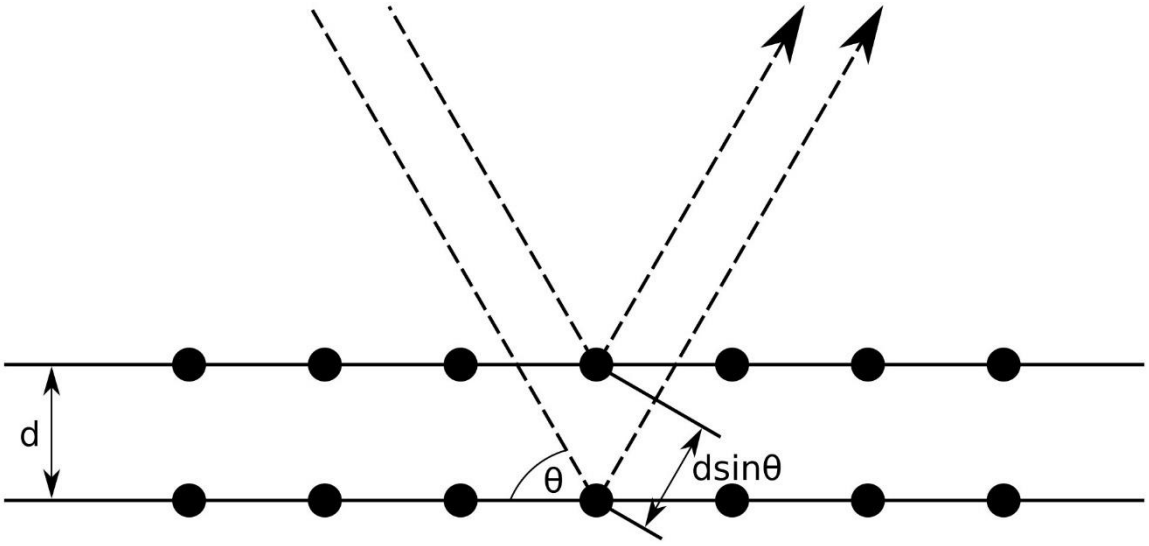

Figure 3-6 Bragg diffraction between two layers of atoms.

The X-ray is known as an electromagnetic wave, and the materials could be regarded as regular arrays of atoms. Thus, the diffraction of the X-ray can happen when it comes to the materials arrays, which is like the ocean wave produces a secondary wave when it strikes the obstacle. When the X-ray waves reach the measured atoms, elastic scattering happens, and secondary waves are produced. Due to the destructive interference, most of the waves which are generated among the arrays of the atoms are cancelled by each other. However, the constructive interference also will occur when certain waves meet the specific directions (Figure 3-6), and this is known as Bragg's law:

$$n\lambda = 2d\ sin\,\theta \qquad \text{Equation 3-1}$$

Here d is the inter-lattice spacing, λ is the wavelength of the X-rays, θ is the angle between the incident beam and the relevant planes and n is an integer. Therefore, by measuring the angle θ and their relative intensity of each diffraction peak for the measured material, the phase information can be obtained with the help of using diffraction peak position and intensity fitting software. Specifically, the XRD system can record the diffraction information of the measured material and generates a diffraction pattern with diffraction peaks at different locations (2θ). The obtained diffraction pattern is then compared with the Joint Committee on Powder

Diffraction Standards (JCPDS) powder diffraction file database, and one or several standard phases can be found out and matched with the obtained pattern. Thus, the measured material can be ascribed to the matched phase or phases.

In this thesis, the XRD analysis was carried out through the Bruker D8 Advance X-ray diffractometer system which was operated at a working condition of 40 kV and 35 mA. The X-Ray source is a Cu K-α radiation and the wavelength (λ) is 0.154 nm. The obtained samples (both powders and pellets) were measured at a 2θ step rotation of 0.02° with a dwell time of 5 s at room temperature (5°~80°). The diffractograms were recorded and then analysed by EVA software. The powders samples were placed in the sample holders and the pellet samples with smooth surface were stuck on the holders.

3.6.1.2. X-ray photoelectron spectroscopy

The X-ray photoelectron spectroscopy (XPS), which is also called the electron spectroscopy for chemical analysis, is a surface-sensitive technique to analyse the elemental composition (i.e., chemical state and electronic state) of the elements that exist within a certain material. Specifically, the monochromatic X-ray beam irradiates the surface of the material; different signals are emitted and recorded by the detectors of the XPS system. When an X-ray reaches an atom or molecule, the electrons can be ejected and escape from the atoms, which needs to overcome the work function dependent on the depth in the material. By measuring the kinetic energy, the binding energy of the emitted electrons can be obtained by considering the photon energy of the incident X-ray and the work function mentioned above. It can be described by the equation below:

$$E_k = h\upsilon - E_b - \varphi_s \qquad \text{Equation 3-2}$$

where the E_k is the kinetic energy of the electron measured, the $h\upsilon$ is the energy of the X-ray photons, the E_b is the binding energy of the electron and the φ_s is the work function.

In this thesis, the X-ray photoelectron spectroscopy (XPS) was recorded on VG ESCALab Mark II photoelectron using Al K-alpha X-ray as an excitation source with a wavelength of 1486.6 eV (hv). It was measured under a condition of anode voltage of 12 kV and an emission current of 20 mA. The XPS spectra are obtained by irradiating a material with a beam of X-rays while simultaneously measuring the kinetic energy and number of electrons that escape from the top 0 to 10 nm of the material. The powders samples and pellet samples with smooth surfaces were both stuck on sample holders for the measurements.

3.6.1.3. Surface area and pore volume

The Brunauer-Emmett-Teller (BET) theory, published by Stephen Brunauer, Paul Hugh Emmett, and Edward Teller [148], aims to explain the physical adsorption of the gas molecules on a certain material's surface and serves as the theoretical basis for the measurement of the specific surface areas. The BET equation is described as below:

$$\frac{1}{v[(p_0/p)]} = \frac{c-1}{v_m c}\left(\frac{p}{p_0}\right) + \frac{1}{v_m c} \qquad \text{Equation 3-3}$$

where p and p_0 are the equilibrium and saturation pressures of the adsorbates, respectively, v is the volume of the adsorbed gas, v_m is the monolayer adsorbed gas quantity and c is the BET constant. Therefore, Equation 3-3 can be plotted as a straight linear line ($y = ax + b$), and y is $\frac{x}{v[(1-x)]}$, a is the slope of the straight liner which is $\frac{c-1}{v_m c}$, x is $\left(\frac{p}{p_0}\right)$ and b which is the y-intercept is $\frac{1}{v_m c}$, and the linear relationship of this equation is maintained only in the range of $0<\frac{p}{p_0}<0.35$.

The v_m can be transferred to the function of the slope (a) and y-intercept (b):

$$v_m = \frac{1}{a+b} \qquad \text{Equation 3-4}$$

Therefore, the total surface area S_{total} and the specific surface area S_{BET} are given by:

$$S_{total} = \frac{(v_m N s)}{V} \qquad \text{Equation 3-5}$$

$$S_{BET} = \frac{S_{total}}{m}$$ Equation 3-6

where N is the Avogadro's number, s is the adsorption cross-section of the adsorbing species, V is the molar volume of the adsorbate gas and m is the mass of the measured sample.

The BET specific surface areas of the samples in this thesis were measured by Micromeritics ASAP 2420 accelerated surface area and porosimetry system, and was calculated from a relative pressure range of 0.05 to 0.20 on an N_2 adsorption isotherm at -196°C, giving positive BET 'C' parameters. Pore volume and size distribution were acquired from the isotherms using NLDFT on carbon slit pore model.

3.6.2 Morphology characterisation methods

3.6.2.1. Scanning electron microscopy

A scanning electron microscope (SEM) was used to investigate the surface morphology of the obtained samples. SEM is a type of electron microscope that could obtain surface morphologies by scanning the sample's surface with a focused beam of electrons. It is known that different kinds of signals [including secondary electrons (SE), back-scattered electrons (BSE), characteristic X-rays and light (CL), absorbed current and transmitted electrons] can be generated when the beam interacted with the atoms at various depths within the sample (Figure 3-7). These signals may be collected and processed to obtain different information about the surface topography and composition of the materials.

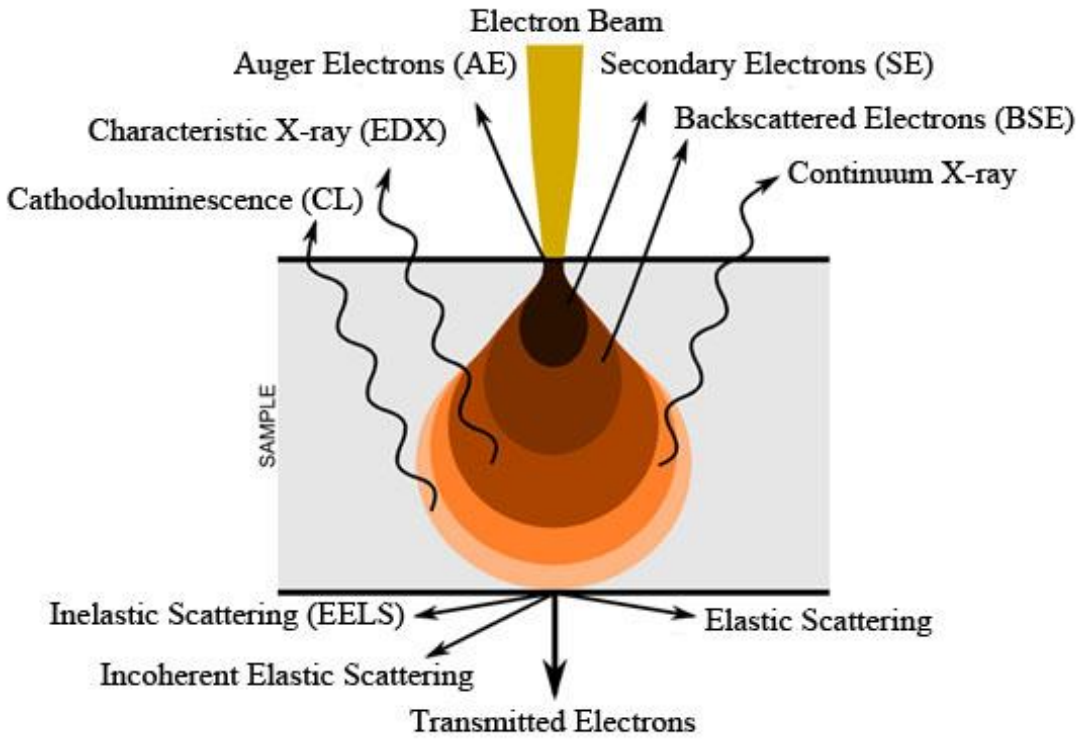

Figure 3-7 Different signals generated by the focused electron beam. [149]

Secondary electrons (SE)

The secondary electron image is the most common mode in the SEM. The secondary electrons usually are the conduction or valence bands electrons that are ejected by inelastic scattering with the incident beam electrons and collected by an Everhart-Thornley detector [150]. Thus, the secondary electrons have very low energy (~50 eV) that can only escape from the very top surface of the materials (only a few nanometres), and hence sensitive to the surface topography of the measured materials. The brightness of the signal highly depends on the number of the SE collected by the detectors, and more SE can escape from the surface when the angle of the incidence beam increases, which results in a shorter escape distance. Therefore, the sharp surface of the materials would lead to a brighter image than the flat surface, and the SE SEM images can reach a relatively high resolution, which is now around 1 nm.

In this thesis, the SE SEM images of the obtained powders were recorded under the JEOL 7100 field emission gun scanning electron microscope with a working voltage of 15 kV and a

working distance of 10 mm. The obtained powder and pellet samples were attached on the sample holders with carbon cement for observation. The polymer samples were coated with 10 nm carbon using a sputtering device.

Back-scattered electrons (BSE)

The back-scattered electrons are the incident beam electrons reflected or back-scattered by elastic scattering with the atoms in the sample. Therefore, the BSEs come from deeper locations of the specimen, and BSE images show less resolution than the SE image. However, since the BSEs can be back-scattered stronger by heavier elements than lighter ones, which would result in a brighter image in places containing heavier elements, the contrast of the specimen areas with different chemical compositions could be easily detected and distinguished. The larger difference of the atomic number between them is, the higher contrast can be obtained in the BSE image. Thus, the BSE image can be used to provide information about the distribution of different elements in the sample.

In this thesis, the BSE SEM images were also obtained with the JEOL 7100 field emission gun scanning electron microscope (SEM) with the working voltage of 15 kV and the working distance of 10 mm.

3.6.2.2. Transmission electron microscopy (TEM)

A transmission electron microscopy (TEM) was used to obtain finer details of the obtained samples. TEM is a microscopy technique that obtains images by the electron beam, which is transmitted through the specimen. Specifically, a beam of electrons is accelerated through high voltage (typically 200 kV) and passes through a very thin sample such that the beam could transmit through the specimen by either transmission or diffraction. The images then can be obtained and recorded by an imaging device (i.e., a fluorescent screen or a photographic film).

According to the TEM system, both the electron microscopy imaging and electron diffraction patterns can be recorded by adjusting the location of the intermediate lens, and information of both the crystal structure and the crystal orientation could be obtained in the specimen. When an aperture is inserted into the back focal plane of the objective lens, the images that are obtained by the direct beam electrons transmission are called the bright-field image. Because of the different thickness of the specimen and different atomic numbers in the specimen, the thicker regions, or the regions with higher atomic number elements, will present dark images, while places where the electron beam can easily go through (like no sample or thin sample) will appear bright. In contrast, when the unscattered electron beam is excluded from the aperture, the scattered electrons are selected instead, and the opposite contrast of the image can be obtained, which is called the dark-field image.

In this thesis, the JEOL 2100+ Transmission Electron Microscopy (TEM) with a working voltage of 200 kV was adopted to obtain the images of obtained samples, while the images of polymer-based composites were obtained under 80 kV to prevent damage to the polymer samples. The powder samples were first dispersed in ethanol and dropped on a copper mesh, and then can be observed after the evaporation of ethanol. The composites TEM samples were cut using a microtome with a fine diamond blade into a thin film of ca. 100 nm thick.

3.6.3 Density evaluation

In this study, the densities of the obtained pellets and samples were measured following the Archimedes principle. The weight of the sample was firstly measured in air and then in water. By considering the density of water is 1 g cm^3, the density of the measured sample can be calculated as follow:

$$D = \frac{W_{air}}{W_{air} - W_{water}} \qquad \text{Equation 3-7}$$

where D is the bulk density of the as-prepared sample, W_{air} is the weight of the sample in air and W_{water} is the weight of the sample in water. Distilled water was used in this work and an analytical balance with an accuracy of 0.0001 mg was employed. The weight measurements in both air and water were repeated three times to avoid errors. The relative densities were then calculated by dividing the calculated density by the theoretical density: 8.96 g/cm^3, 1.80 g/cm^3, 2.26 g/cm^3 and 1.32 g/cm^3 were adopted as the theoretical densities for Cu, CNT, graphene and CNT.

3.6.4 Thermal properties measurements

3.6.4.1. Thermogravimetric analysis

Thermogravimetric analysis (TGA) is a technique measuring the weight change of a sample continuously with the temperature ether is heating or cooling. The curve of the sample weight vs. time (which is equated with temperature) can be used to calculate the ratio of different constitutions under air or inert atmosphere. The weight changes at different times (temperatures) could be ascribed to the oxidation or decomposition of each component in the samples, and then the weight ratio of each component can be calculated accordingly.

In this work, the TGA experiment was performed using TA Q600 SDT. The as-prepared sample was placed in an aluminium pan, and the weight change of it was recorded at a temperature range (i.e., 50 to 900°C) in the air with a ramp rate of 10 °C min^{-1}. Meanwhile, the data analysis of samples was carried out by using the software SDTQ600 (TA Instruments, USA).

3.6.4.2. The differential scanning calorimetry

The differential scanning calorimetry (DSC) is a thermo-analytical technique in which the difference in the amount of heat required to keep the temperature of the sample and reference the same during the whole measurement procedure. As is known, there is a heat change during the physical transformation (including melts, phase transitions, glass transition, and chemical

reaction). For example, when a solid sample melts to a liquid, more heat is required to increase the temperature of the sample at the same rate compared to the reference. This is due to the absorption of heat by the sample as it undergoes the endothermic phase transition from solid to liquid. Likewise, the sample that undergoes the exothermic process requires less heat to raise the temperature. Thus, to maintain the temperature same between the sample and reference, DSC is able to measure the heat absorbed or released during the whole process. The measured heat flow is recorded to keep the temperature same as the reference sample is known as exothermic or endothermic heat.

In this thesis, the DSC behaviour was measured and recorded with the TA DSC2500 system. The sample, which had an average mass of around 10 mg, was sealed in an aluminium pan, and the whole measurement was carried out under the N_2 atmosphere within a certain temperature range (i.e. 30 to 380°C in FGAg-PEEK composites) with a ramping rate of 10 °C min^{-1}.

3.6.4.3. Thermal diffusivity measurement

The thermal diffusivity (α) is one of the most common thermophysical parameters to describe the heat transport property of a certain material. This value describes how quickly a material reacts to the change in temperature. In this thesis, the thermal diffusivities of the as-prepared samples were measured with the Netzsch LFA 467 HyperFlash-Light Flash Apparatus (Germany). As shown in Figure 3-8, the measurement is usually carried out by rapidly heating one side of a sample and measuring the temperature rise curve on the opposite side. Specifically, the as-prepared sample with a plane-parallel surface is placed in a sample holder and then located in the centre of the machine. A laser pulse heats the bottom surface of the samples, and an IR detector which is located on the top will record the temperature rise on the rear surface. The measured thermal diffusivity of the sample will then be calculated and presented by the

system. The thermal diffusivity measurements of all pellets were repeated three times to avoid errors.

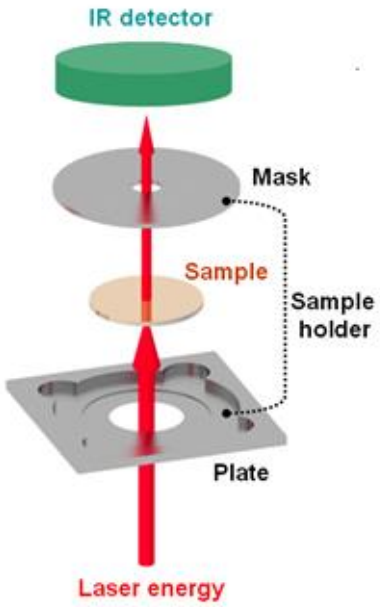

Figure 3-8 Schematic of the measurement of the thermal diffusivity of as-prepared pellet. [48]

3.6.4.4. Specific heat capacity

The specific heat capacity (C_p) of a substance is the heat capacity of the sample divided by its mass, and the heat capacity is defined as the amount of heat to be supplied to a given mass of material to produce a unit change of its temperature. Thus, C_p is the amount of heat that must be added to one unit of mass of the substance in order to cause the increase of one unit temperature. For example, when an amount of heat energy is added to a sample at a known uniform temperature, the heat capacity is obtained to measure the change of its temperature. By dividing the mass of this sample, C_p is obtained. As described above, DSC, known as a thermo-analytical technique, is widely used to look at how the Cp is changed by temperature. In this thesis, the measurement of Cp is carried out by the TA DSC2500 system, and the obtained data was analysed through the TRIOS Software v5.0.0 by TA instruments.

3.6.4.5. Thermal conductivity

Thermal conductivity is the ability of a certain material to conduct heat. According to the second law of thermodynamics, the heat always flows in the direction towards the lower temperature. Thus, the thermal conductivity of a certain sample is calculated by the equation:

$$K = \alpha \times \rho \times C_p \qquad \text{Equation 3-8}$$

Where the K (W m^{-1} K^{-1}) is the thermal conductivity of the material, α (mm^2 s) is the measured thermal diffusivity, ρ (g cm^{-3}) is the density of the material and C_p (J K^{-1} kg^{-1}) is the measured specific heat capacity.

3.6.4.6. The coefficient of thermal expansion (CTE) and thermal durability

To investigate the CTE and thermal durability of the obtained samples, the thermal-mechanical analysis (TMA) was adopted and recorded with the TMA Q400 from the TA instrument.

For both the CTE and thermal durability measurements, the as-prepared pellets were placed between two probes of the machine, and the dimension change of each sample was then measured by recording the movement of the probe. For the CTE measurement, the whole process was carried out from room temperature to 100°C at 5 °C min^{-1} with 0.02 N force under N_2 atmosphere. The obtained CTE can be described as:

$$CTE = {}^{(D \times \Delta T)}/_{t} \qquad \text{Equation 3-9}$$

where D is the dimension change of the sample, ΔT is the temperature change and t is the thickness of the sample. In addition, the thermal durability measurement was carried out from room temperature to 400°C at 10 °C min^{-1} with different applied forces (from 0.01 to 0.1 N) under N_2 atmosphere, and the dimension changes were recorded. The dimension change indicates the structural stability of the measured sample under loads.

3.6.5 Electrical conductivity measurement

Electrochemical impedance spectroscopy (EIS) is a powerful technique used to characterize the electrical properties of materials. The EIS tests were measured by ModuLab XM Materials Test System (Solartron, Hampshire, U.K.), and the EIS curves were recorded at room temperature over the frequency range of 0.01 to 1MHz. Impedance plots were analysed using the Zview software (Scribner Associates, Inc). The values of electrical resistance (R) can be obtained from the intercept of the corresponding semicircle on the real part of the impedance, and the relevant electrical conductivity can be calculated by 1 divide the obtained R. All the measurements were repeated three times to avoid errors.

3.6.6 Dye removal efficiency measurement

3.6.6.1. Physical adsorption measurement

For the physical adsorption measurement, 5 mg GNT hybrids were added into 50 mL obtained dye solution with a range of concentrations (5 ppm to 30 ppm) of RhB or MO, and magnetically stirred. At different time intervals, the GNT hybrids were firstly removed, and the concentration of the solution was then measured by a UV-Vis spectrophotometer (Biochrom Libra S22). The absorbance was measured from 400 nm to 700 nm at a step of 0.5 nm with a scan speed of 375 nm min^{-1}. The maximum adsorption peaks of RhB and MO are located at 554.5 nm and 463.0 nm, respectively. Thus, the dye removal efficiency (E %) of GNT hybrids at different reaction times and the removal capacity (q) was obtained by the equation below:

$$E\% = \frac{(A_0 - A_t)}{A_0} \times 100\% \qquad \text{Equation 3-10}$$

$$q = \frac{(C_0 - C_t)}{m} \times V \qquad \text{Equation 3-11}$$

where A_0 and A_t are the absorbance of UV-Vis intensity initially and at the different measured time, and C_0 and C_t are the obtained concentration before adsorption and at equilibrium time, m is the weight of adsorbents (GNTs) and V is the beginning volume of dye solutions. The adsorption capacity measurements of alls samples were repeated three times to avoid errors.

3.6.6.2. Photo-degradation

The RhB removal performances of the as-prepared products were evaluated under dark and UV irradiation combinations (360 W, 254 nm). The results were recorded using a Carry 50 UV Visible spectrophotometer, and the absorbance was measured from 400 nm to 700 nm at a step of 1 nm with a scan speed of 600 nm min^{-1}. First, 250 mL 5 ppm RhB solution was stirred in the dark condition, and 25 mg obtained FGNi sample was dispersed in the solution. Then, the physical adsorption of RhB within 120 min was first assessed, and the absorbance peak of RhB dye was obtained with a 15 min interval using a UV-Vis spectrometer. To investigate the photocatalytic property, the mixed suspension was initially stirred in the dark for 60 min to allow for adsorption equilibrium. After equilibrium, the suspension was transferred and irradiated under a UV lamp. The absorbance peak of RhB was also recorded every 15 min by the UV-Vis spectrometer for another 120 min. It is known that the RhB solution showed a maximum absorb peak at *ca.* 554.5 nm, and the absorbance of this peak corresponds to the concentration of RhB dye [151]. The photo-degradation efficiency (PE) was calculated according to

$$PE\ (\%) = \frac{A_0 - A_t}{A_0} * 100\% \qquad \text{Equation 3-12}$$

where A_0 and A_t are the UV-VIS absorbance intensities of the RhB dye solution at the initial and a given time interval of irradiation, respectively. To explore the adsorption kinetic of as-prepared samples, 25 mg FG30Ni70 samples were dispersed in 250 mL 5 ppm RhB solution in the dark, and the absorbance was recorded from 5 min to 10, 20, 30, 45, 60 and 90 min. All the

measurements were repeated three times to avoid errors.

3.6.6.3. The scavenger study of the dye adsorption

The scavenger experiment was introduced to clarify the reactions in the photo-degradation process. Specifically, different scavengers, for example, methanol for $OH^{\cdot}$ free radicals, potassium iodide (PI) for holes (h^{+}) free radicals and p-benzoquinone (BQ) for $O_2^{\cdot -}$ free radicals, were added into RhB solution with FGNi samples. After stirring in the dark for 60 min for dark equilibrium, the mixtures were transferred under UV irradiation and recorded the final efficiency. Like the measurement of the photo-degradation process, the absorbance peak of RhB dye was obtained with a 15 min interval and recorded by the UV-Vis spectrometer.

4 Decoration of novel metal nanoparticles on graphene-carbon nanotube nanostructures

In this chapter, the preparation of CNT-GO nanostructures via a freeze-drying method has been studied. Following this, the decorations of different metal nanoparticles (i.e., Cu, Ag, and Ni) on such nanostructures have been obtained through the MLM method with the subsequent reduction process. The well-dispersed metal nanoparticles decorated CNT-GO nanostructures have been successfully obtained based on the facile and universal preparation method as observed by the detailed characterisation (such as XRD, SEM, and XPS).

4.1 Preparation of graphene-carbon nanotubes nanostructures

4.1.1 Carbon nanotubes and the acid treatment carbon nanotubes

XRD patterns of the as-received CNTs and acid-CNTs are displayed in Figure *4-1*. A broad peak from 20-50° can be clearly found in both XRD patterns, and no apparent differences can be detected, which indicated that the acid treatment did not change the crystalline structure of the CNTs.

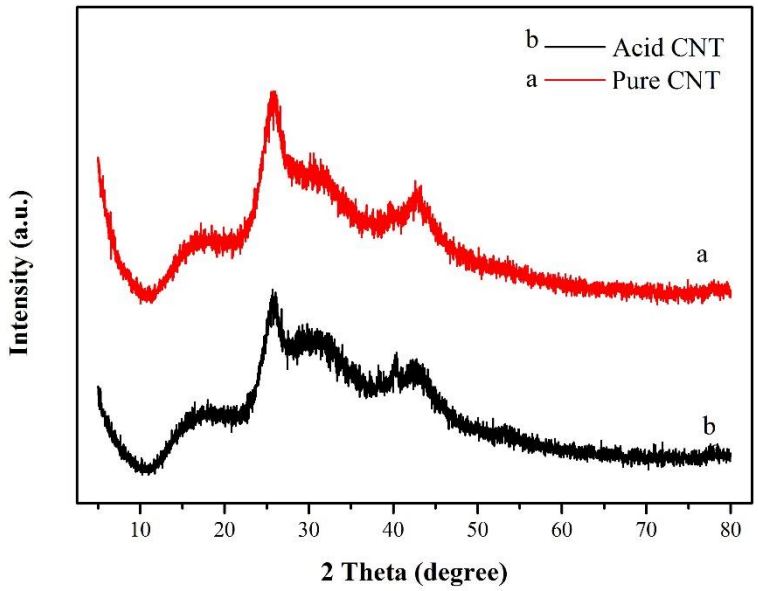

Figure 4-1 XRD patterns of pristine CNTs (a) and acid-treated CNTs (b).

To further investigate the influence of acid treatment, SEM was introduced to examine both samples and typical SEM images are shown in Figure *4-2*. From the low magnification image of as-received CNTs (Figure *4-2*a), the agglomeration of CNTs can be observed clearly. In the high magnification image (Figure *4-2*b), the tubes can be observed bent, curved, and agglomerated, and found into the clusters shown in Figure *4-2*a. The agglomeration can be ascribed to the strong π-π interaction between the carbon atoms on each layer. After the acid treatment and freeze-drying, the secondary SEM images of the acid-CNTs are shown in Figure *4-2* c and d. It can be observed that the agglomerate of CNTs generated a flake-like structure under low magnification (Figure *4-2*c), which can be ascribed to the freeze-drying process. During the fast freeze process, the growth of ice would separate the acid-CNTs into layers between each ice crystalline. Meanwhile, the acid-CNTs can also be found agglomerated under high magnification (Figure *4-2*d). Therefore, though the freeze-drying method may affect the CNTs cluster morphology, the acid treatment did not obviously increase the dispersity of CNTs.

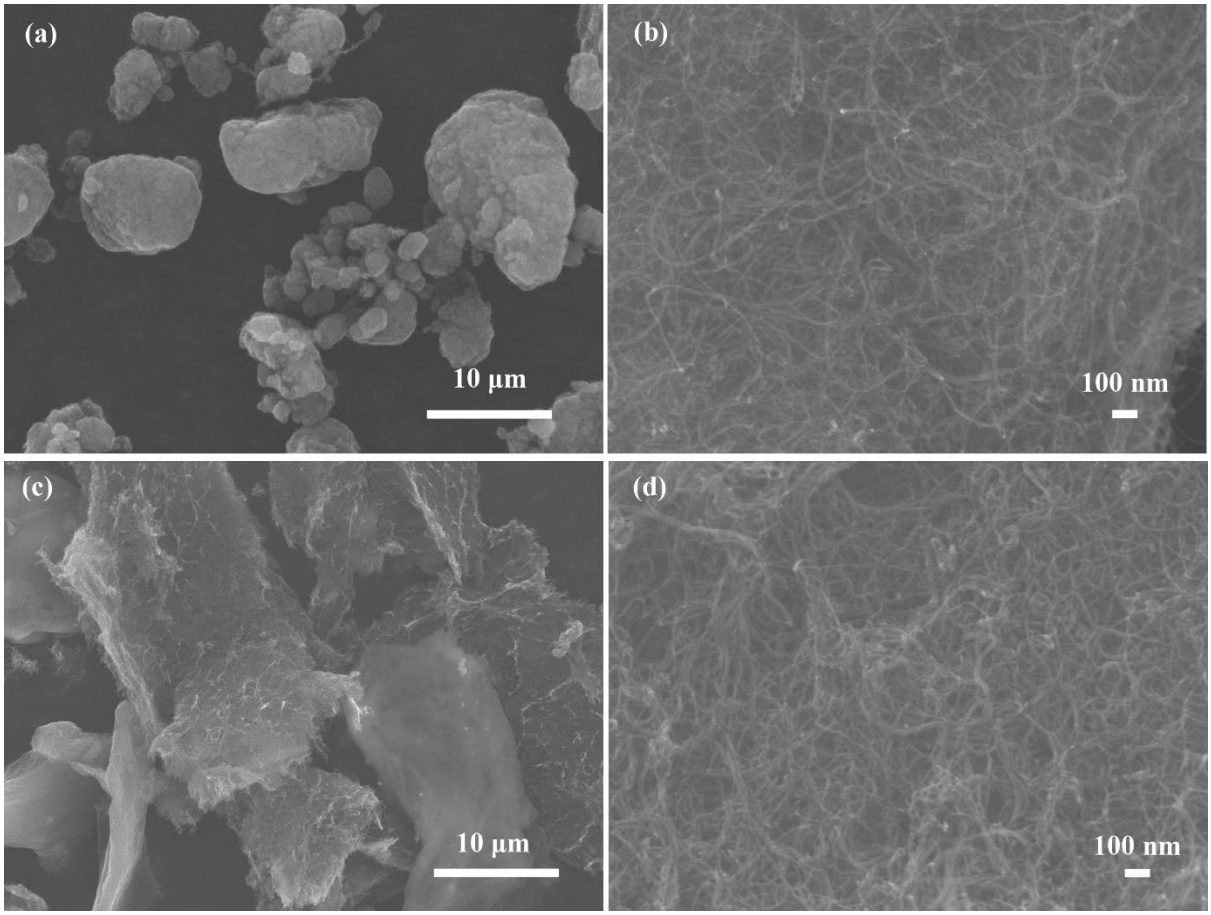

Figure 4-2 SEM images of pristine CNTs and acid CNTs under low (a and c) and high (b and d) resolution.

To further explore the chemical constitution of the as-received CNTs and the acid CNTs, XPS was undertaken and the survey scan results of both samples are displayed in Figure *4-3*. It can be found that the survey scan of the pristine CNTs only shows a sharp characteristic peak of C 1s, which confirms the existence of C element in the pristine CNTs (Figure *4-3*a). In Figure *4-3*b, the survey scan of the acid CNTs shows the evidence of O. The O 1s characteristic peak, which locates at 530 eV and the O KLL peak from 970 to 1000 eV indicates that some oxygen-contained components were generated during the acid treatment. These oxygen-contained components should be carbon-based functional groups (i.e., carboxylic acid and phenolic hydroxyl groups) generated during acid treatment. In the deconvoluted C 1s spectrum of acid CNT sample (Figure *4-3*c), the main peak located at 284.0 eV is the sp^2 hybridized C and a defect containing C peak was observed at 284.7 eV, indicating the formation of defect C

component during acid treatment [152]. The C-O (ether bonds) part corresponding to the hydroxyl groups at 286.3 eV, the C=O groups (ketone bonds) at 288.9 eV and the sp^2 hybrid orbit of the benzene plane at 290.8 eV further confirm the existence of oxygen-containing functional groups [153].

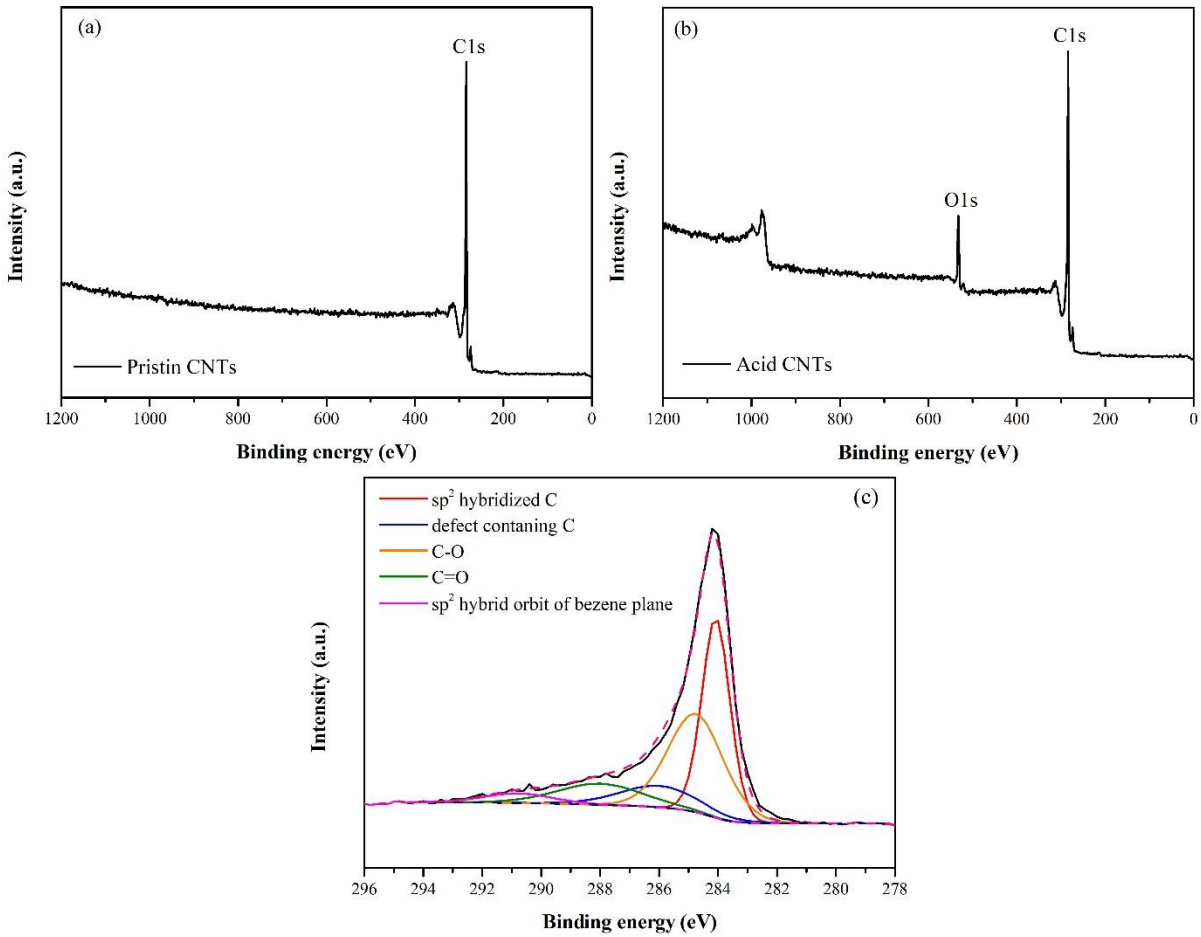

Figure 4-3 XPS survey scan of as-received CNTs (a) and acid CNTs (b), and the high-resolution C 1s spectrum of acid-CNT sample.

4.1.2 Graphene oxide and its relevant characterisation

To evaluate the quality of the as-received GO, XRD and SEM were performed. The XRD pattern of the pure GO is displayed in Figure *4-4*. A typical sharp peak at ca. 10° and a broad peak ranging from 25-40° can be observed. Similar results have been reported, which confirmed the existence of GO [100]. SEM images of the GO are displayed in Figure *4-5*. Under low magnification (Figure *4-5*a), the GO structures can be observed as the graphene-

layer-like structure after the freeze-drying process. Thus, the good dispersity of GOs can be ascribed to the ultra-sonication, which uniformly dispersed the GOs, and the freeze-drying method, which largely kept this well-dispersed structure by fast freezing in LN. After the freeze-drying process, the ice in the sample was completely removed, and the obtained powders were loose structures. In the high magnification image (Figure *4-5*b), the surface of the GO can be found smooth, and no other constitution could be detected.

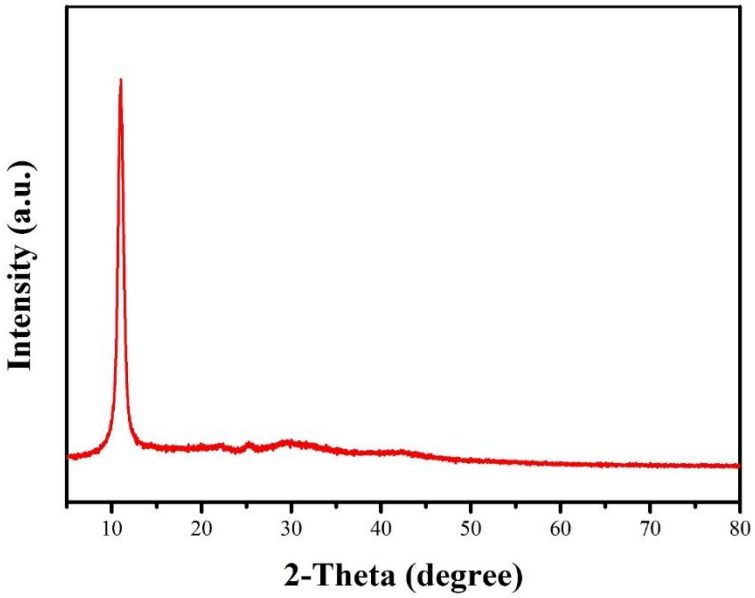

Figure 4-4 XRD patterns of freeze-dried GO powders.

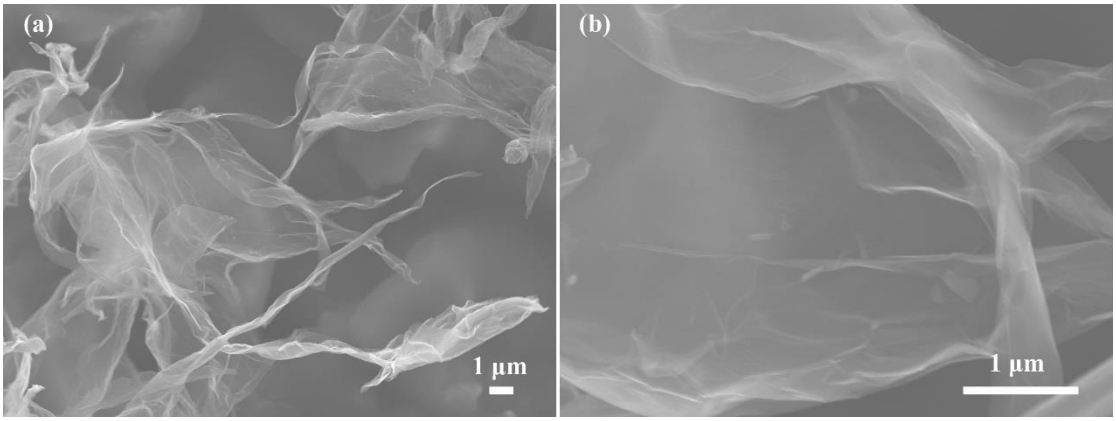

Figure 4-5 SEM images of the freeze-dried GO sample under low (a) and high (b) magnification.

XPS was then adopted to investigate the GOs, the survey scan and high-resolution deconvoluted C 1s spectrum are illustrated in Figure *4-6*. In the survey scan (Figure *4-6*a), the

characteristic peak of C 1s and O 1s can be observed, which confirms the existence of C and O elements in the GO samples. In the deconvoluted C 1s spectrum of the pure GO (Figure *4-6*b), two main peaks can be found, the sp^2 hybridized C (C-C and C=C) component locates at 284.0 eV. The C-O component, which ascribes to the hydroxyl and epoxy groups, locates at 286.2 eV [152]. Meanwhile, a minor peak located at 287.9 eV is the O=C-OH groups. The XPS results of acid-treated CNTs and GOs could confirm the existence of the oxygen-containing functional groups in both acid CNTs and GOs samples.

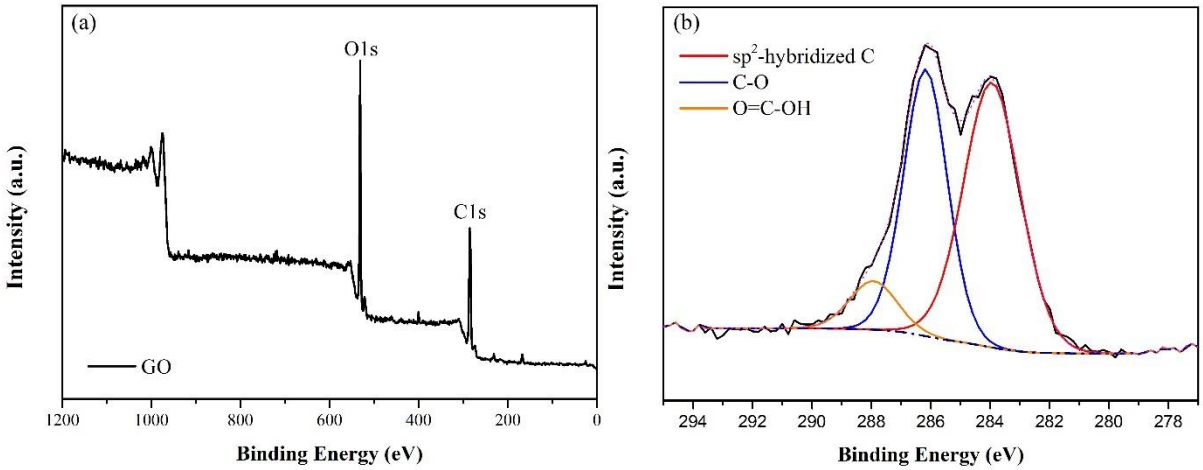

Figure 4-6 Survey scan (a) and deconvoluted C 1s (b) spectrum of GO sample.

4.1.3 GO-CNT nanostructure and its characterisation

The SEM images of both GNT nanostructures before and after reduction are shown in Figure 4-7. Figure 4-7a and b display the GNT nanostructure before reduction. The GNT nanostructures are found to keep the graphene-layer like structure, and no obvious agglomeration can be detected (Figure 4-7a). In Figure 4-7b, the CNTs can be observed attached onto the surface of the graphene layers due to the π–π interactions which existed between each carbon layer. Although the CNTs can still be detected to be bent and curved, they did not agglomerate into clusters or generate thick flake-like structures that were observed in the as-prepared pristine CNTs and acid-CNTs samples (Figure *4-2*) The CNTs are separated by the graphene oxide layers. Thus, the GNT nanostructures show improved dispersity by

combing the CNTs and GOs together with the freeze-drying process. In Figure 4-7c and d, the SEM images of reduced GNT nanostructures illustrate a similar morphology compared with un-reduced ones. They are well-dispersed graphene-layer like structures, and the CNTs are attached onto the surface of graphene layers.

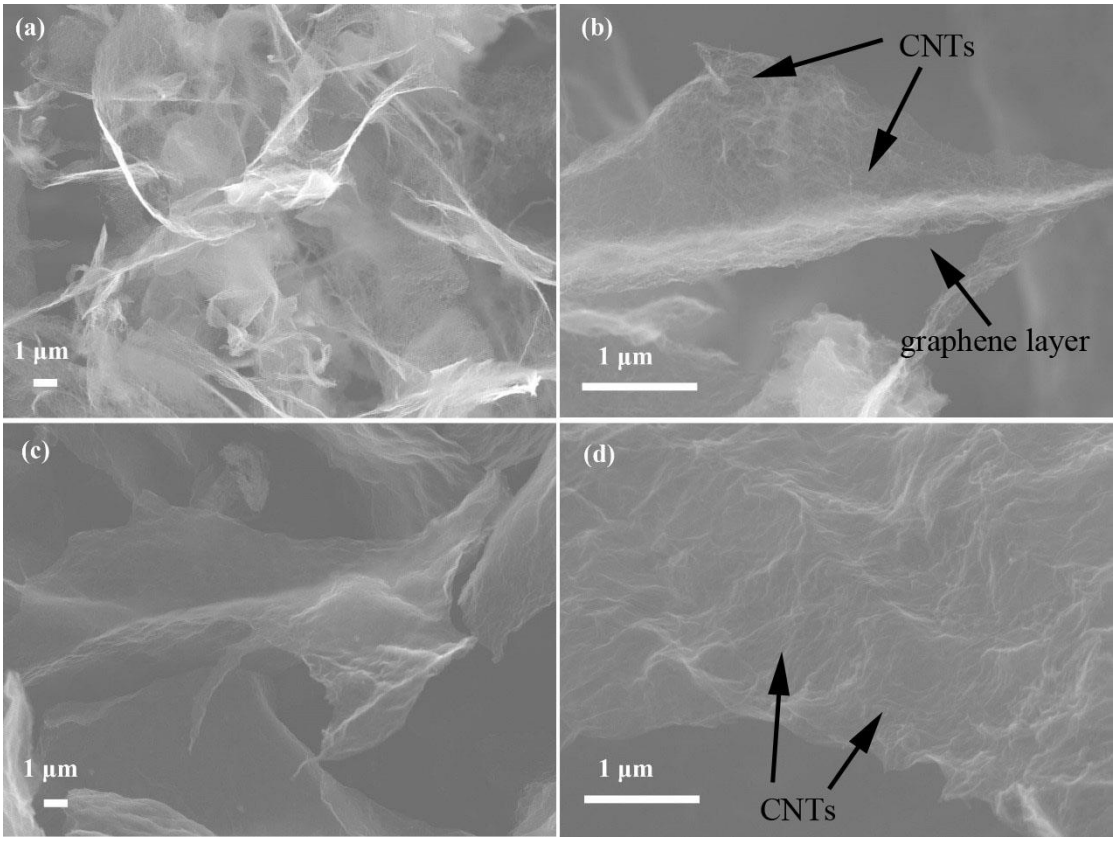

Figure 4-7 SEM images of GNT nanostructure before (a and b)and after (c and d) reduction process.

XPS the results are shown in Figure 4-8. Figure 4-8a displays the survey scan of GNT and reduced-GNT, and it can be found that both samples have the characteristic peaks of C and O elements as expected. However, the intensities are different between GNT and reduced-GNT samples. The intensity of the O characteristic peak is higher in GNT samples when compared with reduced-GNT samples, this is because some of the oxygen-containing functional groups in GNT nanostructure are reduced during the reduction process. The deconvoluted C 1s spectrum of both samples (Figure 4-8 b and c) further confirm this. In the deconvoluted C 1s spectrum of the GNT sample (Figure 4-8b), the peak can be deconvoluted into the sp^2

hybridized C part located at 284.6 eV, the C-O (ether bonds) part corresponding to the hydroxyl groups at 286.3 eV, the C=O groups (ketone bonds) at 288.9 eV and the sp^2 hybrid orbit of benzene plane at 290.8 eV [153]. Similar peaks can be detected in the reduced-GNT sample besides the defect-containing sp^2 hybridized C at 285 eV, resulting from the reduction process in the preparation procedures [154, 155]. The intensities of oxygen-contained functional groups (especially the C-O groups as shown in Figure 4-8b) decrease dramatically compared to the reduced-GNT sample (Figure 4-8c), indicating that although the oxygen-contained functional groups have been partly reduced during the reduction process.

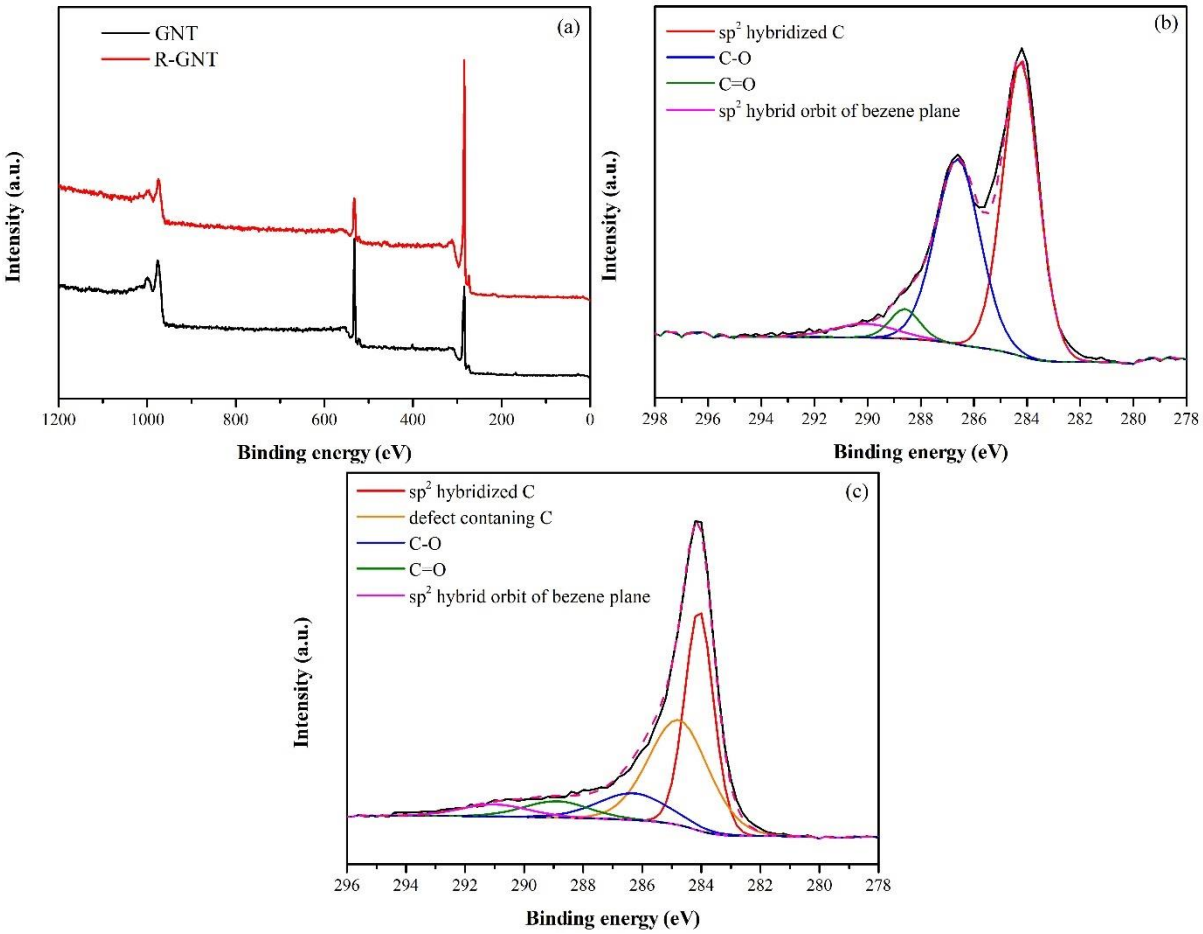

Figure 4-8 XPS survey scan of GNT and R-GNT samples (a), and the deconvoluted C 1s spectrum of GNT (b) and reduced-GNT (c) samples.

4.2 Decorating of Cu nanoparticles on the GNT nanostructures and the effects of different preparation parameters

Although the well-dispersed GNT nanostructures have been successfully prepared, the introduction of metal nanoparticle decoration could further enhance the dispersity. Therefore, to investigate the optimised parameter of decorating copper nanoparticles on the GNT nanostructures, different preparation conditions (including different reduction temperatures and reduction durations) were explored. The FGCu precursors, which were obtained directly from the freeze-drying, were firstly reduced under different temperatures from 150 to 300°C for 3 h (FGCu-150, FGCu-200, FGCu-250, and FGCu-300). After that, different reduction durations from 2 to 4 h at 250 and 300°C (FGCu-250-4h, FGCu-300-2h, and FGCu-300-4h) were studied.

4.2.1 Effect of reduction temperature to the FGCu nanostructures

The XRD patterns of the FGCu precursors are displayed in Figure 4-9. The patterns of the FGCu precursors matched well with the standard peaks of $Cu(CH_3COO)_2 \cdot H_2O$ (ICDD PDF No. 00-27-0145). There is also a broad peak ranging from ca. 20-40° compared to the baseline, and this can be ascribed to the broad peak of the carbon component observed previously. Therefore, the evidence of the copper acetate phase remained after the freeze-drying.

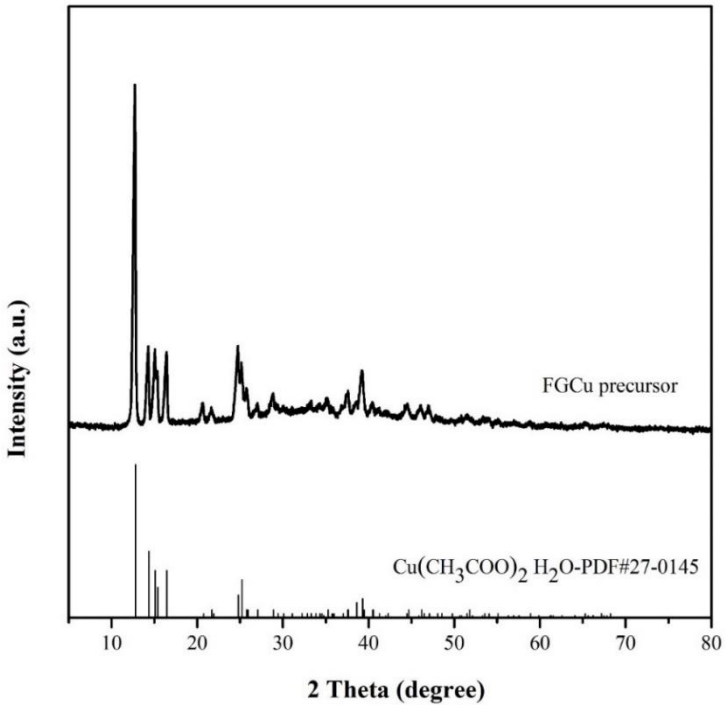

Figure 4-9 XRD patterns of the FGCu precursors and standard $Cu(CH_3COO)_2H_2O$.

Figure 4-10 illustrates the XRD patterns of FGCu samples, which were then reduced under an Ar/H_2 atmosphere at 150°C for 3h. It was named FGCu-150. Compared with the FGCu precursors, the intense diffraction patterns of FGCu-150 could be found to match with standard diffraction peaks of $Cu(CH_3COO)_2$ (ICDD PDF No. 00-27-1126), which indicates that the FGCu precursors lost the crystal water under 150°C Ar/H_2 atmosphere. Some minor peaks located after 40° could be ascribed to $Cu(CH_3COO)$ phase (ICDD PDF No. 00-28-0392). Meanwhile, the broad peak corresponding to the GNT nanostructures still remained in the obtained patterns.

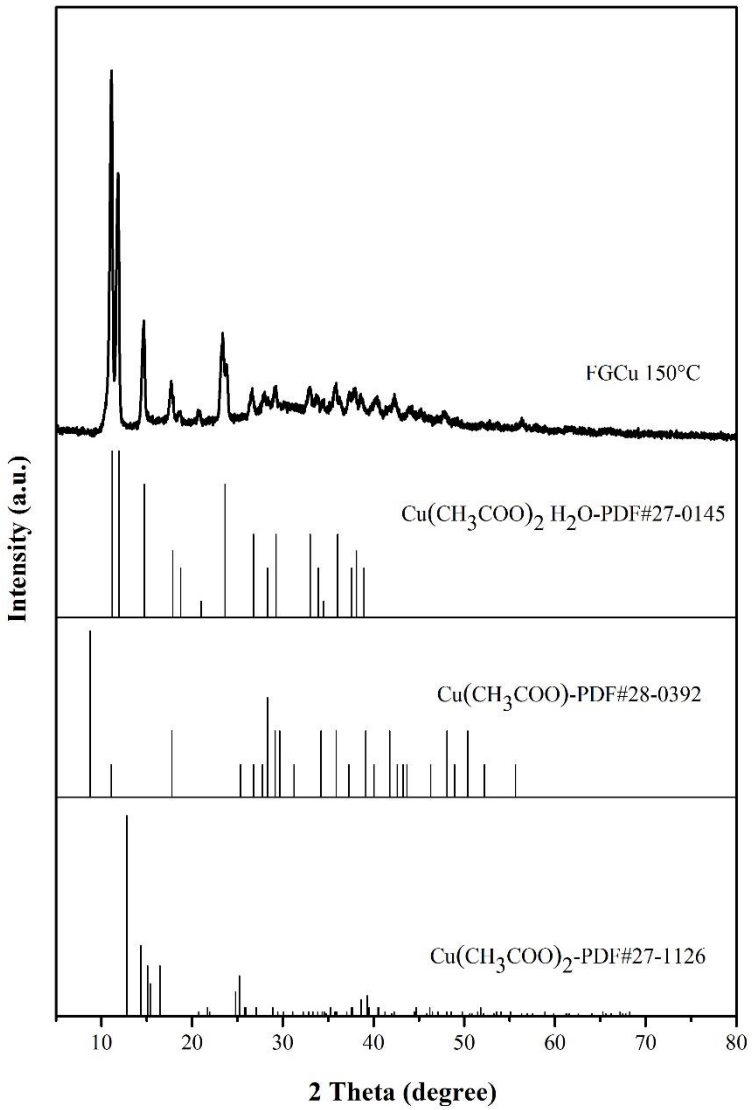

Figure 4-10 XRD patterns of the FGCu-150 samples reduced at 150 °C for 3h under an Ar/H_2 atmosphere, and the standard $Cu(CH_3COO)_2$, $Cu(CH_3COO)$ and $Cu(CH_3COO)_2\ H_2O$ samples.

When the reduction temperature increased to 200°C, the XRD pattern of FGCu-200 (reduced at 200°C under an Ar/H_2 atmosphere) is shown in Figure 4-11, which exhibits a different pattern when compared with FGCu-150. First, there are still diffraction peaks of $Cu(CH_3COO)_2$ (ICDD PDF No. 00-27-1126) remaining in the FGCu-200 patterns, which indicates that the $Cu(CH_3COO)_2$ cannot be completely reduced at 200°C under Ar/H_2 atmosphere. In addition, the diffraction peaks of a new phase [$Cu(CH_3COO)$ ICDD PDF No. 00-28-0392] can be detected among the FGCu-200 patterns, which demonstrate that some copper ions' valences were reduced from Cu II to Cu I. Meanwhile, obvious peaks located at 36°, 43° and 62° can be

attributed to the cuprite (Cu_2O ICDD PDF No. 00-05-0667). Therefore, the FGCu precursors can only be partially reduced to $Cu(CH_3COO)$ and Cu_2O at 200°C under an Ar/H_2 atmosphere for 3 h.

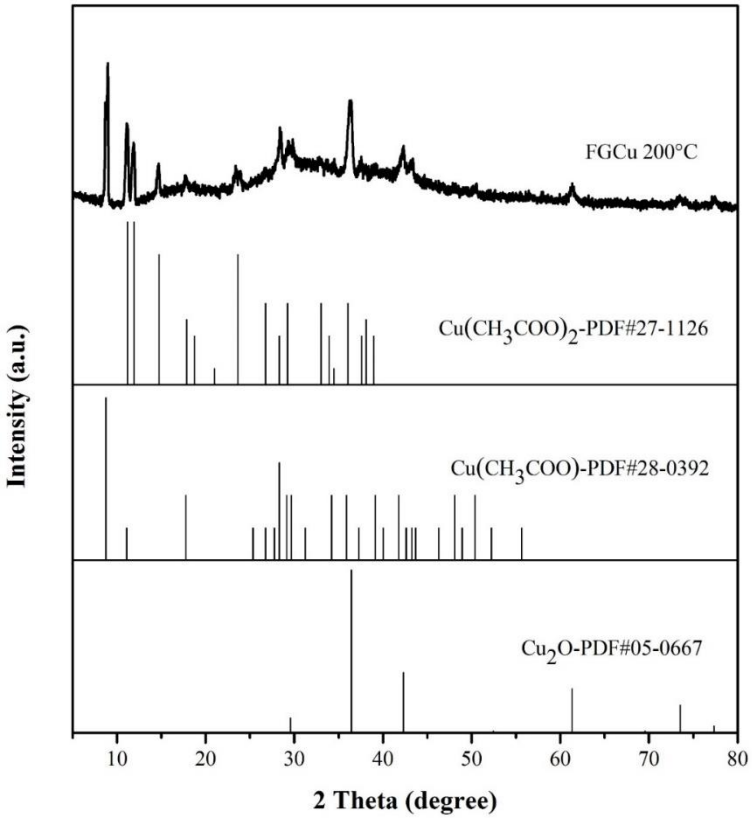

Figure 4-11 XRD patterns of FGCu-200 sample reduced at 200°C under an Ar/H_2 atmosphere for 3 h and the standard peaks of $Cu(CH_3COO)_2$, $Cu(CH_3COO)$ and Cu_2O.

The reduction temperatures were investigated further, XRD patterns of FGCu-250 and FGCu-300 samples (reduced at 250 and 300°C under an Ar/H_2 atmosphere for 3 h) are displayed in Figure 4-12. Three strongest diffraction peaks located at 43.2°, 50.4°, and 74.1° can be observed in both FGCu-250 and FGCu-300 samples, and these three peaks matched well with the standard diffraction peaks of the pure copper phase (ICDD PDF No. 00-04-0836). Therefore, it can be concluded that the FGCu precursors can be reduced to the copper phase when the temperature reaches above 250°C. In addition, there is a minor peak located at around 36.4°, which can be attributed to the cuprite phase (Cu_2O ICDD PDF No. 00-05-0667). Although the diffraction peaks of Cu dominate in the FGCu-250 sample, there is still Cu_2O

phase, which was not completely reduced in the final product. Moreover, the broad peak which is ascribed to the GNT component observed previously can still be witnessed in both FGCu-250 and FGCu-300 samples as expected, which confirms the existence of the GNT in the final reduced productions.

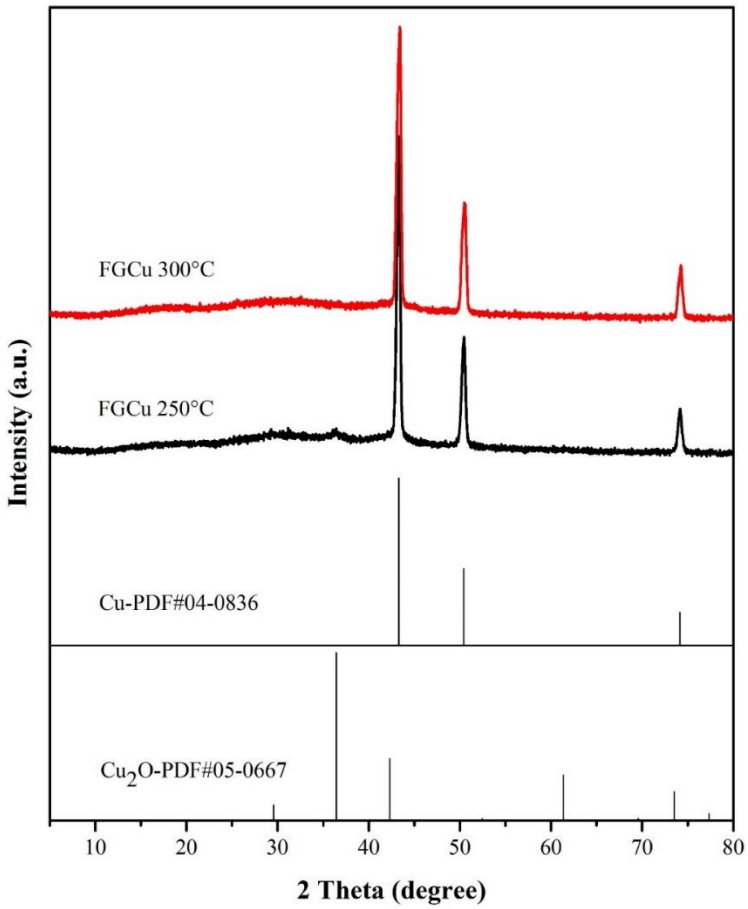

Figure 4-12 XRD patterns of the FGCu-250 and FGCu-300 samples reduced at 250 and 300°C under an Ar/H_2 atmosphere for 3 h, and the standard peaks of Cu and Cu_2O phase.

SEM images of all the FGCu samples, which were reduced at different temperatures, are shown in Figure 4-13. In the SEM images of FGCu-150 (Figure 4-13 a and b), the graphene-layer-like structure can be observed (Figure 4-13a) remaining after reduction at 150°C. The squamous-like morphology can be observed covering the surface of the GNT nanostructures, and this can be ascribed to the $Cu(CH_3COO)_2$ according to the XRD results (Figure 4-10). With the increase of reduction temperature, the morphology of FGCu-200 has changed (Figure 4-13 c and d). Although the GNT nanostructure can still be observed, different kinds of particles are

witnessed (including round and rod particles as well as the squamous like morphologies appeared in FGCu-150). Combined with the XRD results of FGCu-200, it can be assumed that these particles are $Cu(CH_3COO)_2$, $Cu(CH_3COO)$, and Cu_2O, which are not completely reduced under 200°C Ar/H_2 atmosphere for 3 h. When the reduction temperature increases to 250°C, the FGCu-250 sample can be found with a more uniform morphology (Figure 4-13e and f). The GNT based nanostructure remained in Figure 4-13e and the uniform distribution of round nanoparticles can be observed decorated on the surface of GNT layers (Figure 4-13f). These uniformly decorated nanoparticles are around 20-50 nm and can be attributed to the Cu phase according to the XRD result of FGCu-250 (Figure 4-12). Although there is still a minor peak of Cu_2O appearing in the XRD result, it is difficult to distinguish the Cu_2O particles in the SEM image. The images of FGCu-300 sample, which was reduced at 300°C, are displayed in Figure 4-13 g and h. Similar to the morphology of FGCu-250, the FGCu-300 sample shows a similar graphene-layer-like structure and the copper nanoparticles, which were around 50 nm, were uniformly decorated on the GNT nanostructures. Therefore, the Cu nanoparticles decorated GNT nanostructures have been successfully prepared through the MLM method combined with the freeze-drying and the subsequent reduction process. The Cu nanoparticles appeared uniformly coated on the GNT nanostructures when the reduction temperature reached above 250°C under Ar/H_2 atmosphere for 3 h. In addition, combined with the XRD results that the FGCu should be completely reduced in the FGCu-300 sample, the reduction parameter at 300°C in Ar/H_2 atmosphere for 3 h can be selected as the optimised condition.

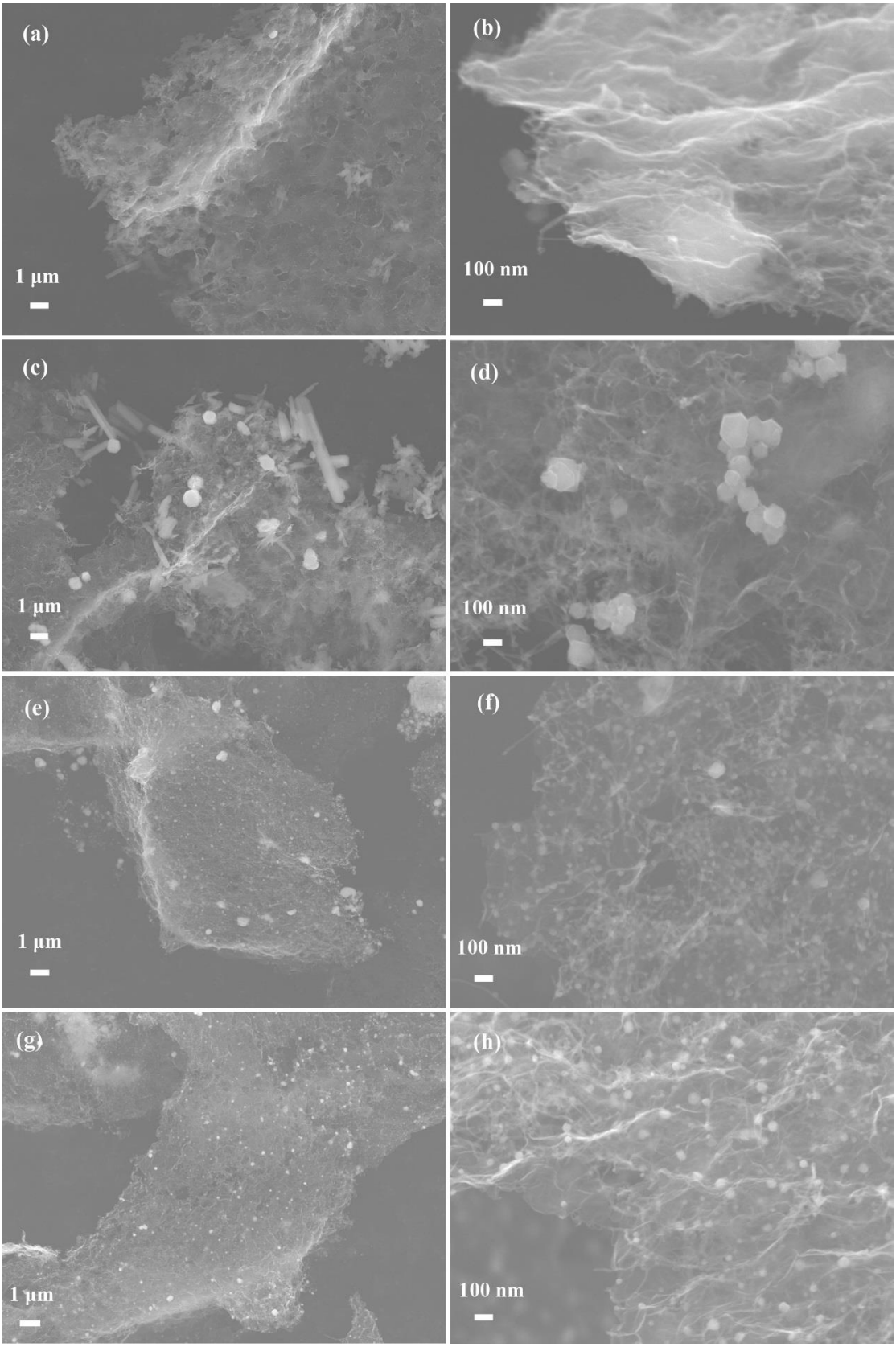

Figure 4-13 SEM images of FGCu nanostructures reduced at 150°C (a and b), 200°C (a and d), 250°C (e and f) and 300°C (g and h).

XPS is used to further investigate the effects of different reduction temperatures to FGCu

precursors, and the results are shown in Figure 4-14. The survey scan spectra of FGCu-150, FGCu-200, FGCu-250, and FGCu-300 are displayed in Figure 4-14a. All four curves show the characteristic peaks of C1s at around 284 eV, O1s at around 530 eV and Cu 2p at around 950 eV, which further confirms the existence of the C, O and Cu element in the products. The high-resolution Cu 2p spectra of each sample are shown in Figure 4-14 b-e. Both the deconvoluted Cu 2p spectra of FGCu-150 (Figure 4-14b) and FGCu-200 (Figure 4-14c) illustrate obvious satellite peaks beside the main Cu 2p peaks, which indicate the high valence of Cu (I and II) in both samples. Specifically, the deconvoluted Cu $2p_{3/2}$ spectrum of FGCu-150 (Figure 4-14b) can be divided into three peaks, the main Cu $2p_{3/2}$ peak located around 933.8 eV, which can be ascribed to the Cu (II) state, accompanied by two satellite peaks at 940.9 and 943.8 eV which are the obvious singles of CuO [156]. This is consistent with the XRD results showing the $Cu(CH_3COO)_2$ phase in the FGCu-150 sample (Figure 4-12). With the reduction temperature increasing to 200°C, different types of divided peaks can be observed in the deconvoluted Cu $2p_{3/2}$ spectrum of FGCu-200 (Figure 4-14c). Besides the Cu (II) peak at around 935.0 eV and the satellite peak at 943.0 eV, a minor peak located at 933.8 eV can be ascribed to the Cu (I), and this is consistent with the XRD results that the $Cu(CH_3COO)_2$, $Cu(CH_3COO)$ and Cu_2O phases existed in FGCu-200 sample (Figure 4-12). In the deconvoluted C 1s spectrum of the FGCu-250 sample (Figure 4-14d), the intensity of the satellite peaks decreases dramatically, and the mean Cu $2p_{3/2}$ spectrum can be divided into two peaks, the intense peak located at 932.8 eV and a minor peak at around 934.0 eV, which can be ascribed to Cu (0) and Cu (II), respectively. When the reduction temperature increases to 300°C, only the sharp Cu $2p_{3/2}$ peak can be found in the spectrum, indicating no oxidation signals in the FGCu-300 sample. The XPS results of all four samples further confirmed the chemical composition in each sample and proved that the FGCu-300 sample was completely reduced, consistent with the XRD results in Figure 4-12.

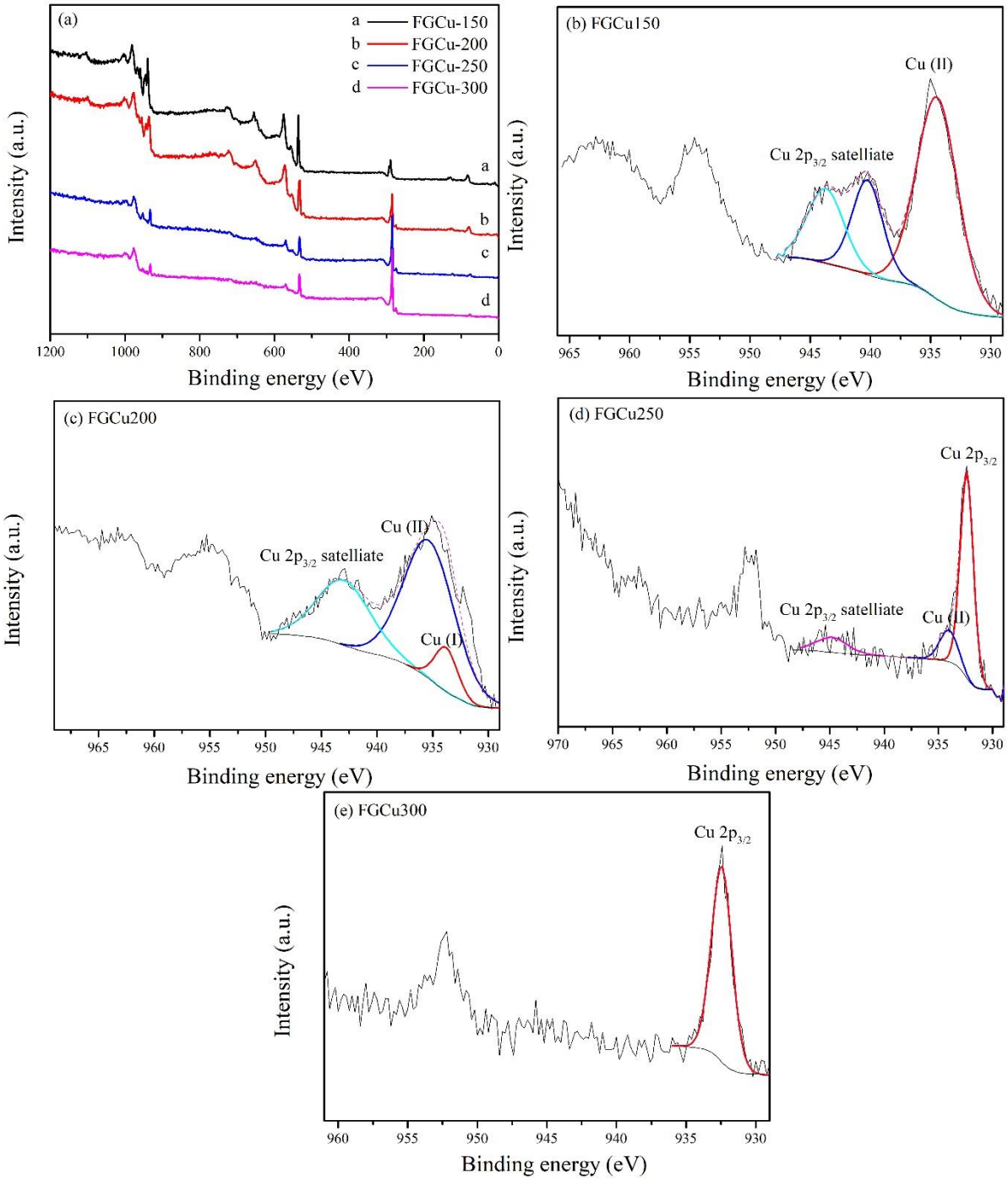

Figure 4-14 XPS survey scan spectrum (a) and the high resolution Cu 2p spectrum of FGCu-150 (b), FGCu-200 (c), FGCu-250 (d), and FGCu-300 (e).

4.2.2 Effects of different reduction durations to the FGCu nanostructures

Based on the parameter obtained above (the FGCu can be completely reduced at 300°C in the Ar/H_2 atmosphere for 3 h), the influence of the reduction duration was then investigated. In the additional experiments, the FGCu precursors were reduced at 250°C for 4 h (FGCu-250-4h)

and compared with 300°C for 2 and 4 h, respectively (FGCu-300-2h and FGCu-300-4h). The XRD results of all three samples are displayed in Figure 4-15. For the FGCu-250-4h samples (Figure 4-15a), the three strongest peaks match the pure Cu phase (ICDD PDF No. 00-04-0836), which indicates that the main phase in FGCu-250-4h sample is still Cu. However, similar to the FGCu-250 sample, there is still a minor peak located at 36.4°, which can be attributed to the cuprite phase (Cu_2O ICDD PDF No. 05-0667). Thus, the extension of reduction duration cannot completely reduce the FGCu precursors at 250°C in the Ar/H_2 atmosphere for the FGCu precursors. The XRD results of FGCu-300-2h (Figure 4-15b) show similar diffraction peaks, and there is still a minor peak of Cu_2O, however, this peak disappeared in the pattern of the FGCu-300-4h sample.

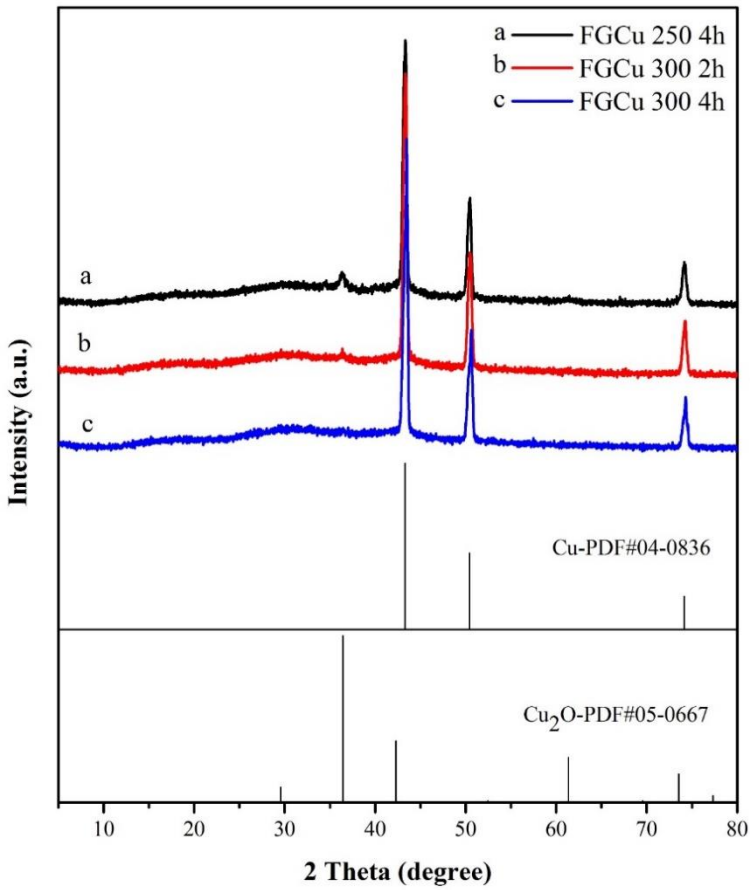

Figure 4-15 XRD patterns of the FGCu samples reduced at 250°C for 4 h (a), 300°C for 2 h (b), and 300°C for 4 h (c), and the standard peaks of Cu and Cu_2O phase.

The morphologies of the FGCu samples reduced at 250°C for 4 h and 300°C for 2 and 4 h have

also been investigated. In the SEM images of the FGCu-250-4h sample (Figure 4-16), the GNT based graphene-layer like structure can be observed in the low magnification image (Figure 4-16a), and the Cu nanoparticles are also uniformly coated on the GNTs (Figure 4-16b, c, and d). The Cu nanoparticles show larger sizes around 50-100 nm compared with the FGCu-250 samples (Figure 4-13 e and f) due to additional diffusion time.

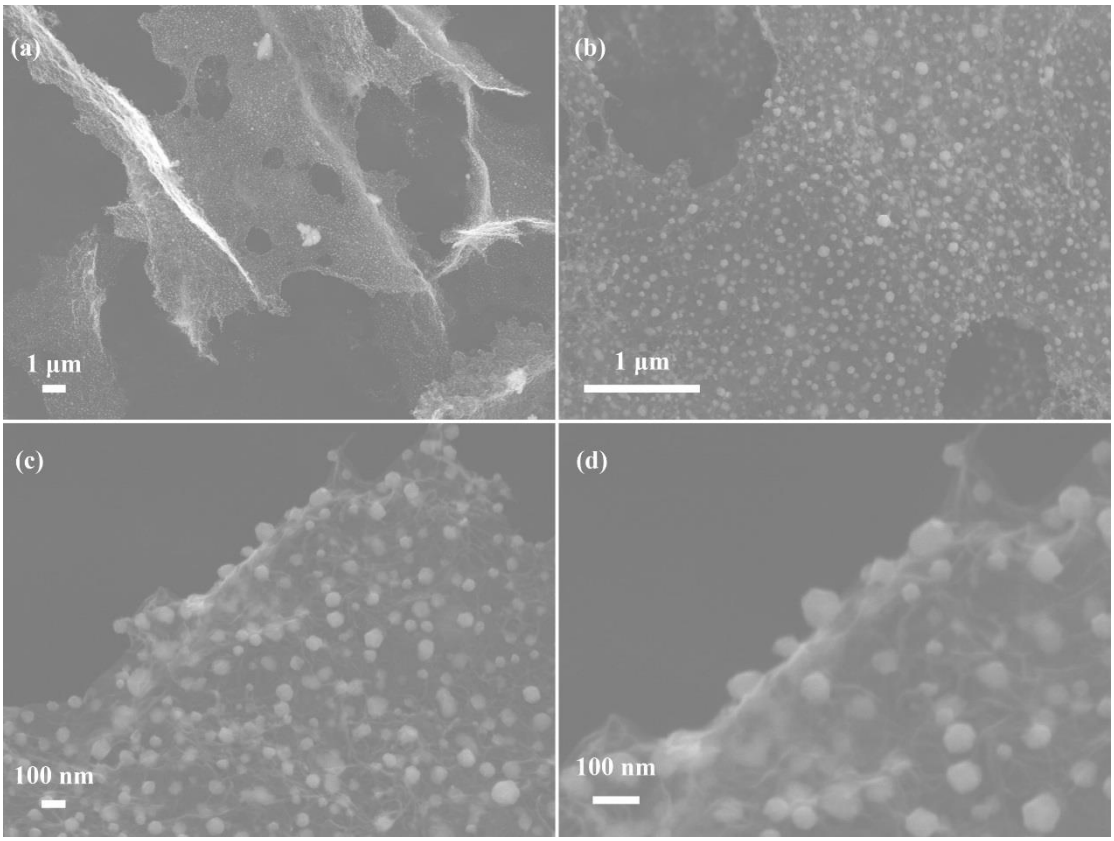

Figure 4-16 SEM images of the FGCu-250-4h samples under low (a and b) and high (c and d) magnifications.

When the reduction temperature increases to 300°C, the SEM images of FGCu-300-2h and FGCu-300-4h samples are displayed in Figure 4-17 and Figure 4-18, respectively. Although both samples kept the graphene-layer-like structure, the FGCu-300-4h sample exhibits much larger Cu nanoparticle sizes, typically above 100 nm. It can be found that the FGCu-300-2h sample illustrates a good distribution of Cu nanoparticles decorated on the GNT nanostructures. The particle size is also around 20-50 nm, smaller than the ones at 250°C for 4 h. The FGCu-300-4h sample shows the largest particle size among all the obtained samples. Thus, when

combined with the XRD results, only when the reduction temperature reaches 300°C can the FGCu precursors be completely reduced into Cu phase and the reduction duration also must be above 3 h. However, the longer reduction time resulted in further diffusion and an increase in particle size.

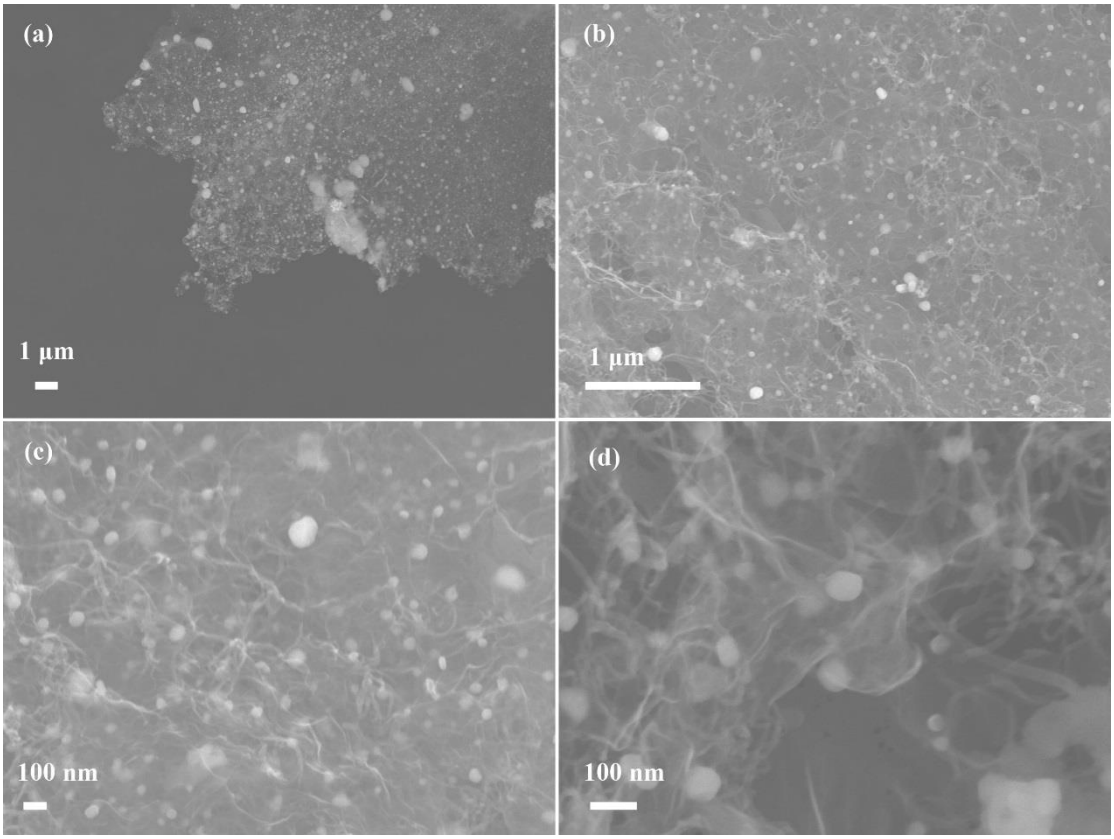

Figure 4-17 SEM images of the FGCu-300-2h samples under low (a and b) and high (c and d) magnifications.

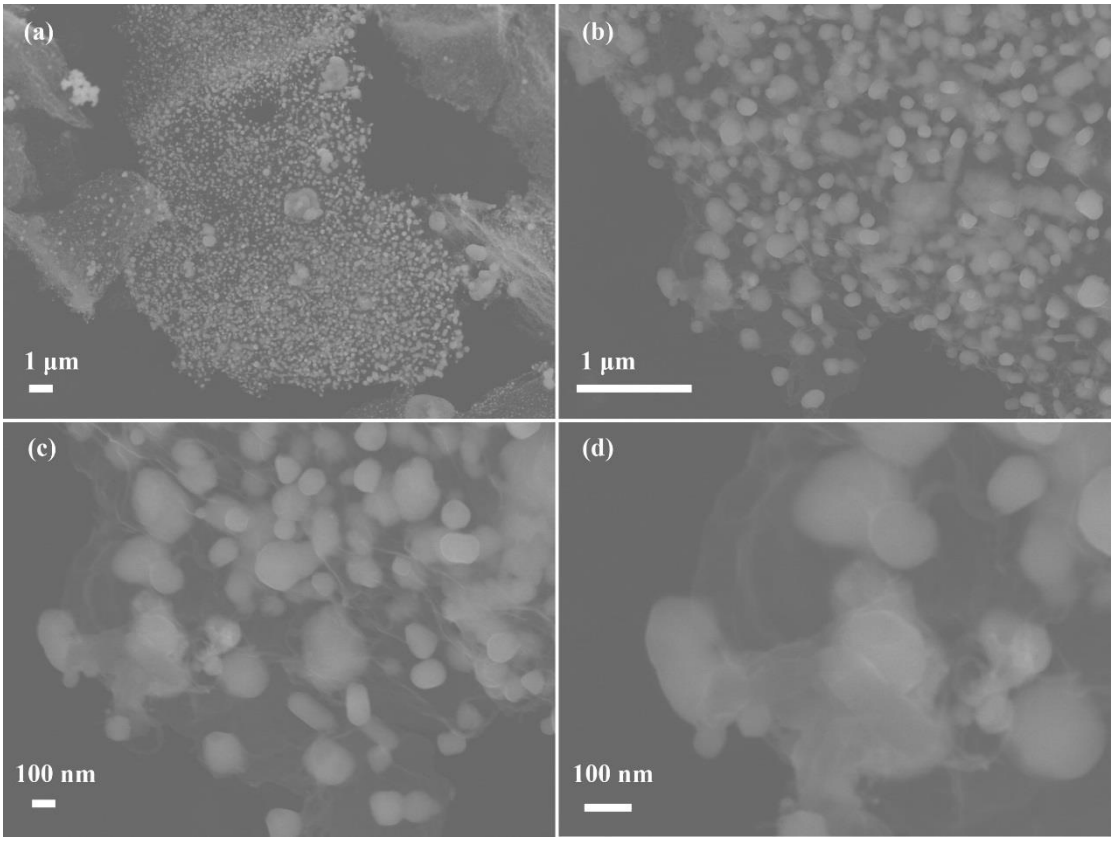

Figure 4-18 SEM images of the FGCu-300-4h samples under low (a and b) and high (c and d) magnifications.

The XPS spectra of FGCu-250-4h, FGCu-400-2h and FGCu-400-4h shown in Figure 4-19 demonstrate the chemical composition in these samples. The survey scan spectra of FGCu-250-4h, FGCu-400-2h and FGCu-400-4h displayed in Figure 4-19a show the characteristic peaks of C1s at around 284 eV, O1s at around 530 eV, and Cu 2p at around 950 eV. The Cu 2p spectra of each sample are shown in Figure 4-19 b-d. The Cu 2p spectra of FGCu-250-4h (Figure 4-19b) both illustrate the satellite peaks at ca. 945 eV and 963 eV beside the main Cu 2p peaks, which indicates the high valence of Cu (I and II) in both samples. This is consistent with the XRD results the precursors were not completely reduced in both samples (Figure 4-15). Fro FGCu-250-4h sample, two obvious peaks can be observed in the deconvoluted Cu 2p3/2 peak, the sharp peak at 932.8 eV and a minor peak at around 934.0 eV, which can be ascribed to Cu (0) and Cu (I). In FGCu-300-2h (Figure 4-19c), the deconvoluted Cu 2p3/2 peak can be attributed to the Cu (0) and Cu (I) peaks. However, in the high-resolution Cu 2p spectrum of

the FGCu-300-4h sample (Figure 4-19d), the satellite peaks disappear, confirming the complete reduction of the FGCu precursors under this condition.

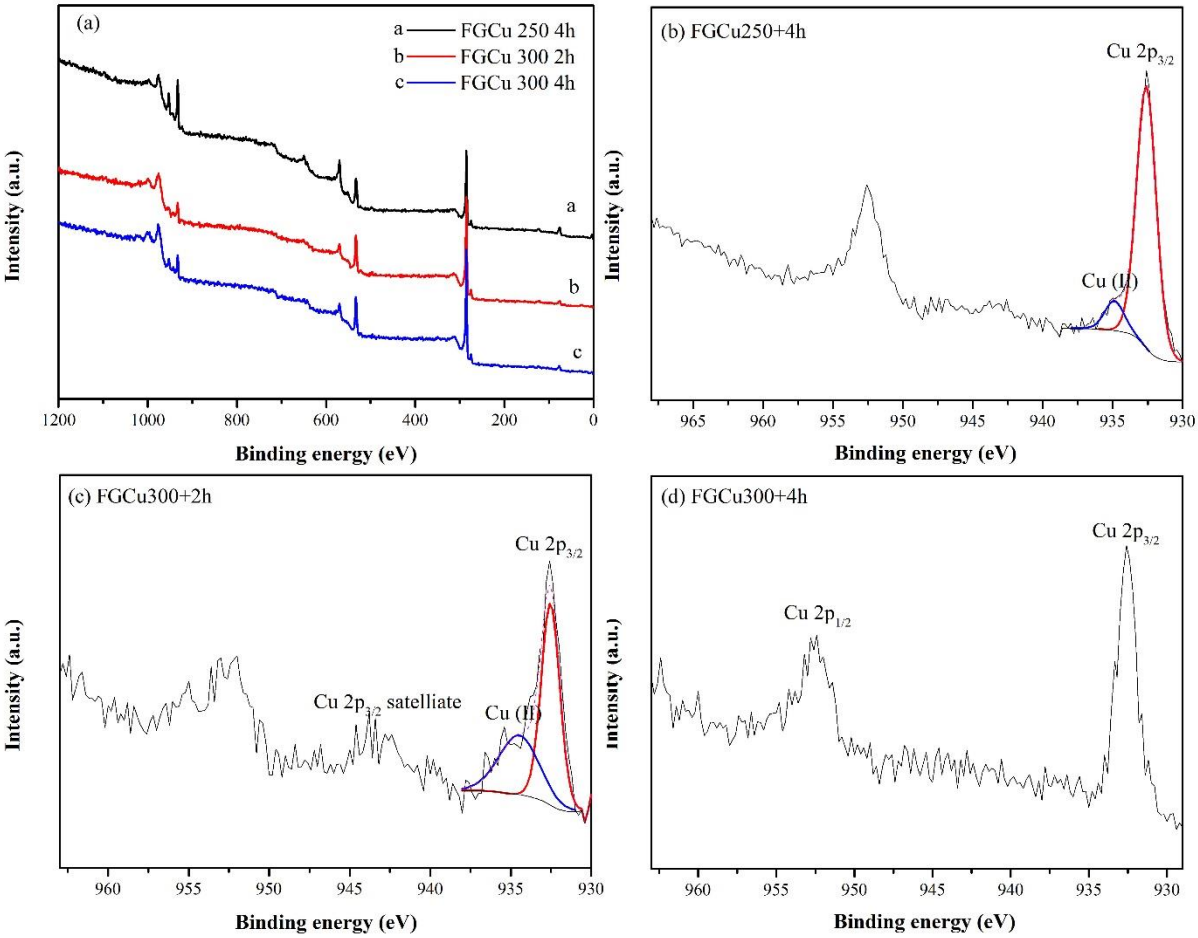

Figure 4-19 The XPS survey scan spectrum (a) and the high resolution Cu 2p spectrum of FGCu-250-4h (b), FGCu-300-2h (c), and FGCu-300-4h (d).

4.3 Synthesis of Ni nanoparticles coated FGNi nanostructures and the effects of different reaction conditions

Inspired by the success of the preparation of FGCu nanostructures, another exploration has been carried out to investigate the possibility of other transition metals that can decorate the GNT nanostructures. Nickel acetate is adopted instead of copper acetate to prepare the FGNi samples through the MLM and freeze-drying process. Different parameters [including different reduction temperatures (FGNi-200, FGNi-300, and FGNi-400), reduction atmospheres (FGNi-

300-Ar and FGNi400-Ar), and different reduction durations (FGNi-300-1+2 and FGNi-400-1+2)] were studied.

4.3.1 Temperature effect to the FGNi nanostructures

Different reduction temperatures were explored to investigate the reduction parameters of preparing FGNi nanostructures under an Ar/H_2 atmosphere. Figure 4-20 shows the XRD patterns of FGNi precursors and the corresponding reduction products at different temperatures from 200 - 400°C for 3 h. The XRD patterns did not change after the 3 h reduction at 200°C compared with the XRD patterns of the FGNi precursors (Figure 4-20a and b). When the temperature was increased to 300°C (Figure 4-20c), the XRD patterns show three intense peaks at 2θ of 44.5°, 51.8°, and 76.3°, which match the pure Ni metallic phase (ICDD PDF No. 00-04-0850). No other obvious peaks can be found. In the XRD patterns of FGNi-400 sample (Figure 4-20d), similar diffraction peaks were observed. Thus, it confirms that the FGNi precursors can be completely reduced at a temperature above 300°C. In addition, similar to the FGCu samples discussed above, the broad peak located at around 25-40°, which can be ascribed to the GNT nanostructures, also appears in all four diffraction patterns (Figure 4-20).

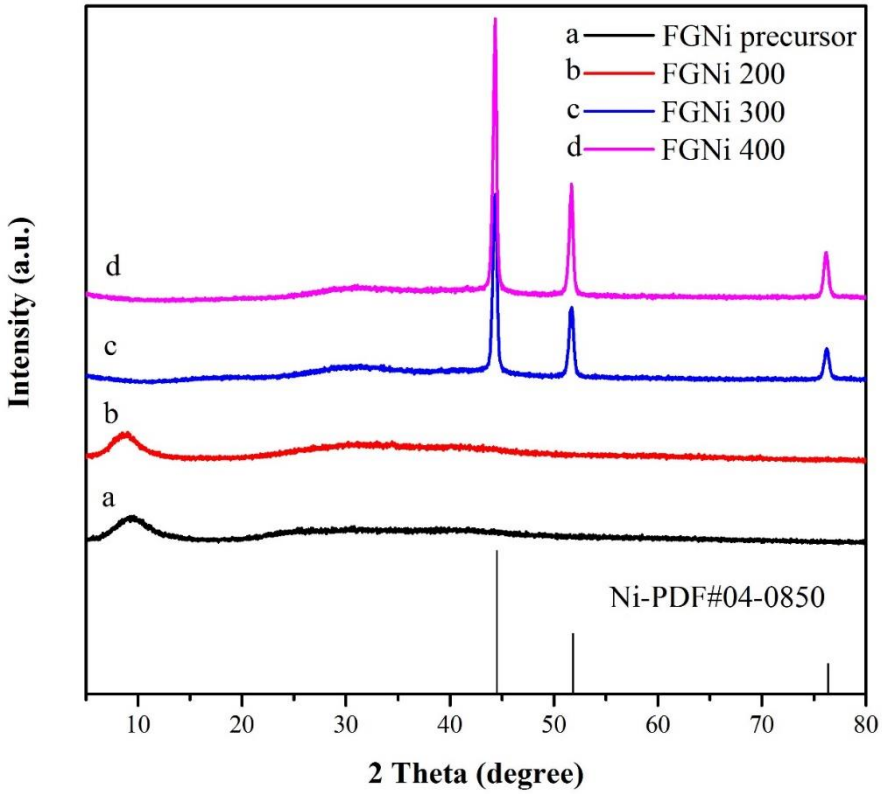

Figure 4-20 XRD patterns of the FGNi precursors (a), FGNi-200 (b), FGNi-300 (c) and FGNi-400 (d).

SEM was performed to investigate the morphology of the products, and typical images are displayed in Figure 4-21. All the products kept the graphene-layer-like structure which indicates that the freeze-drying and subsequent reduction process did not destroy the GNT nanostructures. Same as the FGCu precursors, the squamous like morphology can also be observed in the FGNi-200 samples covered on the surface of the GNT nanostructures (Figure 4-21a and b), which is consistent with the XRD result (Figure 4-20). When the reduction temperature increased to 300°C, obvious bright particles are generated on the surface of the graphene layers (Figure 4-21c). In the high-resolution image of FGNi-300 (Figure 4-21d), the particles did not show the uniform distribution as in the FGCu samples. The XRD results confirm that the non-uniform particles are Ni (ICDD PDF No. 00-04-0850) phase. In the FGNi-400 sample (Figure 4-21e and f), the morphology can be observed similar to the FGNi-300 sample. Thus, different reduction parameters should be adopted to ensure a better uniform distribution of Ni particle on the GNT nanostructures.

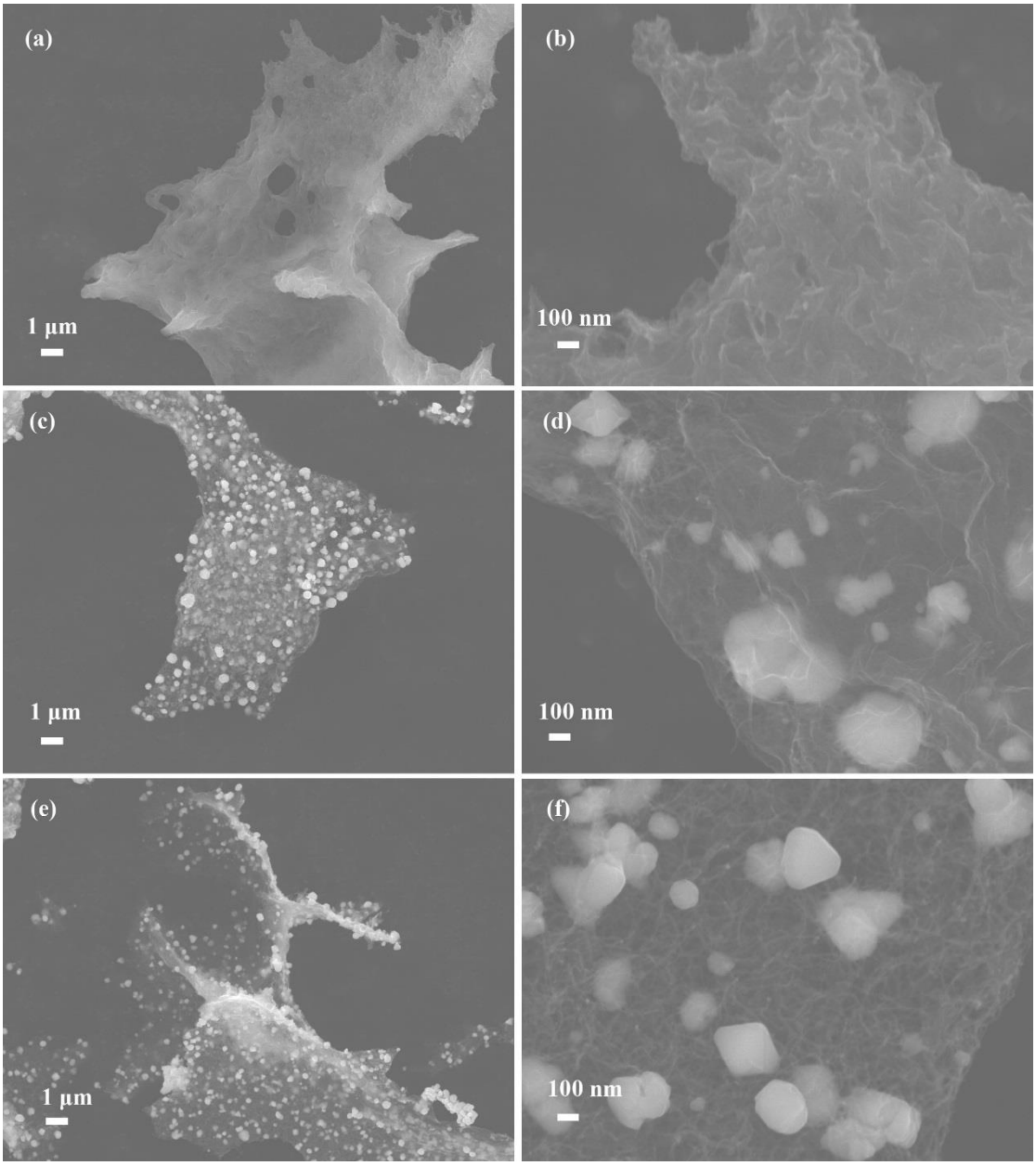

Figure 4-21 SEM images of FGNi-200 (a and b), FGNi-300, (c and d) and FGNi-400 (e and f).

4.3.2 Effect of reduction atmosphere to the FGNi nanostructures

Since the Ni particles grew too large and their distribution was not uniform on the GNT nanostructures under Ar/H_2 atmosphere, different reduction atmospheres were introduced. The FGNi precursors were firstly placed under the pure Ar atmosphere. As the FGNi precursors did not show any differences at 200°C (Figure 4-20b), Figure 4-22 displays the XRD patterns of FGNi samples reduced under pure Ar atmosphere starting from 300°C (a) to 400°C (b) for 3 h.

After 300°C in Ar atmosphere for 3 h (Figure 4-22a), two main phases can be detected in the pattern. The diffraction peaks match with the hcp Ni (ICDD PDF No. 00-45-1027) and fcc Ni phase (ICDD PDF No. 00-04-0850). In addition, a minor peak at 43.2° and a broad peak at 63.0° can be ascribed to the NiO phase (ICDD PDF No. 00-44-1159), indicating that FGNi precursors were also not reduced completely. When the temperature increases to 400°C, diffraction peaks of the hcp Ni phase disappear. The three strongest peaks match well with the fcc Ni phase. Three broad peaks at 37.2°, 43.2°, and 63° were preserved and can be ascribed to the NiO phase (ICDD PDF No. 00-44-1159). Meanwhile, the broad peak of GNT nanostructures at around 25-40° is observed in both samples, confirming the existence of GNT nanostructures. However, the NiO phase is detected in both XRD patterns, indicating that the FGNi precursors cannot be completely transferred to a pure Ni phase under the pure Ar atmosphere.

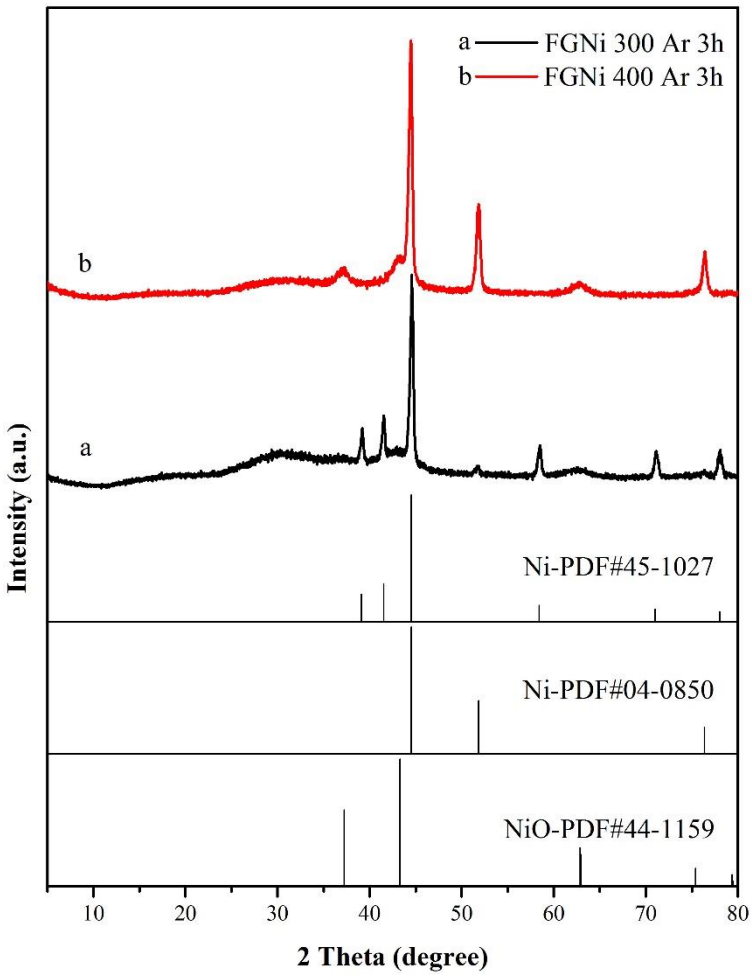

Figure 4-22 XRD patterns of FGNi-300-Ar (a) and FGNi-400-Ar (b) that reduced under pure Ar atmosphere at 300 and 400°C, respectively.

The SEM images of these samples are displayed in Figure 4-23. In Figure 4-23a, the FGNi-300-Ar sample exhibits the graphene-layer-like structure, and no obvious agglomeration can be observed. In higher resolution images (Figure 4-23b and c), smaller particles, similar to those formed under Ar/H_2 atmosphere, are uniformly decorated on the surface of GNT nanostructures. In Figure 4-23c, the squamous-like morphology can still be observed, which indicates that the FGNi precursors may have not completely decomposed. Small particles also appear among these squamous like morphologies. According to the XRD results, these particles can be attributed to either hcp Ni or fcc Ni nanoparticles. There are also uniform Ni particles coating on the exposed CNTs in Figure 4-23 b and d.

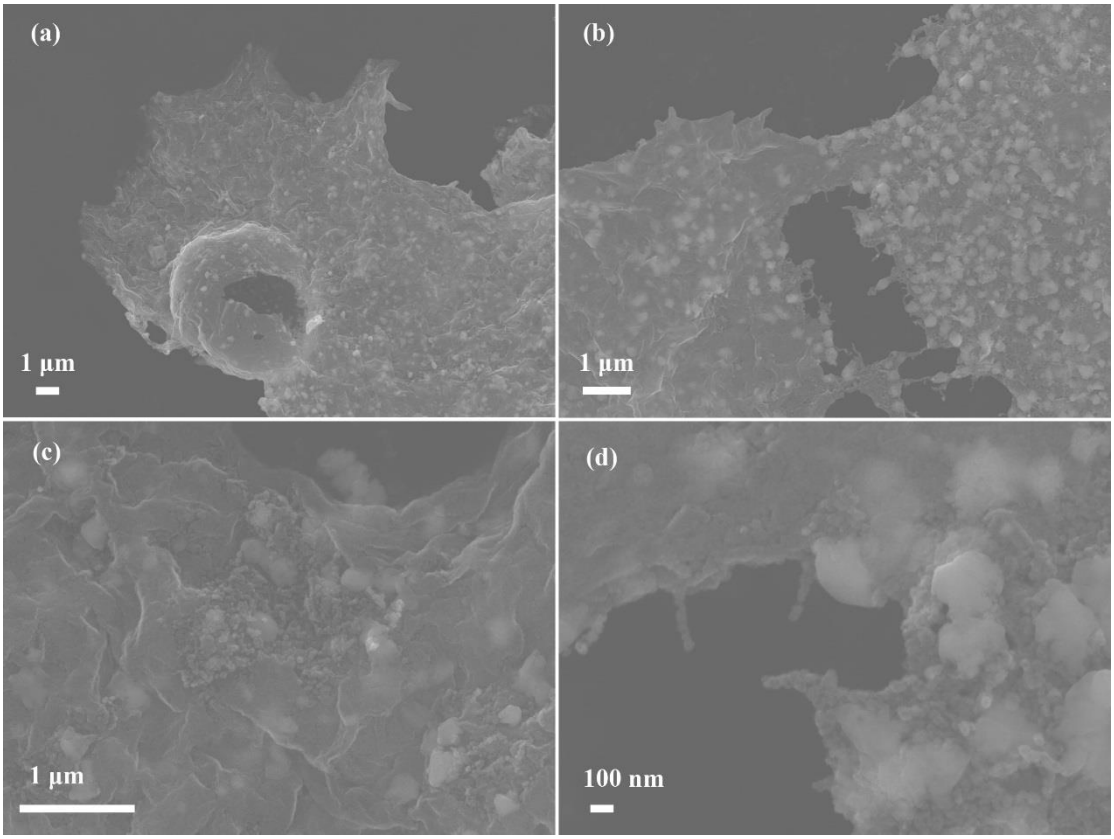

Figure 4-23 SEM images of FGNi-300-Ar nanostructures under low (a and b) and high (c and d) magnifications.

SEM images of the FGNi products reduced at 400°C are shown in Figure 4-24. Similar to the other GNT based products, the FGNi-400-Ar sample also exhibits the graphene-layer-like structure, and the nanoparticles are uniformly coated on the GNTs. In higher magnification images (Figure 4-24b and c), a uniform distribution of Ni nanoparticles is found on the GNT nanostructures with some larger particles distributed among the small nanoparticles. In Figure 4-24d, the size of the small Ni nanoparticles is around 50 nm, and the size of the larger ones is around 200 nm. There are also nanoparticles of around 50 nm uniformly decorated on the exposed CNTs on the edge of the GNT nanostructures. The XRD result of FGNi-400-Ar sample (Figure 4-22b) indicates that these particles can be attributed to the fcc Ni phase and the NiO phase. In addition, the squamous like morphologies that normally appear in the precursors cannot be detected in FGNi-400-Ar samples, which indicates that the FGNi precursors are completely decomposed at 400°C under pure Ar atmosphere. However, combined with XRD

results, it can be found that there is still a NiO phase existing in the FGNi-400-Ar samples as stated above. Thus, a further investigation is still needed to obtain a pure Ni phase.

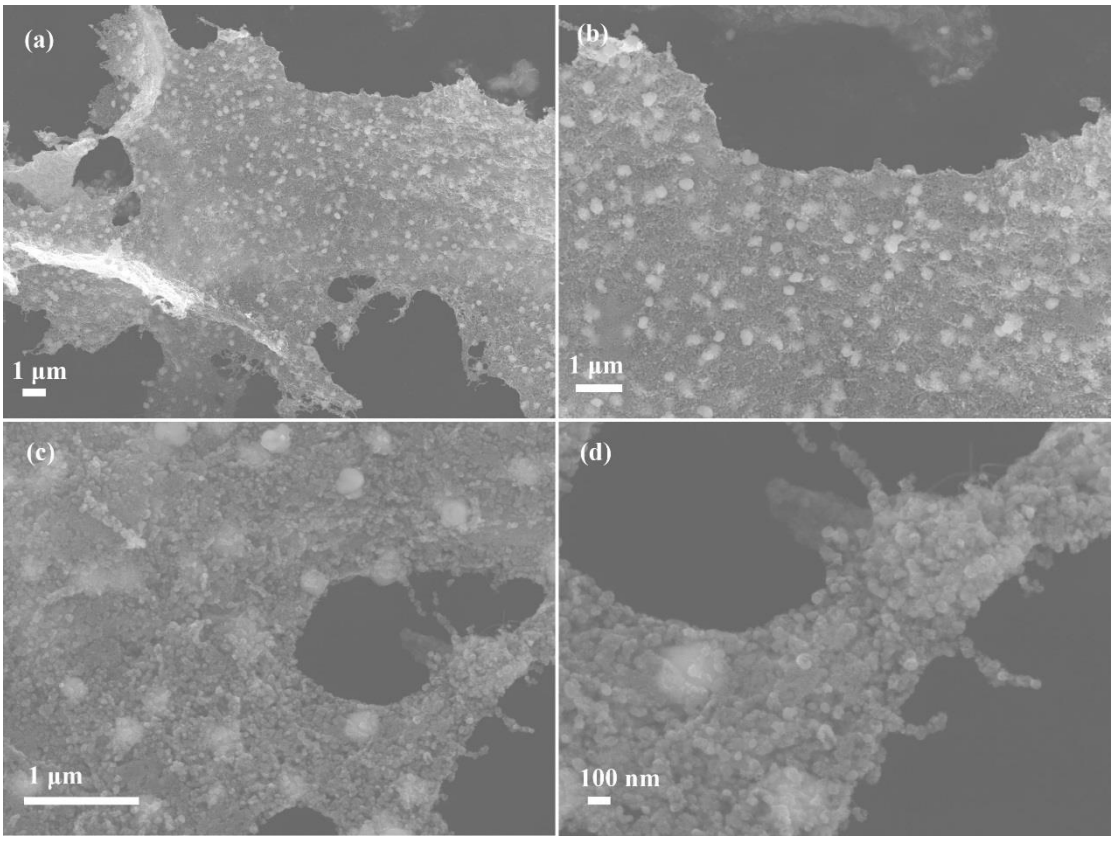

Figure 4-24 SEM images of FGNi-400-Ar nanostructures under low (a and b) and high (c and d) magnifications.

To prepare a pure Ni phase in the final FGNi products, both pure Ar and Ar/H_2 atmospheres are adopted. The FGNi precursors were placed in the pure Ar atmosphere for 1 h and then the Ar/H_2 atmosphere for another 2 h at 300°C and 400°C, and the samples are named as FGNi-300-1+2 and FGNi-400-1+2. The XRD patterns of FGNi-300-1+2 and FGNi-400-1+2 samples are shown in Figure 4-25. Similar to the FGNi-300-Ar sample, the FGNi-300-1+2 sample (Figure 4-25a) shows both hcp and fcc phases of pure Ni. It can be found that the signal of the hcp Ni phase is dominant, and this is consistent with the fact that hcp Ni can be obtained at a lower temperature. However, the signal of NiO phase (ICDD PDF No. 00-44-1159) disappears (especially the broad peak at around 63°), confirming that Ar/H_2 atmosphere introduced

afterward is beneficial to reduce the remained NiO. In the XRD patterns of FGNi-400-1+2 sample (Figure 4-25b), the diffraction peaks can match with the fcc Ni phase (ICDD PDF No. 00-04-0850) and there are no patterns of the NiO phase. Therefore, the pure fcc Ni phase has been obtained after reduction at 400°C for 1 h in an Ar atmosphere and another 2 h in Ar/H_2 atmosphere. In addition, the broad peak at around 25-40°, which is ascribed to GNT nanostructures, is still preserved in both FGNi-300-1+2 and FGNi-400-1+2, which confirms the existence of GNT in both samples.

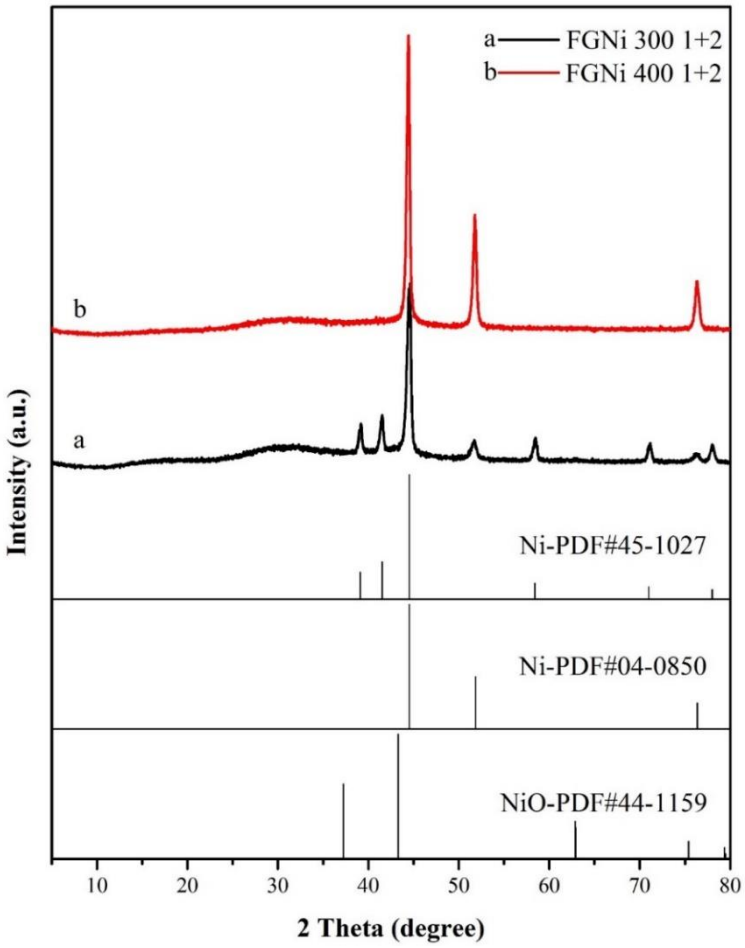

Figure 4-25 XRD patterns of FGNi-300-1+2 (a) and FGNi-400-1+2 (b).

SEM was performed to investigate the morphologies of FGNi-300-1+2 and FGNi-400-1+2 samples, and the images are displayed in Figure 4-26 and Figure 4-27. In Figure 4-26, the SEM images of FGNi-300-1+2 sample exhibit the graphene-like-structure (Figure 4-26a) as expected, and the uniform distribution of Ni particles can also be observed (Figure 4-26b). In

Figure 4-26 c and d, the nanoparticles, which are around 20-50 nm, are coated on the GNT nanostructures with some large particles among them. According to the XRD results (Figure 4-25a), these uniformly decorated particles can be ascribed to both hcp Ni (ICDD PDF No. 00-45-1027) and fcc Ni phase (ICDD PDF No. 00-04-0850). Similar to the FGNi-300-1+2 samples, SEM images of FGNi-400-1+2 samples are shown in Figure 4-26. It can be found that the FGNi-400-1+2 samples also exhibit the graphene-like-structure with no obvious agglomeration (Figure 4-27a). The morphology of some big particles located among the uniformly coated nanoparticles is observed in FGNi-400-1+2 sample, and these particles can be ascribed to the fcc Ni phase (ICDD PDF No. 00-04-0850) (Figure 4-25b). Figure 4-27 c and d display the high-resolution images of FGNi-400-1+2 samples. The uniform distribution of fcc Ni nanoparticles can be observed coated on both GNTs and the exposed CNTs on the edge of GNT layers. Therefore, the combination of the pure Ar and Ar/H_2 atmosphere enabled the uniform Ni nanoparticles decorated GNT nanostructures, while the Ni nanoparticles are both hcp and fcc phase at 300°C and only fcc phase at 400°C.

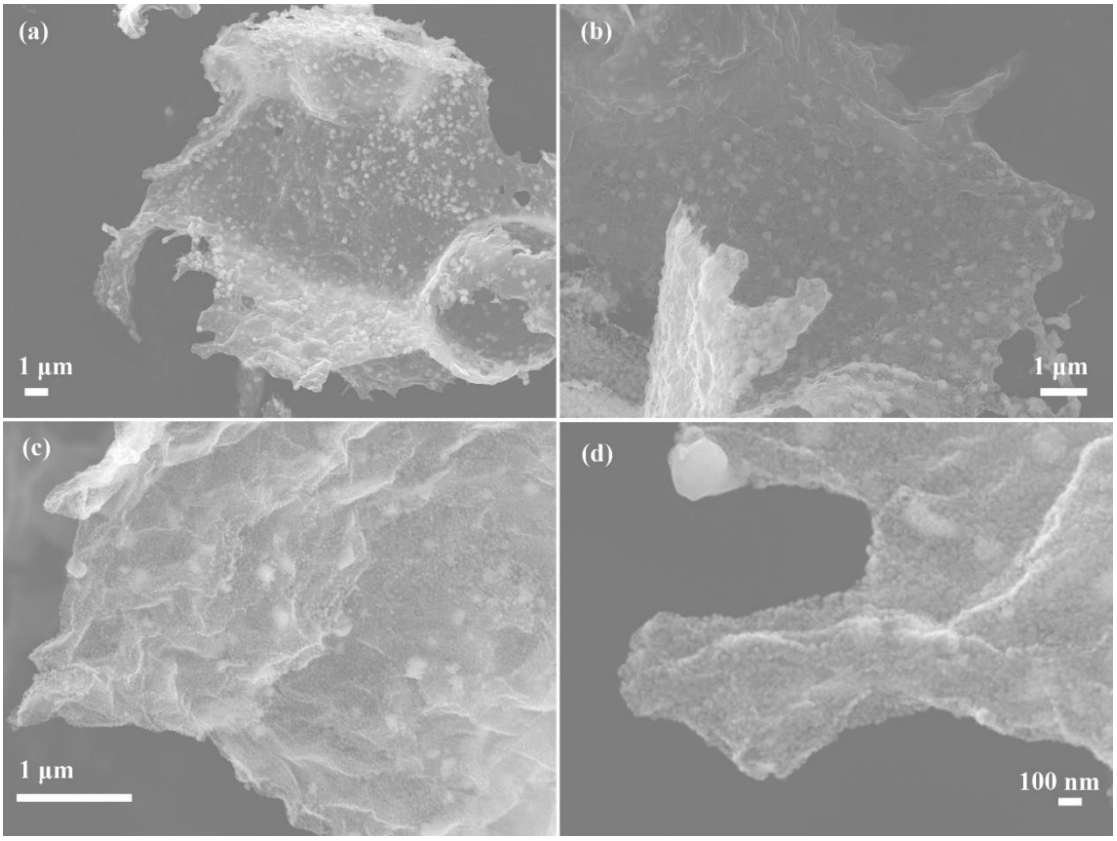

Figure 4-26 SEM images of FGNi-300-1+2 nanostructures under low (a and b) and high (c and d) magnifications.

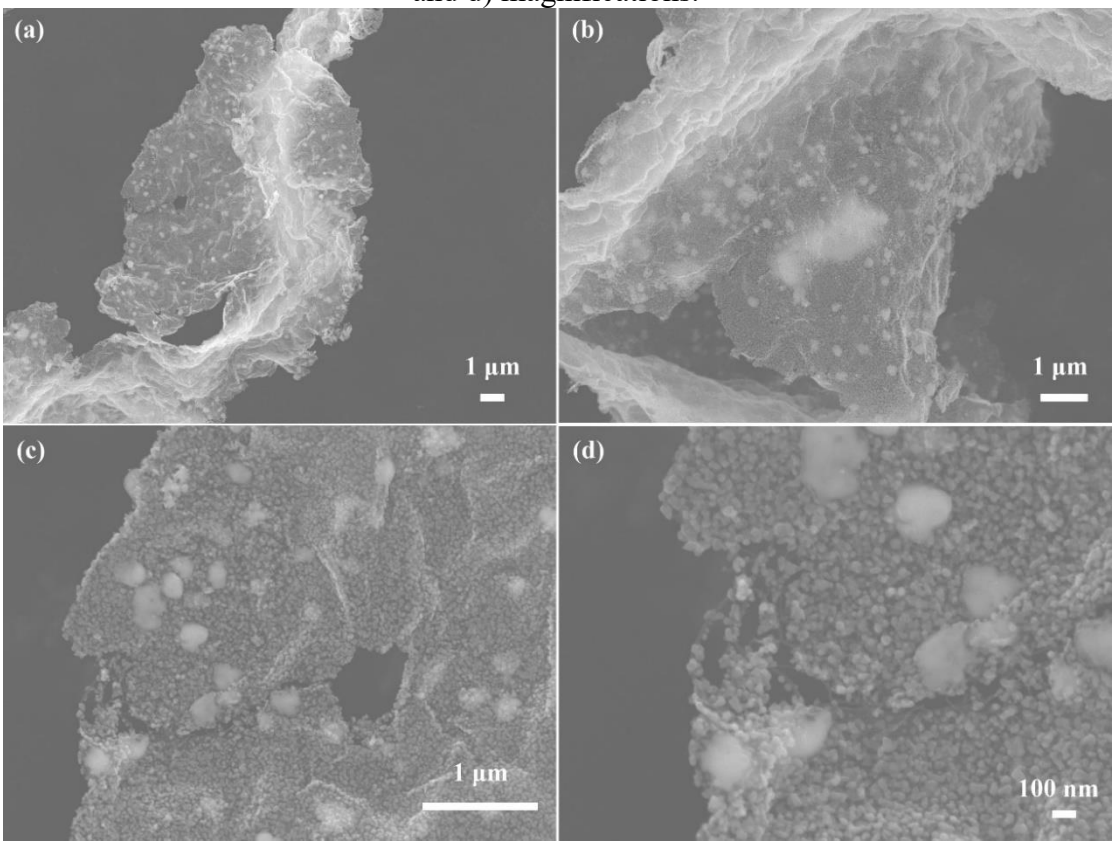

Figure 4-27 SEM images of FGNi-400-1+2 nanostructures under low (a and b) and high (c and d) magnifications.

4.4 Ag nanoparticles decorated GNT nanostructures and the effects of different reduction conditions

Based on the preparation of both FGCu and FGNi nanostructures, another transition metal, Ag, was introduced to decorate the GNT nanostructures. Silver acetate is adopted instead of copper and nickel acetate to prepare the FGAg precursors through the MLM and freeze-drying process. Different reaction parameters [including different reduction temperatures (FGAg-150, FGAg-200, FGAg-250, and FGAg-300), different reduction durations (FGAg-200-3h and FGAg-250-3h), and reduction atmospheres (FGAg-250-Ar and FGAg-300-Ar)] were also explored to prepare completely reduced Ag decorated GNT nanostructures.

4.4.1 Temperature effects on the FGAg nanostructures

Before the exploration of the FGAg nanostructures, the FGAg precursors, which are obtained directly from the MLM process through the freeze-drying method, are firstly characterised. XRD patterns of the FGAg precursors are shown in Figure 4-28. It can be found that the diffraction peaks of the FGAg precursors match the standard peaks of silver acetate (ICDD PDF No. 00-04-0096), indicating that the precursors kept the silver acetate phase after the sublimation process, similar to the FGCu precursors. In addition, compared with the flat baseline, the diffraction peaks of the FGAg precursors also display a broad peak ranging from 25-40°, which can be ascribed to the GNT nanostructures.

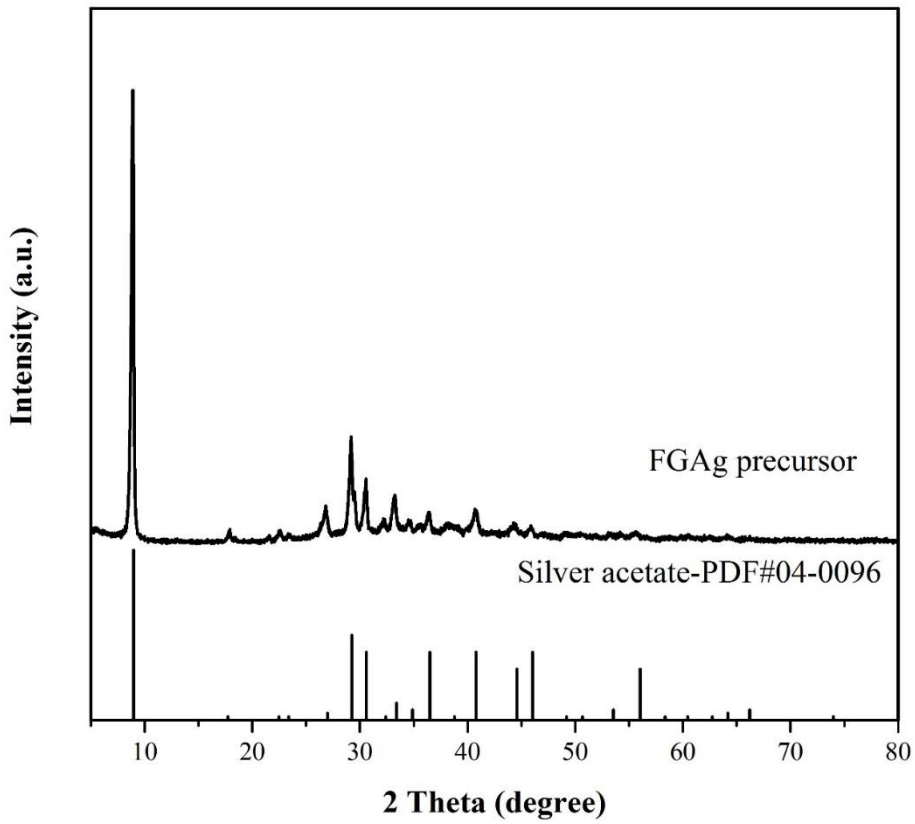

Figure 4-28 XRD patterns of the FGAg precursors and the standard silver acetate peaks.

The FGAg products reduced from 150 to 300°C under Ar/H_2 atmosphere for 2 h are named as FGAg-150, FGAg-200, FGAg-250 and FGAg-300. The XRD patterns of these samples are displayed in Figure 4-29. In the diffraction peaks of the FGAg-150 sample (Figure 4-29a), the diffraction peaks match the standard diffraction peaks of the pure Ag phase (ICDD PDF No. 00-04-0783), which confirms that the FGAg precursors have been reduced to Ag phase at 150°C under Ar/H_2 atmosphere for 2 h. However, a peak is located at around 9.8° only in the FGAg-150 samples, which can be attributed to the silver acetate phase (ICDD PDF No. 00-04-0096), indicating that some silver acetates cannot be completely reduced at 150°C. When the reduction temperature increases to 200°C, XRD patterns of the FGAg-200 sample match the standard Ag peaks, and no other peaks can be observed, which confirms that the FGAg precursors can be completely reduced at 200°C under Ar/H_2 atmosphere for 2 h. Similar to the diffraction peaks of FGAg-200 sample, the XRD patterns of the FGAg-250 and FGAg-300 (Figure 4-29c and d) samples also exhibit the diffraction peaks that match well with the

standard Ag phase (ICDD PDF No. 00-04-0783). Therefore, it can be concluded that the FGAg precursors can be completely reduced to pure Ag phase when the reduction temperature is above 200°C under Ar/H_2 atmosphere for 2 h. Despite the high intensity of the Ag phase in the XRD patterns of FGAg sample, a tiny signal of the broad peak located around 25-40°, which ascribe to the GNT nanostructures, can still be observed in all samples, confirming the existence of the GNT nanostructures in all the FGAg products.

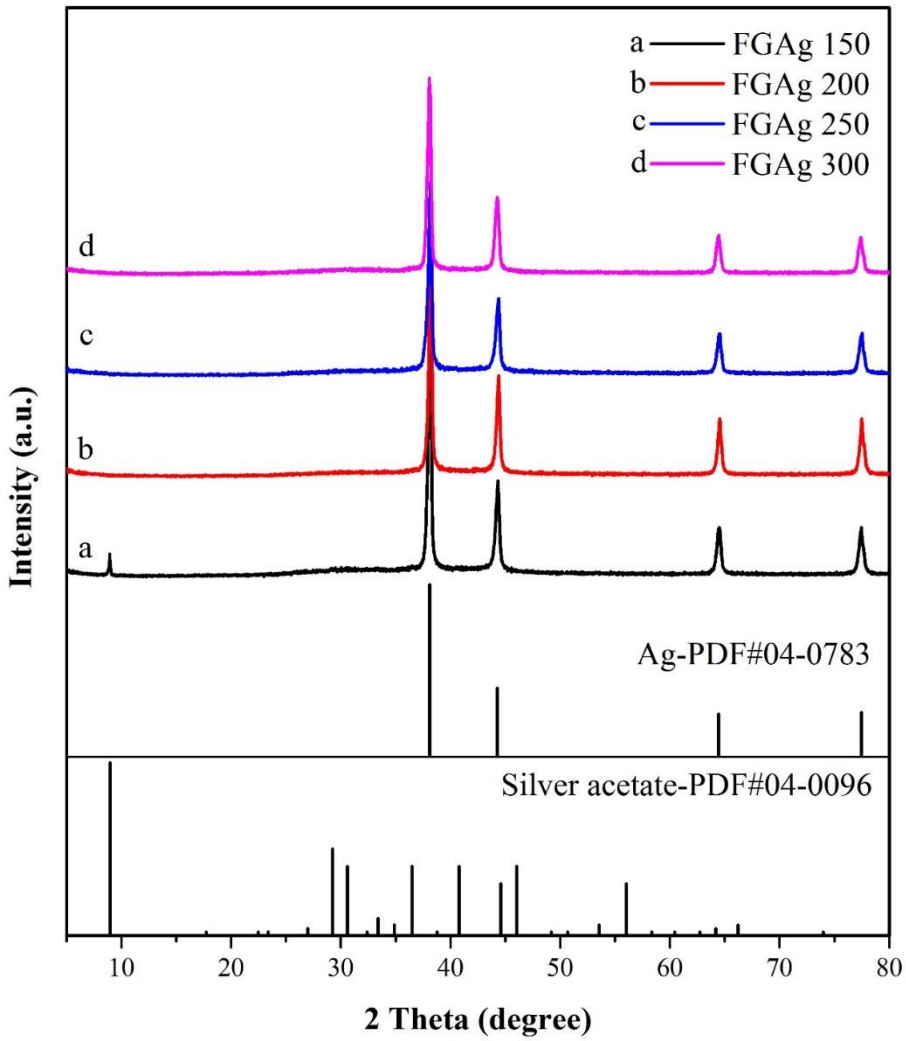

Figure 4-29 XRD patterns of the FGAg-150 (a), FGAg-200 (b), FGAg-250 (c) and FGAg-300 (d) samples.

SEM images of the obtained FGAg samples under an Ar/H_2 atmosphere for 2 h at different temperatures are exhibited in Figure 4-30. Figure 4-30a exhibits the low magnification image of the FGAg-150 sample, it can be found that the reduced products kept the graphene-layer-

like structure and the bright round particles were decorated on the GNT nanostructures. In Figure 4-30 b and c, the distribution of the particles is random, and the particle size is around 100 nm. In the high magnification image (Figure 4-30d), the particles can be observed on the edge of the graphene layer. The obtained particles are also not uniformly coated on CNTs as bare CNTs can be witnessed on the edge of the GNT nanostructures.

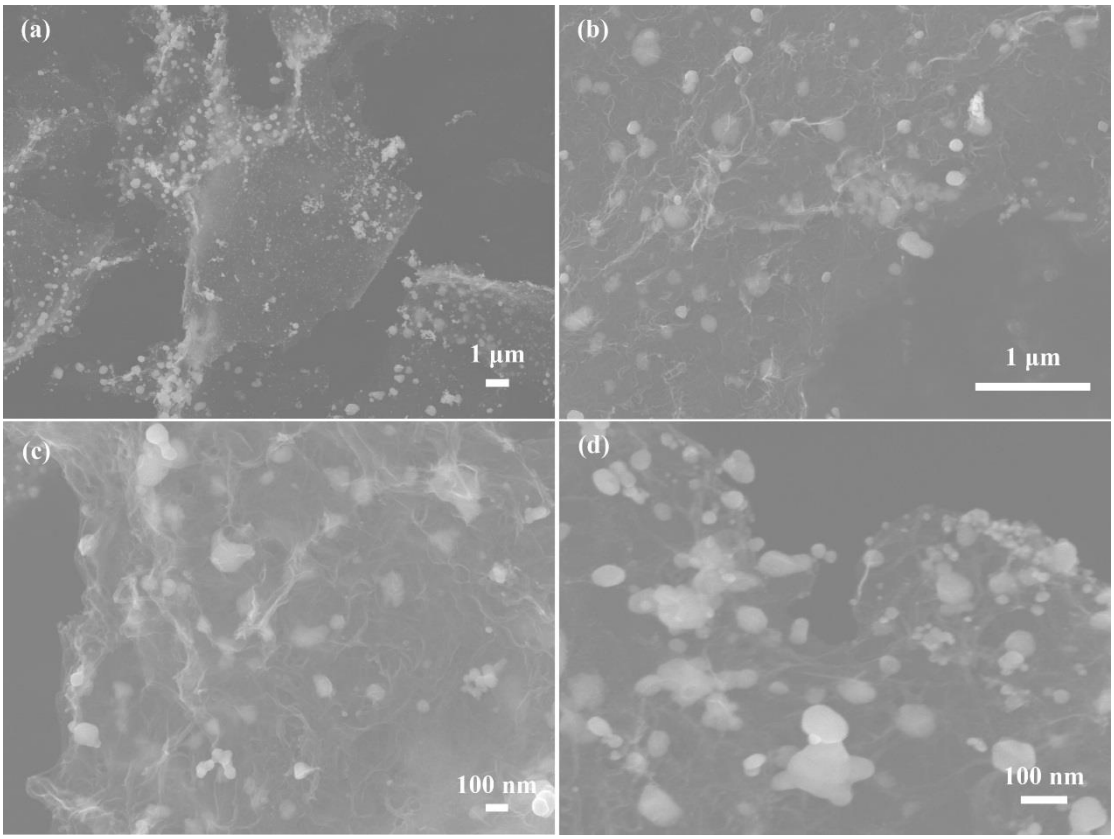

Figure 4-30 SEM images of FGAg-150 nanostructures reduced at 150°C under an Ar/H_2 atmosphere for 2 h at low (a and b) and high (c and d) magnifications.

When the reduction temperature is increased to 200°C, SEM images of the FGAg-200 sample are displayed in Figure 4-31. In Figure 4-31a, the FGAg sample can be found to keep the graphene-layer-like structure with no obvious agglomeration. The bright particles were uniformly distributed on GNTs compared to the FGAg-150 sample, and all the particles can be attributed to the Ag phase according to the XRD result. In Figure 4-31 b and c, the particle size of these Ag particles is around 20-50 nm combined with few larger ones (around 100 nm). In the high magnification image (Figure 4-31d), the Ag nanoparticles can be clearly found

decorated on the sidewalls of CNTs and graphene layers.

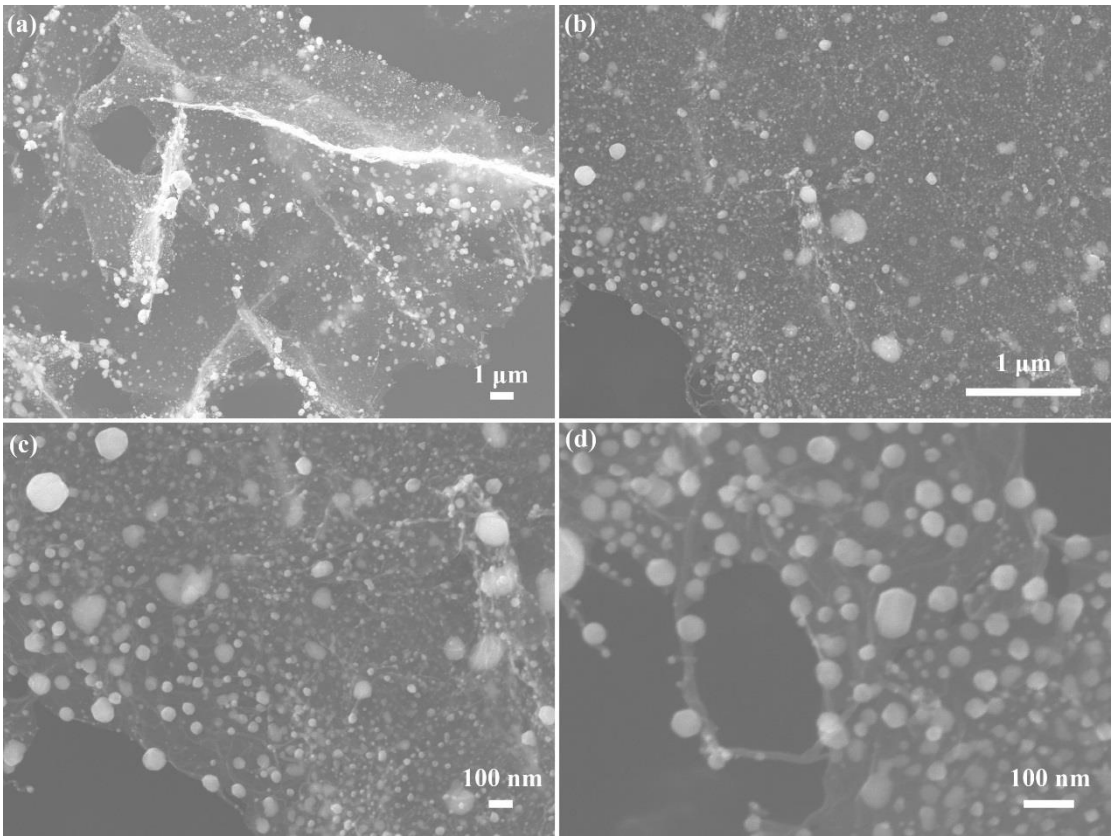

Figure 4-31 SEM images of the FGAg-200 nanostructures reduced at 200°C under an Ar/H_2 atmosphere for 2 h at low (a and b) and high (c and d) magnifications.

Figure 4-32 exhibits the SEM images of the FGAg-250 products. The as-prepared products also kept the well-dispersed structures when the reduction temperature increased to 250°C. Combined with the XRD result, the particles that can be ascribed to Ag nanoparticles were uniformly decorated on the GNT nanostructures. The particle size of Ag particles increased (Figure 4-32 b and c) when compared with the FGAg-200 samples (Figure 4-31 b and c). For example, the large Ag particle displayed in Figure 4-32d is around 200 nm, indicating that temperature growth could increase the Ag particle size. Meanwhile, Ag nanoparticles ranging from around 20-50 nm can also be observed uniformly decorated on the surface of both graphene-layers and CNTs (Figure 4-32 c and d) and show similar morphology to the FGAg-200 samples.

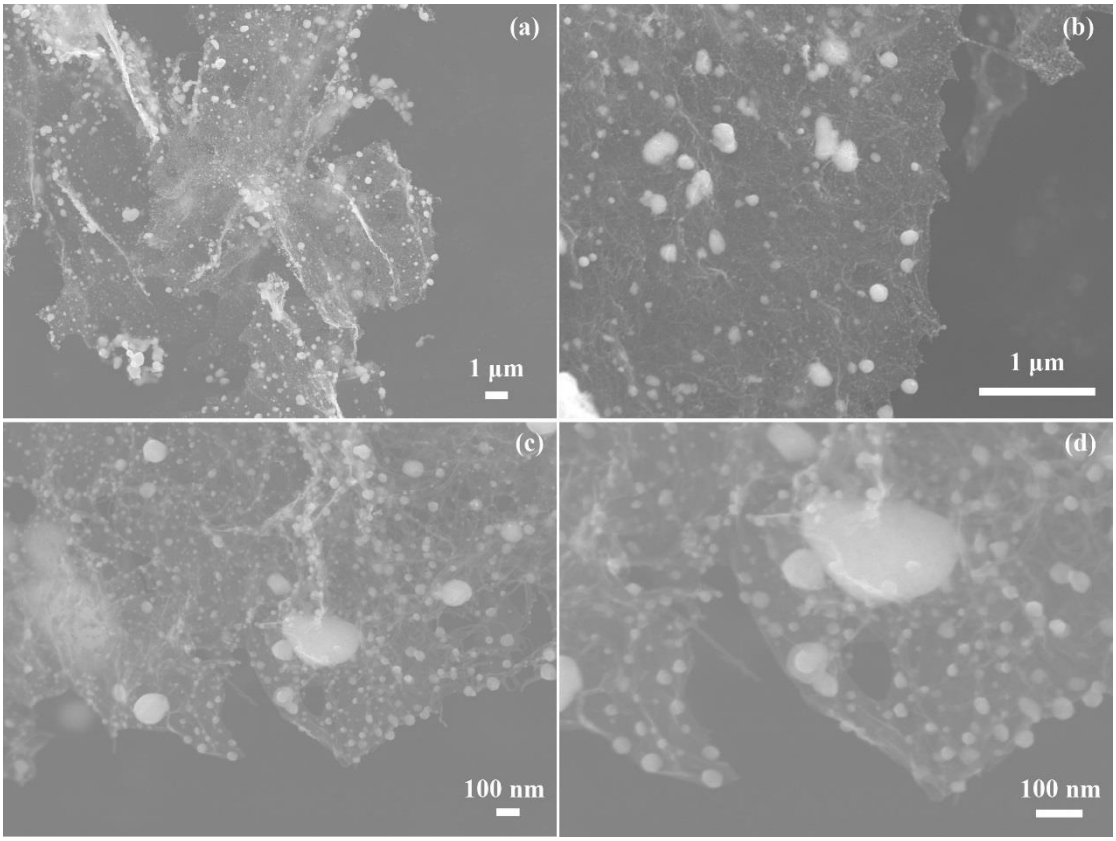

Figure 4-32 SEM images of the FGAg-250 nanostructures reduced at 250°C under an Ar/H_2 atmosphere for 2 h at low (a and b) and high (c and d) magnifications.

In Figure 4-33a, the graphene-layer-like structure can still be observed in the FGAg-300 product, and the bright round particles which can be ascribed to the Ag phase are also uniformly coated on the GNT nanostructures. Under a higher magnification image (Figure 4-33b), particles can be observed on the GNT nanostructures, which is consistent with the fact that larger Ag particles are obtained at higher reduction temperature as expected due to diffusion. Therefore, it can be concluded that the FGAg nanostructures can be successfully prepared through the MLM method with the freeze-drying and subsequent reduction process under an Ar/H_2 atmosphere for 2 h. According to the XRD results, the FGAg precursors can be completely reduced when the reduction temperature reaches above 200°C. The obtained FGAg nanostructures exhibit a well-dispersed graphene-layer-like structure, and the Ag nanoparticles are uniformly decorated on the surface of the GNT nanostructures.

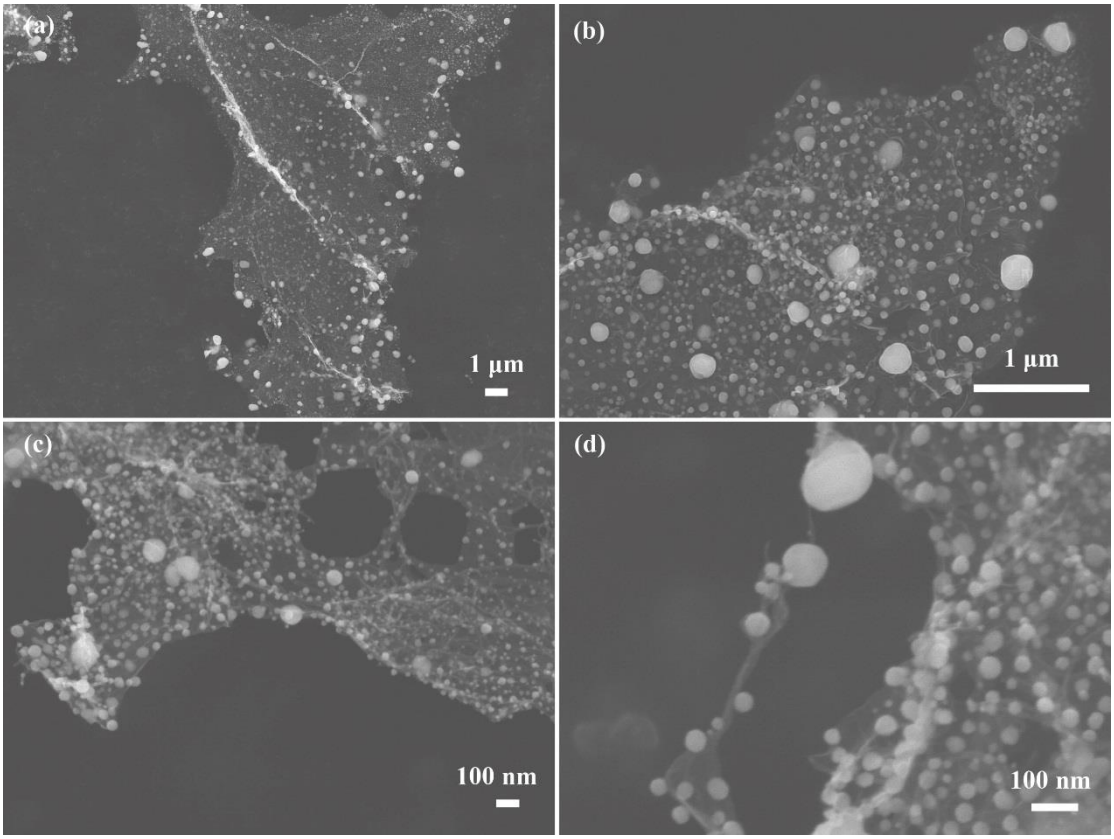

Figure 4-33 SEM images of the FGAg-300 nanostructures reduced at 300°C under an Ar/H_2 atmosphere for 2 h at low (a and b) and high (c and d) magnifications.

To further investigate the chemical constitution of the FGAg samples, the XPS results are shown in Figure 4-34. The survey scan of the FGAg samples, which are reduced from 150-300°C is displayed in Figure 4-34a. The characteristic peaks of C (C1s), O (O1s), and Ag (Ag 3d and Ag 3p) can be observed, indicating the existence of these elements. In the high-resolution Ag 3d curve of the FGAg-150 sample (Figure 4-34b), two satellite peaks besides the main Ag 3d peaks, which are located at ca. 366 eV and 374 eV, respectively. These satellite peaks can be attributed to the Ag (I) in the products. Meanwhile, the Ag $3d_{5/2}$ and $3d_{3/2}$ peaks can be divided into four peaks, the main Ag $3d_{5/2}$ and $3d_{3/2}$ peaks at 368.5 eV and 374.0 eV, which can be attributed to Ag (0), and the minor peaks at 370.0 eV and 376.8 eV which can be ascribed to the Ag_2O [157, 158]. This is consistent with the XRD results that the FGAg-150 products contain the pure Ag (ICDD PDF No. 00-04-0783) and the silver acetate (ICDD PDF No. 00-04-0096) phases. The satellite peaks disappear in the high-resolution Ag 3d curves

when the reduction temperature increases above 200°C (Figure 4-34c-e).

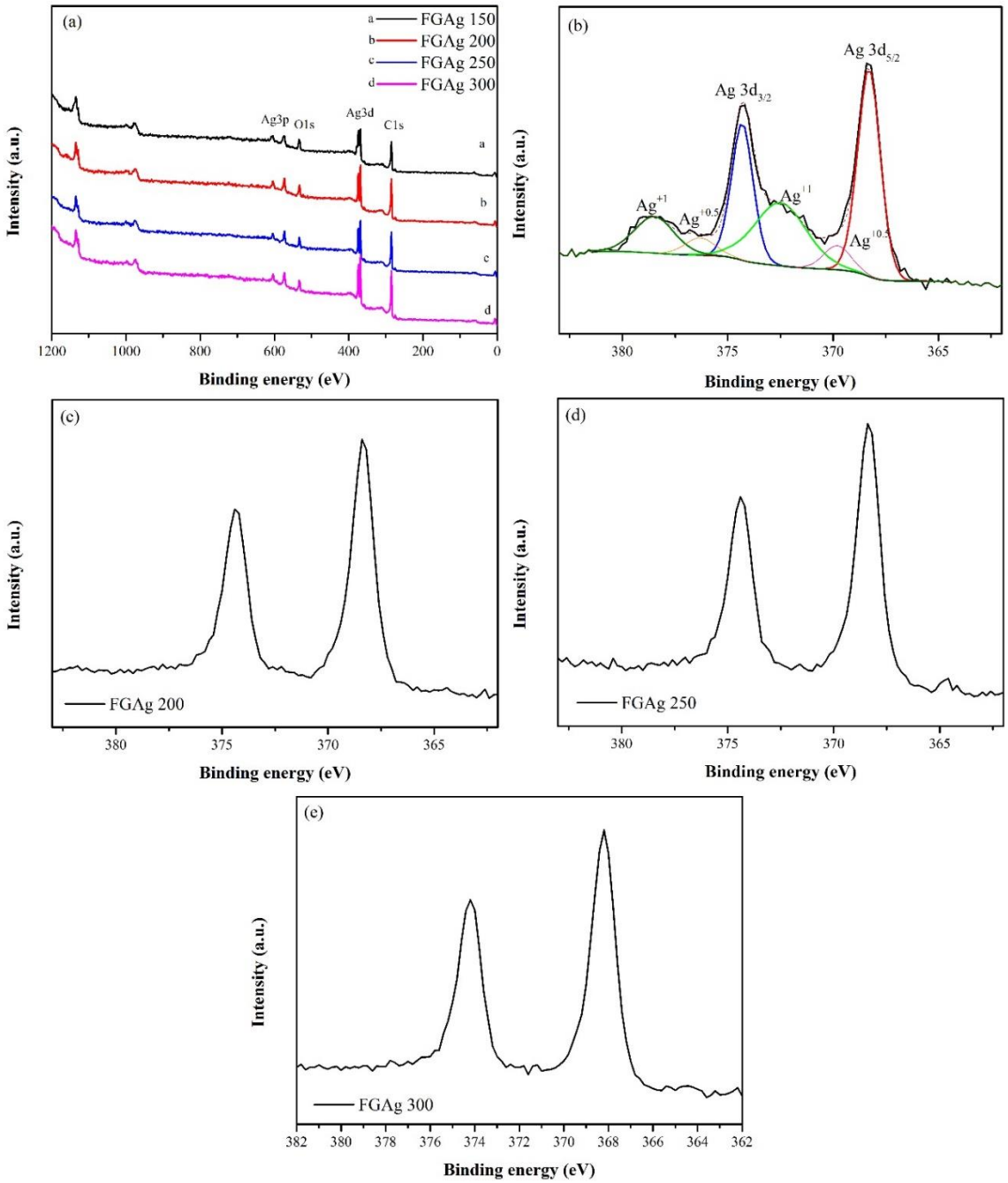

Figure 4-34 XPS survey scan (a), Ag 3d spectrum of FGAg-150 (b), FGAg-200 (c), FGAg-250 (d and FGAg-300 (e) samples.

4.4.2 The effect of reaction duration to the FGAg nanostructures

As the reduction duration plays an important role in preparing the FGNi nanostructures, this section investigates the effect of longer reduction duration to the FGAg precursors at 200°C and 250°C, and both samples are named as the FGAg-200-3h and FGAg-250-3h. Firstly, the

XRD patterns of the FGAg-200-3h and FGAg-250-3h samples are shown in Figure 4-35. The diffraction peaks of the FGAg-200-3h and FGAg-250-3h samples both match well with the standard peaks of pure Ag phase (ICDD PDF No. 00-04-0873), indicating that the FGAg precursors could be completely reduced from silver acetate phase to pure Ag phase at both conditions.

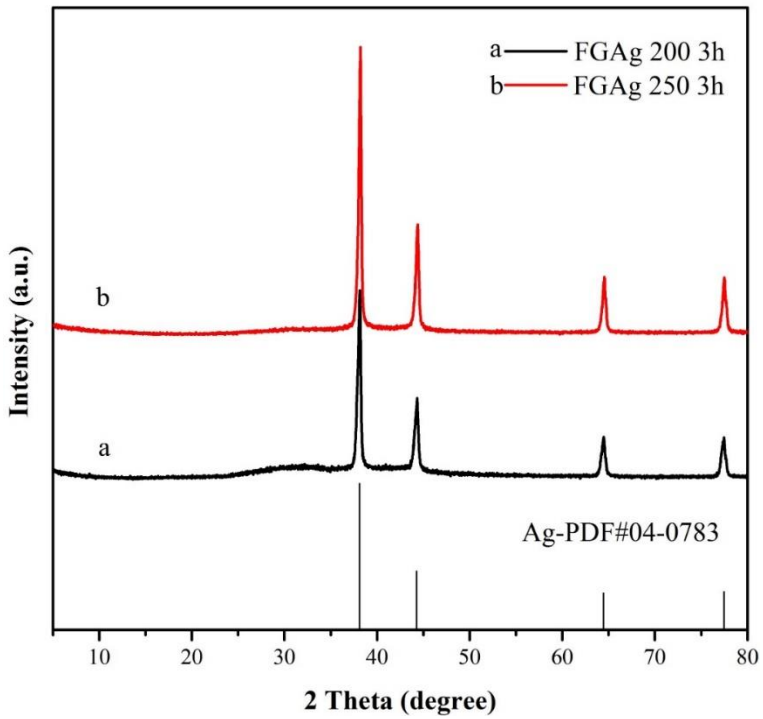

Figure 4-35 XRD patterns of the FGAg precursors reduced under an Ar/H_2 atmosphere at 200°C (a) and 250°C (b) for 3h, and the standard Ag sample.

SEM images of the FGAg-200-3h sample are shown in Figure 4-36. In Figure 4-36a, like most GNT based products, the morphology of the FGAg-200-3h sample kept the graphene-layer-like structure, and bright particles can be clearly observed decorated on the surface of the GNT nanostructures. According to the XRD results, all the coated particles can be ascribed to the Ag phase (ICDD PDF No. 00-04-0783). In Figure 4-36 b and c, the Ag nanoparticles are uniformly coated on both the graphene layers and CNTs. The Ag nanoparticles show the best distribution among all the obtained FGAg products, which can be concluded that a longer preparation duration is beneficial for the diffusion. In the high magnification image (Figure 4-36d), Ag

nanoparticles ranging from 20-100nm can be decorated on CNTs and graphene.

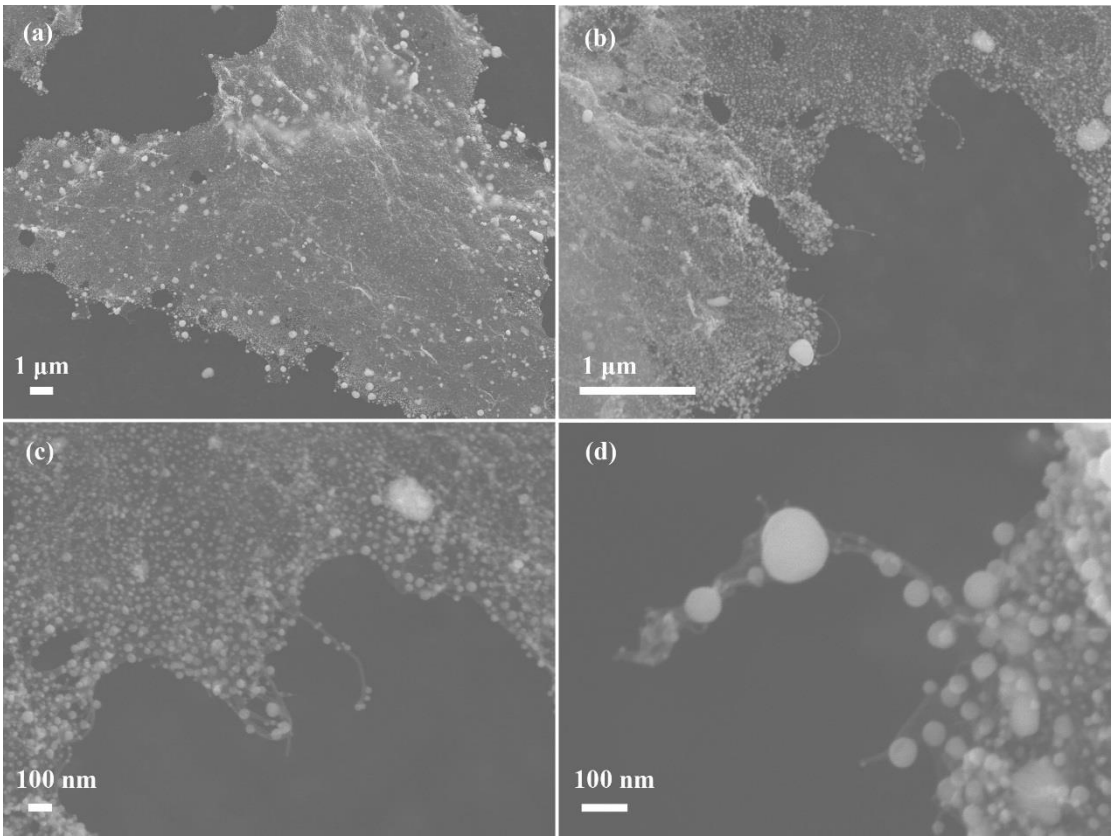

Figure 4-36 SEM images of FGAg-200-3h nanostructures reduced under an Ar/H_2 atmosphere at 200°C for 3h at low (a and b) and high (c and d) magnifications.

When the reduction temperature increases to 250°C under Ar/H_2 atmosphere for 3 h, SEM images of the FGAg-250-3h sample are displayed in Figure 4-37. In Figure 4-37a, the morphology of the FGAg-250-3h sample keeps the graphene-layer-like structure, and the bright particles also can be observed decorated on the GNT nanostructures. However, the particle size of the obtained Ag grew due to the diffusion compared to previous FGAg products. In Figure 4-37 b and c, the Ag particles are ranging from 50-500 nm. Large Ag particles that are around 500 nm can be observed on graphene layers, indicating that the long duration reduction process at 250°C allows the Ag particle to grow into huge ones. In the high magnification image (Figure 4-37d), the huge Ag particle in the center is around 400 nm, although there are also small Ag particles around 50-100 nm that can be observed both on the CNTs and graphene layers.

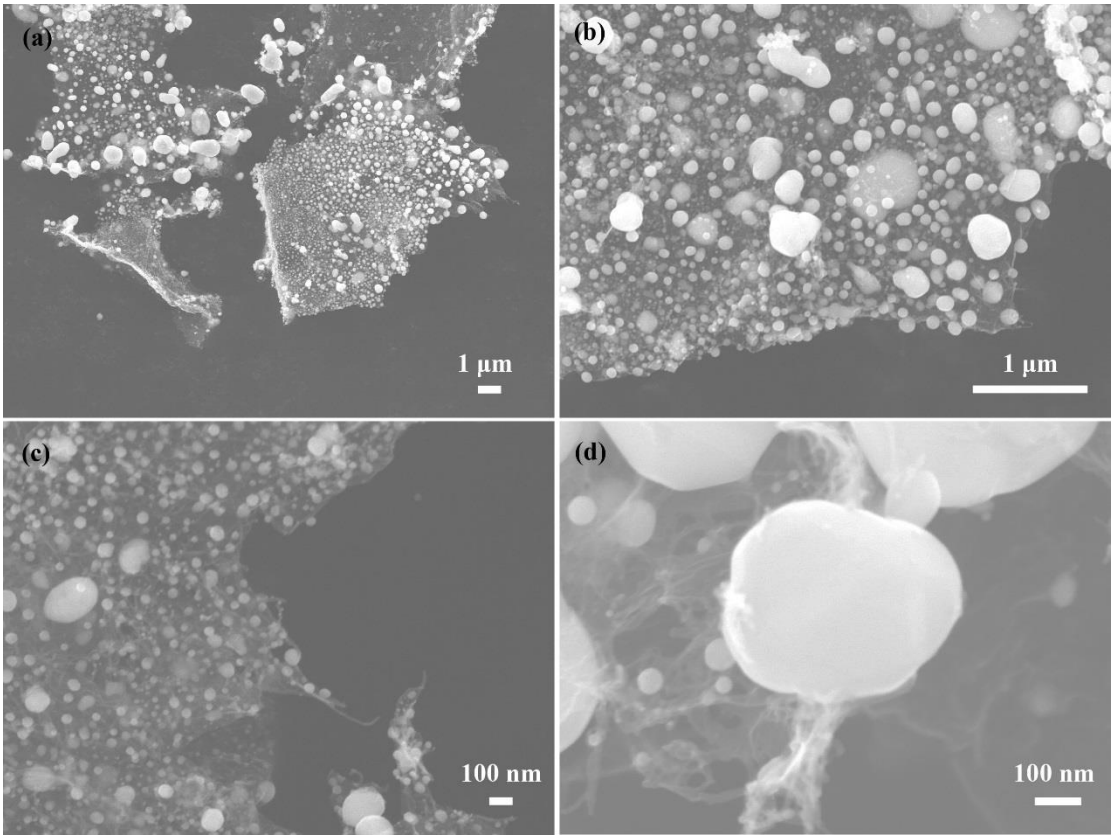

Figure 4-37 SEM images of the FGAg-250-3h samples under an Ar/H_2 atmosphere at 300°C (b) for 3h at low (a and b) and high (c and d) magnifications.

XPS results are shown in Figure 4-38. Similar to the previous FGAg samples, the survey scan (Figure 4-38a) of the FGAg-200-3h and FGAg-250-3h products present the characteristic peaks of C 1s, Ag 3d and Ag 3p, which confirms the existence of the above elements in both samples. In the high-resolution Ag 3d spectra of FGAg-200-3h and FGAg-250-3h sample (Figure 4-38b), both the samples display the Ag 3d characteristic peaks, and no satellite peaks corresponding to the Ag (I) can be detected. This XPS result has further confirmed the complete reduction of the FGAg precursors, and this is also consistent with XRD results. Thus, all the longer reduction duration results show that the FGAg-200-3h samples display the best distribution of Ag nanoparticles, while the FGAg-250-3h samples show the over-growth of Ag particles.

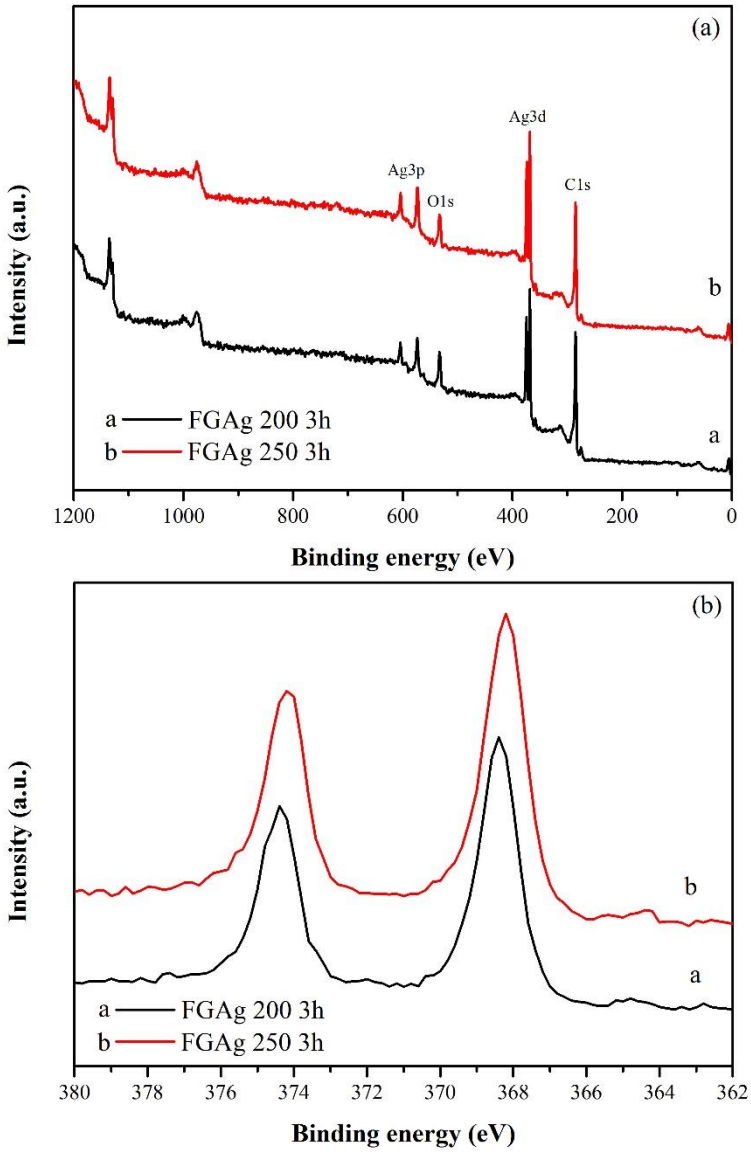

Figure 4-38 XPS survey scan (a) and high resolution of Ag 3d peaks of the FGAg-200-3h and FGAg-250-3h samples.

4.4.3 The effect of reaction atmosphere to the FGAg nanostructures

Here, the FGAg precursors were placed under pure Ar atmosphere for 2 h at 200°C and 250°C, and the samples are named as FGAg-200-Ar and FGAg-250-Ar. The XRD patterns of both samples are shown in Figure 4-39. The diffraction peaks of both the FGAg-200-Ar and FGAg-250-Ar samples match well with the pure Ag phase (ICDD PDF No. 00-04-0873), indicating that the FGAg precursors have been completely reduced at both temperatures under pure Ar atmosphere. However, compared with the previous FGAg products, the diffraction peaks of

both FGAg-200-Ar and FGAg-250-Ar samples do not show a clear peak for the GNT nanostructures.

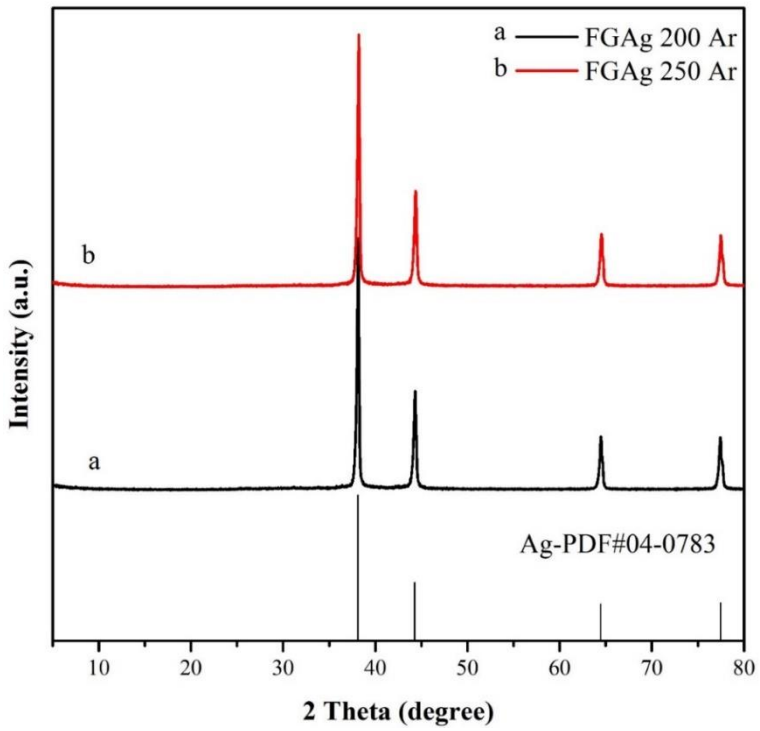

Figure 4-39 XRD patterns of the FGAg-200-Ar (a) and FGAg-250-Ar (b) samples reduced under a pure Ar atmosphere at 200°C (a) and 250°C (b) for 2h, and the standard Ag sample.

The morphologies of FGAg-200-Ar and FGAg-250-Ar samples are displayed in Figure 4-40 and Figure 4-41, respectively. In Figure 4-40a, the FGAg-200-Ar sample exhibits the well-dispersed structure, but the bright particles decorated on the GNT nanostructures are overgrowth than previous samples (up to 1 μm) even at 200°C. The XRD results explain the coating particles are attributed to the Ag phase (ICDD PDF No. 00-04-0873). In a higher magnification image (Figure 4-40b), the Ag particles can be observed randomly distributed. In Figure 4-40 c and d, although small Ag particles around 20 nm can be detected coated on the CNTs, the huge particles are still dominant. Therefore, it can be assumed that the pure Ar atmosphere is beneficial to the aggregation of medium size Ag particles into large particles.

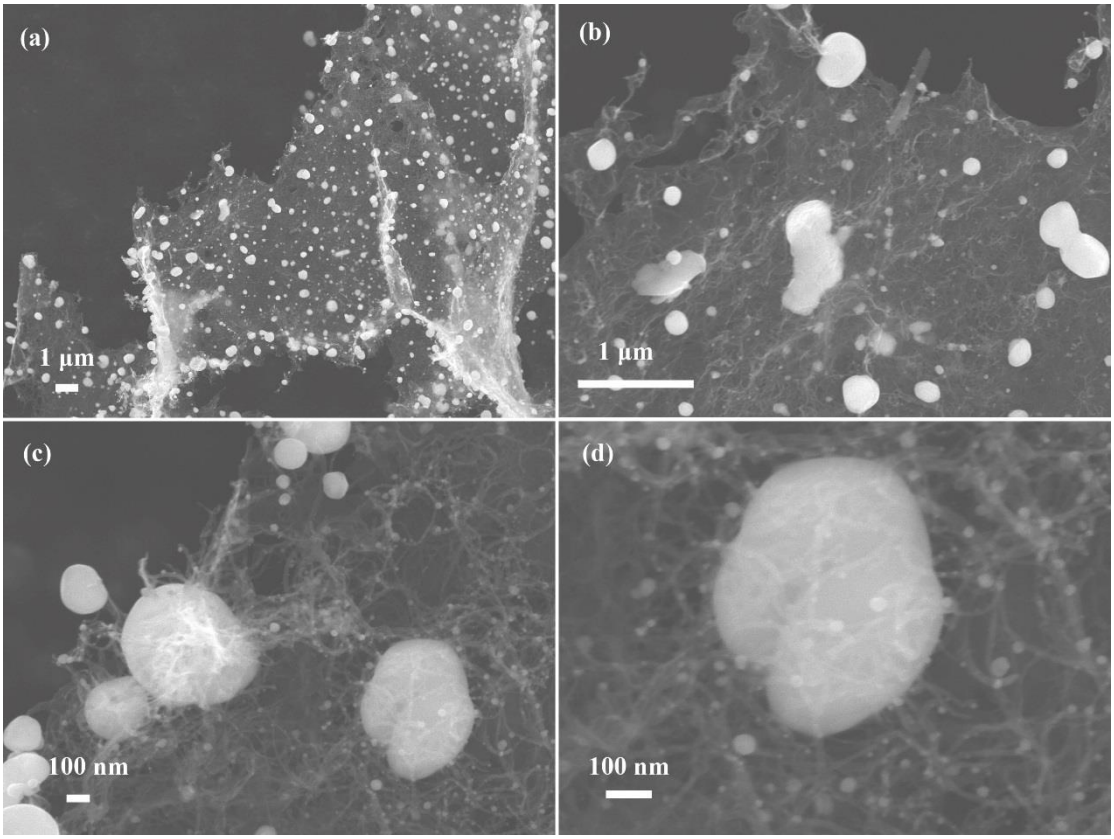

Figure 4-40 SEM images of the FGAg-200-Ar samples under low (a and b) and high (c and d) magnifications.

When the reaction temperature increases to 250°C, the FGAg-250-Ar sample (Figure 4-41a) also displays a similar well-dispersed structure, and bright particles of ca. 1 μm are found on the GNT nanostructures. In Figure 4-41b, the Ag particles with large size can be observed covered on the GNT nanostructures and the distribution of Ag particles is random in the FGAg-250-Ar sample. In higher magnification images (Figure 4-41 c and d), although Ag particles around 30 nm can be observed on the GNT nanostructures, the large particles are still obvious in the FGAg-250-Ar sample. Therefore, although both the FGAg-200-Ar and FGAg-250-Ar samples can be completely reduced under a pure Ar atmosphere, the morphologies of the obtained samples are not as uniform as the Ar/H_2 atmosphere reduced ones.

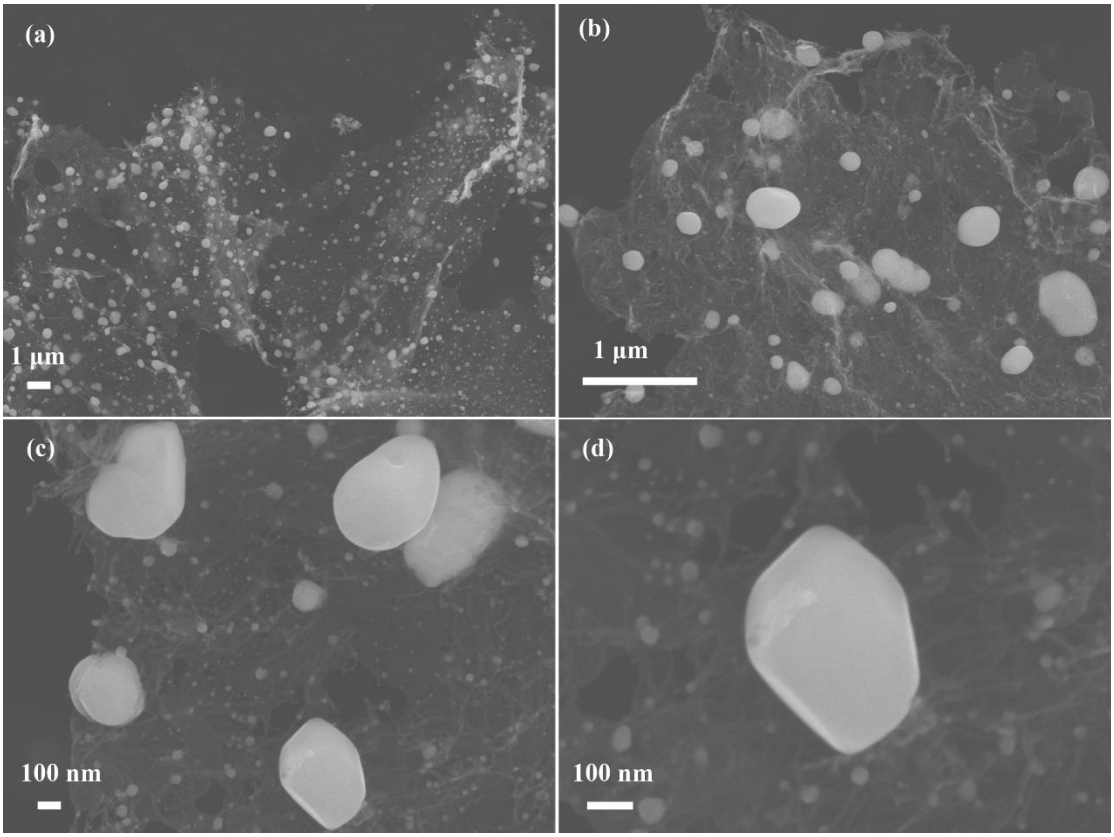

Figure 4-41 SEM images of the FGAg-250-Ar samples under a pure Ar atmosphere at 250°C (b) for 2h at low (a and b) and high (c and d) magnifications.

4.5 Discussion

4.5.1 The preparation of GNT nanostructures

Before the preparation of GNT nanostructures, CNTs were firstly acid-treated and the characterisation results proved that functional groups are attached onto the sidewalls of CNTs. The XRD and SEM results (Figure *4-1* and Figure *4-2*) do not demonstrate obvious differences between the as-received and acid-treated CNTs, indicating that 25 min acid treatment does not change the crystalline structure and morphology of the CNTs. However, an obvious O 1s characteristic peak can be observed in the XPS survey scan of the acid-treated CNTs sample (Figure 4-3b), which confirms that the oxygen-containing components were formed during the acid treatment. The high-resolution C 1s further confirmed these oxygen-containing components to be carbon-based functional groups (i.e., carboxylic acid and phenolic hydroxyl

groups). Similar to the acid-treated CNT sample, the XPS results of GO also displayed clear evidence of oxygen-contained components (Figure 4-6). By mixing the acid-treated CNTs and GOs, these functional groups could prevent the agglomeration between CNTs and GOs due to the electrostatic repulsion by the negative charge and provide abundant sites for metal ions nucleation in the subsequent sample preparation process[16].

Through the ultrasonication mixing and freeze-drying method, the GNT nanostructures were obtained. From the SEM images (Figure 4-7), the graphene-layer-like structures of the as-prepared products indicate that the well-dispersed structures were largely kept after the freeze-drying method. The higher magnification images further confirm that the CNTs were attached on the GO layers rather than agglomerating into clusters shown in Figure 4-2, which can be attributed to the strong π–π interactions between CNTs and graphene materials. Meanwhile, the successful attachment of CNTs onto the GO layers can also further prevent the agglomeration of GO layers. In the XPS results of the GNT and R-GNT samples (Figure 4-8), the intensity of the oxygen-contained components in the survey and C 1s deconvoluted spectra both decreased after the reduction process. When comparing the deconvoluted C 1s spectrum before and after reduction (Figure 4-8), the peak of defect containing C component appeared in the R-GNT sample, indicating that the defect C was obtained in the products as a result of the reduction process in the preparation procedures [154, 155]. Meanwhile, the oxygen-contained components, especially the C-O components, were reduced dramatically during the reduction process. As shown in Figure 4-42, such a unique 3D structure via the freeze-drying method has been successfully prepared, and such functional groups attached onto GNTs nanostructures were proved to prevent the agglomeration of GNTs and be suitable for the nucleation of metal particles.

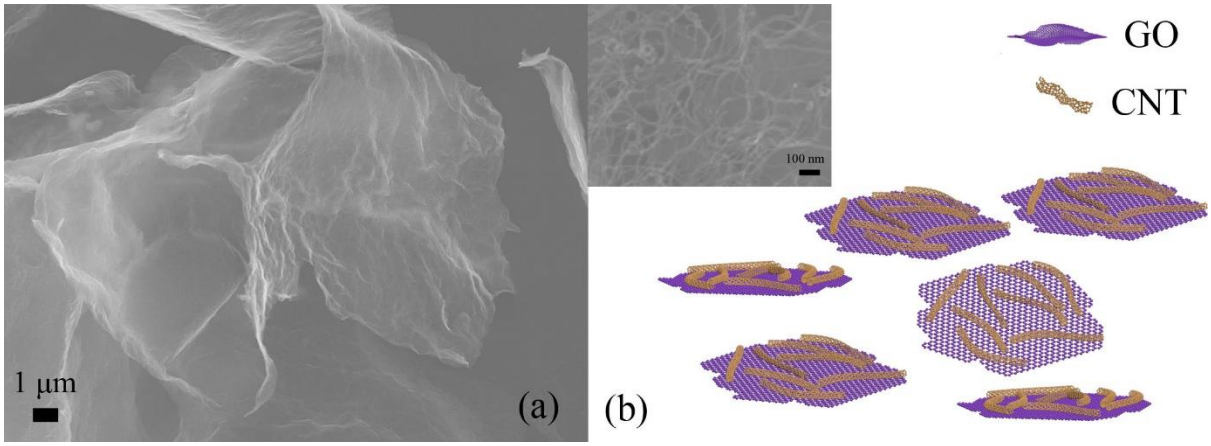

Figure 4-42 SEM images and schematic of the as-prepared GNT nanostructures.

4.5.2 The effect of different parameters on the composition and morphology of FGCu nanostructures

Based on the GNT nanostructures, copper nanoparticles were introduced through the MLM and subsequent reduction processes. By mixing the GNT dispersion with $Cu(CH_3COO)_2$ solution, the FGCu precursors were obtained via freeze-drying the mixture. The XRD result of the freeze-drying powders (Figure 4-9) shows obvious diffraction peaks of $Cu(CH_3COO)_2 \cdot H_2O$ (ICDD PDF No. 00-27-0145) phase, confirming that the copper acetate was successfully introduced with GNT nanostructures and no other chemical reactions occurred during the whole procedure. The FGCu precursors were then reduced at different reduction temperatures in Ar/H_2 atmosphere for 3 h, different phases (i.e., $Cu(CH_3COO)_2$, $Cu(CH_3COO)$, Cu_2O, and Cu phases) have been obtained depending on the reduction temperatures. From the XRD results, the obtained products transferred from Cu (II) state [$Cu(CH_3COO)_2$] to Cu (I) state [$Cu(CH_3COO)$ and Cu_2O] and finally to pure Cu (0), and the only diffraction peaks of pure Cu phase (ICDD PDF No. 00-04-0836) appeared when the reduction temperature reached 300°C. The XPS results (Figure 4-14) further confirmed the composition of different products under different reduction temperatures.

Meanwhile, the SEM images demonstrated that a uniform distribution of Cu nanoparticles can

be obtained after reaction at 250°C under an Ar/H_2 atmosphere, although there is still a minor peak of Cu_2O phase according to XRD results (Figure 4-12). Therefore, the condition of 300°C under Ar/H_2 atmosphere for 3 h can be regarded as a reasonable reaction condition to prepare Cu nanoparticles coated GNT nanostructures with the freeze-dried precursors. Figure 4-43 shows the SEM images of as-prepared products from literature (a and b) [56, 57] and in this research (c), and the schematic of the FGCu nanostructures (d). In Figure 4-43a, the Cu coated GO nanostructures could be observed via the MLM method, but there were also large Cu particles beside them. Figure 4-43b displays a Cu decorated GO nanostructure through the MLM process. Cu nanoparticles showed a better distribution, but there is still an obvious agglomeration trend existing in the final products. In our results (Figure 4-43c), the well-dispersed GNT nanostructure was kept and the Cu nanoparticles were uniformly coated (as demonstrated in Figure 4-43d). Therefore, the combination of freeze-drying and MLM methods were proved to be an effective process to prepared this unique structure.

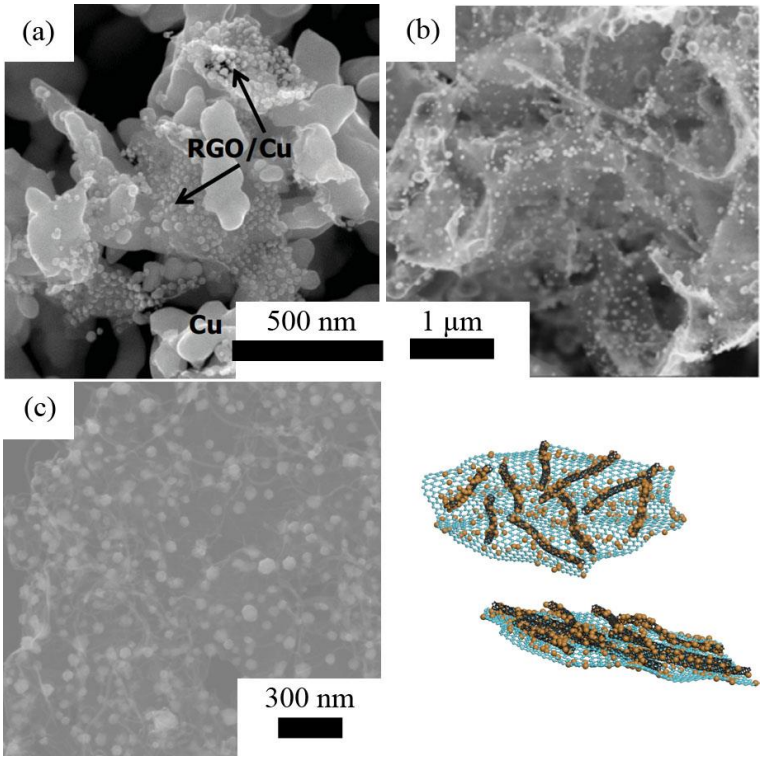

Figure 4-43 SEM images of Cu-carbon samples from literature (a and b) [56, 57], and the SEM image and schematic of FGCu nanostructures.

To further investigate the effects of reduction conditions, different reduction periods and different temperatures have also been explored. The Cu_2O phase can still be detected in the final products even reduced for 4 h at 250°C (Figure 4-15a), indicating that the simple extension of reaction duration cannot completely reduce FGCu precursors. Meanwhile, the same Cu_2O peak appears in the curve of products reduced at 300°C for only 2 h (Figure 4-15 b), but it disappears in both 3 h and 4 h curves (Figure 4-12 and Figure 4-15). Therefore, it can be concluded that the FGCu precursors could be completely reduced under Ar/H_2 atmosphere only when the reduction temperature reaches 300°C and the duration is longer than 3 hours. The XPS results also further confirmed that the satellite peaks of the oxidised Cu component appear in both 250°C for 4 h and 300°C for 2 h samples.

SEM images give another information on the morphologies of the final products under different conditions. The longer reaction period would result in the overgrowth of the Cu particles due to the diffusion, and the Cu nanoparticle size could be found even larger in the FGCu-250-4h (Figure 4-16) and FGCu-300-4h (Figure 4-18) samples when compared with 2 h or 3 h products. By adjusting the preparation parameters, the reduction at 300°C for 3 h could be selected as the optimised condition to prepare the Cu nanoparticles decorated GNT nanostructures. Therefore, based on the well-dispersed GNT nanostructures, uniform decoration of Cu nanoparticles has been introduced through the MLM process followed by the freezing-drying and reduction methods. The subsequent investigation shows that the optimal preparation parameter is at 300°C for 3 h under Ar/H_2 atmosphere.

When the FGCu samples were successfully prepared, the storage of the products becomes another important issue as metals, especially Cu, are easy to be oxidised when exposed in the open air. Figure *4-44* displays the XRD patterns of the FGCu samples stored in the open air for a month. An obvious diffraction peak of Cu_2O phase can be observed, indicating that the FGCu

samples were oxidised during storage in air. Thus, all the obtained products were stored in the vacuum bag as mentioned in Chapter 3. Meanwhile, the Cu 2p XPS spectra of FGCu samples before and after re-reduction are shown in appendix 2. It can be found that the oxidised signals of Cu disappeared after the re-reduction process. Although the FGCu samples can be reduced when exposed in air for long, it is still suggested to use newly produced samples or store them in a vacuum bag if not take long.

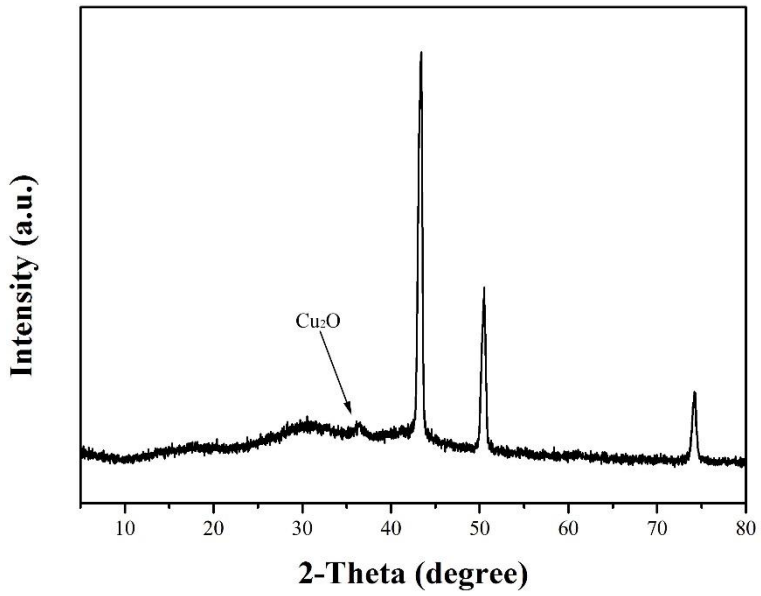

Figure 4-44 XRD patterns of FGCu samples stored in the open air.

4.5.3 The effects of different parameters on the constitution and morphology of FGNi nanostructures

The preparation of Ni-based nanostructures has been investigated based on the results of FGCu nanostructures. The reduction temperature was first studied, and the FGNi precursors obtained via MLM and freeze-drying processes have been reduced under an Ar/H_2 atmosphere for 3 h from 200 - 400°C. In the XRD patterns (Figure 4-20), the pure Ni phase (ICDD PDF No. 00-04-0850) could be detected after 300°C. This is different from the FGCu samples that oxidised components were changed during the increase of reduction temperature. Thus, the FGNi products could be completely reduced when the reduction reached 300°C. Meanwhile,

although the SEM images of the FGNi-200 sample (Figure 4-21) also show the well-dispersed graphene-layer-like structures, the morphology and distribution of obtained Ni particles are not as uniform as the FGCu samples showed. There are only large particles formed on the GNT nanostructures in FGNi-300and FGNi-400 samples. Therefore, different preparation parameters are required to produce a uniform decoration of Ni particles, and further study is needed for the preparation parameters.

The reaction atmosphere was then changed to a pure Ar atmosphere. Figure 4-22 displayed the XRD results of FGNi products obtained under the pure Ar atmosphere from 300 - 400°C for 3 h. Three different phases (NiO, fcc Ni, and hcp Ni) have been detected in the patterns of the FGNi-300-Ar sample (Figure 4-22a), indicating that NiO phase was remaining and the precursors could not be completely reduced. Meanwhile, some of the precursors can be reduced to either fcc or hcp Ni phases. When the reduction temperature increased to 400°C, only two phases (NiO and fcc Ni) can be observed. This can be ascribed to the fact that the fcc Ni phase is more stable under higher temperatures, consistent with previous literature [159, 160]. SEM images of both samples (Figure 4-23 and Figure 4-24) displayed different morphologies compared with products under Ar/H_2 atmosphere. The uniform distribution of Ni nanoparticles can be observed in both samples, and the huge particles disappeared. Therefore, the pure Ar atmosphere is regarded as a better reaction condition to prepare uniform nanoparticle coated GNT products compared to the Ar/H_2 atmosphere.

The combination of pure Ar and Ar/H_2 atmosphere was then investigated. The FGNi precursors were placed in pure Ar atmosphere for 1 h and then transferred into Ar/H_2 atmosphere for another 2 h. The XRD results (Figure 4-25) demonstrated that no diffraction peaks of NiO phase remaining in both samples, consistent with the previous results that the NiO phase has been completely reduced under an Ar/H_2 atmosphere. Meanwhile, the hcp and fcc Ni phases

are still kept in the FGNi-300-1+2 sample, which is also consistent with the fact that both Ni phases can exist under 300°C conditions (Figure 4-22). With the increase of reduction temperature, the FGNi-400-1+2 sample shows only the fcc Ni phase. In the SEM images of both samples (Figure 4-26 and Figure 4-27), the good dispersion of Ni nanoparticles from pure Ar atmosphere remained, indicating that the subsequent Ar/H_2 atmosphere could not further change the distribution of Ni nanoparticles. Meanwhile, the obtained FWHM from the XRD result increases from 0.348 of FGNi-400 sample to 0.401 of FGNi-400-Ar sample and 0.387 of FGNi-400-1+2 sample, further confirming that the FGNi-400 sample had the largest particles.

Figure 4-45 displays the SEM images of Ni-graphene composites from literature and the FGNi samples in this research. Figure 4-45a shows the Ni@graphene composites via thermal annealing by Zhou [161]. The Ni particles with particle sizes of around 20-40 nm can be observed on graphene, but the particles still agglomerate in the image , indicating that the thermal annealing could not effectively prevent the agglomeration between NI and graphene. In Figure 4-45b, Shen has presented the Ni nanoparticles modified graphene sheets by using the metal-oleate complex as precursors and sodium sulfate as a template [162]. The Ni nanoparticles can be observed decorated on graphene sheets, but agglomeration still occurred between each graphene-based composite. The Ni-RGO nanocomposites via an in situ co-reduction and surfactant-free method reported by Li [124] are displayed in Figure 4-45c. Ni nanoparticles with sharp thorns are dispersed on the graphene layers, but the particle size is larger than 100 nm and the distribution is random. For the FGNi samples in this research, the well-dispersed graphene-layer-like structure was kept through the freeze-drying method and the Ni nanoparticles can be found uniformly decorated on the GNT nanostructures (Figure 4-45d). Therefore, the parameter at 400°C under pure Ar atmosphere for 1 h followed by another 2 h Ar/H_2 atmosphere reduction has been the optimal parameter for the preparation of

Ni nanoparticles decorated GNT nanostructures.

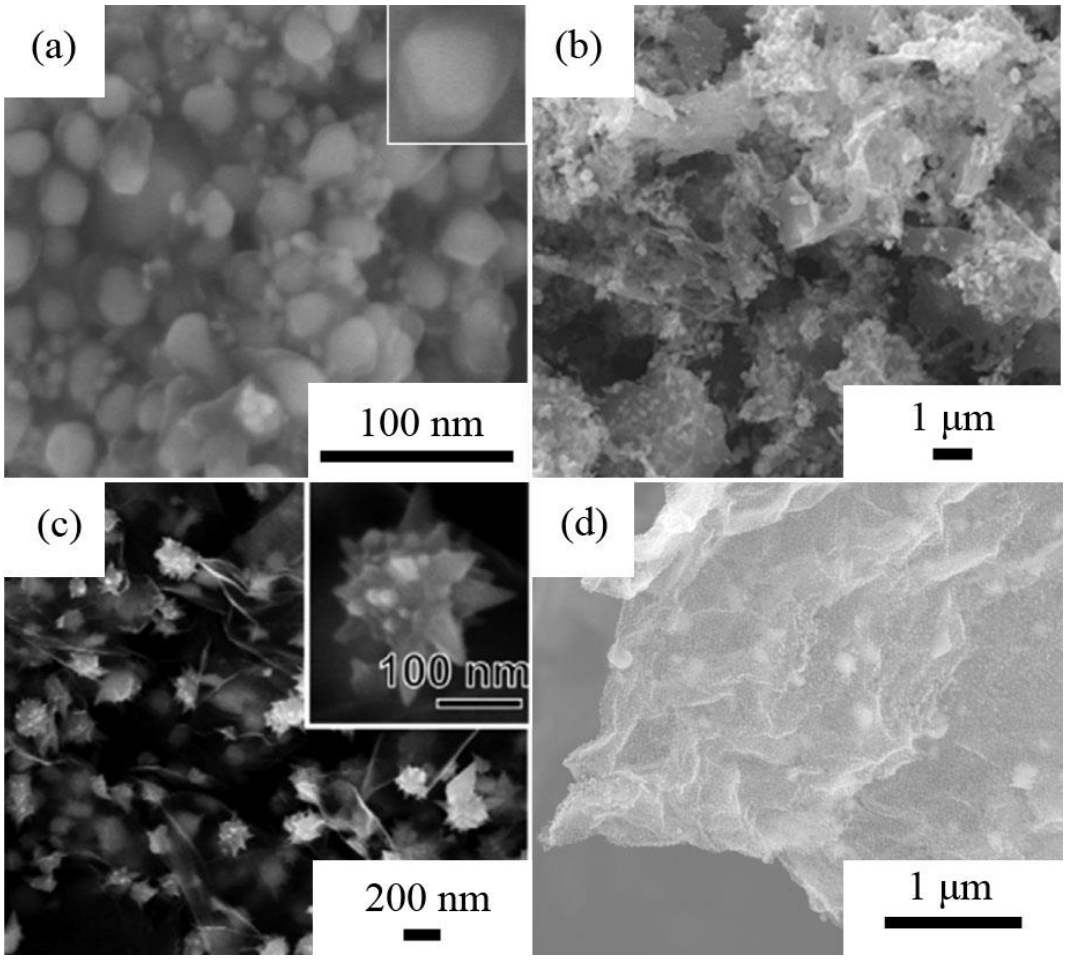

Figure 4-45 SEM images of the Ni-graphene-based samples from literature (a-c) [124, 161, 162] and the FGNi nanostructures (d).

4.5.4 The effect of different parameters on the constitution and morphology of FGAg nanostructures

Through the MLM and freeze-drying approaches, the FGAg precursors have been obtained, and the XRD result (Figure 4-28) demonstrated that the diffraction curve matches well with the silver acetate (ICDD PDF No. 00-04-0096) phase. After that, the reduction temperature was initially investigated from 150 - 300°C under Ar/H_2 atmosphere for 2 h. Despite the strong diffraction peaks of pure Ag phase (ICDD PDF No. 00-04-0783) in the patterns FGAg-150 sample (Figure 4-29a), a minor peak of silver acetate phase (ICDD PDF No. 00-04-0096) still

remained, indicating that the FGAg precursors cannot be completely reduced at 150°C. With the temperature increasing, the peak of silver acetate disappeared, indicating a complete reduction after 200°C. The XPS results (Figure 4-34) also showed the oxidised signals in the FGAg-150 sample, which further confirms that 200°C was a critical temperature to reduce silver acetate. SEM images of the FGAg-150 sample (Figure 4-30) demonstrated a random distribution of the obtained particle and the obtained particles were also not uniform. The distribution of Ag nanoparticles improved with the reduction temperature increasing, while the Ag particles grow larger in the FGAg-300 sample, which is consistent with the results of FGCu samples.

In the FGCu system, the longer reduction period could result in better reduction products, while the combination of the reduction atmosphere in the FGNi system leads to a better distribution of decorated nanoparticles. Thus, these two factors have then been investigated in the FGAg system. The extension of reduction temperature under Ar/H_2 atmosphere for 3 h has been studied at both 200 and 300°C. The XRD and XPS results demonstrated that the long duration completely reduced the FGAg precursors, and no obvious impure phase can be detected. In the SEM images of both samples (Figure 4-36 and Figure 4-37), the FGAg-200-3h sample displays a uniform distribution of Ag nanoparticles on the GNT nanostructures, while the FGAg-250-3h sample showed the overgrowth of Ag particles. Meanwhile, the obtained FWHM from the XRD result increases from 0.0.362 of FGAg-250-3h sample to 0.311 of FGAg-300-3h sample, further indicating that the particle size increased in the FGAg-300-3h sample.

The pure Ar atmosphere has been introduced into the FGAg system, and the FGAg precursors were reduced at 200 and 300°C for 3 h, respectively. From the XRD results (Figure 4-39), only the diffraction peaks of pure Ag phase (ICDD PDF No. 00-04-0873) appear, the intensities of the diffraction peaks were higher than the previous results that the signal of the GNT

component is too weak to be detected. The obtained FWHM values of both samples are 0.229 and 0.238, respectively. Both values are much higher than those reduced under the Ar/H_2 atmosphere, indicating a significant increase in particle size in the products. Meanwhile, SEM images of both samples (Figure 4-40 and Figure 4-41) displayed only large Ag particles coating on the GNT nanostructures under pure Ar atmosphere, and the distribution of larger Ag particles is random rather than the uniform distribution of previous samples under Ar/H_2 atmosphere. Therefore, unlike the effect of the pure Ar atmosphere in FGNi system, it cannot further enhance the distribution of decorated nanoparticles.

Figure 4-46 compares the morphology of Ag-graphene based samples from literature with the FGAg nanostructures in this research. The Ag decorated MWCNT composites (Figure 4-46a) were prepared via the electroless deposition method by Lee [163], and they investigated the effect of temperature on the final morphology. It can be found that the Ag nanoparticles fully coved on the MWCNT at 90°C. However, this method cannot effectively avoid agglomeration during the reaction. Figure 4-46b displays the Ag-rGO-CNT composites via electroless-position by Zhang [164]. In their research, the large Ag particles can be observed on the GO-CNT structures, and the particles are also found to be aggregate. Thus, the reaction in water for a long time has side-effects in preparing well-dispersed products. Khan reported the Ag-rGO-CNT through hydrothermal treatment and the SEM image of the product is shown in Figure 4-46c [165]. The authors concluded the morphology as the sandwich amorphous graphene with embedded Ag particles. Thus, the hydrothermal process still could not avoid the agglomeration during the reaction. As for the FGAg nanostructures, the uniform decoration of Ag nanoparticles is observed decorating on GNT nanostructures (Figure 4-46d). Therefore, based on the well-dispersed GNT nanostructures, uniform decoration of Ag nanoparticles has been obtained through the MLM process followed by the freezing-drying and reduction methods, and the optimal preparation parameter is at 200°C for 3 h under Ar/H_2 atmosphere.

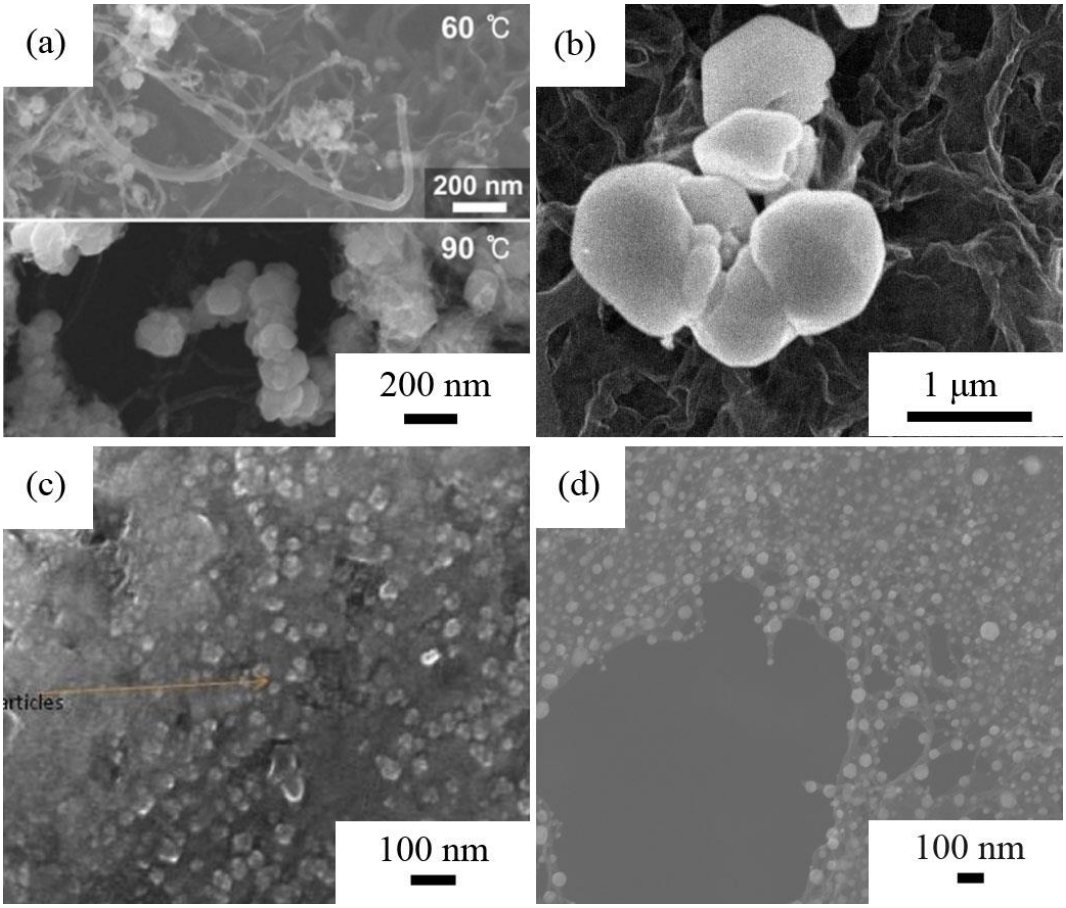

Figure 4-46 SEM images of the Ag-graphene-based samples from literature (a-c) [163-165] and the FGAg nanostructures (d).

4.6 Summary

A systematic exploration has been carried out to study the preparation of GO-CNT nanostructures as well as their metal nanoparticles decorating samples in this chapter, and several conclusions can be drawn:

- The well-dispersed GNT nanostructures have been successfully prepared through the freeze-drying method after ultrasonic dispersion. The fast frozen in LN largely kept the well-dispersed structure, and the subsequent freeze-drying process effectively removed the solution (ice) in the system and further prevented the agglomeration of GNTs. The obtained powders displayed a graphene-like structure and the CNTs are attached onto the GO layers.

- Based on the GNT nanostructures, Cu nanoparticles decorated GNT (FGCu) nanostructures have been prepared through the MLM process combined with the freeze-drying and subsequent reduction process. The relevant research showed that reduction at 300°C under Ar/H_2 atmosphere for 3 h is the optimal reduction parameter to prepare the uniformly Cu nanoparticles coating GNT nanostructures.
- Similar to the FGCu system, Ni nanoparticles decorated GNT (FGNi) nanostructures were obtained via this MLM process combined with the freeze-drying followed by the subsequent reduction process. The experimental data showed that the combination of the pure Ar atmosphere for 1 h followed by the Ar/H_2 atmosphere for another 2 h is beneficial to prepare uniform decoration of the products.
- The uniform Ag nanoparticles decorated GNT (FGAg) nanostructures have been produced via the same MLM process combined with the freeze-drying and subsequent reduction process. Unlike the FGNi products, the uniform decoration of Ag nanoparticles must be obtained under the Ar/H_2 atmosphere.

Therefore, a universal and facile preparation method has been developed based on the freeze-drying process to prepare well-dispersed GNT 3D nanostructures. The uniform decoration of metal nanoparticles (including Cu, Ag, and Ni) on these 3D nanostructures was then obtained through the MLM process followed by the freezing-drying and subsequent reduction methods. Because of the unique morphology obtained, the as-prepared nanostructures exhibit great potential in different applications, as discussed in the following chapters.

5 Silver and Nickel decorated GNT samples and their enhancement with polymer matrix composites

Polymers, including the thermoset or thermoplastic types, have already played important roles in our daily lives and various industrial fields, such as electronics, aerospace, and automobile. To meet the increasing demands of polymer-based technologies, advanced polymer materials with enhanced properties are required depending on their applications. In this chapter, the Ag and Ni nanoparticle decorated GNT samples have been applied as fillers to reinforce both the PEEK and epoxy resin, respectively. The enhancements in different properties (i.e., thermal and electrical conduction performances) are discussed.

5.1 PEEK based composites and their property enhancement by FGAg nanostructures as reinforcements

5.1.1 Structure and morphology characterisation

The XRD patterns of FGAg, pure Ag and pure GNT samples are displayed in Figure *5-1*a. In the XRD patterns of FGAg and pure Ag samples, three strong diffraction peaks at 2θ of 38.1°, 44.3° and 64.2° indicate the (111), (200), and (220) planes of Ag (ICDD PDF No. 00-04-0783). As before, no obvious sharp diffraction peaks can be observed in pure GNT samples (Peak 3) except for a broad peak that can be attributed to carbon material ranging from 25-45°[166]. When comparing the diffraction peaks of pure Ag and FGAg composites (1 and 2), the XRD patterns of FGAg sample also show a minor broad peak around 30° (insert picture of Figure *5-1*a), which further confirms the existence of GNT component in FGAg samples. In addition, no other peaks can be detected in the patterns of FGAg and pure Ag samples, indicating that

both the precursors were reduced to pure Ag phase under Ar/H_2 atmosphere at 200°C for 3 h. The XPS spectra of FGAg and pure GNT samples are illustrated in Figure *5-1* b-d. In Figure *5-1*b, the survey scan spectra of both samples display the characteristic peak of C1s and O1s, while the Ag3d and Ag3p characteristic peaks can be observed in the survey scan of FGAg samples. The C1s spectra and their deconvolution peaks of pure GNT and FGAg samples are displayed in Figure *5-1* c and d, respectively. For the deconvolution peaks of pure GNT samples (Figure *5-1*c), the C1s characteristic peak can be deconvoluted into five peaks, the sp^2 hybridized C located at 284.6 eV, the defect-containing sp^2 hybridized C at 285 eV, the C-O (ether bonds) which corresponds to the hydroxyl groups at 286.3 eV, the C=O groups (ketone bonds) at 288.9 eV and the sp^2 hybrid orbit of benzene plane at 290.8 eV [153]. The C1s deconvolution peaks of FGAg sample show similar peaks as pure GNT samples.

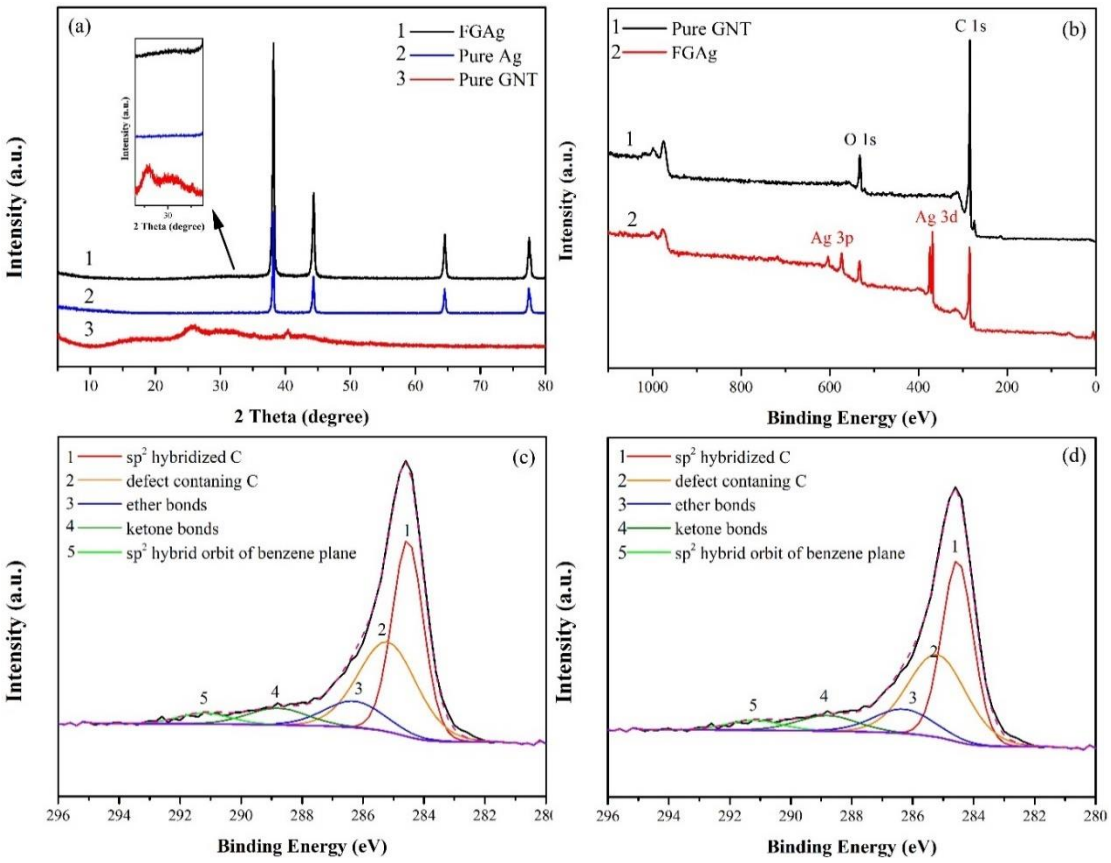

Figure 5-1 (a) XRD patterns of FGAg, pure Ag and pure GNT samples, (b) the XPS survey scan of pure GNT and FGAg sample, C 1s spectra of pure GNT (c) and FGAg (d).

The Thermogravimetric (TGA) result of FGAg sample is shown in Figure 5-2. The weight decrease, which starts from around 200°C, can be ascribed to the oxidation of the carbon content (GNT component) in the sample. This also corresponds to the exothermic peak shown as the blue curve in Figure 5-2. The weight loss stops at around 350°C and the remaining weight percentage of the FGAg sample is 82.5 wt.%. As the remaining part is the Ag phase, the calculated Ag : C weight ratio is close to the value of 8:2, which is consistent with the initial weight ratio of Ag to C in the sample preparation procedure.

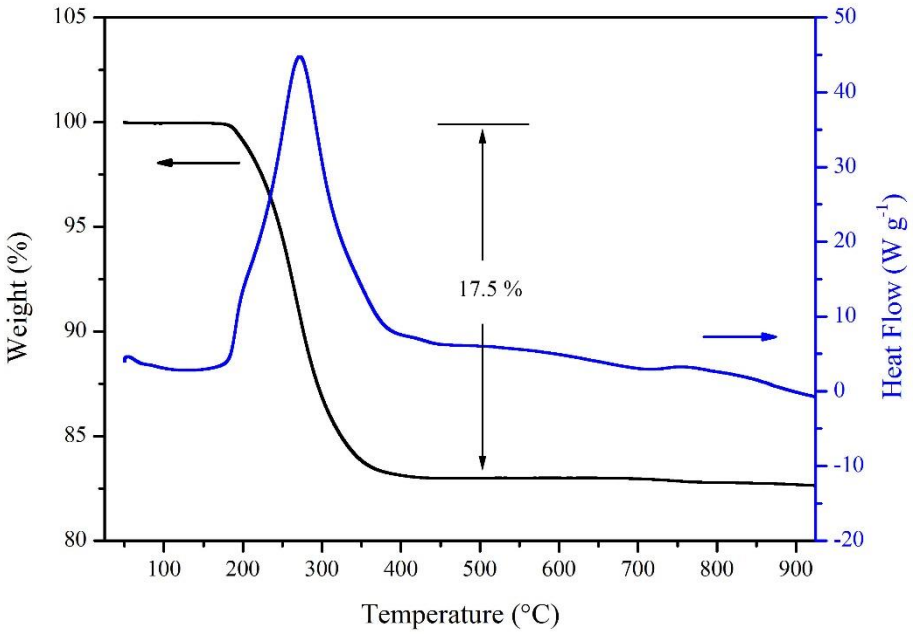

Figure 5-2 TGA and DSC results of FGAg sample.

To investigate the morphology of the FGAg sample, secondary electron SEM and bright-field TEM techniques images are shown in Figure 5-3. Figure 5-3a displays the well-dispersed FGAg nanostructures, it can be found that the sample kept the graphene-layer like structure and no apparent agglomeration could be observed which can be attributed to the freeze-drying process. The subsequent reduction process also did not destroy the structure. At higher resolution, the uniform distribution of Ag nanoparticles can be found on the graphene layer structure (Figure 5-3b), as well as on the surface of CNT walls (Figure 5-3c). The particle size of the Ag nanoparticles that are coated on GNT is mainly ranged from 10-50 nm, while a large

particle around 100 nm can be observed in Figure 5-3c. In the TEM image of FGAg sample (Figure 5-3d), the Ag nanoparticles can be easily detected as high contrast (dark) features, while the graphene and CNTs are low contrast (light). In the insert image of Figure 5-3d, the selected area electron diffraction (SEAD) displays four ring patterns, which can be ascribed to the (111), (200), (220) and (311) planes of Ag, which is also consistent to the XRD results. In the HRTEM (Figure 5-3 e), an Ag nanoparticle can be observed attaching onto the surface of a MWCNT. The typical lattice fringe spacing is measured to be 0.24 nm which can be ascribed to the (111) crystal plane of Ag.

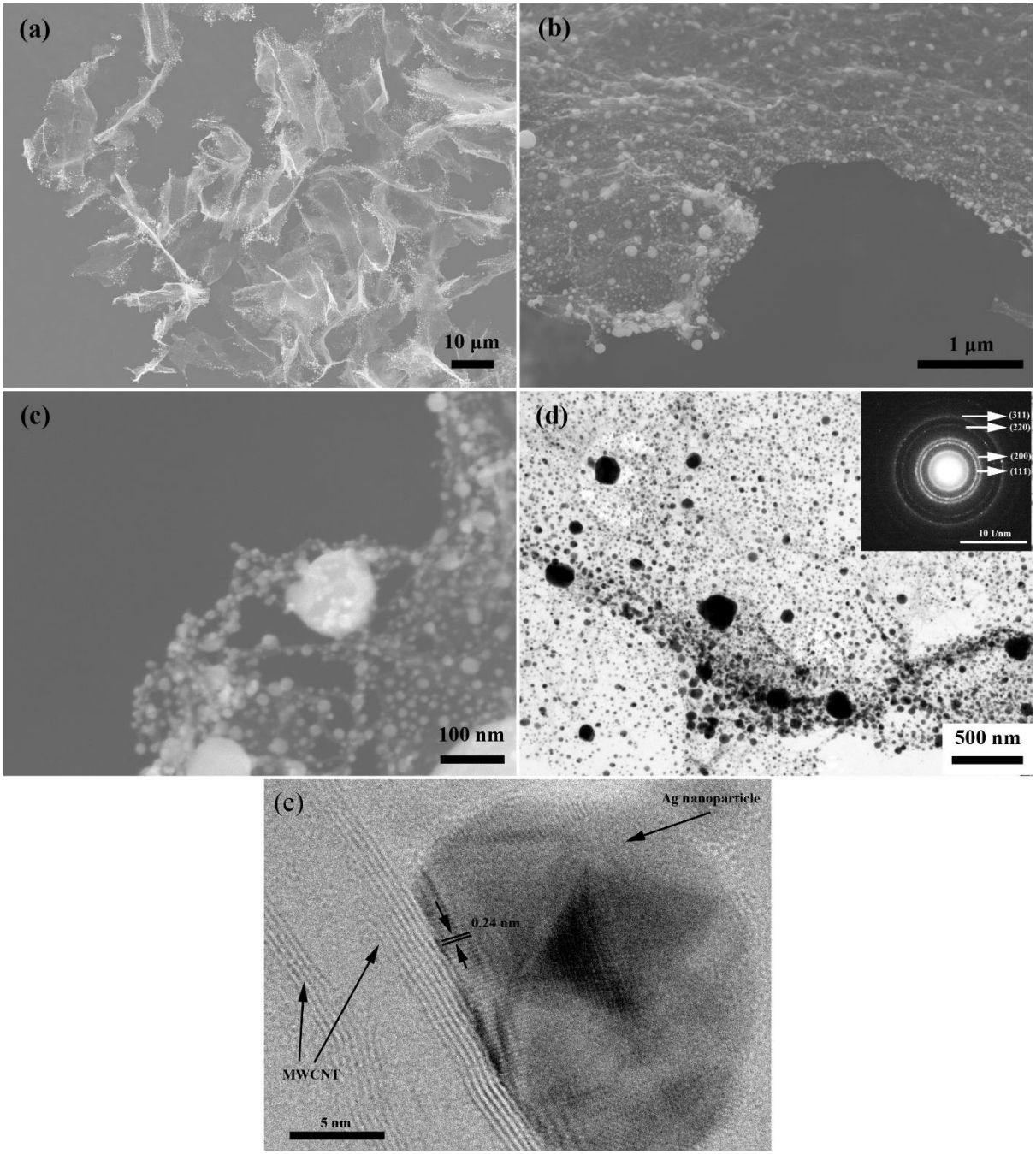

Figure 5-3 SEM images of FGAg sample (a, b and c, and TEM images (e and f) of FGAg sample, the insert image of Figure 2d is the electron diffraction (SEAD) patterns.

By way of reference, the SEM images of pure Ag and pure GNT samples are illustrated in Figure *5-4*. The pure Ag particles can be found agglomerated even after the similar freeze-drying method and subsequent reduction process (Figure *5-4* a and b). The obtained Ag particles also show a larger particle size that is over 100 nm when compared with the particles decorated on GNT hybrids. The morphology of pure GNT shows a similar well-dispersed

structure to FGAg sample. The graphene-layer-like structure can be observed and no obvious agglomeration is found (Figure *5-4*c), which is consistent with the previous results in chapter 4. In the high-resolution image (Figure *5-4*d), CNTs are found attached onto the surface of the graphene layer, which can be attributed to the π-π interaction between CNT walls and graphene.

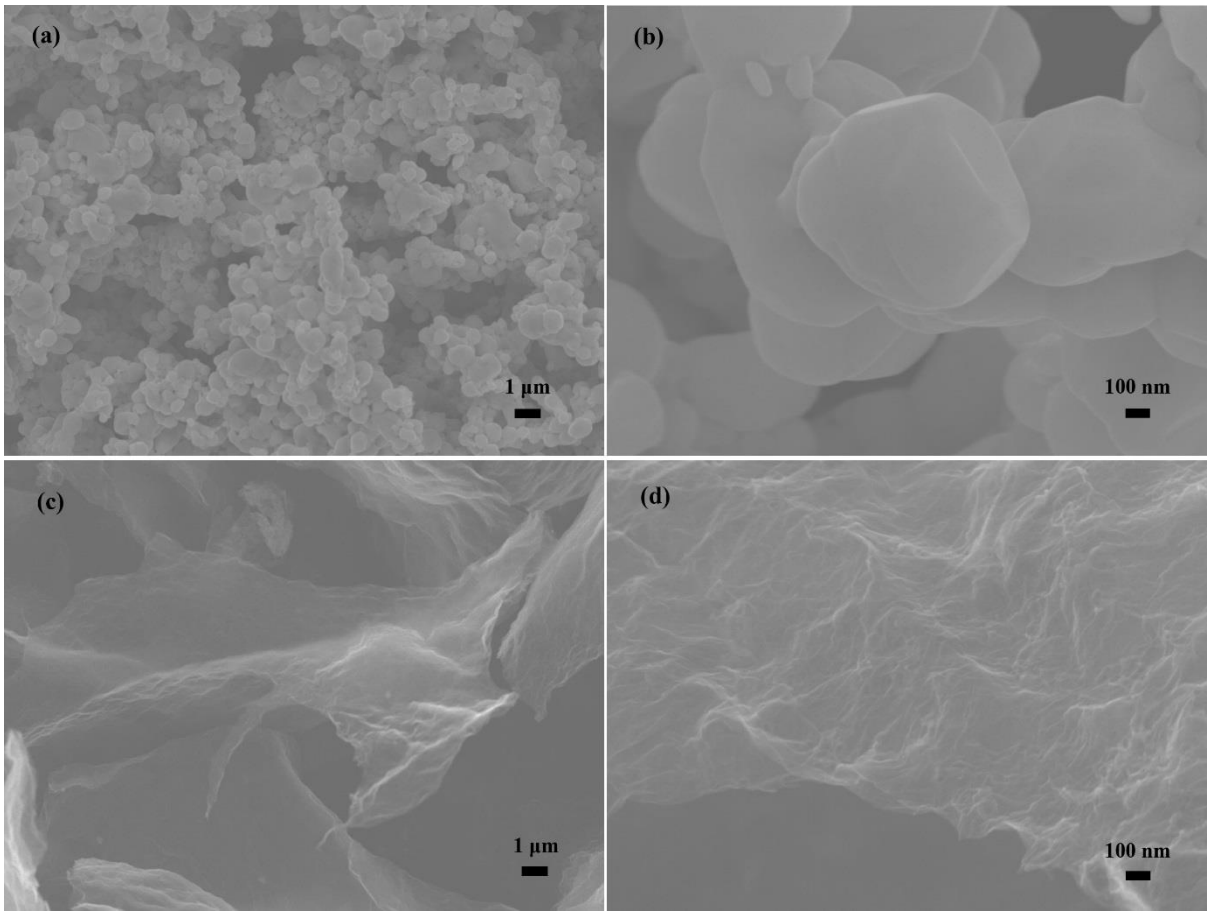

Figure 5-4 SEM images of pure Ag (a and b) and pure GNT (c and d) samples.

5.1.2 Characteristics of as-prepared pellets composites

After the preparation of PEEK-based composites, the XRD patterns of pure PEEK, GNT-PEEK composites, Ag-PEEK composites and FGAg-PEEK composites are displayed in Figure 5-5. For the XRD pattern of pure PEEK (Figure 5-5a), four obvious diffraction peaks locate at 18.8°, 20.8°, 22.8° and 28.9° match well with the diffraction peak of PEEK, corresponding to the (110), (111), (200), and (211) planes of PEEK. The GNT-PEEK composite (Figure 5-5b) displays a similar XRD pattern to pure PEEK as the pure GNT diffraction peak in Figure *5-1*a

is covered by the peak diffraction intensity. The XRD patterns of Ag-PEEK and FGAg-PEEK composites show diffraction peaks of Ag phase, which indicates the existence of Ag phase in both composites. The characteristic peaks of PEEK also can be observed in both composite samples.

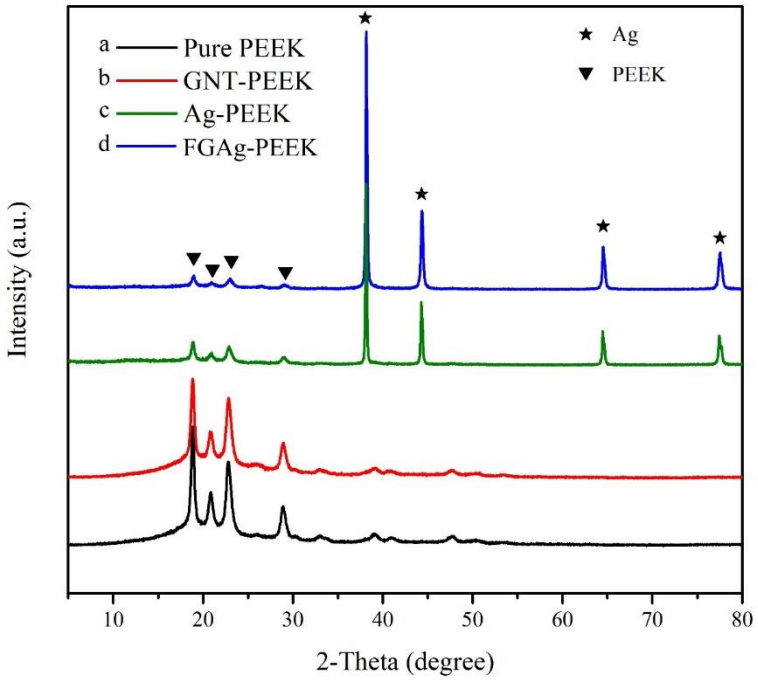

Figure 5-5 The XRD patterns of pure PEEK (a), GNT-PEEK (b), Ag-PEEK (c), and FGAg-PEEK (d).

The cross-section SEM images of the obtained composites are shown in Figure *5-6*. A typical SE image of pure PEEK is displayed in Figure *5-6*a, while similar morphology is recorded in the BSE (Figure *5-6*b). The SE and BSE images of PEEK-GNT composites are illustrated in Figure *5-6* c and d. A similar squamous-like morphology can be observed in both images and no obvious contrast could be detected as expected as they are both carbonaceous materials. The back-scattering image of Ag-PEEK composites (Figure *5-6*f) shows a clear contrast of Ag particles in the PEEK matrix. The pure Ag particles agglomerate and distribute randomly among the PEEK matrix. The secondary electron image of FGAg-PEEK composites (Figure *5-6*g) shows a rougher fracture surface compared to pure PEEK composites (Figure *5-6*a), which can be ascribed to the appearance of FGAg samples on the cross-section surface. The

distribution of FGAg samples can be observed uniformly dispersed in the PEEK matrix (Figure *5-6*h).

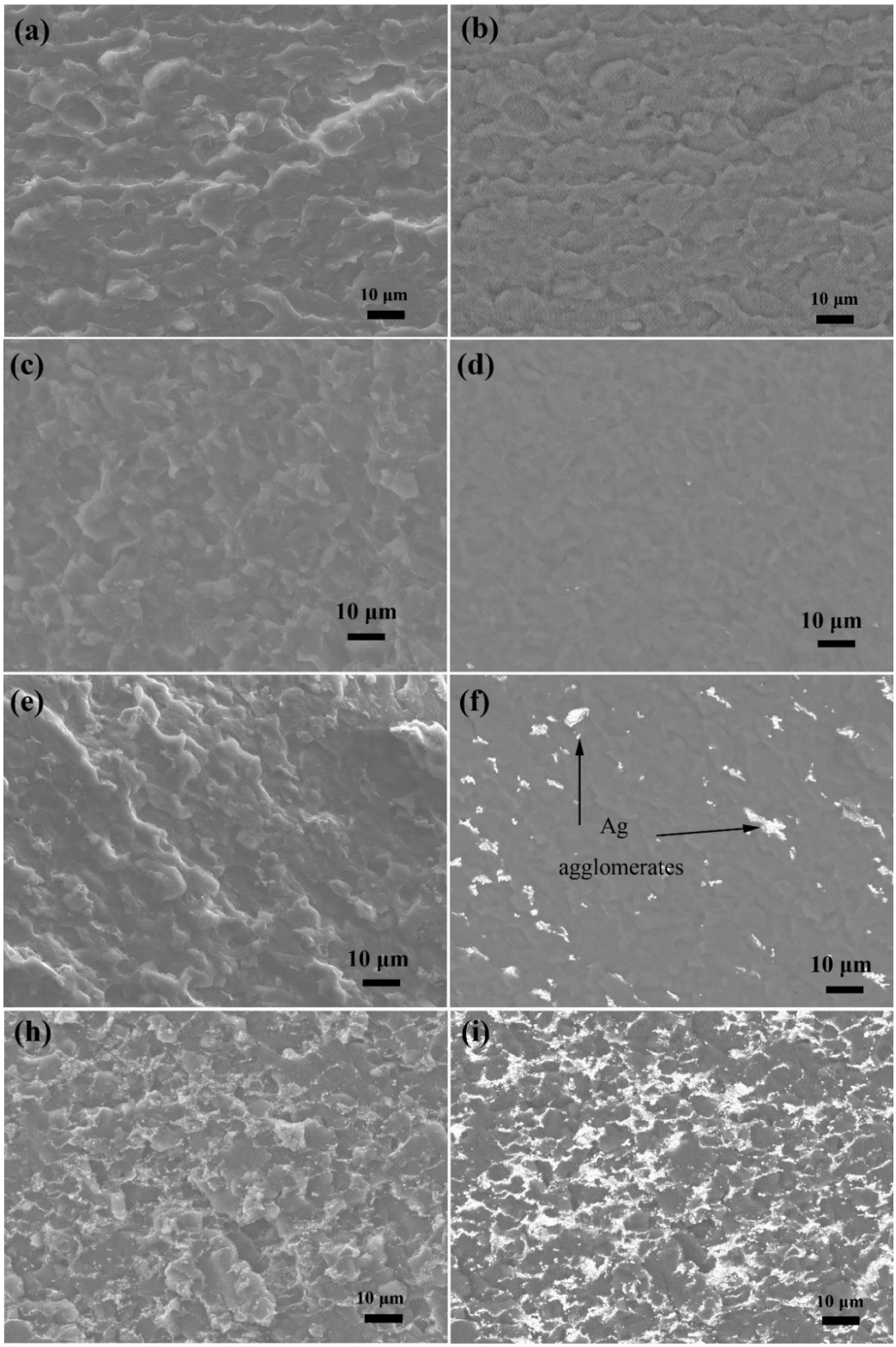

Figure 5-6 The SE SEM image of the pure PEEK (a), GNT-PEEK (c), Ag-PEEK (e) and FGAg-PEEK (g) composites and the BSE SEM image of the pure PEEK (b), GNT-PEEK (d), Ag-PEEK (f) and FGAg-PEEK (h).

To further investigate the morphology of FGAg samples in the PEEK matrix, TEM images are displayed in Figure *5-7*. In Figure *5-7*a, the FGAg sample can be observed embedded in the PEEK matrix, and the FGAg samples remain the graphene-layer-like structure as there is no clear void between the interface of FGAg and PEEK. No bend or agglomeration happened during composite preparation, which indicates that the whole pellet preparation process did not destroy the FGAg structure. In the high-resolution image (Figure *5-7*b), the ends of carbon nanotubes and Ag particles can be clearly observed. There is no obvious void that can be found between the PEEK and the FGAg sample. Thus, it can be concluded that there is a good interface between the FGAg samples and the PEEK matrix.

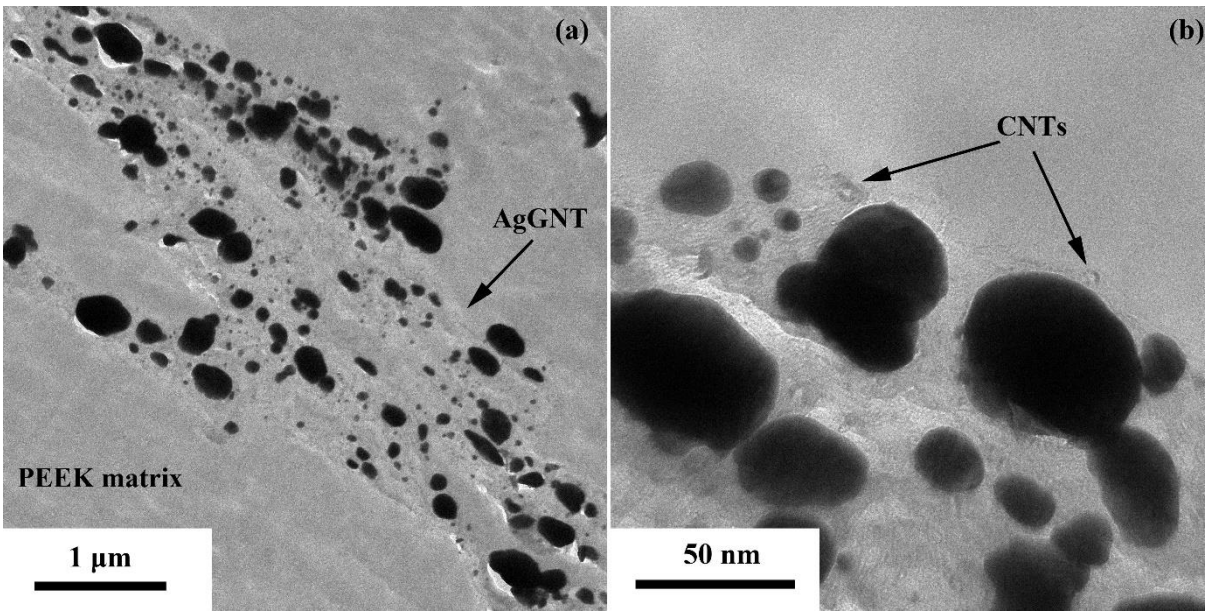

Figure 5-7 TEM images (a and b) of FGAg-PEEK composites.

5.1.3 Thermogravimetric and DSC analysis

Thermogravimetric analysis (TGA) results are shown in Figure *5-8*a. A rapid decomposition stage at around 590°C can be observed in all four composites. The residual weight percentage of pure PEEK sample is 52.4% after 800°C, which can be regarded as remaining ether and aromatic structures [167]. The remaining weight percentage of GNT-PEEK sample is 55.6%, and this value is 63.7% for Ag-PEEK sample and 68.7% for FGAg-PEEK sample, respectively.

In Figure *5-8*b, an obvious endothermic peak from DSC measurements can be detected in all four curves, indicating the melting of PEEK during ramping [101]. The heat of fusion (ΔH_f) during melting for all four samples are concluded in Table *5-1*. ΔH_f of pure PEEK is 41.18 J g^{-1}, and this value decreases to 38.44 J g^{-1} for GNT-PEEK composite, 32.48 J g^{-1} for AG-PEEK composite and 29.28 J g^{-1} for FGAg-PEEK composite. This decrease of ΔH_f can also be ascribed to the decrease of PEEK amount in different composites, and the calculated ratios from ΔH_f are listed in Table *5-1*. Comparing with the ΔH_f of pure PEEK, the calculated weight ratio of FGAg samples among the matrix is around 29 wt.%, which is close to the design value (3:7). The melting temperatures are all around 343-344°C, consistent with melting of PEEK at ca. 344°C.

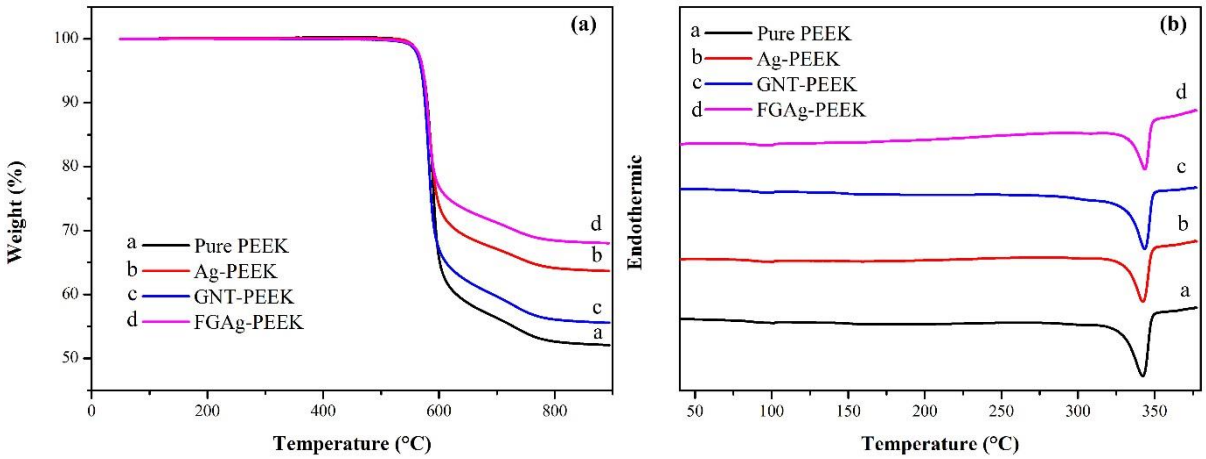

Figure 5-8 TGA (a) and DSC (b) curves of pure PEEK, GNT-PEEK, Ag-PEEK and FGAg-PEEK composites.

Table 5-1Heat of fusion and melt temperature of pure PEEK, GNT-PEEK, Ag-PEEK and FGAg-PEEK composites

Sample	ΔH_f (J g^{-1})	SE	Calculated percentage (%)	T_m (°C)	SE
Pure PEEK	41.18	±0.9	-	343.94	±0.3
Ag-PEEK	32.48	±1.5	78.8	343.21	±0.5
GNT-PEEK	38.44	±1.9	93.3	344.27	±0.4
FGAg-PEEK	29.28	±2.5	71.1	344.89	±0.5

5.1.4 Thermal and electrical conductivity

The thermal diffusivity and conductivity of all four PEEK based samples are detailed in Figure *5-9*. In Figure *5-9*a, it can be found that the thermal diffusivities increase after the addition of each filler. The FGAg-PEEK composite shows the highest value (0.255 mm^2 s^{-1}), while this figure is 0.194 mm^2 s^{-1} for Ag-PEEK and 0.195 mm^2 s^{-1} for GNT-PEEK, which are all higher than pure PEEK (0.180 mm^2 s^{-1}). The obtained thermal conductivities of all samples calculated by the equation $K = \alpha \times \rho \times C_p$ are shown in Figure *5-9*b. The pure PEEK sample exhibit a thermal conductivity of 0.229 W $m^{-1}K^{-1}$. After the addition of pure Ag particles, the thermal conductivity increases to 0.354 W $m^{-1}K^{-1}$, while the GNT-PEEK composite shows the thermal conductivity of 0.310 W $m^{-1}K^{-1}$, which is lower than the Ag-PEEK composites. The AgGNT-PEEK composite exhibits the best thermal conductivity (0.431 W $m^{-1}K^{-1}$) among the four samples.

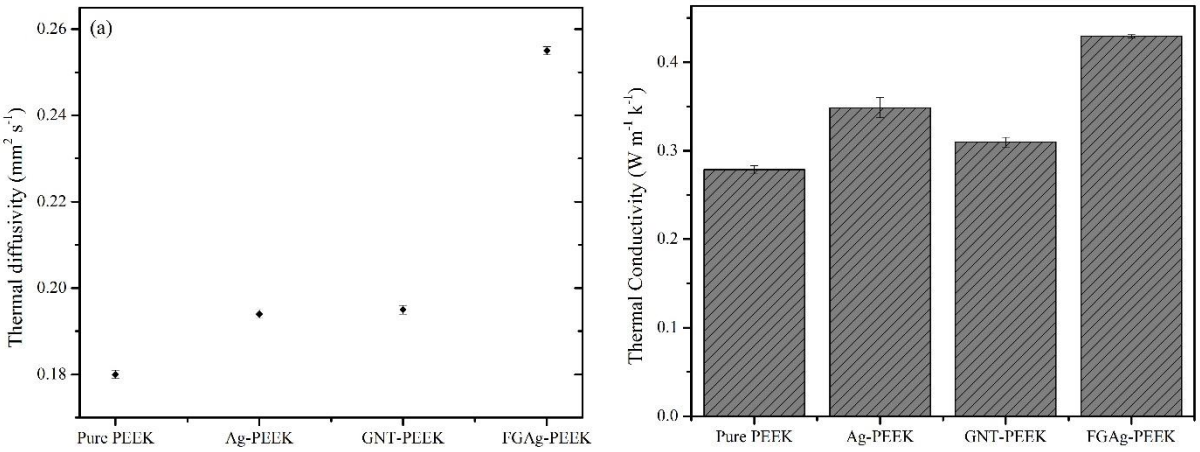

Figure 5-9 The thermal diffusivity (a) and thermal conductivity (b) of pure PEEK, Ag-PEEK, GNT-PEEK and FGAg-PEEK samples.

In addition to the thermal conductivity, the investigation of electrical conduction was performed using the ModuLab XM Materials Test System. The results are shown in Figure *5-10*. For the pure PEEK sample, the electrical resistance value of 5.8×10^{10} Ω m^{-1}. After the addition of 3.82 vol.% (24 wt.%) of Ag particles, there is a slight decrease in electrical

resistance to $3x10^{10}$ Ω m^{-1}. A dramatic decrease of the electrical conduction performances could be observed after the addition of fillers, from $5.8x10^{10}$ Ω m^{-1} of pure PEEK to $1.8x10^{2}$ and 11 Ω m^{-1}, respectively. After the addition of FGAg samples, the FGAg-PEEK sample displays an enhanced result even compared with GNT-PEEK composites, which rises to around 10 Ω m^{-1}. Thus, the FGAg-PEEK composites also exhibit the best electrical conductivity when compared with the rest three samples.

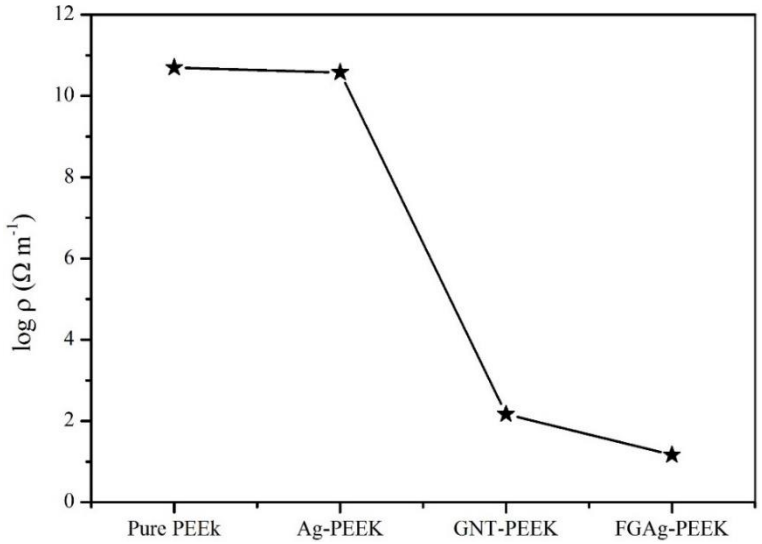

Figure 5-10 Electrical resistance of pure PEEK, Ag-PEEK, GNT-PEEK and FGAg-PEEK samples.

5.1.5 Thermal durability analysis

As an important index of the short-term heat resistance of PEEK, the thermal durability properties of all four PEEK-based composites were studied using thermal-mechanical analysis (TMA), and the results are displayed in Figure *5-11*. Under lower pressure of 10^{3} Pa (Figure *5-11*a), it can be found that pure PEEK displayed a sharp dimension change after 350℃, which is also consistent with the melting temperature obtained in DSC measurement. The dramatic decrease of measured thickness indicates that the pure PEEK pellet melted and spread under pressure. The Ag-PEEK composite also showed a decreasing trend after 350℃, indicating the melting and collapsing of the Ag-PEEK pellet. However, both the GNT-PEEK and FGAg-

PEEK pellets did not show obvious dimension decreases under10^3 Pa, indicating that the pellets of the GNT-PEEK and FGAg-PEEK both kept the initial structure rather than collapsing. When the pressure increases to 5x10^3 Pa (Figure *5-11*b), a similar result can be observed in all four samples when compared with 10^3 Pa, the structures of pure PEEK and Ag-PEEK composite collapsed after 350°C, while the GNT-PEEK and FGAg-PEEK still didn't show large dimension change. However, when the pressure increased to 10^4 Pa (Figure *5-11*c), the dimension change of GNT-PEEK composite decreased dramatically compared with Figure *5-11* a and b, indicating that the GNT-PEEK pellet also collapsed under higher pressure. Meanwhile, the dimension change of FGAg-PEEK pellet still kept its structure.

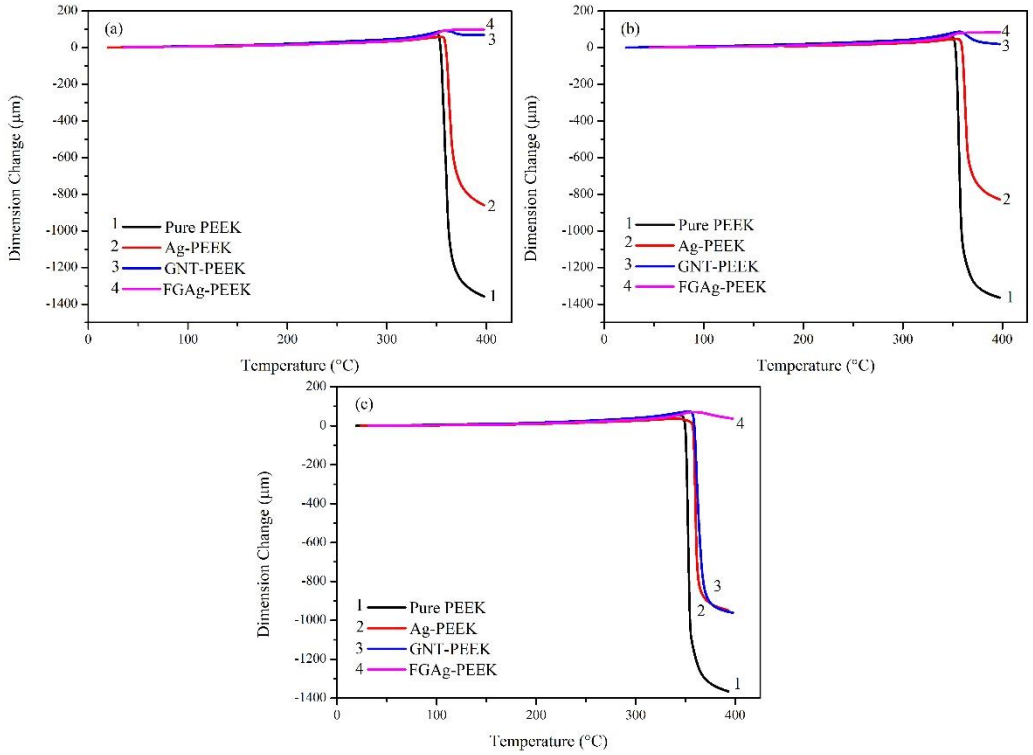

Figure 5-11 Dimension changes vs temperature of pure PEEK, Ag-PEEK, GNT-PEEK and FGAg-PEEK pellets under different pressure: (a) 10^3 Pa, (b) 5x10^3 Pa and (c) 10^4 Pa.

Figure 5-12 shows the pictures of all four pellets after 400°C annealing for 2 h. It can be found that the pure PEEK and Ag-PEEK samples both melted, and the structure of the pellets spread away. However, the GNT-PEEK sample still keeps the round pellet structure (12 mm diameter × 1.5 mm thickness pellet) and only a bubble can be observed on the surface, while the FGAg-

PEEK composite shows no visible change and keeps the entire pellet morphology. This phenomenon is consistent with the TWA result that the PEEK composites will exhibit better thermal durability after the addition of GNT.

Figure 5-12 Photo of pure PEEK, Ag-PEEK, GNT-PEEK and FGAgT-PEEK composites after 400℃ annealing.

5.2 Epoxy based composites and the property enhancements by the alignment of FGNi nanostructures

5.2.1 Structure and morphology characterization of FGNi samples

Figure *5-13*a displays the XRD patterns of the obtained FGNi and pure GNT samples. In the patterns of pure GNT sample, a broad peak ranging from 30-40 degrees can be detected as observed in section 4.3. Three strongest diffraction peaks at 44.5°, 51.8° and 76.4° 2θ in the FGNi samples indicate to the (111), (200) and (220) planes of metallic Ni (ICDD PDF No. 00-04-0850). As before, the broad peak, which is similar to the peak in the pure GNT sample, confirms the existence of carbon materials in the samples. Apart from the Ni and carbon signals, no other peaks are detected. The TGA was performed to investigate the composition of the as-prepared sample and the results are displayed in Figure *5-13*b. It can be found that there is almost no mass remaining in curve 1 (pure GNT sample) to up to 600°C. For the FGNi sample (curve 2), a slight weight increase, which is around 13.4% can be found when the temperature reaches 700°C. The mass increase can be attributed to the oxidation of Ni into NiO phase in the air atmosphere.

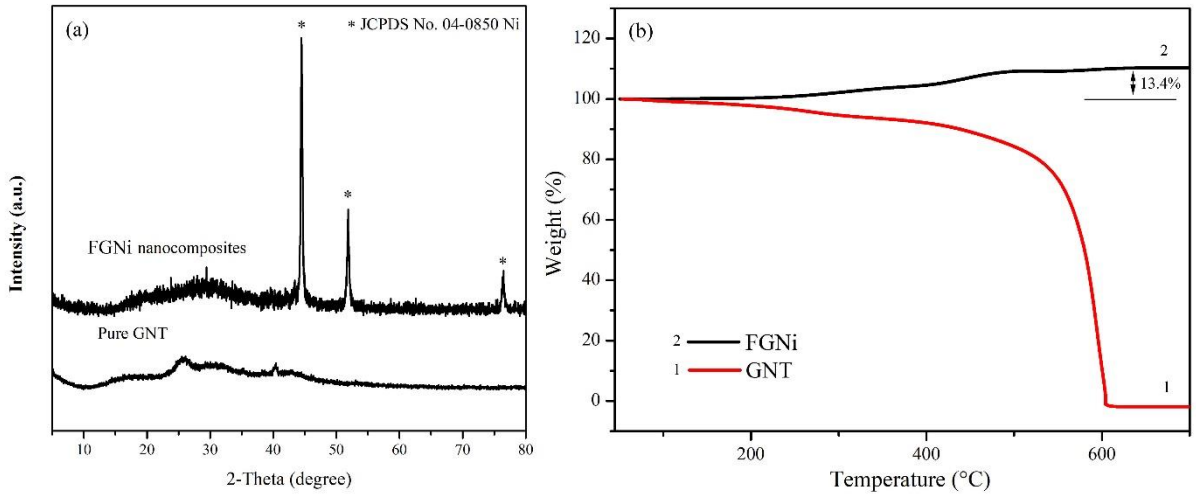

Figure 5-13 XRD patterns (a) and TGA results (b) of FGNi and pure GNT sample.

SEM and TEM images of FGNi sample are displayed in Figure *5-14*. In Figure *5-14*a, the graphene-layer-like structure indicates the good dispersion of the obtained products. Nanoparticles attributed to the Ni phase (ICDD PDF No. 00-04-0850) according to the XRD results are found uniformly coated on the graphene-layer structures. Under higher magnification (Figure *5-14*b), CNTs can be detected in the edge of the nanostructure and the Ni nanoparticles are also coated on them. From the SEM images, the Ni nanoparticles, which uniformly cover on both GO and CNTs, are mainly ranging from 20-50 nm, while several large Ni particles are around 100 nm among the obtained nanostructures. To further investigate the morphology and structure of the FGNi samples, TEM images are displayed in Figure *5-14* c and d. In Figure *5-14*c, the unique morphology of CNTs was observed on the edge of the nanostructure and between Ni nanoparticles and GO layer. The Ni nanoparticles are attached to the CNTs and the obtained typical lattice fringe spacing is measured to be 0.203 nm, which can be ascribed to the (111) crystal plane of Ni (ICDD PDF No. 00-04-0850), consistent with the XRD result.

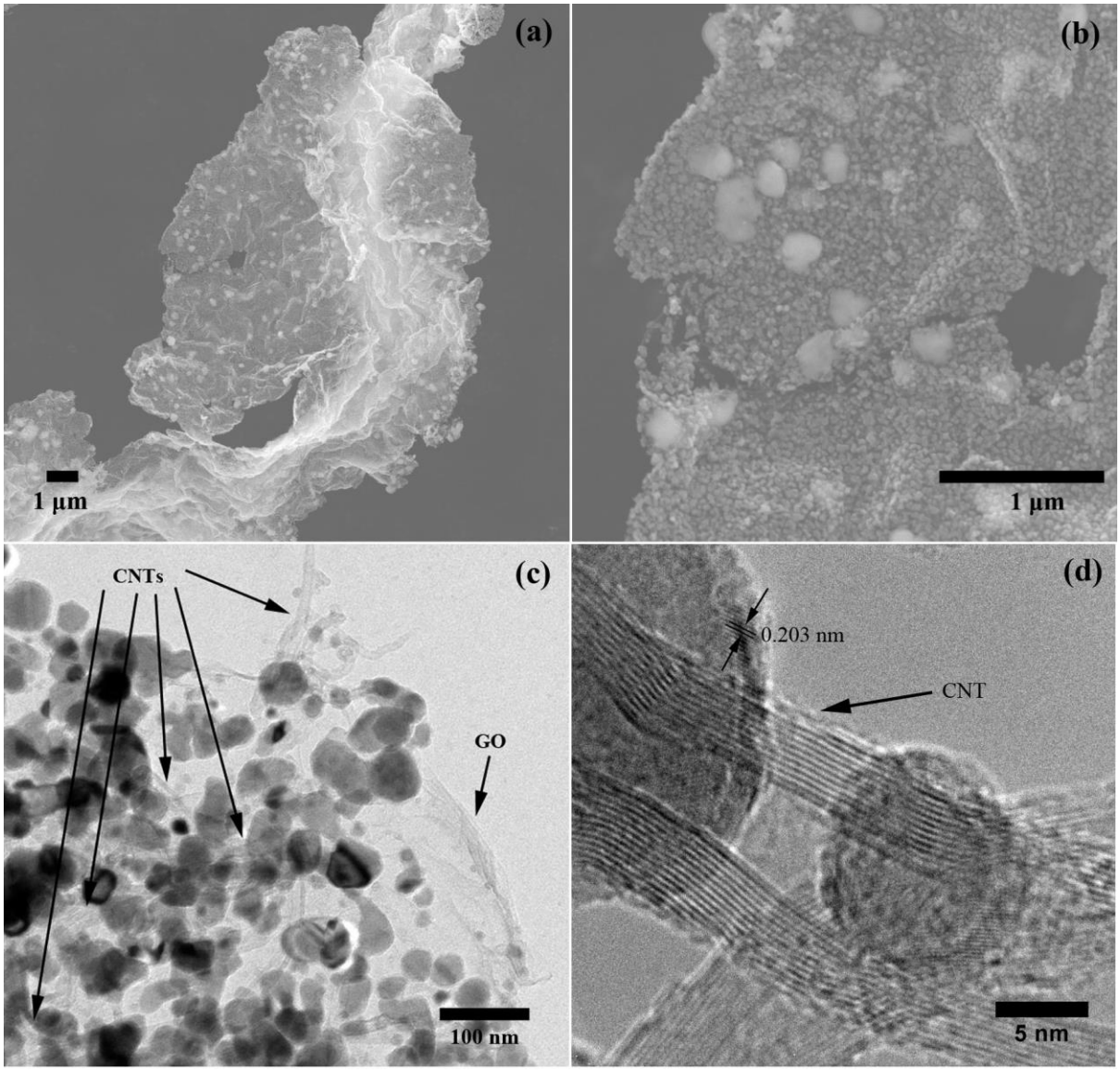

Figure 5-14 SEM (a and b) and TEM images (c and d) images of FGNi nanostructures.

5.2.2 Structural features and morphology of the epoxy based composites

To explore the effect of magnetic field assistance in the epoxy composites preparation process, XRD results of FGNi nanostructures reinforced epoxy composites and their reference samples are shown in Figure *5-15*a. From the XRD patterns of the pure epoxy, a wide and broad peak locating at around 10-30° is observed. This broad peak appears in all other FGNi reinforced epoxy composites, indicating the existence of epoxy in all composites. Meanwhile, the characteristic peaks of the (111), (200) and (220) planes of Ni (ICDD PDF No. 00-04-0850) at 44.5°, 51.8°, and 76.4° 2θ are observed in all FGNi reinforced composites as expected,

confirming the Ni phase in different composites. No obvious peaks of the GNT show in the diffraction patterns due to the intensity of GNT may not strong enough to be detected. The intensities of the epoxy peak are different between the magnetic assisted samples (3, 5, and 7) and the reference samples (2, 4, and 6). The intensities of all three reference samples show lower intensities of the epoxy component than their corresponding magnetic field-assisted samples (Figure *5-15*a). Thermogravimetric analysis (TGA) results are displayed in Figure *5-15*b. Although the distribution of FGNi fillers may differ among the epoxy matrices with and without the magnetic field, the weight ratio of FGNi fillers is the same in each ratio group of composites. Only the magnetic field-assisted composites were measured with the TGA. As can be seen in curve 1, the pure epoxy sample illustrates the continuous trend of weight loss until reaching 0, which means all the components were oxidised in the air after 600 °C. There are three clear weight decrease stages in the whole process. The first stage is located around 180-350°C, which indicates the first stage of thermal oxidative degradation of neat epoxy [168]. Two other sharp decreases can be observed at around 380 and 500°C, which is attributed to the further oxidation of the macromolecular chains and the release of other small molecular degradation products [168, 169]. The other three FGNi contained composites displayed similar TGA curves but with different mass remaining, which can be ascribed to different amounts of the NiO. The remaining mass of 10-FGNi-epoxy composites is around 12 wt.%, which is calculated as 9.4 wt.% of pure Ni, and this figure for 20- FGNi -epoxy and 30- FGNi-epoxy composites is 18.5 wt.% and 27.8 wt.%, respectively. This is consistent with the initial design of the composite preparation stage.

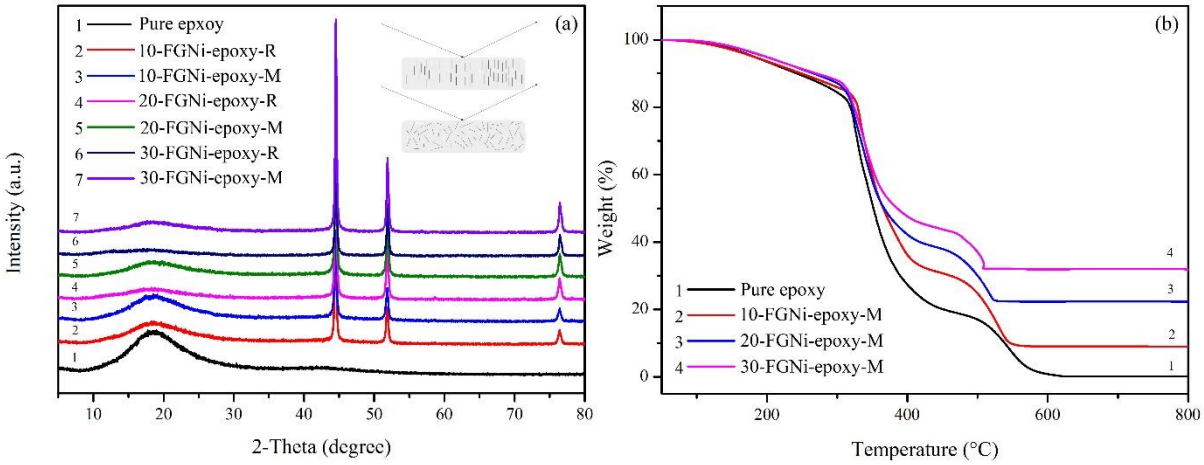

Figure 5-15 (a) XRD patterns and TGA (b) curves of the epoxy based composites.

SEM images of all the FGNi-epoxy composites are shown in Figure *5-16*. The FGNi nanostructures could be observed clearly among the epoxy matrix due to the different molar weights of Ni and epoxy contents. In the back-scattering images of 10-FGNi-epoxy composites (Figure *5-16* a and b), it can be found that the FGNi samples randomly distributed in the cross-section of the sample (Figure *5-16*a), while the FGNi fillers are aligned among the cross-section of the 10-FGNi-epoxy-M sample (Figure *5-16*b). As the magnetic field introduced during the composite preparation process was vertical to the pellets, the FGNi fillers show dispersion in the magnetic field direction. Both the 10-FGNi-epoxy-R and M composites also show large spaces without FGNi fillers among the cross-section, which indicates that 10 wt.% of FGNi fillers could not fully fill the epoxy matrix. With the increase of the filler ratio (Figure *5-16* c and d), the FGNi fillers are still randomly dispersed in the epoxy matrix in the reference sample without obvious agglomeration (Figure *5-16*c). With the assistance of the magnetic field (Figure *5-16*d), the FGNi fillers demonstrate uniform and aligned distribution among the epoxy matrix. Similar to the 10 wt.% sample, the FGNi fillers are also in the magnetic field direction, but fewer empty spaces could be detected in the 20 wt.% composites. In the 30 wt.% FGNi-epoxy composites (Figure *5-16* e and f), similar distribution trends of FGNi fillers can be observed in both reference and magnetic field assistance composites compared with 10 wt.% and 20 wt.% samples, but with denser filler distribution in the epoxy matrix.

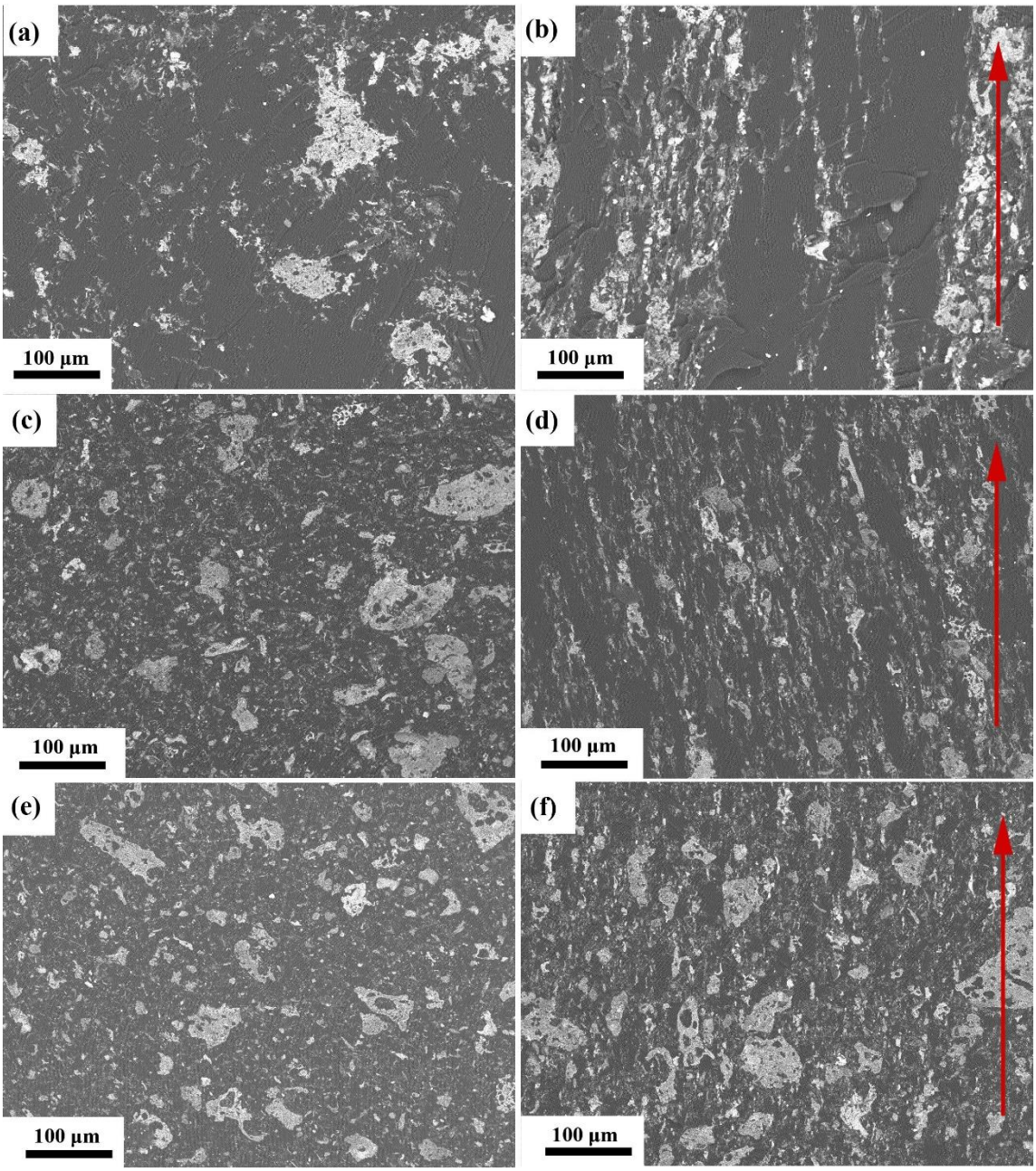

Figure 5-16 The back-scattering SEM images of the 10-FGNi-epoxy-R (a), 10- FGNi-epoxy-M (b), 20-FGNi-epoxy-R (c), 20- FGNi-epoxy-M (d), 30- FGNi-epoxy-R (e) and 30- FGNi-epoxy-M (f) composites, the red arrow indicates the direction of the magnetic field.

TEM images of the 10-FGNi-epoxy-M sample are displayed in Figure *5-17*. In Figure *5-17*a, the FGNi nanostructures can be observed embedded in the epoxy matrix, and the FGNi samples still keep the graphene-layer-like structure as there is no clear void between the interface of FGNi and PEEK. No bend or agglomeration happened during composite preparation. There is a straight scratch across the image, which can be ascribed to the TEM sample preparation. In

the high-resolution image (Figure *5-17*b), the CNTs and Ni nanoparticles can be observed. There is no obvious void detected between the epoxy and the FGNi nanostructures, indicating a good interface between the FGNi samples and the epoxy matrix.

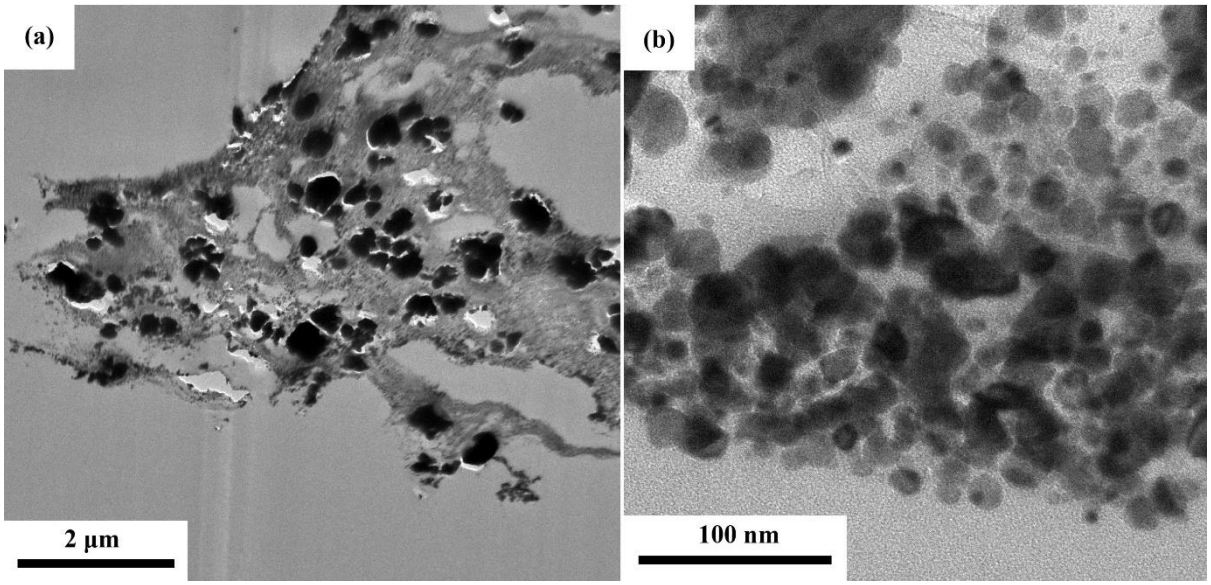

Figure 5-17 TEM images of FGNi-epoxy composites at different magnification (a and b).

5.2.3 Thermal conductivity and the coefficient of thermal expansion

To investigate the thermal management properties of the FGNi-epoxy composites, the measurements of the thermal conductivity and coefficient of thermal expansion were carried out. Due to the requirement of the sample holder, the measurement direction is parallel to the aligned direction of FGNi fillers in the FGNi-epoxy-M sample, and the relevant results are displayed in Figure *5-18*. In Figure *5-18*a, it can be found that the thermal diffusivities increased with the addition of FGNi fillers. The aligned samples show better thermal diffusivities in higher concentrations. Specifically, the thermal diffusivity of pure epoxy resin is 0.107 $mm^2\ s^{-1}$. This value increases to 0.119 $mm^2\ s^{-1}$ in 10-FGNi-epoxy-R composites, indicating that the addition of FGNi fillers further increases the thermal conduction property of the epoxy matrix. The 10-FGNi-epoxy-M composites show improved thermal diffusivity (0.141 $mm^2\ s^{-1}$) with magnetic field assistance. The thermal diffusivities of 20-FGNi-epoxy-R

and 30-FGNi-epoxy-R composites are 0.138 and 0.154 $mm^2 s^{-1}$, respectively, while the values for 20-FGNi-epoxy-M and 30-FGNi-epoxy-M composites are 0.159 and 0.184 $mm^2 s^{-1}$. The thermal conductivities of all the epoxy-based composites are shown in Figure *5-18*b. The pure epoxy sample displays a thermal conductivity of around 0.173 W $m^{-1}K^{-1}$. After the addition of FGNi fillers, the thermal conductivity increases, and this value increases to 0.217 W $m^{-1}K^{-1}$ for 10-FGNi-epoxy-R sample and 0.242 W $m^{-1}K^{-1}$ for 10-FGNi-epoxy-M sample. When the weight ratio reached 20 wt.%, the 20-FGNi-epoxy-R sample shows the thermal conductivity of 0.271 W $m^{-1}K^{-1}$, and this value is 0.326 W $m^{-1}K^{-1}$ for 20-FGNi-epoxy-M sample. For the 30-FGNi-epoxy composites, the obtained thermal conductivities demonstrate further increase and reach 0.362 W $m^{-1}K^{-1}$ for 30- FGNi-epoxy-R and 0.462 W $m^{-1}K^{-1}$ for 30-FGNi-epoxy-M, respectively.

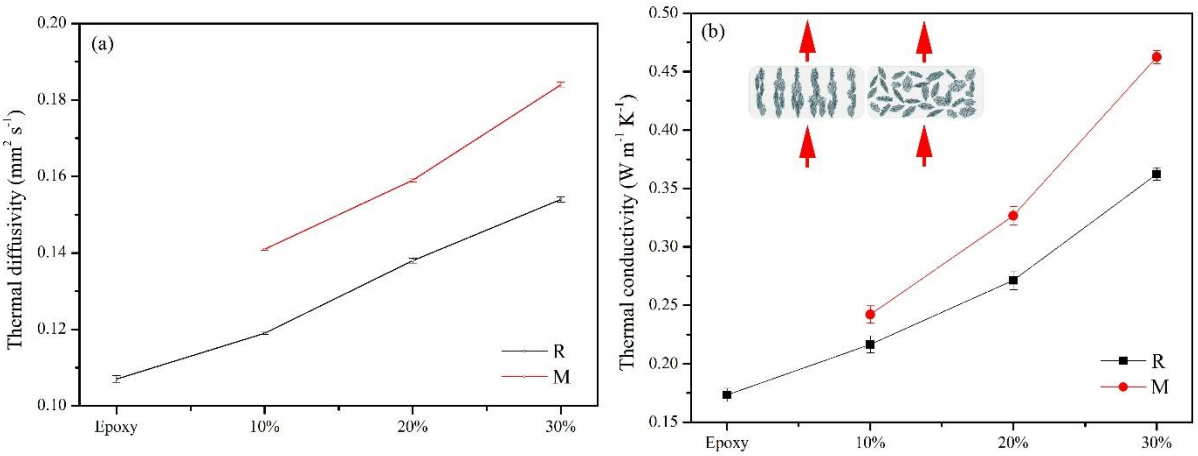

Figure 5-18 Thermal diffusivities (a) and thermal conductivities (b) of as-prepared epoxy-based samples (the measured direction is parallel to the aligned direction of FGNi fillers in FGNi-epoxy-M sample).

The coefficients of thermal expansion of the FGNi-epoxy composites below the glass transition temperature (T_g) are displayed in Figure *5-19*. It can be found that the pure epoxy sample (blue) shows a CTE of around 13.45 μm $m^{-1}°C^{-1}$ and the FGNi-epoxy reference samples demonstrate similar CTE when compared with the pure epoxy sample. However, the FGNi-epoxy-M composites display obvious enhancement with the increase of filler ratios. The obtained CTE

of 10-FGNi-epoxy-M composites is 9.15 μm $m^{-1}°C^{-1}$ which is lower than the 10-FGNi-epoxy-R sample and even lower than the 30-FGNi-epoxy-R sample. With the increase of FGNi contents, the CTE of 20-FGNi-epoxy-M composites decreases to 8.74 μm $m^{-1}°C^{-1}$, and this value further drops to 7.87 μm $m^{-1}°C^{-1}$ for the 30-FGNi-epoxy-M sample.

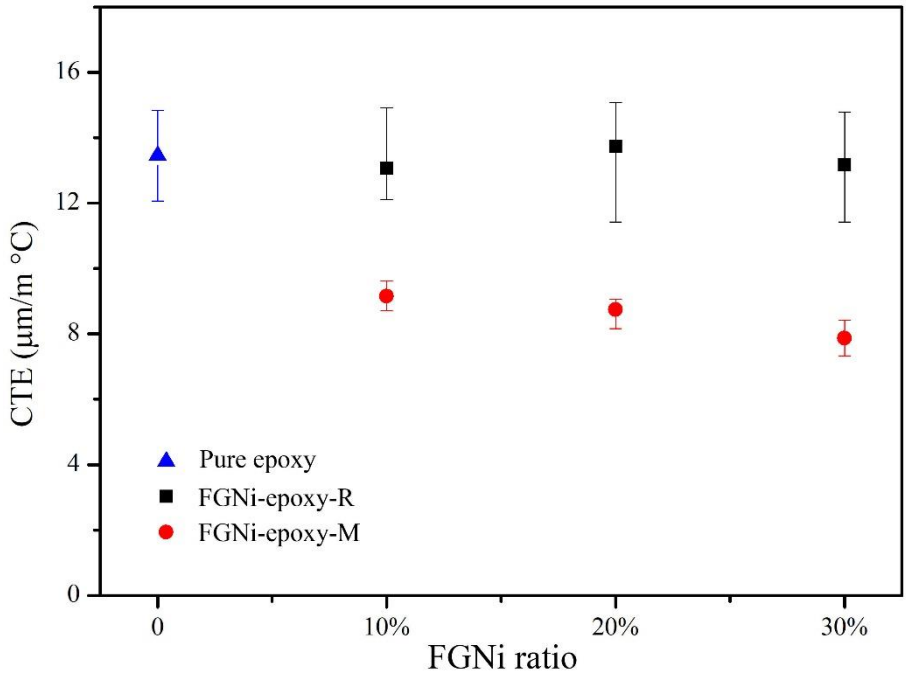

Figure 5-19 CTE values of the pure epoxy resin and FGNi-epoxy composites with different ratio below the T_g range (the measured direction is parallel to the aligned direction of FGNi fillers in FGNi-epoxy-M sample).

5.2.4 Electrical conduction performance

Figure *5-20* shows the electrical conduction performances of obtained composites, the measured direction is parallel to the aligned direction of FGNi fillers in FGNi-epoxy-M sample. Similar to the thermal conductivity, the electrical resistance also shows a decreasing trend with filler amounts grow. For the pure epoxy sample, the electrical resistance is ca. 10^{10} Ω m^{-1}, indicating poor electrical conduction ability of the pure epoxy sample. A minor increase of the obtained value, which is around 2×10^{9} Ω m^{-1} can be found in the 10-FGNi-epoxy-R sample, and this value shows a further increase to 1.6×10^{8} Ω m^{-1} in 10-FGNi-epoxy-M sample. With the further increase of the filler amount, the electrical conduction performance continues to

grow from 7.1×10^{7} Ω m^{-1} of 20-FGNi-epoxy-R sample to 5.3×10^{6} Ω m^{-1} of 20-FGNi-epoxy-M sample and a further improvement from 6.2×10^{6} Ω m^{-1} of 30-FGNi-epoxy-R sample to 4.6×10^{5} Ω m^{-1} of 30-FGNi-epoxy-M sample.

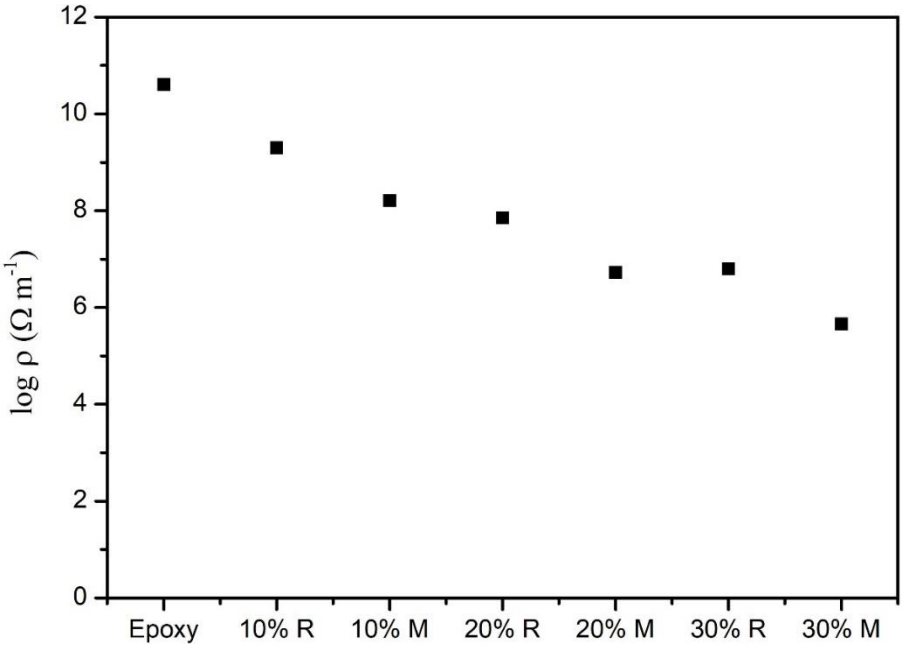

Figure 5-20 Electrical resistance of pure epoxy and FGNi-epoxy samples with different ratios and distribution (the measured direction is parallel to the aligned direction of FGNi fillers in FGNi-epoxy-M sample).

5.3 Discussion

5.3.1 The effect of FGAg nanostructures as fillers in PEEK composites

XRD results (Figure *5-1*a) confirmed the existence of silver and GNT parts in the FGAg products, and XPS results (Figure *5-1*b-d) have further confirmed it. Meanwhile, the existence of such oxygen contained peaks in the XPS results (Figure *5-1*c and d) demonstrated the attachment of the functional groups (like carboxyl and hydroxyl groups) on the surface of CNTs and GOs. These functional groups are believed not only to prevent the agglomeration between CNTs and GOs due to the electrostatic repulsion by the negative charge of each other [16] but also to provide abundant sites for metal ions nucleation. The appearance of the defect-containing sp2 hybridized C (Figure *5-1*c and d) should come from the sp2 hybridized C due

to the high-temperature reduction process in the preparation procedures [154, 155]. Combining this with the SEM results (Figure 5-3 and Figure *5-4*), the Ag nanoparticles were obtained uniformly decorated on the well-dispersed GNT nanostructures, while the pure Ag sample, which was also obtained from the same methods except for the addition of GNT, shows larger particle sizes as well as the obvious agglomeration trend between particles. Thus, it can be concluded that the graphene-layer-like GNT nanostructure was successfully prepared through the freeze-drying method, and the Ag nanoparticles were also uniformly coated on the surface of GNTs, and the addition of GNT effectively prevent the agglomerating of Ag particles and restrict the growth of Ag particles. The unique well-dispersed nanostructure shows great potential as the promising fillers, which can also function as bridges amongst the matrix.

After adding each product as filler into the PEEK matrix, the XRD confirmed the success of the preparation of all PEEK based composites (Figure 5-5). The SEM images (Figure *5-6*) of all four samples clearly displayed the distribution of fillers, especially the Ag and FGAg fillers due to their obvious contrast with the PEEK matrix (Figure *5-6* f and i). Although the same mass of Ag was added into the PEEK matrix, the FGAg-PEEK composites displayed a more uniform distribution of the FGAg samples, while the pure Ag agglomerates were randomly dispersed among the PEEK matrix. The TEM images (Figure *5-7*) of the FGAg nanostructures also showed that the graphene-layer-like structure became embedded in the PEEK matrix and no obvious void can be found between the PEEK and the FGAg samples. Therefore, the well-dispersed GNT makes the Ag nanoparticles uniformly and widely distributed and forms a 3D network in the PEEK matrix, and the well-dispersed 3D network structures of FGAg nanostructures can be regarded as a bridge which provides the continuous pathways of either heat or electrons and hence exhibits the good conductivity performance.

Figure *5-9* illustrates the thermal conductivities of all four samples, and the FGAg-PEEK

composites exhibited the best thermal conductivity when compared with the pure PEEK, Ag-PPEK, and GNT-PEEK composites. The FGAg-PEEK composite exhibits the best thermal conductivity (0.370 W $m^{-1}K^{-1}$, which is almost 160% of the pure PEEK) among all the four samples despite the fact it has the same mass of fillers when compared with Ag-PEEK and GNT-PEEK composites. Thus, combined with the SEM results of the PEEK based composites (Figure *5-6*), it can be concluded that a well-dispersed 3D network structure of FGAg nanostructures was obtained among the PEEK matrix, and the best thermal conductivity performance can be ascribed to the 3D network which provided the continuous pathways of heat and hence exhibits good heat transfer among the composites. In addition, the Ag-PEEK composites show slightly higher thermal conductivity than the GNT-PEEK composites (Figure *5-9*b), which indicated that the Ag-PEEK composites still display better thermal performance than the GNT-PEEK cones although the Ag particles were randomly distributed in the PEEK matrix (Figure *5-6*f). This can be attributed to the original high thermal conduction of Ag. By combining the Ag and GNT, the perfect thermal conduction of Ag can be brought together with the 3D network that largely increased the thermal conductivity in FGAg-PEEK composites (Figure *5-9*b).

As shown in Figure *5-10*, the electrical resistance of Ag-PEEK shows a limited increase compared with pure PEEK. In the back-scattering SEM image of the Ag-PEEK sample (Figure *5-6*f), the Ag particle agglomerates randomly dispersed among the PEEK matrix, and there is no connection between each other. Thus, these Ag particles can be regarded as isolated islands in the PEEK matrix. According to Riviere's research [170], it was shown that the electrical resistance of PEEK-Ag nanoparticle composites could be significantly improved with over 10.8 vol.% of Ag nanoparticles (from 10^{14} to ca. 1 Ω m^{-1}), and such an increase can be ascribed to the large amount of Ag particles that achieved the electrical percolation threshold in the PEEK matrix. Although Ag having good electrical conductivity, the Ag particles cannot exhibit

a good connection in the PEEK matrix under the ratio (3.82 vol.%) in this research. In the GNT-PEEK composites, the electrical resistance shows a significant increase of two orders of magnitudes with only 4.04 vol.% (6 wt.%) of GNTs. Mphiuddin's research also showed that a percolation threshold always occurred between 3 wt.% - 4 wt.% in the carbon material (i.e., CNTs) [171], but the best result was still 10^3 Ω $m^{-1,}$ which is still lower than the obtained GNT-PEEK composites in our research ($1.8x10^2$ Ω m^{-1}). A similar phenomenon has been reported in the graphene-PEEK system, the graphene-PEEK showed a sharp electrical conduction enhancement from around 10^{12} (2 wt.%) to 10^3 (3 wt.%) Ω m^{-1} and the authors also ascribed this improvement to a conductive network formed by graphene [85]. Meanwhile, the FGAg-PEEK sample displays further enhancement of electrical resistance to 10 Ω m^{-1}. Further improvement could be ascribed to the introduction of Ag nanoparticles, which were uniformly coated on the GNT structure.

Table *5-2* presents the comparison of thermal and electrical performances between the FGAg-PEEK composites and some reported results. Although little research reported both the thermal and electrical conduction performances with PEEK based composites, it can still be found that the FGAg-PEEK composites displayed improved thermal and electrical conduction performances compared with either CNT or graphene reinforced PEEK composites [85, 86, 101, 171-174]. Because of the isolated distribution of Ag nanoparticles, the Ag NP-PEEK composites showed poor performances [102], which is similar to the Ag-PEEK composites in this research. Therefore, due to the 3D network formed by the GNT nanostructure, although the FGAg-PEEK and Ag-PEEK composites have the same weight percentage of Ag, the combination of Ag and GNT largely decreases the percolation threshold and hence exhibit perfect thermal and electrical conduction performances.

Table 5-2 Comparison of thermal and electrical conduction performances between AgGNT-PEEK composites and previous results.

Sample	Thermal conductivity ($W\ m^{-1}K^{-1}$)	Electrical resistance ($\Omega\ m^{-1}$)	Reference
AgGNT-PEEK	0.43	10	This work
GO in PEEK	0.35	--	[86]
CNT-PEEK	--	10^4	[171]
MWCNT-PEEK	--	6×10^2	[173]
CNT-PEEK	--	9×10^3	[172]
PEEK/graphene/carbon fibre	0.38	--	[100]
Graphene-PEEK	--	10^4	[85]
Carbon fibre-PEEK	0.21	10^6	[101]
Graphene/carbon loofah/PEEK	--	10^2	[174]
Ag NPs-PEEK	0.30	10^{13}	[102]

Although the DSC results demonstrate that all four PEEK composites displayed an obvious endothermic peak in each curve (Figure *5-8*b), the thermal durability of each sample varies. The FGAg-PEEK composite shows the best performance among the four samples. With the increase of applied load on the pellet, the FGAg-PEEK sample always demonstrates the best thermal durability even above the melting temperature of PEEK, indicating an improved deflection temperature under loads. The pellet structure of the rest three composites collapsed more or less with the increase of applied loads, which further confirmed the perfect heat-resistance of FGAg-PEEK sample. Meanwhile, Figure 5-12 also shows all four samples after 400°C annealings and the FGAg-PEEK sample still displays the best thermal durability. As an important index of short-term heat resistance, the FGAg-PEEK sample displayed improved deflection temperature under loads. Thus, it is believed that the uniform 3D network acted as a

skeleton among the PEEK matrix, which prevents the PEEK structure spread away when above the melting temperature, while the increased thermal conductivity of Ag-PEEK composites also allows this superior heat dissipation than the other three composites.

The Ag nanoparticles decorated GNT nanostructures have been successfully prepared through the MLM method with the subsequent freeze-drying method and reduction process. They also function as the reinforcement in the PEEK matrix. The results showed that the FGAg-PEEK composites displayed excellent electrical and thermal conductivity as well as thermal durability even above the melting temperature of pure PEEK, especially compared with the pure PEEK, Ag or GNT-PEEK composites. As shown in Figure 5-21, owing to the 3D structures of FGAg nanostructures generated among the PEEK matrix, the 3D structures played as bridges that connected the Ag nanoparticles and provided paths and channels that are beneficial to the conduction of electrons and heat. The obtained pure Ag particles prepared through the same process were randomly distributed among the PEEK matrix. Thus, the thermal and electrical conductivity of Ag-PEEK composites is also lower than FGAg-PEEK composites as the Ag particles were like isolated islands in the PEEK matrix and cannot effectively enhance the PEEK materials. The Ag-GNT 3D structures can be also regarded as a skeleton in the PEEK matrix, which prevented the melting of the PEEK matrix.

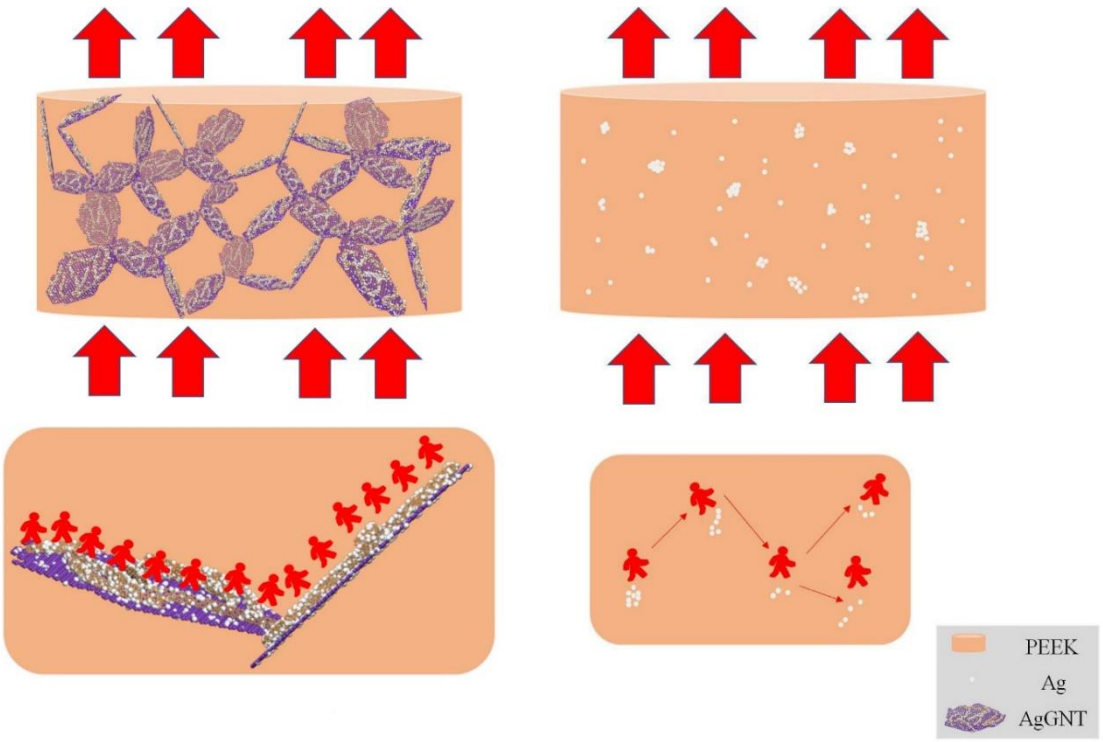

Figure 5-21 Schematic of structure and the conduction performances in AgGNT-PEEK and Ag-PEEK composites.

5.3.2 The effects of the aligned distribution of FGNi nanostructures in epoxy composites

XRD and TGA results shown in Figure *5-13* confirmed the constitution of the FGNi sample, which contains both GNT (a broad peak connected to the carbon content [166]) and Ni (ICDD PDF No. 00-04-0850) components. In the TGA result (Figure *5-13*b), the obtained weight increase of FGNi samples is 13.5 wt.%. As the remaining component after 700°C is NiO and the burning of carbon content in the sample, the calculated weight percentage of carbon content is 11.5 wt.%. This is consistent with the initially designed proportion (Ni : C as 9:1). After that, SEM and TEM were introduced to explore the morphologies of the as-prepared sample. The obtained images showed that the graphene-like-structure was prepared and the Ni nanoparticles are uniformly decorated on the GNT nanostructure through the MLM process combined with the freeze-drying and subsequent reduction methods. In the HRTEM image (Figure *5-14*d), the multi-wall structures of CNTs are observed and the number of walls is around 10. The Ni

nanoparticles are attached to the CNTs and the obtained typical lattice fringe spacing is measured to be 0.203 nm, which can be ascribed to the (111) crystal plane of Ni (ICDD PDF No. 00-04-0850), and this is also consistent with the XRD result above. Therefore, it can be concluded that a well-dispersed GNT nanostructure decorated by the uniform distribution of Ni nanoparticles on them was successfully obtained.

As shown in Figure *5-15*, the XRD results confirmed the adding of FGNi in the epoxy matrix. It is interesting to notice that intensities of the epoxy peak are different between the magnetic assisted samples (3, 5 and 7) and references samples (2, 4 and 6), and all three reference samples show lower intensities of the epoxy component than their corresponding magnetic field-assisted samples (2 to 3, 4 to 5 and 6 to 7). One possible reason for the different intensities between magnetic assistant and reference samples could be the distribution of the fillers in the epoxy matrix. As shown in Figure *5-22*, regular distribution of FGNi fillers has been obtained in magnetic field-assisted samples, which results in less contact with the X-ray, while the random distribution of the FGNi fillers in the reference sample would make the FGNi sample have more surfaces contacting with X-ray which indeed leads to higher intensity of Ni phase as well as the lower intensity of epoxy. SEM images of the FGNi-epoxy composites (Figure *5-16*) also confirm the FGNi nanostructures could be uniformly dispersed in the epoxy matrix without obvious agglomeration, and display alignment with the help of an external magnetic field alongside the magnetic field direction. Table *5-3* concluded the TGA results of epoxy-based composites, it can be found that the obtained ratio between FGNi and epoxy supports the initial design.

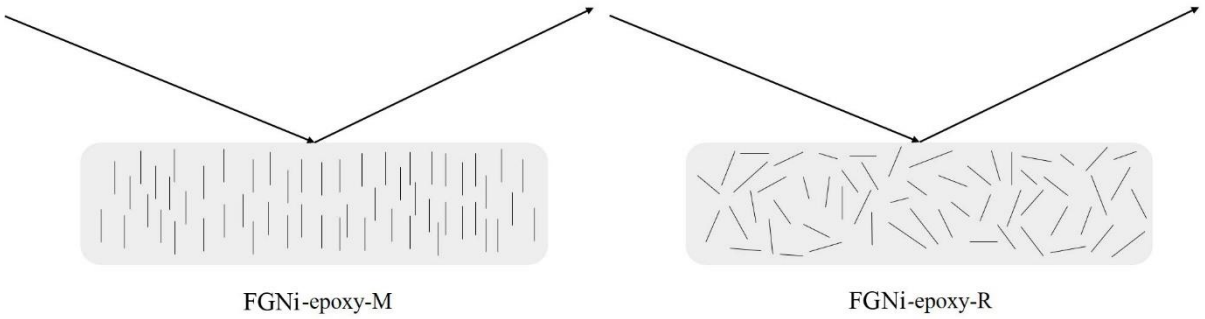

Figure 5-22 Schematic of the X-ray reaction with FGNi-epoxy M and R composites.

Table 5-3 TGA results of the epoxy-based composites.

Sample name	Remaining wt.%	Calculated wt.%	Preparation wt.%
Pure epoxy	0	-	-
10-FGNi-epoxy-M	12.1	9.4	10.0
20-FGNi-epoxy-M	23.7	18.5	20.0
30-FGNi-epoxy-M	35.6	27.8	30.0

Figure *5-18* shows the thermal diffusivity and conductivity of all epoxy-based samples, and the 30-FGNi-epoxy-M composite exhibites the best thermal performance compared with other samples. The pure epoxy sample shows the thermal conductivity of around 0.173 W $m^{-1}K^{-1}$, and the thermal conductivity of the rest of the FGNi-epoxy-R composites increases as the amount of FGNi does from 0.217 W $m^{-1}K^{-1}$ of 10-FGNi-epoxy-R to 0.362 W $m^{-1}K^{-1}$ of 30-FGNi-epoxy-R composite. It can be concluded that the FGNi nanostructures could effectively improve the thermal conduction performance of the epoxy matrix and the more fillers added the better thermal conductivity can be achieved. Meanwhile, the magnetic field resistance FGNi-epoxy composites demonstrate further enhancements, and this value increases from 0.242 W $m^{-1}K^{-1}$ of 10-FGNi-epoxy-M composite to 0.462 W $m^{-1}K^{-1}$ of 30-FGNi-epoxy-M composite. The obtained thermal conductivity of the 30-FGNi-epoxy-M composite is almost 2.7 times that of the pure epoxy sample. As shown in Figure *5-20*, the epoxy-based samples also show different electrical conduction performances depending on the different ratios as well

as the distributions. As insulation materials, the pure epoxy sample's electrical resistance is ca. 10^{10} Ω m^{-1}, and it rises along with the increase of the FGNi filler ratios. Meanwhile, the aligned FGNi-epoxy composites also illustrate the further improvement of electrical conduction performance, and the electrical resistance finally reaches 4.6×10^{5} Ω m^{-1} of 30-FGNi-epoxy-M composite, which is almost 10^{5} magnitudes higher than the pure epoxy samples. Similar phenomena have been presented. Table *5-4* displays the conduction performances of polymer-based composites with different fillers and FGNi-epoxy composites in this work. The multilayer graphene flakes (GnPs) reinforced epoxy composites showed enhanced thermal and electrical conductivity [103]. The aligned GnPs in the epoxy by an external electric field had similar results as ours The Fe_3O_4 modified graphene samples have been aligned in an epoxy resin by a weak magnetic field, and the measured electrical conductivity increased from 10^{13} to 10^{9} Ω m^{-1} [175]. Kim reported that Fe_3O_4-carbon nanofiber hybrids have been aligned to form a chain-like structure in the epoxy resin, and the electrical conductivity has also been improved from 10^{13} to 10^{8} Ω m^{-1} [176]. The enhancements of these fillers were similar to ours. However, the Ag wire generated by Ag particles in the epoxy matrix with the help of an external electrical field, and the obtained electrical conductivity of the composites significantly improved from 10^{8} to 10^{2} Ω m^{-1} due to the alignment. Thus, we can see the potential of metal fillers, especially when they generated uniform pathways in the matrix. Although the reinforcements in current FGNi-epoxy composites are still not as good as predicted, there is still great potential for further improvement.

Table 5-4 Comparison of conduction performances between FGNi-epoxy composites and previous results.

Sample	Electrical resistance (Ω m^{-1})	Thermal conductivity (W m^{-1}K^{-1})	Ref
GNPs-epoxy (aligned)	10^5	0.45	[103]
(Non-aligned)	10^6	0.40	
MWCNT-NR (aligned)	-	0.39	[80]
(Non-aligned)	-	0.35	
Fe_3O_4-GNP (aligned)	10^9	-	[175]
(Non-aligned)	10^{11}	-	
Fe_3O_4-CF (aligned)	10^8	-	[176]
(Non-aligned)	10^{10}	-	
Ag-wire (aligned)	10^2	-	[177]
(Non-aligned)	10^8	-	
FGNi (aligned)	10^5	0.46	This work
(Non-aligned)	10^6	0.36	

Combined with the SEM image shown in Figure *5-16*, it can be concluded that the 3D FGNi nanostructures aligned in the epoxy matrix can also be beneficial to electrical conduction performance. In the schematic of both FGNi-epoxy-M and FGNi-epoxy-R samples (Figure *5-24*), the uniform distribution of aligned FGNi fillers could be regarded as generating a straight 3D pathway between the top and bottom side of the composites, while the FGNi fillers in reference composites can be considered as randomly distributed. Therefore, the best thermal and electrical conduction performances can be ascribed to this straight 3D network that provided continuous pathways and shortens the distance when compared with reference samples. The introduction of FGNi nanostructures as fillers in the epoxy matrix could effectively increase the electrical conduction performance by both increasing the filler ratio and improving the filler distribution.

Figure 5-23Schematic of the distribution of FGNi fillers in FGNi-epoxy-M and FGNi-epoxy-R composites.

In Figure *5-19*, the obtained epoxy-based composites showed different CTE performances between FGNi-epoxy-M and FGNi-epoxy-R samples. The dimension change in the direction of alignment in the FGNi-epoxy-M sample displayed a decrease compared with the FGNi-epoxy-R sample. A possible reason for this difference could be ascribed to the aligned distribution of FGNi fillers, which uniformly point to one direction. As shown in the schematic (Figure *5-24*), the alignment of FGNi fillers effectively prevents expansion in the obtained FGNi-epoxy-M pellet, while the reference sample could not restrict the expansion of the epoxy matrix due to the random distribution fillers. It can be concluded that the vertical distribution of FGNi fillers with the assistant of the magnetic field demonstrated an obvious effect in restricting the expansion of the epoxy matrix along the vertical direction, and the increase of filler amount could further enhance the restriction.

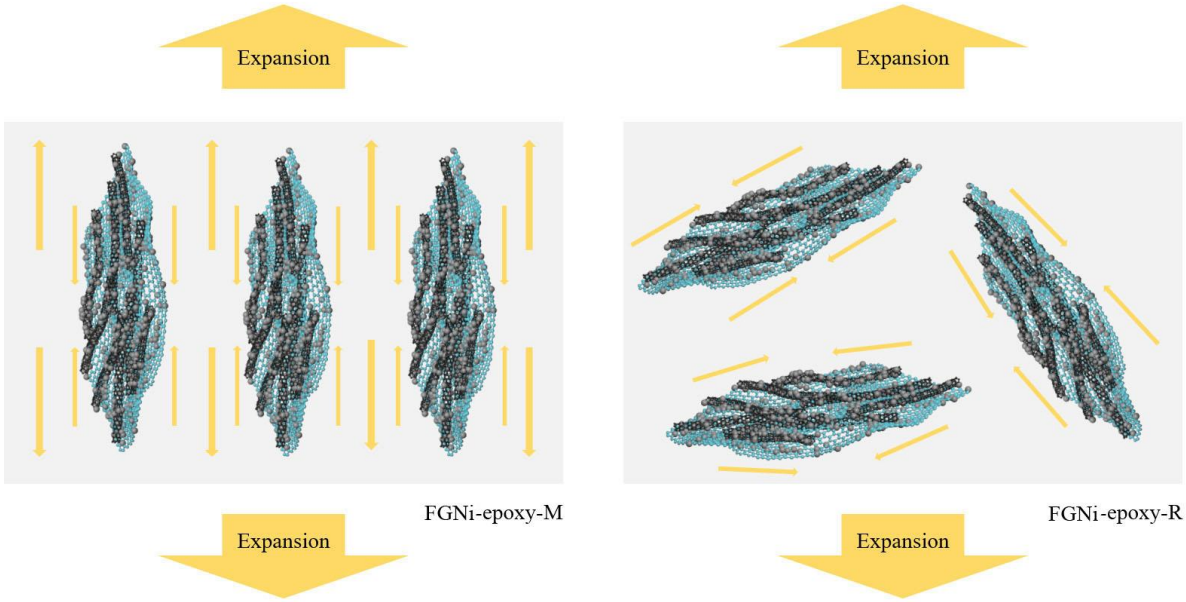

Figure 5-24 Schematic of the roles of FGNi fillers during thermal expansion in FGNi-epoxy-M and FGNi-epoxy-R pellets.

5.4 Summary

To conclude, both the uniform Ag and Ni nanoparticle decorated GNT (FGAg and FGNi) nanostructures were successfully prepared through the universal MLM process followed by the subsequent freeze-drying and reduction method. The obtained samples show a well-dispersed graphene-like structure which is similar to the pure GNT nanostructure and could prevent the agglomeration of Ag and Ni nanoparticles. The FGAg nanostructures then functioned as a promising filler in the PEEK matrix, and the fillers have been proved to form a 3D network in the PEEK matrix and displayed enhanced thermal and electrical properties. Because of this 3D network and the intrinsic properties of Ag and GNT, FGAg-PEEK composites show enhanced thermal conductivity (around 1.62 times to pure PEEK) and significantly improve the electrical conductivity (form around 10^{-10} Ω m^{-1} of pure PEEK to 10^{-1} Ω m^{-1} of FGAg -PEEK composites), as well as the perfect thermal durability even above the melting temperature of pure PEEK. Meanwhile, the FGNi-epoxy composites demonstrate improved thermal and electrical conduction performances as well, especially the magnetic field assistant sample. In the FGNi-

epoxy-M composites, the aligned distribution of FGNi nanostructure fillers generated straight 3D pathways, which could effectively enhance the thermal and electrical conduction performances, as well as prevent the thermal expansion of the epoxy matrix. Thus, the results show that the enhancement of FGAg and FGNi nanostructures will play important roles in reinforcing PEEK and epoxy matrix and make them potential candidates in fields like aerospace, automobile, and electronics.

6 Water purification application

In this chapter, the novel 3D GNT and the Ni decorated GNT (FGNi) nanostructures are applied as water purification materials due to their well-dispersed structures and large surface areas. The dye removal performances of the GNT nanostructures with different ratios between CNT and GO have been investigated with both the cationic (Rhodamine B, RhB) and anionic (Methyl orange, MO) dyes in the aqueous solution. The adsorption kinetics and adsorption isotherms studies have also been carefully discussed. Meanwhile, the FGNi samples have been explored as the photo-catalysts in removing RhB under UV irradiation and dark conditions. The corresponding dye removal performances have also been comprehensively discussed.

6.1 Rhodamine B and Methyl orange adsorption by GNT hybrid nanostructure

6.1.1 Characteristics of as-prepared GNT hybrids

Figure *6-1* displays the XRD patterns of all the GNT samples with different ratios as well as the pure CNT and pure GO samples. In the patterns of the pure GO sample, a clear characteristic peak at around 12° can be observed, confirming the existence of GO. In the patterns of the pure CNT, a peak at around 27° and a broad peak from 30-40° can be detected. Meanwhile, in the diffraction patterns of the GNTs samples, it can be found that the characteristic peak of the GO could still be observed in GNT 5-1 sample, while this signal disappears from GNT 2-1 sample. This can be ascribed to the attachment of CNTs on the surface of the graphene-layer, which reduces the intensity of GO and finally covers it. The broad peak remains in all GNT samples. A similar broad peak has also been reported in previous research, which is related to the carbon content [178].

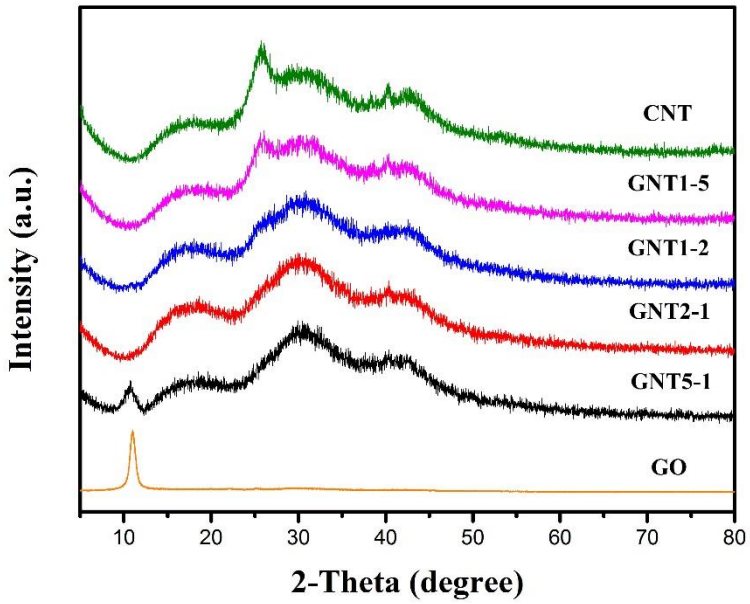

Figure 6-1 XRD patterns of CNT, GO, and GNT with different ratios.

Figure *6-2* illustrates the N_2 sorption isotherm (a-f) and the calculated surface areas of each sample (g). In Figure *6-2* a-f, , all the N_2 sorption isotherm can be recognised as the typical IV isotherm, indicating the mesoporous structures of all samples, and the hysteresis loops are varied from H2 to H1 type [179]. Specifically, the isotherm of pure GO shows a type H2(b) hysteresis loop, it changes to H2(a) type in GNT 5-1 and GNT 2-1 sample due to a narrow range of pore necks. This can be ascribed to the CNTs attached on the graphene layers that generated more mesopores. With the increase of carbon content, the H1 type hysteresis loop can be observed in GNT 1-2, GNT 1-5 and pure CNT samples, indicating that more mesopores have been obtained in the products. Figure *6-2*g is a bar chart of the calculated surface area of each sample calculated from the sorption isotherm. The surface area of pure GO is 119.42 m^2 g^{-1}, with a minor decrease to 101.30 m^2 g^{-1} for GNT 5-1 sample, this value is increased dramatically to 257.56 m^2 g^{-1} for GNT 1-5 sample, while the pure CNT is 235.67 m^2 g^{-1}.

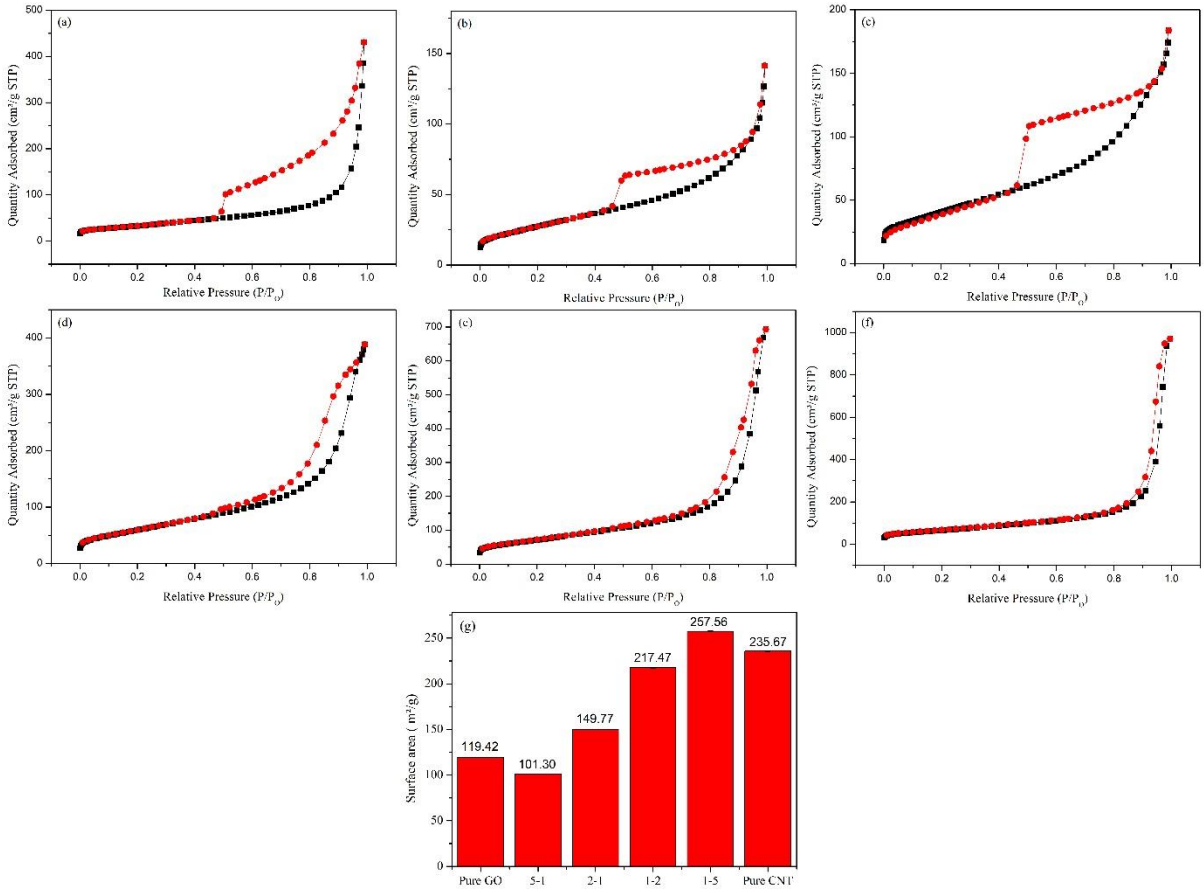

Figure 6-2 N_2 sorption isotherm of pure GO(a), GNT5-1 (b), GNT2-1 (c), GNT 1-2 (d), GNT 1-5 (e), pure GNT (f) and conclusion of the BET surface area of each sample (g).

Figure *6-3* a and b are the images of the structure of the pure GO sample. In the low magnification (Figure *6-3*a), a graphene layer structure can be observed clearly, and no obvious agglomeration was found. At higher magnification (Figure *6-3*b), the surface of GO is smooth, and no other morphology can be detected. After adding CNTs, the GNT 5-1 (Figure *6-3* c and d), there is still no apparent agglomeration. The CNTs can be observed on the surface of the graphene layer (Figure *6-3*d). With an increased amount of CNTs, the structures of GNT 2-1 and GNT 1-2 samples still show the graphene-layer structure without obvious agglomeration (Figure *6-3* e and h) and a rougher surface can be found under higher resolution (Figure *6-3* f and g). In GNT 1-5 sample (Figure *6-3* i), the graphene-layer structure remained, indicating that the agglomeration did not occur even when 25 times the amount of the CNTs amount was introduced into the nanostructures system. However, in the high magnification image (Figure

6-3 j), the thickness of the graphene layer structure increases, and more CNTs attached onto the graphene layers when compared to other nanostructures. The pure CNT sample displays the agglomeration structure at both low and high resolution (Figure *6-3* k and l).

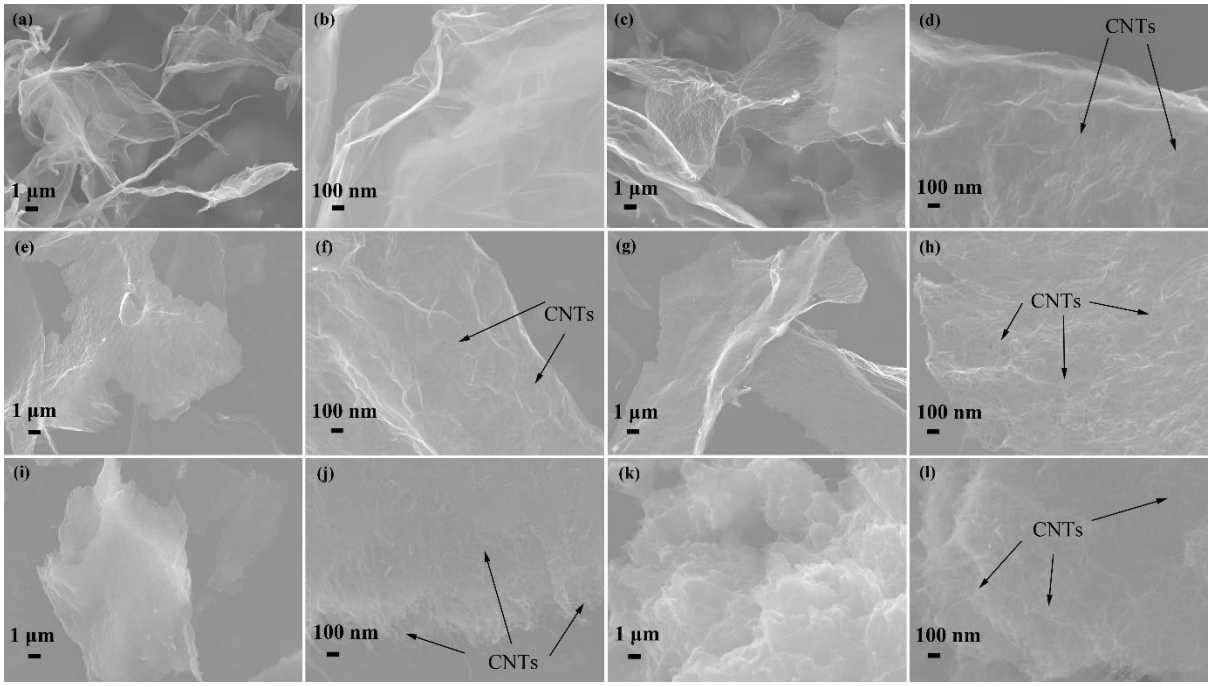

Figure 6-3 SEM images of pure GO (a and b), GNT5-1 (c and d), GNT 2-1 (e and f), GNT 1-2 (g and h), GNT 1-5 (I and j) and pure CNT (k and l) nanostructures.

Figure 6-4 shows the XPS spectra of as-received CNT, acid-treated CNTs, pure GO, and GNT 1-5 samples. The survey scans of these four samples are displayed in Figure 6-4a. It can be found that only the C peak can be observed in as-received CNT samples, while the C and O signals appear in acid CNT sample, indicating that the oxygen contained component is obtained after acid treatment with the CNTs. The C and O peaks can also be detected in GO and GNT 1-5 samples. In the deconvoluted C 1s spectrum of pure GO (Figure 6-4b), two main peaks can be found, the sp^2 hybridized C (C-C and C=C) component located at 284.0 eV and the C-O component, which corresponds to the hydroxyl and epoxy groups located at 286.2 eV [152]. The minor peak, which is located at 287.9 eV is the O=C-OH groups. The C 1s spectrum of acid CNTs (Figure 6-4c) can be deconvoluted into three peaks. The main peak located at 284.0

eV is the sp^2 hybridized C and a defect containing C peak was observed at 284.7 eV, indicating the formation of defect C component during acid treatment. The oxygen-containing component can be found in a broad peak located around 287.3 eV, which also confirms the existence of oxygen-containing functional groups. The C 1s peak in GNT 1-5 sample shows a similar deconvolution as acid CNTs, which can be ascribed as the CNTs attached to the graphene layers shown in Figure *6-3* i and g. The XPS results confirm that oxygen-containing functional groups existed in both acid CNTs and GOs and remained after mixing.

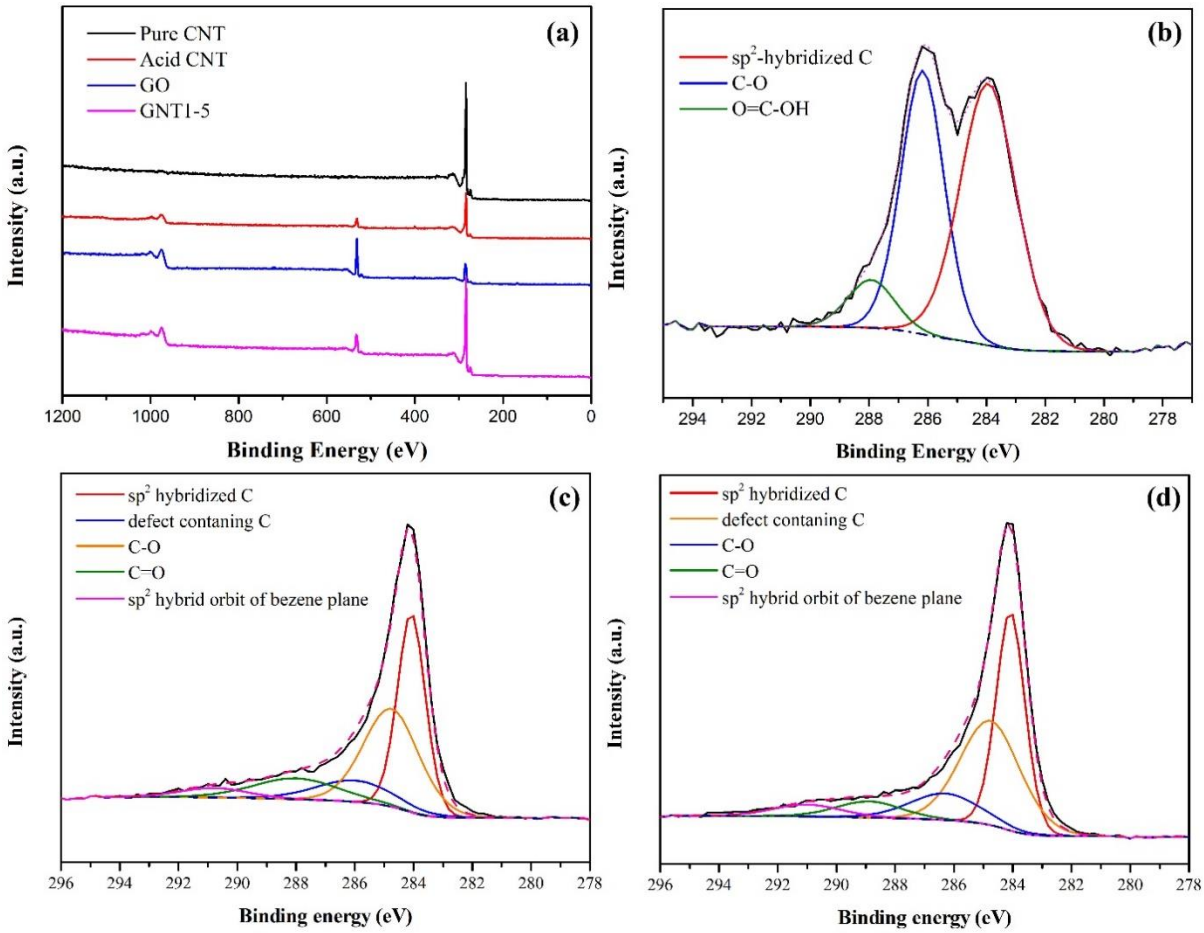

Figure 6-4 XPS survey scan spectra of pure CNT, acid CNT, pure GO and GNT 1-5 samples (a) and C 1s spectra of GO (b), acid CNT (C) and GNT 1-5 (d)

6.1.2 Adsorption performance of GNT nanostructures with RhB and MO

To investigate the dye removal performance, the as-prepared GNT products with different ratios are added into 10 ppm RhB aqueous solution and the time-based removal capacity curves

of RhB are displayed in Figure *6-5*a. It can be found that the removal capacities vary with the ratio of GNT samples in 10 ppm RhB aqueous solution. The pure GO illustrates a removal capacity of 51.6 mg g^{-1} after 120 min, while this value for GNT 5-1 sample is 50.1 mg g^{-1}. The GNT 2-1 sample displays a removal capacity of around 65.5 mg g^{-1}, increasing to 92.5 mg g^{-1} for GNT 1-2 sample, 95.4 mg g^{-1} for GNT 1-5 sample and 91.1 mg g^{-1} for pure CNT sample after 120 min. Despite the removal capacity differences in all samples, the capacities become stable after 120 min. Figure *6-5*b illustrates the time-based absorbance of GNT 1-5 samples, which shows the best RhB removal performance. It can be noted that the absorbance decreases dramatically within the initial 5 min, from around 1.9 a.u. to only 0.2 a.u., which is consistent with Figure *6-5*a. Thus, the GNT1-5 samples are regarded as the most efficient adsorbent, which exhibits a removal ability of 95.43 % in 10 ppm RhB aqueous solution.

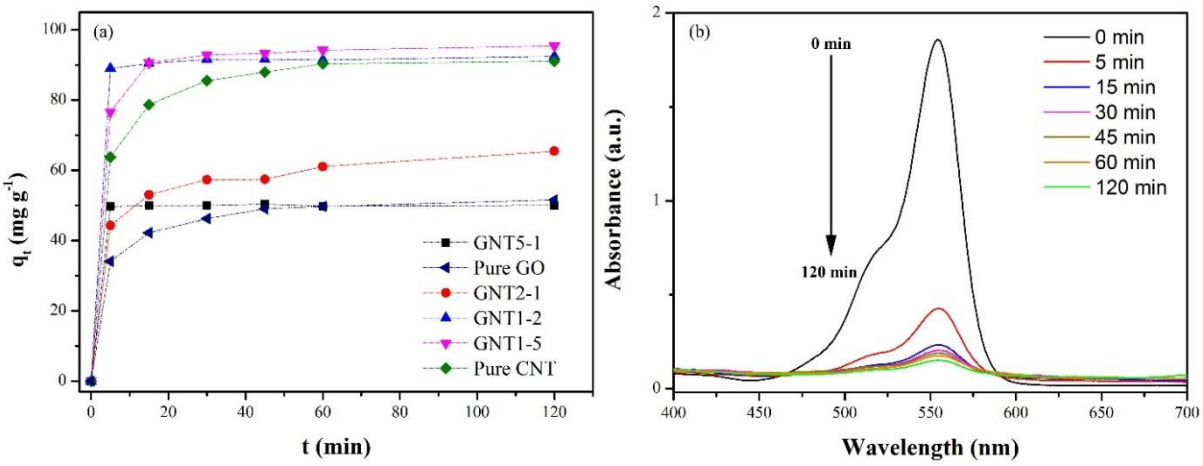

Figure 6-5 (a) Removal capacity of as-prepared products in 10 ppm RhB aqueous solution and (b) Time-based RhB absorbance of GNT 1-5 sample in 10 ppm RhB aqueous solution.

Based on the results above, the adsorption performance of GNT 1-5 sample has been further investigated at different concentrations of both cationic (Rhodamine B) and anionic (Methyl orange) dyes (Figure *6-6*). The removal capacities of RhB under different concentrations with GNT 1-5 sample are displayed in Figure *6-6*a. It can be found that the removal capacity increases from 49.8 mg g^{-1} in 5 ppm RhB solution to 95.4 mg g^{-1} in 10 ppm RhB solution,

120.47 mg g^{-1} in 15 ppm RhB solution, 123.67 mg g^{-1} in 20 ppm solution and finally 145.4 mg g^{-1} in 25 ppm RhB solution after 300 min. The adsorption capacity of 49.8 mg g^{-1} in 5 ppm RhB solution is equal to that of 5 ppm RhB (corresponding to 99.5%), indicating that all RhB is adsorbed. In Figure *6-6*b, the removal capacity of MO in the GNT 1-5 sample exhibits a similar curve but with a lower capacity. It increases from 35.3 mg g^{-1} in 5 ppm MO solution to 48.3 mg g^{-1} in 10 ppm MO solution, 55.2 mg g^{-1}in 20 ppm MO solution, and 57.8 mg g^{-1} in 30 ppm MO solution. Although similar adsorption trends are obtained in both RhB and MO solutions, there is still a significant difference between the adsorption capacity of RhB and MO with GNT 1-5 samples.

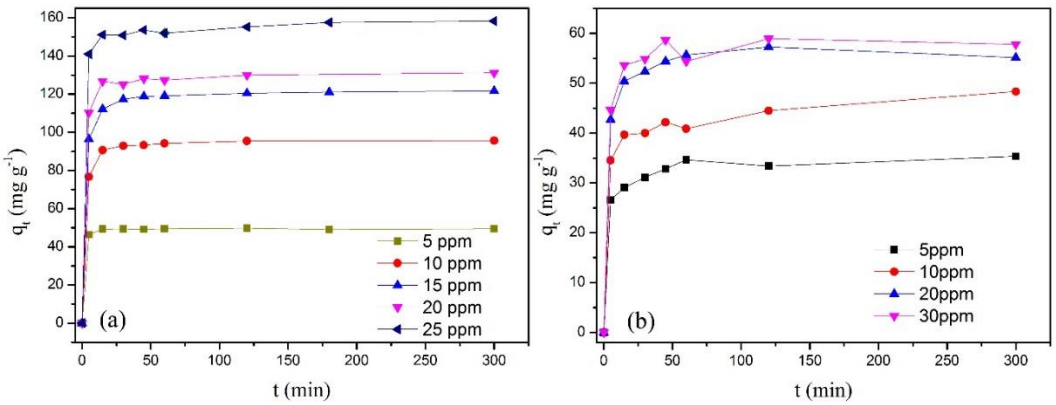

Figure 6-6 Time-based RhB (a) and MO (b) removal adsorption capacity with GNT 1-5 samples.

To investigate the adsorption differences between RhB and MO in GNTs samples, a further characterisation has been carried out through Zeta potential measurement to clarify whether the surface charge of the GNT samples would affect the adsorption capacity. The results of GNT 5-1, 2-1 and 1-5 samples are displayed in Figure 6-7. All these three GNT samples are all highly negatively charged when dispersing in water at a 0.1 mg ml^{-1} concentration. The GNT 1-5 sample shows the lowest Zeta potential among these three samples and it is obvious that the Zeta potential decreases with the increase of the ratio of CNTs in the samples. It displays a similar trend with BET surface area results. Thus, it is consistent with the results that more cationic dyes (RhB) could be adsorbed through electrostatic interactions due to the negative

charge on the surface of GNT samples.

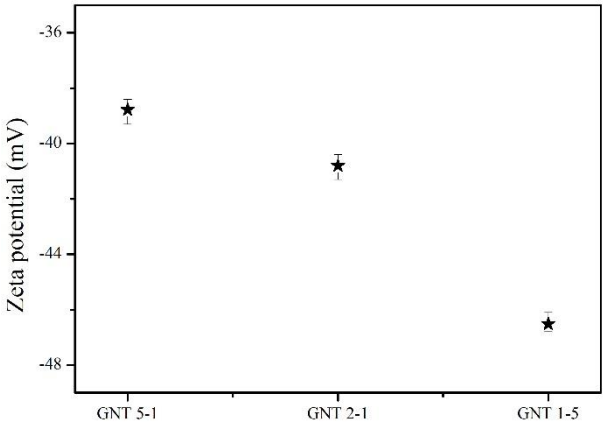

Figure 6-7 Zeta potential of GNT 5-1, 2-1, and 1-5 samples at a dispersion concentration of 0.1 mg ml^{-1}.

6.2 Rhodamine B removal of uniform Ni nanoparticle decorated GNT hybrid nanostructure

6.2.1 Structural features and morphology

Figure 6-8 displays XRD patterns of the pure GNTs, pure Ni, and FGNi samples with different ratios of carbon content. As expected, diffraction peaks at 44.5°, 51.8° and 76.4° of 2θ are observed in all Ni containing samples (Figure 6-8 a-e) matching the (111), (200) and (220) planes of standard metallic Ni (ICDD PDF No. 00-04-0850). The intensity of the diffraction peaks decreases with the increase of the carbon content in the samples. A broad peak ranging from 20-30° can be attributed to the existence of carbon materials [166, 178], and becomes more prominent with an increase of carbon content and the pure GNT sample shows the highest intensity (Figure 6-8f). Apart from the Ni and carbon signals, no other peaks are detected. This result confirms that the products were completely reduced to Ni and the GNT content was preserved under treatment at 400°C for 2 h in Ar/H_2 atmosphere.

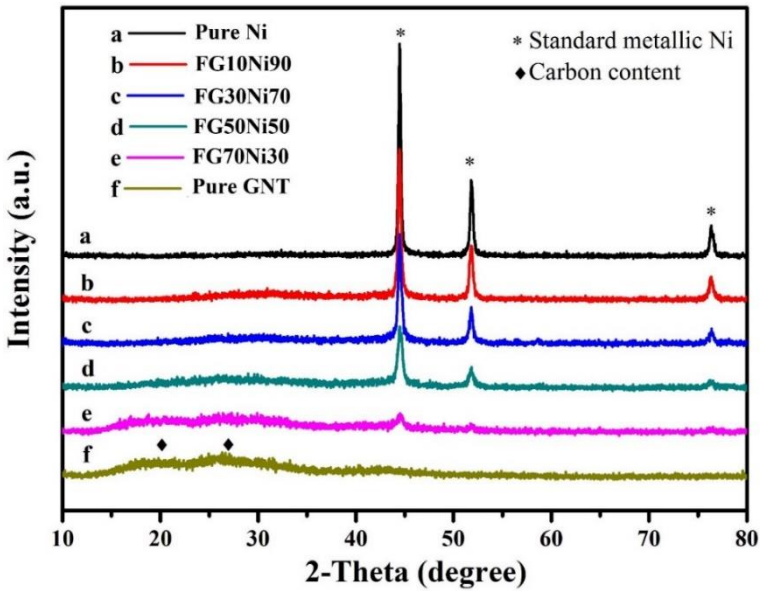

Figure 6-8 XRD patterns of FGNi, pure Ni, and GNT samples.

To further confirm the composition of the as-prepared samples, the Ni/C ratio of each product has been studied based on TGA results (Figure 6-9). In the pure Ni sample (Figure 6-9 a), the weight increases after 200°C and reaches a maximum weight change at 125 % then remains stable after 600°C, indicating the Ni phase was oxidised into NiO phase in air. For the rest of the carbon-containing samples, the trend of their weight change varies (Figure 6-9 b-e). The weight of each sample initially increases after 200°C, which can also be ascribed to the oxidation of Ni in air. After that, the weight decreases, with the decrease being more pronounced with increasing carbon content, except the FG10Ni90 sample, due to the oxidation of carbon. Specifically, the FG10Ni90 sample displays a weight increase but less than the pure Ni sample, caused by the loss of carbon content, and the calculated carbon content of the FG10Ni90 sample from TGA results is 12.5 wt.%. With increasing carbon content, the calculated carbon percentage of each sample from TGA results is 24.6 wt.% of carbon content for FG30Ni70, 47.8 wt.% for FG50Ni50 and 64.8 wt.% for FG70Ni30. The Ni/C ratio in all FGNi samples could be confirmed to be the same as the designed proportion in the sample preparation stage.

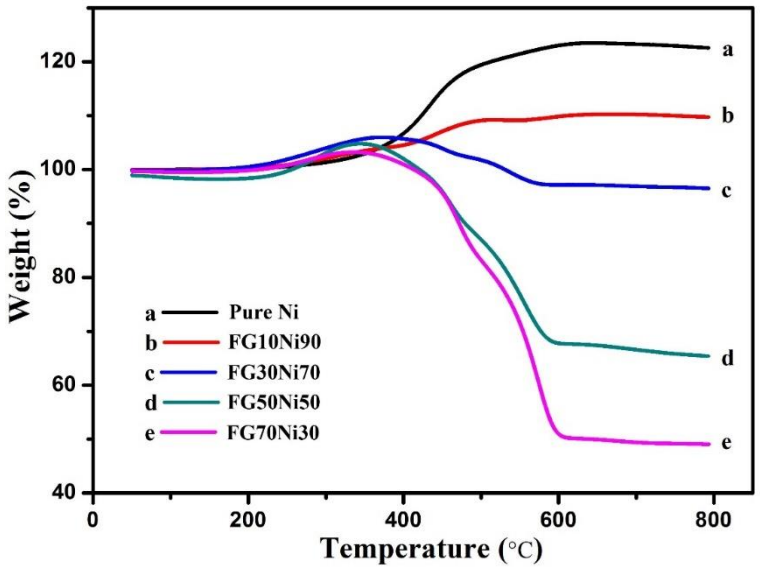

Figure 6-9 TGA results of Pure Ni, FG10Ni90, FG30Ni70, FG50Ni50, and FG70Ni30 samples.

The N_2 sorption isotherms displayed in Figure 6-10 show a type IV isotherm feature for each product, with an H2 hysteresis loop, demonstrating the mesoporous structural feature of all samples [180]. A bar chart in Figure 6-10b summarises the BET surface area of each sample. Against 9.01 m^2 g^{-1} for pure Ni, the surface area was increased to 31.8 m^2 g^{-1} for FG10Ni90 sample, 71.7 m^2 g^{-1} for FG30Ni70 sample, 82.7 m^2 g^{-1} for FG50Ni50 sample, 175.4 m^2 g^{-1} for FG70Ni30 sample and 197.9 m^2 g^{-1} for pure GNT nanostructure. The surface areas are increased when the GNT nanostructure was introduced and increased with GNT contents. In the pore volume and size distribution histogram shown in Figure 6-11, the total pore volume (up to 100 nm) increased with higher carbon content. In addition, the pore diameter ranging from 2-50 nm is dominant for all samples, which also further confirmed the mesoporous structures of the products. Thus, a mesoporous structure with a high surface area can be confirmed in the FGNi samples with different carbon contents and the pure GNTs sample.

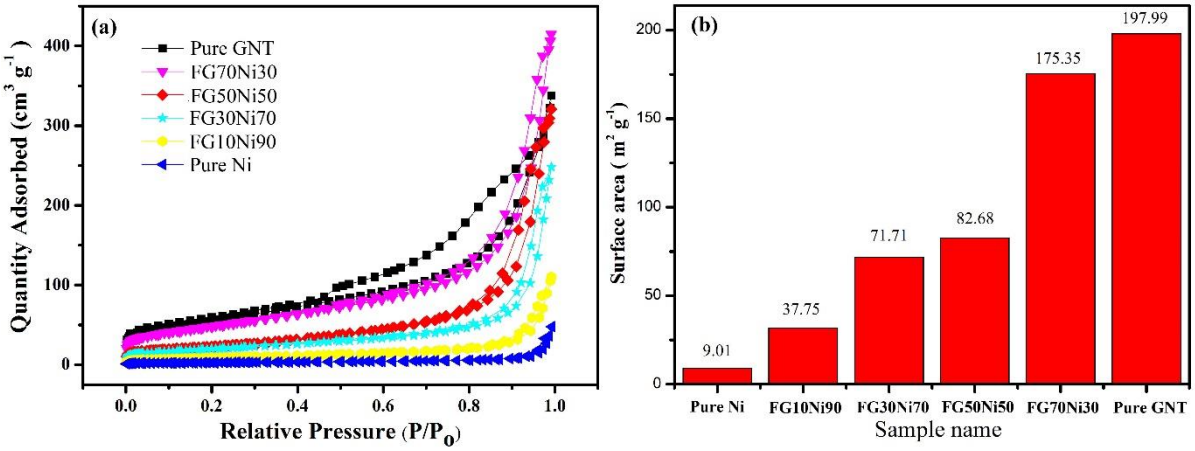

Figure 6-10 (a) N_2 adsorption-desorption isotherm curves of all samples and (b) calculated BET surface area of each composition.

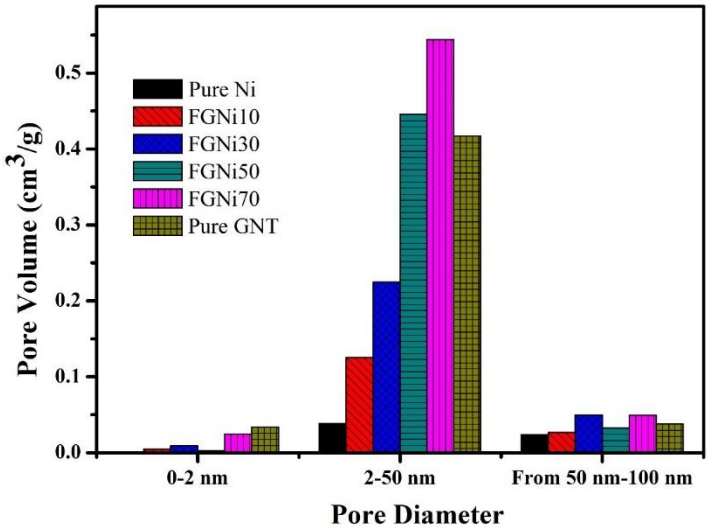

Figure 6-11 Pore volume and size distribution histogram using the NLDFT carbon slit pore model with N_2 at -196℃.

Typical SE SEM and bright-field TEM images of prepared samples are displayed in Figure 6-12 and Figure 6-13. For pure GNTs, a well-dispersed structure could be observed (Figure 6-12a), with no obvious stacks or agglomeration that are normally associated with graphene-based materials [16]. At high resolution, CNTs are recognised sitting on the surface of graphene layers (Figure 6-12b) due to the π-π interactions between carbon atoms. After adding Ni acetate as precursors, the 3D graphitic structures of the FGNi sample can still be observed (Figure 6-12 c and d), with Ni nanoparticles uniformly dispersed on the surface of GNTs. For sample FG30Ni70, graphene and CNTs could be easily detected as lighter features in the bright field images, whilst Ni nanoparticles on the surface of both graphene and CNTs appeared dark, as

shown in Figure 6-12e, with the particle size of around 50 nm. The insert image of Figure 6-12e displays the selected area electron diffraction (SEAD) patterns and indicates the Ni (111), (200), (220) and (311) planes. At higher magnification (Figure 6-12f), clear morphology of CNTs can be found and Ni nanoparticles were successfully coated on them. The CNTs also can be confirmed as multi-wall tubes. For other Ni containing samples (Figure 6-13), it can be found that the Ni particles ca. 100 nm in size were obtained after the reduction process in pure Ni sample. The particles are much bigger than the ones coated on GNTs (Figure 6-12 c and d, Figure 6-13 c-f), which indicates that the introduction of GNT could effectively restrict the growth of Ni particles when particles nucleated on GNTs.

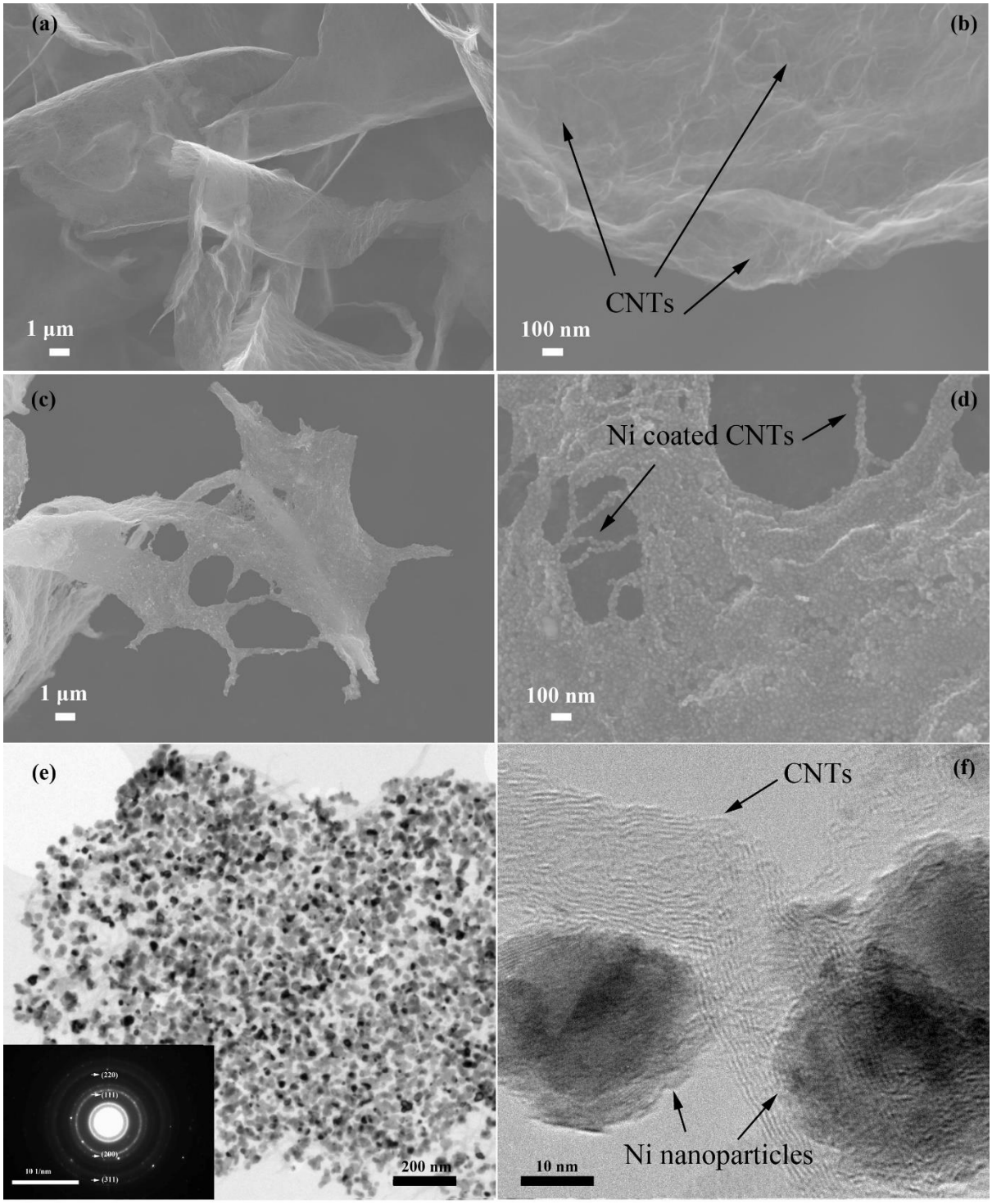

Figure 6-12 SEM images of pure GNTs (a and b) and FG30Ni70 (c and d) nanostructures, and TEM images (e and f) of FG30Ni70 nanostructures, the insert image of Fig 3e is the electron diffraction (SEAD) patterns.

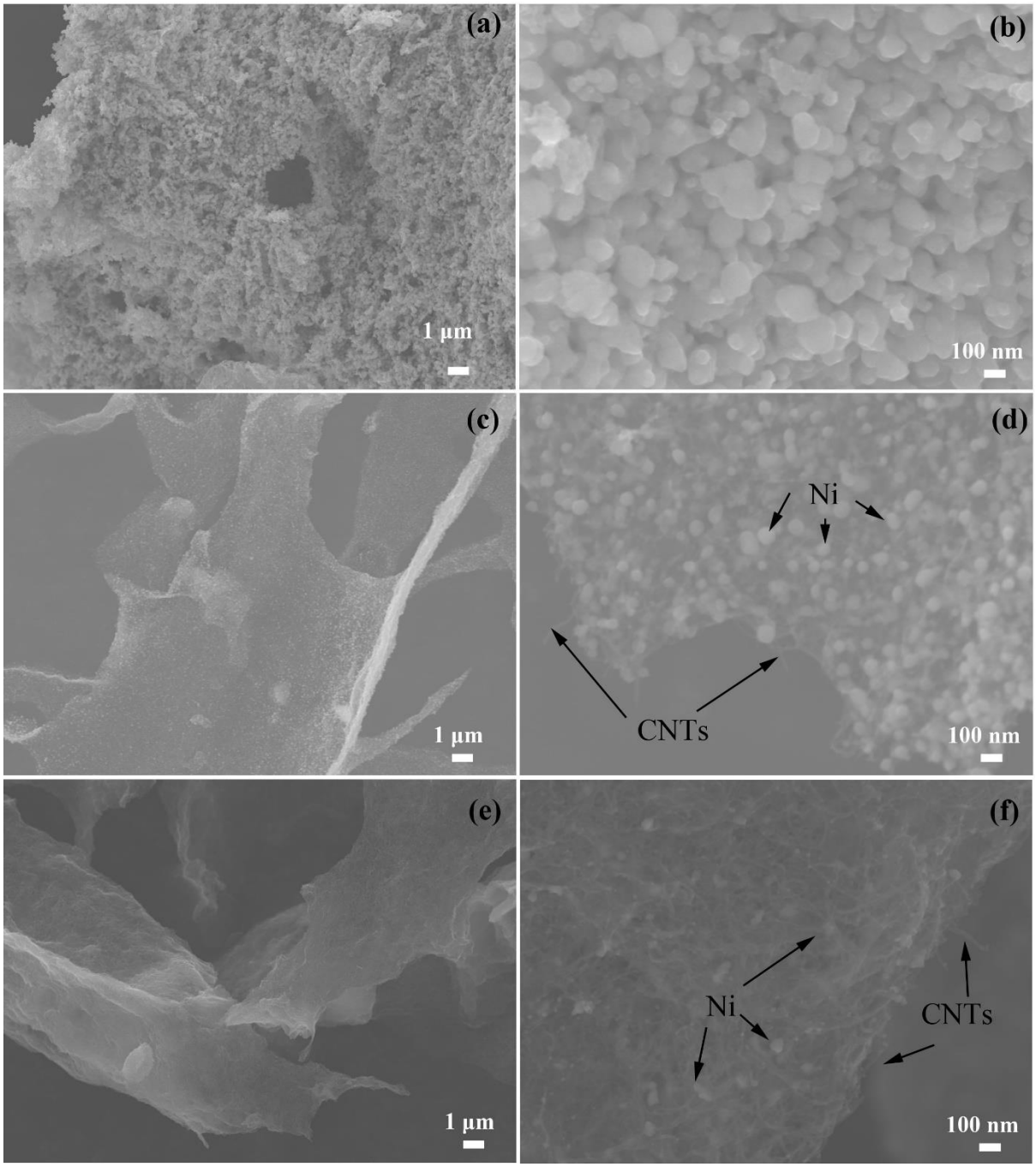

Figure 6-13 SEM images of pure Ni (a, b), FG50Ni50 (c, d), and FG70Ni30 (e, f) samples under different magnifications.

The XPS spectra of pure GO, pure GNT, and FGNi samples are shown in Figure 6-14. FG30Ni70 sample is selected to represent FGNi samples as all FGNi samples showed similar XPS signals. From the XPS survey scan (Figure 6-14a), the peaks of C1s and O1s are observed for all three samples, demonstrating the existence of C and O. The Ni 2p peak appears in FG30Ni70, showing the presence of Ni. For the prepared GO samples (Figure 6-14 b), the C

1s spectrum could be deconvoluted into three peaks, the sp^2 hybridized C (C-C and C=C) component at 284.0 eV [153], the C-O which corresponds to the hydroxyl and epoxy groups at 286.3 eV, and the O=C-OH groups at 288.0 eV [152]. The characteristic peaks of O containing components confirm that the functional groups are successfully attached to the graphene layers during the preparation of GOs. The decrease of O-containing functional groups can be ascribed to the reduction process under H_2 atmosphere during the preparation of GNTs and FGNi samples. Meanwhile, similar deconvoluted peaks can be observed in both samples, the C-O (ether bonds) groups at 286.3 eV, the C=O groups (ketone bonds) at 288.9 eV and the sp2 hybrid orbit of benzene plane at 290.8 eV [181], which also can be ascribed to the reduction process. In addition, the main C peaks in both GNT and FG30Ni70 samples become the sp^2 hybridized C (at around 284.0 eV) and defect-containing sp^2 hybridized C (at around 285.0 eV).

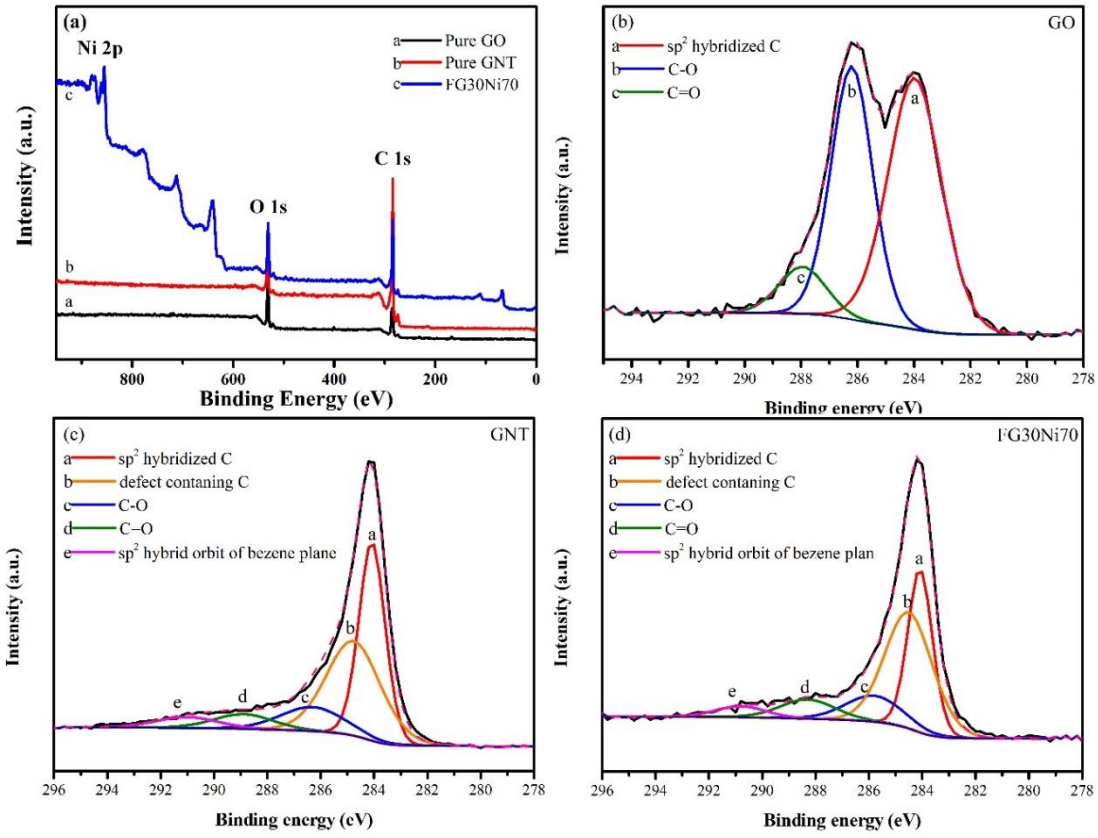

Figure 6-14 XPS survey scan spectra of GO, GNTs, and FG30Ni70 samples (a) and C 1s spectra of GO (b), GNT (c) and FG30Ni70 (d) samples.

6.2.2 RhB removal performance of as-prepared samples

The dye removal performance of the products is presented in Figure 6-15. Under dark and UV irradiation, the UV-VIS absorbance spectra of the FG30Ni70 sample shows a maximum absorbance peak at around 554.5 nm for the RhB solution (Figure 6-15 a and b). The initial absorbance is located at around 1.0 a.u., corresponding to the initial RhB concentration of 5 ppm. The peak decreases dramatically within the first 15 min and then stabilises at an absorbance of around 0.6 a.u. after 30 min, which indicates an equilibrium being reached with the initial 15 min. The removal efficiency of FG30Ni70 under dark is calculated as 34.7 %. Under UV light irradiation after 1 h in the dark to reach equilibrium, the RhB adsorption results for FGNi samples are displayed in Figure 6-15b. The start point is from 0.6 a.u., similar to the equilibrium point in the dark. The absorbance peak of RhB decreases gradually to 0.15 a.u. after exposing under UV light for 120 min irradiation (corresponding to an additional 73.6 % of removal efficiency after physical adsorption). The RhB reduction at this stage can be regarded as photo-degradation. There is no obvious wavelength shift for the absorbance peak, which indicates the complete removal of RhB during the process rather than being converted into other by-products. The time-based adsorption efficiency and total removal efficiency of all samples are displayed in Figure 6-15 c and d. Under dark conditions (Figure 6-15 c), the removal efficiencies of all samples reach equilibrium within the initial 15 min are the same as the FG10Ni90 sample, which is described in Figure 6-15a. However, the removal efficiencies rise with the increased carbon content in the sample (Figure 6-15c). Under UV irradiation after 1 h in the dark, the removal efficiency continues to increase, especially the pure Ni, FG10Ni90, FG30Ni70, and FG50Ni50 samples (Figure 6-15d).

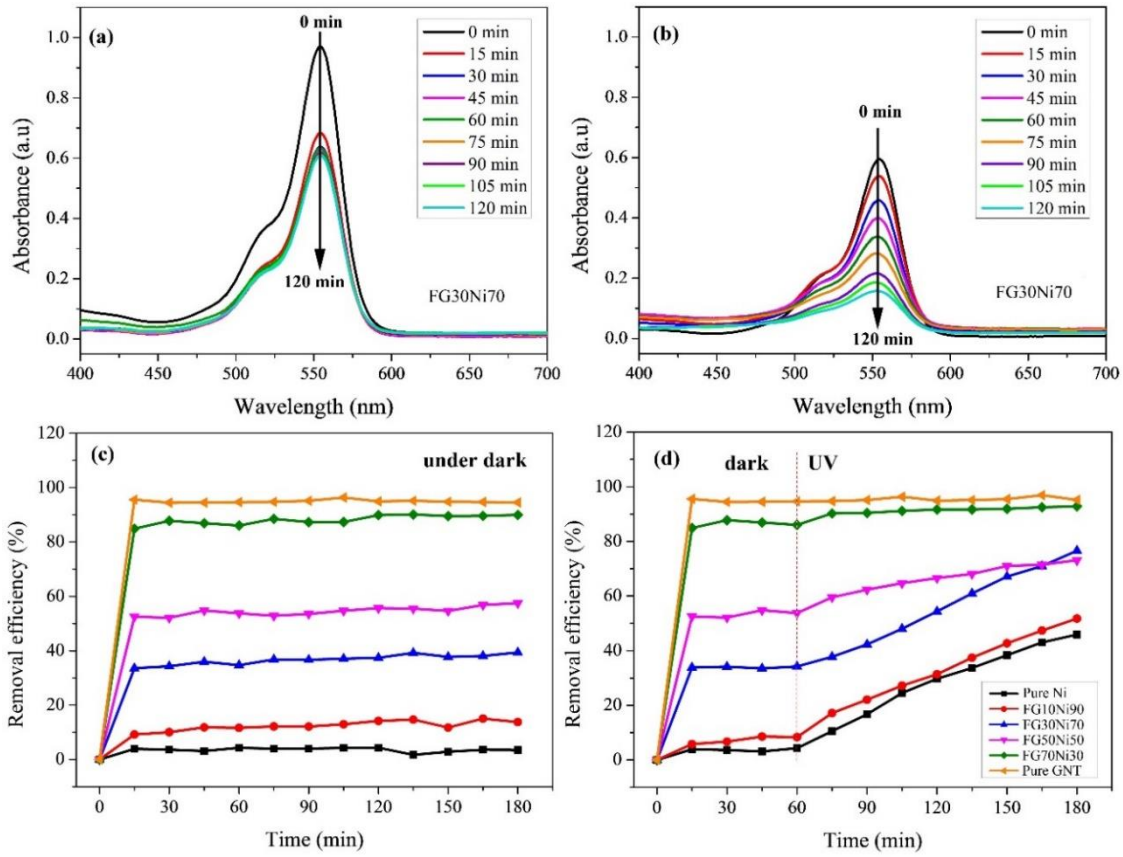

Figure 6-15 Time-based UV-VIS absorbance spectra of FG30Ni70 (a) under dark and (b) under U) and time-based removal efficiency of all samples: (c) under dark and (d) dark with UV.

The final removal efficiencies of all samples are summarised in Figure 6-16a. Under dark conditions (Figure 6-16b), the removal efficiency ranges from 4.31 % of pure Ni to 94.7 % of Pure GNTs after 2 h. The amount of RhB adsorbed by pure GNTs reaches as high as 47.5 mg g^{-1}. By subtracting the dark efficiency, the removal efficiency under UV can be obtained as 41.61 % for pure Ni, 40.1 % for FG10Ni90, 49.1 % for FG30Ni70, 19.3 % for FG50Ni50, 6.81 % for FG70Ni30 and 0.53 % for pure GNTs as shown in Figure 6-16c. Because the initial concentrations for UV degradation, after physical adsorption, are different from sample to sample with different carbon/metal ratios, the degradation efficiency under UV irradiation is calculated by considering the remaining RhB in solutions as 100 %, and the results are presented in Figure 6-16d. The histogram shows that the UV degradation efficiency of pure Ni, FG10Ni90, FG30Ni70, and FG50Ni50 is 43.5 %, 47.9 %, 73.6 %, and 65.5 %, respectively. It

is merely 29.3 % for FG70Ni30 and 1.55 % for pure GNTs, as much fewer dyes remained after the physical adsorption of GNTs in both samples.

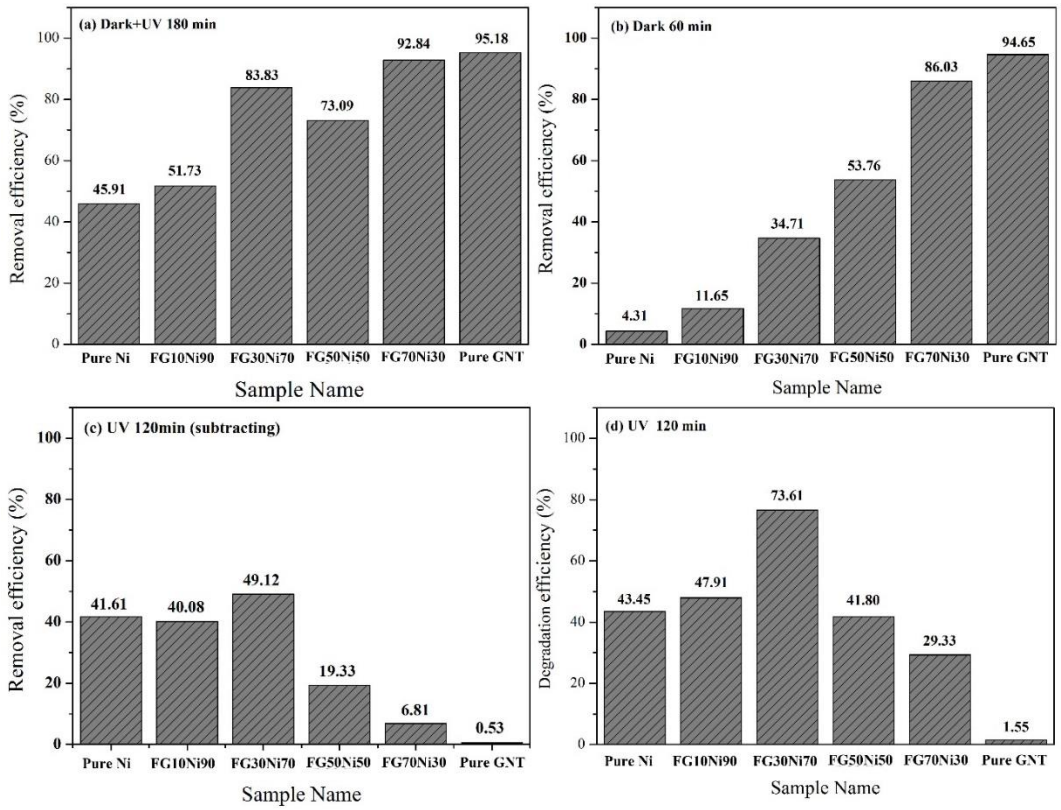

Figure 6-16 Removal efficiency of samples under: (a) dark for 60min and UV for 120 min, (b) dark 60 min, (c) UV 120 min (subtracting) and (d) UV 120 min.

6.2.3 Physical adsorption performance of FGNi nanostructures

To assess the effect of different RhB concentrations on the samples, Figure 6-17a summarises the removal performance of FG30Ni70 samples with different RhB concentrations from 1, 5, 10 to 15 ppm. Although the removal efficiency under dark decreases with the increase of the RhB concentration (Figure 6-17b), the calculated adsorption capacity of FG30Ni70 increased from 9.82 mg g^{-1} in 1ppm RhB solution to 24.8 mg g^{-1} in 15ppm solution (Figure 6-17c). The decrease of the removal percentage of RhB in solution with increased initial concentration can be ascribed to the saturation of adsorption sites on the samples [104]. Meanwhile, the increase of total adsorption capacity was caused by the high driving force for mass transfer at high RhB

concentration [182].

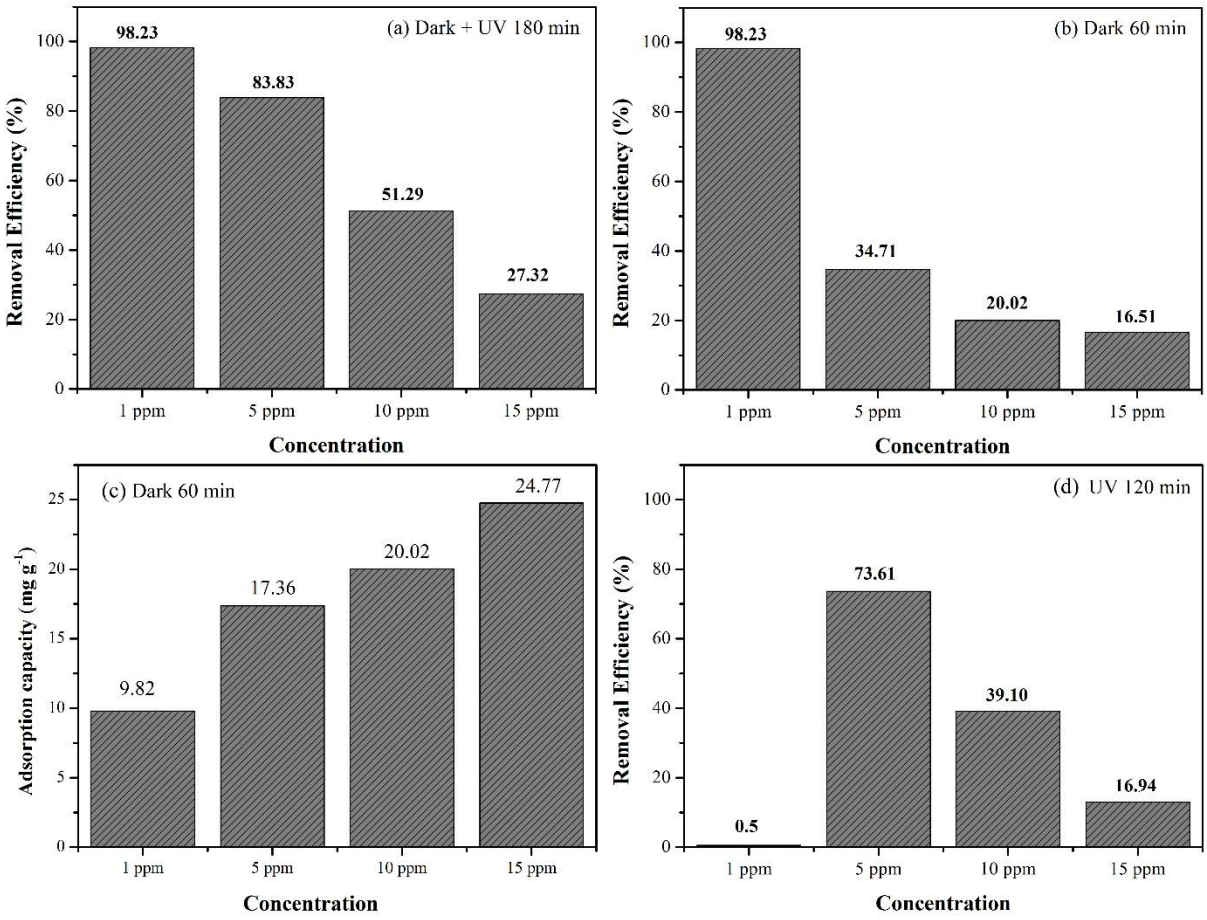

Figure 6-17 The removal Efficiency and adsorption capacity of FG30Ni70 samples at different concentrations of RhB solutions.

6.2.4 Photo-degradation and scavenger experiment of FGNi nanostructures

Under UV irradiation, the as-prepared FGNi nanostructures (Figure 6-17d) exhibit good removal performance with RhB. The FG30Ni70 sample shows the best removal ability with a total efficiency of 83.0 % via synergetic physical adsorption and photo-degradation, which could be translated to a removal capacity of around 41.5 mg g^{-1} in a 5 ppm RhB solution, precisely. This includes a 34.7 % physical removal under dark and a further 76.3 % photo-degradation for the remaining RhB under UV irradiation (Figure 6-17 d).

To further investigate the photo-degradation mechanism, a scavenger experiment was introduced to clarify the reactions, and the results are displayed in Figure 6-18. Specifically, different scavengers, for example, methanol for $OH^{\cdot}$ free radicals, potassium iodide (PI) for holes (h^{+}) free radicals, and p-benzoquinone (BQ) for $O_2^{\cdot -}$ free radicals, were added into RhB solution with FG30Ni70 samples. As can be seen (Figure 6-18b), the degradation efficiency decreases dramatically from 73.6 % of FG30Ni70 to 4.9 % by adding methanol ($OH^{\cdot}$ free radicals), to 23.8 % by adding BQ ($O_2^{\cdot -}$ free radicals) and to 46.3% by adding potassium iodide (h^{+} free radicals). This result confirmed the involvement of $OH^{\cdot}$ free radicals as the main reactive species, followed by $O_2^{\cdot -}$ free radicals in the degradation process. The involvement of h^{+} was not as active as $OH^{\cdot}$ free radicals and $O_2^{\cdot -}$ free radicals, as the degradation efficiency only decreased to 46.3% when potassium iodide was used in the scavenger test. The decorated Ni on this nanostructure enhanced the generation of strong oxidant ($OH^{\cdot}$ free radicals) which was much needed in the photocatalytic work, and a similar result was also reported by Zhao and et al. [147].

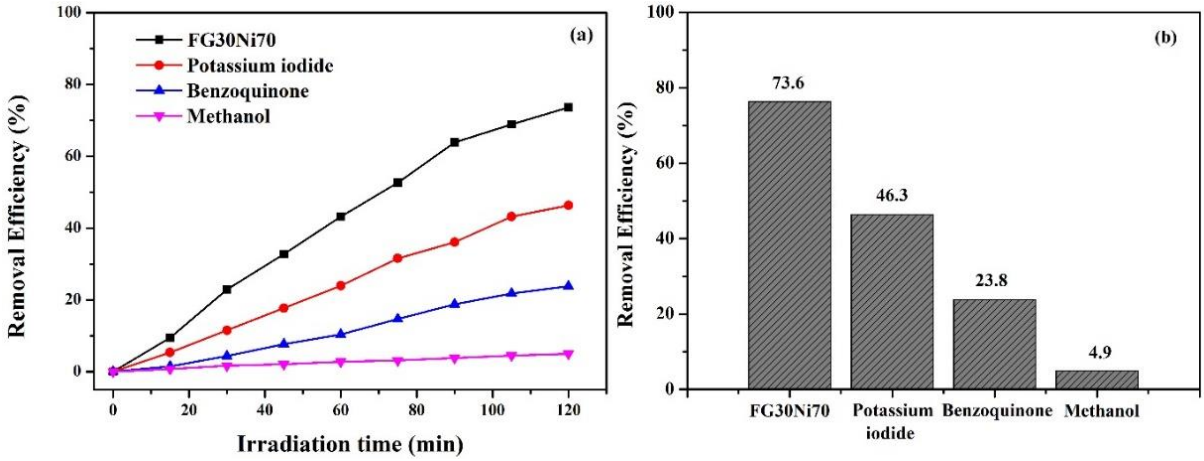

Figure 6-18 Photo-degradation efficiency of FG30Ni70 and its species scavenger samples (potassium iodide, p-benzoquinone, and methanol): (a) time-based curve and (b) histogram.

6.3 Discussion

6.3.1 The physical adsorption of RhB and MO with GNT

The well-dispersed GNT nanostructures have demonstrated dye removal properties with both RhB and MO dyes, especially the GNT1-5 sample showed the highest adsorption performance. This is consistent with the BET results that it displayed the largest BET surface are and lowest Zeta potential. Such a negative charge can be attributed to the ionization of the functional groups (i.e., carboxylic acid and phenolic hydroxyl groups) generated on the surface of acid-treated CNTs and GOs. Thus, it can be assumed that the higher surface area could provide more sites with functional groups, which would lead to higher negative charges. The adsorption kinetics and adsorption isotherms analysis are then discussed below.

Adsorption kinetics analysis of GNT nanostructures with RhB and MO

From the adsorption results of both RhB and MO above, the adsorption capacities of both RhB and MO in GNT 1-5 samples tend to reach equilibrium after 60 min and remain stable even reach 120 min. Before the kinetic analysis, we investigate the stability of the GNT samples after 120 min experiment in water. The SEM images of GNT nanostructures after 120 min dye adsorption are shown in appendix 2. It can be found that the graphene-layer-like structure of GNT samples remained after 120 min adsorption. Thus, a further investigation of the adsorption mechanism of both RhB and MO with GNT 1-5 samples was introduced, and two different models (the pseudo-first-order and pseudo-second-order model [105]) are adopted to analyse the kinetic characteristics of the adsorption process.

The pseudo-first-order model and pseudo-second-order model can be described as:

$$\log(q_e - q_t) = \log q_e - \frac{k_1 t}{2.303} \qquad \text{Equation 6-1}$$

$$\frac{t}{q_t} = \frac{1}{k_2 q_e^2} + \frac{t}{q_e} \qquad \text{Equation 6-2}$$

where q_e and q_t are the amounts of dye (RhB and MO, mg g^{-1}) adsorbed at the different time (t) and equilibrium (e), while the k_1 (1 min^{-1}) and k_2 (g mg^{-1} min^{-1}) are the rate constants of pseudo-first-order model and pseudo-second-order model, respectively.

The fitted curves of RhB adsorption with GNT 1-5 samples are displayed in Figure 6-19. The obtained kinetic parameters and correction coefficients (R^2), determined by linear regression, are listed in Table 6-1. In Figure 6-19a, the obtained experimental data cannot be fitted well with the pseudo-first-order equation, and the poor R^2 coefficients shown in Table 6-1 of the pseudo-first-order model suggest the process does not follow the pseudo-first-order model. Meanwhile, the pseudo-second-order model fitted curves displayed in Figure 6-19b showed a good fit with experimental data at all initial RhB concentrations. The R^2 in Table 6-1 for all concentrations are also around 0.9999, which confirms that the RhB adsorption follows the pseudo-second-order model. The calculated q_e of pseudo-second-order (Table 6-1) indicates that the equilibrium adsorption capacity of RhB with GNT 1-5 samples increases from 96.30 mg g^{-1} in 10 ppm solution to 146.16 mg g^{-1} in 25 ppm solution. In addition, the adsorption results of 5 ppm RhB solution is not adopted as the amount of RhB is far lower than the adsorption capacity and all the dyes can be adsorbed in 5 ppm solution.

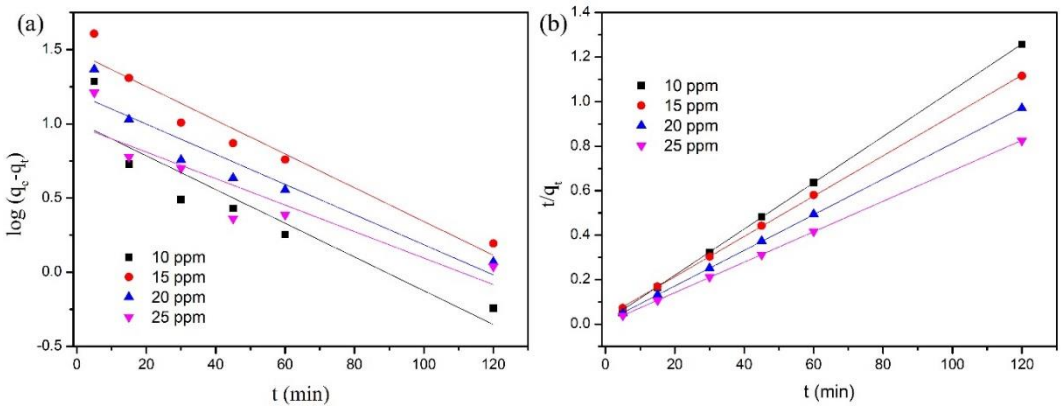

Figure 6-19 The kinetic plots of (a) pseudo-first-order and (b) pseudo-second-order in RhB adsorption with GNT 1-5 samples.

Table 6-1 The calculated kinetic parameters for the RhB adsorption with GNT 1-5 samples with different models.

C_0 (ppm)	Pseudo-first-order				Pseudo-second-order		
	k_1 (min^{-1})	$q_{e,exp}$ (mg g^{-1})	$q_{e,cal}$ (mg g^{-1})	R^2	k_2 (g mg^{-1} min^{-1})	$q_{e,cal}$ (mg g^{-1})	R^2
10	0.0262	95.43	12.63	0.8268	0.0087	96.30	0.9999
15	0.0262	107.57	30.17	0.9275	0.0025	110.46	0.9999
20	0.0037	123.67	15.91	0.8873	0.0055	124.91	0.9999
25	0.0048	145.39	9.74	0.7784	0.0094	146.16	0.9999

A similar investigation of the MO adsorption with GNT 1-5 sample has also been carried out and the fitted curves and kinetic parameters are displayed in Figure 6-20 and Table 6-2. The obtained experimental data does not match well with the pseudo-first-order model (Figure 6-20a), there are differences between experimental capacity ($q_{e,exp}$) and calculated capacity ($q_{e,cal}$). The pseudo-second-order model fitted results shown in Figure 6-20 b and Table 6-2 illustrate a good fit with experimental data, and the high R^2 (all > 0.99) confirmed that the MO adsorption also follows the pseudo-second-order model. The obtained adsorption capacities at different concentrations ($q_{e,cal}$ Table 6-2) show that the capacity increases from 35.58 mg g^{-1} in 5 ppm MO solution to 58.17 mg g^{-1} in 30 ppm MO solution.

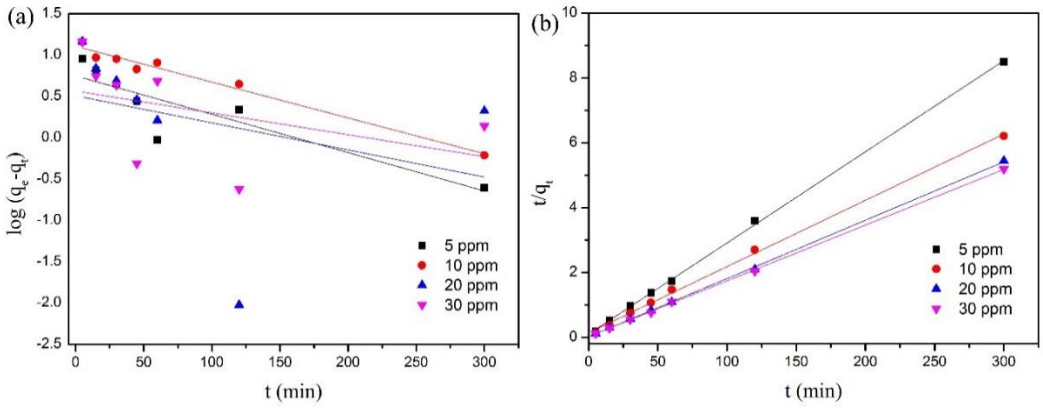

Figure 6-20 The kinetic plots of (a) pseudo-first-order and (b) pseudo-second-order in MO adsorption with GNT 1-5 samples.

Table 6-2 The calculated kinetic parameters for the MO adsorption with GNT 1-5 samples with different models.

C_0 (ppm)	Pseudo-first-order				Pseudo-second-order		
	k_1 (min^{-1})	$q_{e,exp}$ (mg g^{-1})	$q_{e,cal}$ (mg g^{-1})	R^2	k_2 (g mg^{-1} min^{-1})	$q_{e,cal}$ (mg g^{-1})	R^2
5	0.0107	35.33	5.59	0.7549	0.0078	35.58	0.9995
10	0.0010	48.32	12.76	0.9746	0.0030	48.94	0.9982
20	0.0076	57.26	3.21	0.0748	0.0283	55.57	0.9996
30	0.0061	58.93	3.66	0.0203	0.0136	58.17	0.9996

Adsorption isotherms analysis

The adsorption isotherm aiming to describe the relationship between the adsorption capacities of the adsorbent (q_e) and the different concentrations of dyes is shown in Figure 6-21. This can help identify the adsorption mechanism and the heterogeneity of the adsorbent surface [128]. In this study, two well-known isotherm models, the Langmuir [183] and the Freundlich [136] model, are used to describe the adsorption relationship, and they can be presented as the below equations:

$$\frac{C_e}{q_e} = \frac{1}{bq_m} + \frac{C_e}{q_m} \quad \text{Equation 6-3}$$

$$lnq_e = \frac{1}{n} lnC_e + lnK_f \quad \text{Equation 6-4}$$

where the C_e (mg L^{-1}) is the initial dye concentration at the different point, q_e (mg g^{-1}) is the obtained adsorption capacity at different concentration (C_e), b (L mg^{-1}) is a constant in Langmuir isotherm and q_m (mg g^{-1}) is the Langmuir monolayer adsorption capacity which can indicate the maximum adsorption. The 1/n in the Freundlich isotherm model is a constant related to the adsorption intensity and the K_f is a Freundlich constant related to adsorption capacity.

The Langmuir adsorption isotherm theory describes monolayer adsorption, which assumes that

the adsorbates display a homogeneous monolayer coverage on the surface of the adsorbent [183], while the Freundlich adsorption isotherm theory describes adsorption which happens on a heterogeneous surface of the adsorbent as well as there is also multi-layer sorption [136]. The isotherms based on obtained experimental data of RhB with GNT 1-5 samples and the correlation parameters between the theory and experimental data are illustrated in Figure 6-21a and its insert table. It can be found that the Freundlich isotherm exhibits higher R^2 (around 0.98), which indicates that the multi-layer adsorption has happened on the surface of GNT 1-5 samples. In addition, the adsorption capacity can be estimated up to 248.5 mg g^{-1} according to the Langmuir model with an R^2 of 0.956. Thus, it can be assumed that by combining the electrostatic interactions and π-π interaction, the adsorption of RhB with GNT 1-5 samples exceeds the monolayer process and exhibits a multi-layer adsorption process, and the maximum adsorption can be estimated over 248.5 mg g^{-1}. The MO adsorption isotherms are displayed in Figure 6-21b. It is noted that the MO adsorption experimental data is fitted well with the Langmuir isotherm model with an R^2 of 0.9801, which is significantly higher than that of the Freundlich model (0.8826), indicating homogeneous monolayer adsorption. The maximum adsorption capacity of MO with GNT 1-5 samples can reach 66.9 mg g^{-1}. Based on the Zeta potential results, due to the negative charges on the surface of GNT samples and the different charges of the dyes, much more RhB can be adsorbed, indicating the multi-layer sorption, while less MO were adsorbed with the homogeneous monolayer adsorption mainly based on π-π interaction.

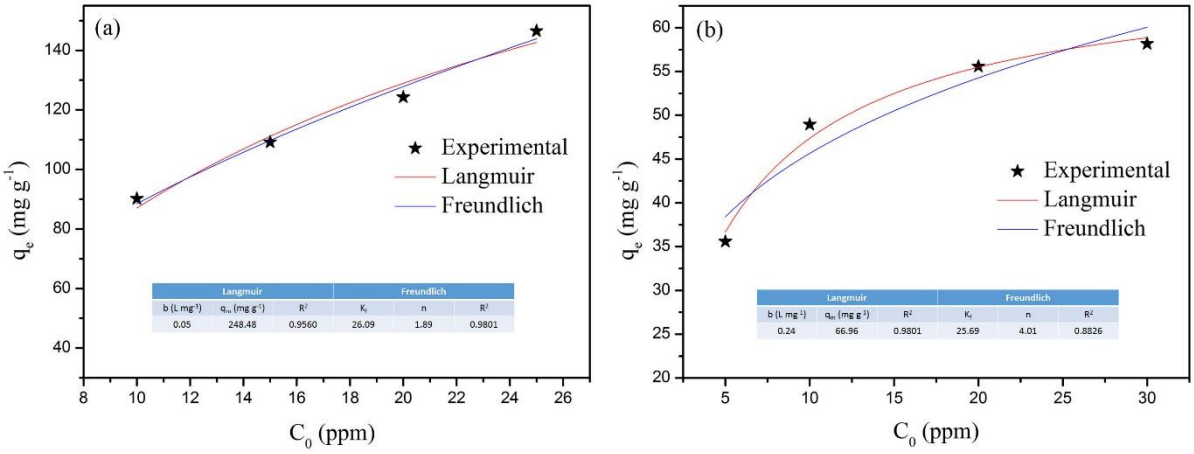

Figure 6-21 Adsorption isotherm curves of the RhB (a) and MO (b) on the GNT 1-5 samples, and the insert tables show the regression parameters between each model and experimental measurements.

Table 6-3 exhibits some RhB and MO adsorption capacity results with different adsorbents reported and the results presented in this research. The GNT 1-5 sample shows adsorption capacities with both RhB and MO than other adsorbents (i.e., red mud and montmorillonite [184, 185]). The 3D GO-based hydrogel, which had a calculated surface area of 298.2 m^2 g^{-1}, only exhibited an RhB adsorption capacity of only 29.4 mg g^{-1} [114], which is less than the GNT 1-5 samples. In addition, the Ni embedded graphitic carbon, which exhibited a surface area of 790 m^2 g^{-1}, has an adsorption capacity of 168.1 mg g^{-1} [118], indicating that although the GNT samples showed lower BET surface area than the materials above, the unique structure may provide more active sites to adsorb organic dyes. Thus, the GNT samples prepared through a facile freeze-drying method show great potential as an efficient adsorbent, and the prepared 3D GNT nanostructures have shown great potential in waste-water treatment to remove organic dyes.

Table 6-3 Table of adsorption capacity of RhB and MO with different adsorbents.

Adsorbents	Dye	Adsorption capacity (mg/g)	References
GNT 1-5 sample	RhB	248.5	This work
	MO	66.9	This work
Ni embedded graphitic carbon	RhB	168.1	[118]
Reduced GO-based hydrogels	RhB	29.4	[136]
Bentonite-CNT nanocomposite	RhB	142.8	[115]
Red mud	RhB	92.5	[184]
MWCNTs	MO	54.8	[116]
Calcium alginate-MWCNTs	MO	12.5	[117]
SiO_2/Fe_3O_4	MO	53.2	[186]
Modified montmorillonite	MO	24.0	[185]

6.3.2 The physical adsorption of RhB with FGNi nanostructures

Using the pseudo-first-order and pseudo-second-order models [104, 105], the adsorption kinetic study of the physical adsorption process in the FG30Ni70 sample was carried out at 5 ppm of RhB solution under dark.

The pseudo-first-order model could be presented as:

$$\log(q_e - q_t) = \log q_e - \frac{k_1 t}{2.303} \quad \text{Equation 6-5}$$

The pseudo-second-order model could be presented as:

$$\frac{t}{q_t} = \frac{1}{k_2 {q_e}^2} + \frac{t}{q_e} \quad \text{Equation 6-6}$$

where q_e and q_t are the amounts of RhB (mg g^{-1}) adsorbed at time t and equilibrium, while k_1 and k_2 are the rate constants of pseudo-first-order adsorption (min^{-1}) and pseudo-second-order

adsorption (g mg^{-1} min^{-1}). As shown in Figure 6-22, the adsorption capacity of FG30Ni70 samples in 5 ppm solution increases rapidly in the initial 10 minutes, before stabilizing later. The capacity reaches 14.6 mg g^{-1} in 90 min, with a minor increase afterward. The data fitting based on those two kinetic models (blue line for pseudo-first-order and red line for pseudo-second-order) is also shown in Figure 6-22. The relevant fitted results, including correlation coefficients (R^2), are illustrated in the insert table of Figure 6-22. According to the R^2 of both models, the pseudo-second-order model is a better fit than the pseudo-first-order model, which is 0.9920 to 0.9675. In the fitted curve (Figure 6-22), the pseudo-first-order shows plateaus after 30 mins, while the second-order model continues to increase. The physical adsorption of RhB with FGNi nanostructures shows a pseudo-second-order model with R^2. The calculated equilibrium adsorption capacity from the pseudo-second-order model (15.5 mg g^{-1}) is also more accurate than the pseudo-first-order model (13.6 mg g^{-1}) when compared with the experimental data (14.8 mg g^{-1}).

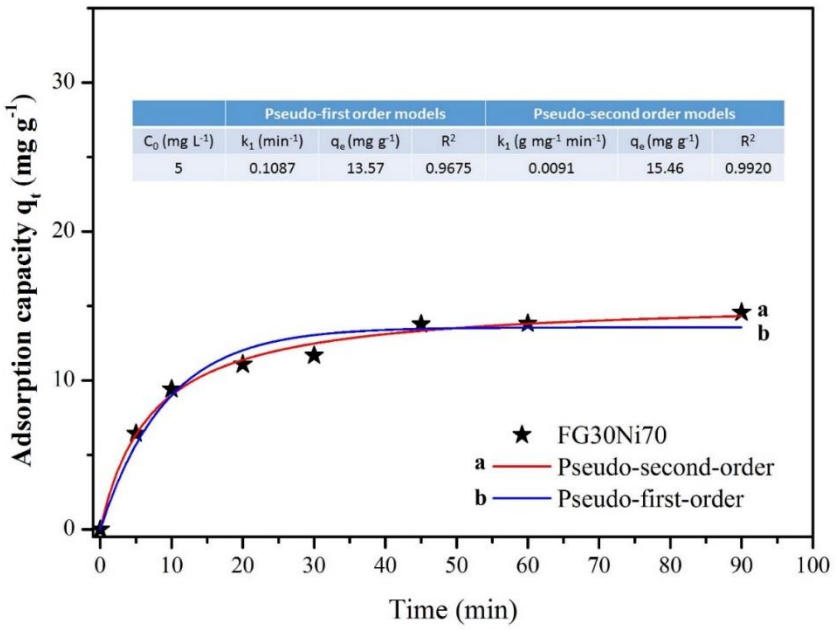

Figure 6-22 Kinetic plots of FG30Ni70 samples in 5 ppm RhB solution, the insert table is the adsorption kinetic parameters fitted by the pseudo-first-order and pseudo-second-order models.

6.3.3 Photo-degradation of RhB under UV irradiation with FGNi nanostructures

The possible mechanism of the dye degradation with novel Ni decorated carbon composites is proposed in Figure 6-23. As shown in Reaction (1), it is believed that the electrons can be excited from the dye (i.e., $RhB^{\cdot +}$), trapped by the surface absorbed O_2 and generated several reactive radicals [54, 187]. The electrons injection rate has been proven to be faster in graphene-based materials than that in traditional semiconductors [146, 147]. But the faster transfer of electrons may lead to faster recombination of electrons and $RhB^{\cdot +}$, which resulted in poor degraded performance. However, after the coating of Ni nanoparticles, due to the higher work function of CNTs and Ni (-4.8 eV and -5.15 eV, respectively), higher than graphene (-4.42 eV) [146, 147]. It is believed that the electrons can be transferred to Ni and CNTs, which enhanced the separation process of $dye^{\cdot +}$ and electrons rather than the recombination between them. The electrons were then trapped by surface absorbed O_2 to produce $O_2^{\cdot -}$ free radicals that would degrade the RhB dyes as described in Reaction (2). That is why the removal efficiency decreased to 23.2% after the addition of BQ (Figure 6-18). Meanwhile, the more dominant degradation process was caused by $OH^{\cdot}$ free radicals as shown in the scavenger test (Figure 6-18). Although the generation of $OH^{\cdot}$ free radicals normally occurred through the oxidation of holes as shown in Reaction (3) [110, 151], this not happened in this case, as demonstrated by the scavenger experiment. Therefore, the generation of $OH^{\cdot}$ free radicals in this system is likely from the oxidation of water molecules by $O_2^{\cdot -}$ free radicals as described in Reaction (4). That is why the scavenger of either $O_2^{\cdot -}$ or $OH^{\cdot}$ free radicals would significantly decrease the removal efficiency. Finally, the obtained free radicals then react with dyes and produce environmental products (i.e., H_2O and CO_2) [187].

$RhB \rightarrow RhB^{\cdot +} + e^-$, Reaction (1)

$e^- + O_2 \rightarrow O_2^{\cdot -}$, Reaction (2a)

$O_2^{\cdot -} + RhB^{\cdot +} \rightarrow$ Degradation products (i.e. H_2O and CO_2) Reaction (2b)

$h^+ + OH^- \rightarrow OH^{\cdot}$ Reaction (3)

$e^- + O_2 \rightarrow O_2^{\cdot -} + H_2O \rightarrow 2\ OH^{\cdot}$, Reaction (4)

$OH^{\cdot} + RhB^{\cdot +} \rightarrow$ Degradation products (i.e. H_2O and CO_2), Reaction (5)

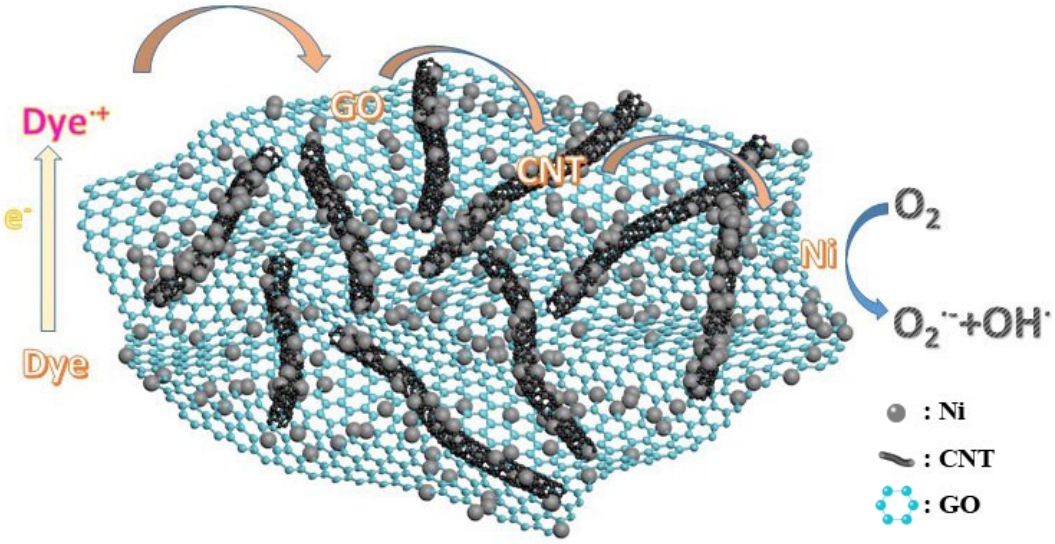

Figure 6-23 Proposed schematics of the photocatalytic mechanism with FGNi nanostructures.

Ni or ferrite-based carbon materials were initially adopted as physical adsorbents due to their ferromagnetism property, which made these adsorbents easy to collect. Very few Ni-based products were reported as photocatalytic materials. Based on the RhB removal performance, the removal capacity of the FG30Ni70 sample far outperformed them. Table 6-4 presents the comparison of dye removal performance between this work with previous results. In the 3D hierarchical Ni/C nanocomposites, the products show only 12.5 mg g^{-1} adsorption capacity even with 10 ppm solution [188], though only physical adsorption was investigated in their study. The values for FG30Ni70 nanostructures in this work are 17.4 mg g^{-1} at 5 ppm and 20.0

mg g^{-1} in 10 ppm solution (Figure 6-17). The Ni@graphene nanocomposites only displayed an adsorption capacity of 4 mg g^{-1} even under 20 ppm RhB solution. In the Ni - carbon shell - graphene nanocomposites, a removal capacity of 21.1 mg g^{-1} was obtained with 5 ppm RhB solution [189], while it is 41.5 mg g^{-1} for FG30Ni70 nanostructures in the current study. Meanwhile, the graphene-Au nanocomposite, which was adopted as the photocatalytic material showed a photo-degradation capacity of 29.7 mg g^{-1} [147]. This value for the 3D CNT-pillared RGO nanostructure (with Ni particles as the catalyst for CNT growing) was around 24.2 7 mg g^{-1} [146]. In addition, the ferromagnetism of Ni nanoparticles coating makes FGNi nanostructures easy to collect after reaction using magnets (Figure 6-24). Thus, the recycling usage of FGNi sample becomes possible, and this will be explored in our further investigation.

Table 6-4 Comparison of RhB dye removal performance between this work and previous results.

Samples	Initial concentration (ppm)	Adsorption (mg g^{-1})	Photo-degradation (mg g^{-1})	Reference
3-d hierarchical Ni/C nanocomposites	10	12.5	--	[188]
Ni@graphene nanocomposites	20	4	--	[126]
Ni - carbon shell - graphene nanocomposites	4.8	21.1	--	[189]
graphene–gold nanocomposites	2.5		29.7	[147]
3D CNT-pillared RGO nanostructure	2.5		24.2	[146]
FG30Ni70	5.0		41.6	This work

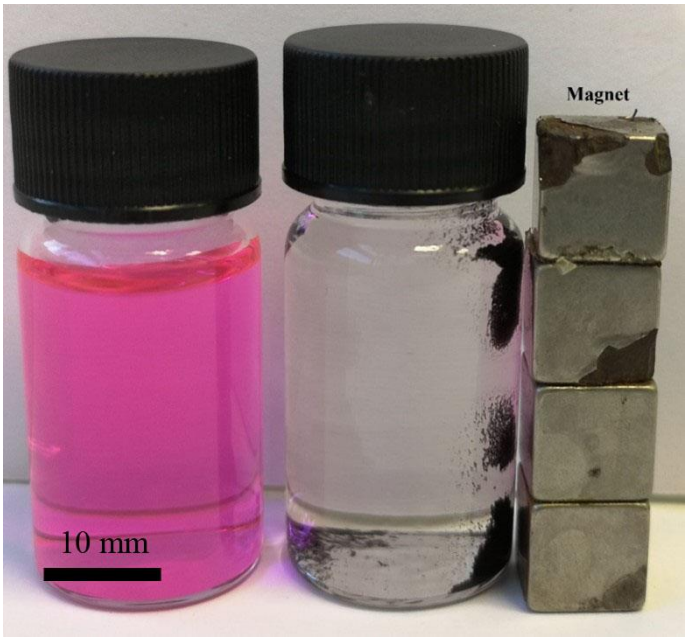

Figure 6-24 RhB removal performance of FG30Ni70 samples in the RhB solution.

6.4 Summary

In summary, a facile preparation method based on the freeze-drying process has been introduced to synthesise GO-CNTs nanostructures. The uniform dispersion through ultrasonication and fast freezing in LN has largely kept the well-dispersed structures, and the subsequent freeze-drying approach completely removed the water. Thus, a well-dispersed 3D structure was obtained, and the SEM results also confirm that no obvious agglomeration occurred in final products. In addition, N_2 sorption measurement indicates that the GNT nanostructures have a mesoporous structural feature with a high surface area of 257.56 m^2 g^{-1} in GNT 1-5 sample. The dye removal performances show that both cationic (RhB) and anionic (MO) dyes can be adsorbed by GNT samples, and the GNT 1-5 sample displays the best adsorption performances with an adsorption capacity of 248.5 mg g^{-1} for RhB and 66.9 mg g^{-1} for MO. The adsorption difference can be ascribed to the different charges of the dyes in the solution. Meanwhile, the uniformly distributed Ni nanoparticles decorated onto such GNTs have also been successfully prepared by combing the MLM process with a subsequent

reduction method. The obtained products possess a unique structure with a high surface area and exhibit excellent dye removal performance. The RhB removal test demonstrates a synergistic effect of physical adsorption and photodegradation under UV irradiation. The FG30Ni70 samples displayed a removal capacity of 41.5 mg g^{-1} in 5 ppm RhB solution, which outperformed the most reported Ni/C products. Considering the ferromagnetism of Ni nanoparticles, the FGNi samples are easy to collect after reaction with dyes by magnetic separation technology. Therefore, the novel FGNi nanostructures through a facial preparation method showed great potentials as an efficient material in removing organic dyes.

7 Copper-based composites and the exploration of their thermal management property

Copper, which demonstrates relatively high thermal conductivity (around 400 W $m^{-1}K^{-1}$), has now been widely applied as commercial thermal management material. However, traditional thermal management materials cannot match the rapidly increasing thermal conductivity requirements resulting from the development of modern technologies. Advanced materials with enhanced thermal management properties have become one of the important approaches to deal with this problem. As described in chapter 4, the Cu nanoparticles decorating GNT nanostructures displayed well-dispersed structures with a uniform distribution of Cu nanoparticles, which make them potential fillers in reinforcing Cu matrix. In this chapter, different consolidation approaches have been explored in preparing dense pellets and the thermal conduction performance has been carefully measured and discussed.

7.1 Exploration of consolidation parameters with pure copper powders

7.1.1 Characterisation of commercial Cu micron powders

Micron copper powders [325 mesh (0.1%> 63μm, 96.1%<45μm)], which are supplied from Inoxia Ltd., have been used to prepare Cu based pellets. Before consolidation, basic characterisation measurements have been introduced to analyse the purchased powders. The XRD patterns of the purchased Cu micron powders are displayed in Figure *7-1*a (curve 1). It can be found that the three strongest diffraction peaks can be matched well with the pure Cu phase, and no other apparent peaks can be detected, which indicates that there is no distinct

impurity among the purchased Cu powders via XRD. However, obvious oxidised copper signals (both the satellite peak at around 945 eV and the high valence peaks of Cu in Cu $2p_{1/2}$ and Cu $2p_{3/2}$) can be detected in the XPS high-resolution Cu 2p peaks, indicating surface oxidisation on the Cu micron powders. Although the XRD cannot detect impurity phases in the Cu micron powders, it can be speculated that there was slight surface oxidisation on the purchased Cu powders, and this oxidisation would be harmful to the consolidation of the powders as the oxidisation layer would hinder the Cu particles pressing together. Therefore, the purchased Cu powders have been then pre-reduced under Ar/H_2 atmosphere at 450°C for 2h, and the XRD and XPS results are shown in Figure *7-1* a and b. The XRD patterns of the reduced powders (curve 2 in Figure *7-1*a) demonstrate no difference when compared with purchased powders, but the high-resolution XPS data (curve 2 in Figure *7-1*b) shows sharp peaks of Cu $2p_{1/2}$ and $2p_{3/2}$ and no more oxidised of Cu can be detected, indicating pre-reduction was successful.

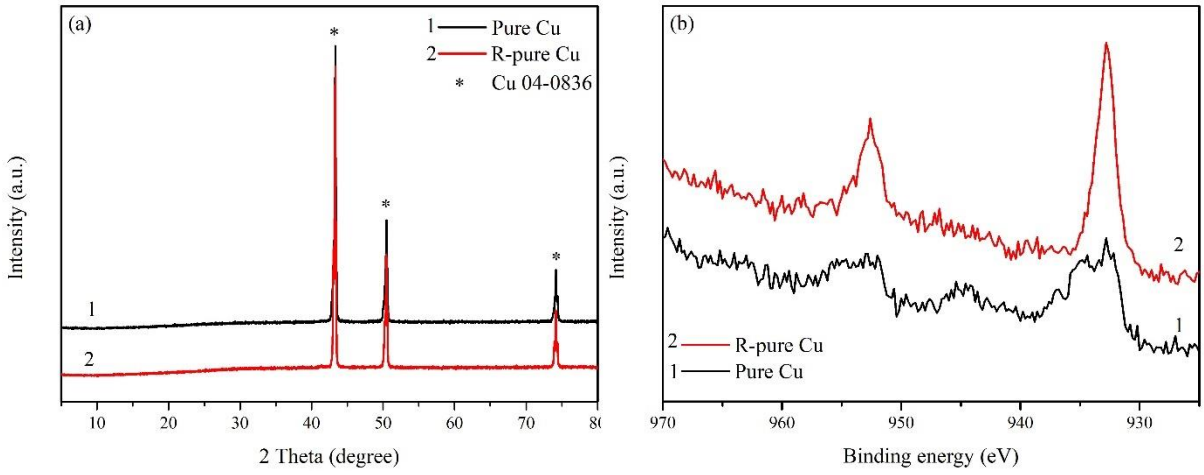

Figure 7-1 XRD (a) and XPS (b) results of pure Cu and pre-reduced-pure Cu samples.

SEM has been introduced to investigate the morphologies of the purchased Cu and pre-reduced Cu powders, and the results are displayed in Figure *7-2*. For the SEM images of purchased Cu (Figure *7-2* a and b), a large range of particle sizes can be observed, ranging from 10 - 50 μm, which is consistent with the supplier's introduction. In the high-resolution image, the round Cu

particles can be clearly observed, and the surface of the particle also looks smooth. After being pre-reduced under Ar/H_2 atmosphere at 450°C for 2 h, the SEM images of reduced Cu powders are shown in Figure *7-2* c and d. No obvious differences in morphologies can be detected between the pure and reduced powders, and the surface of the reduced particle also looks smooth. The reduced Cu micron powders have been adopted for the subsequent experiments and measurements based on the XRD, XPS, and SEM results.

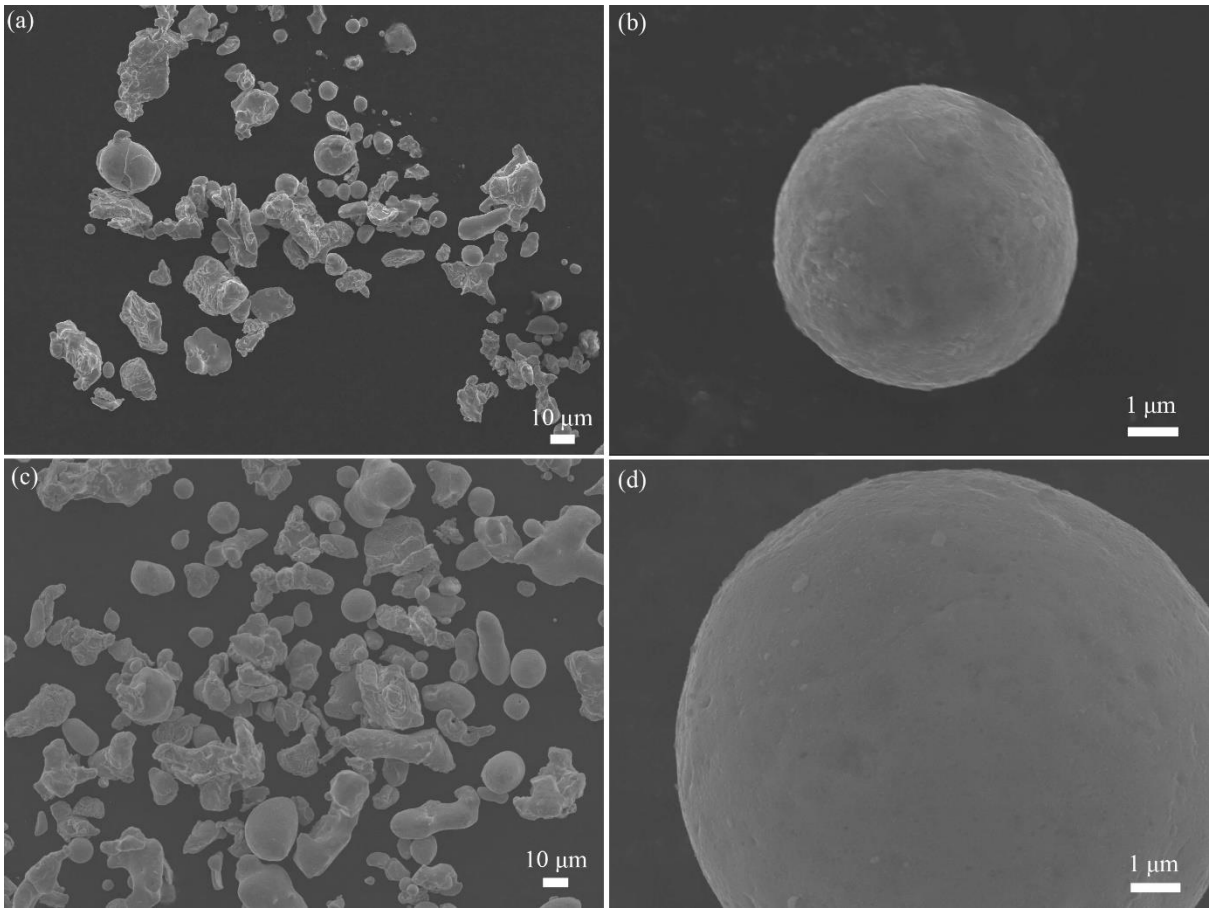

Figure 7-2 SEM images of purchased (a and b) and reduced (c and d) Cu powders.

7.1.2 Manual pressing and sintering, and relevant parameter exploration

After the confirmation of being completely reduced, the pre-reduced Cu micron powders have then been densified through a common manual pressing and sintering process. Specifically, the as-reduced powders are initially pressed through the manual hydraulic press and then annealed at different temperatures. The densities of the obtained pellets at each pressing condition have

then been investigated and the results are displayed in Table *7-1*. Sample 1 is the pellet obtained after pressing with a vertical pressure of 376 MPa for 5 min without annealing. The measured density is around 8.06 g cm^{-3}, which is 89.9% of pure Cu. After annealing at 500°C for 1 h under vacuum, pellet 2 displays a density of 8.33 g cm^{-3} (92.3%), indicating that the annealing process after pressing is beneficial to obtain a denser pellet. Based on sample 2, two more explorations have been introduced with higher annealing temperatures at 600 and 800°C, respectively. It can be found that the density of the obtained pellet increases continuously with the growth of annealing temperature. However, although the relative density of the sintered pellet rises from 89.9% to 94.4%, the relative density is still too low compared to solid Cu and cannot achieve the requirement for further application.

Table 7-1 Density of the manual pressing and sintering Cu pellets.

Sample	Consolidation condition	Density (g cm^{-3})	Relative density (%)
1	376 MPa for 5 min without annealing	8.06	89.9
2	376 MPa for 5 min at 500°C for 1 h+376 MPa for 5 min	8.33	92.3
3	2+600°C for 1 h+376 MPa for 5 min	8.34	93.1
4	2+800°C for 1 h+376 MPa for 5 min	8.46	94.4

To improve the density of the obtained Cu pellets and simplify the consolidation process, pressure-assisted sintering (SPS) has been introduced and different pressing conditions have been investigated. Table *7-2* demonstrates the density of SPS pressed Cu samples under different temperatures and pressures. It can be found that the Cu pellet obtained at 600°C 50 MPa for 5min displays better density (8.49 g cm^{-3}) than the best sample (sample 4) produced through manual pressing and sintering, and the obtained density of the Cu pellet increased with the growth of the holding pressure, and the optimal density can reach 8.88 g cm^{-3} which is around 99.1% of relative density compared with pure Cu. Thus, the Cu pellet prepared through SPS at 800°C 60 MPa for 5min could be considered as dense as pure Cu solid, and this condition could be adopted for further application.

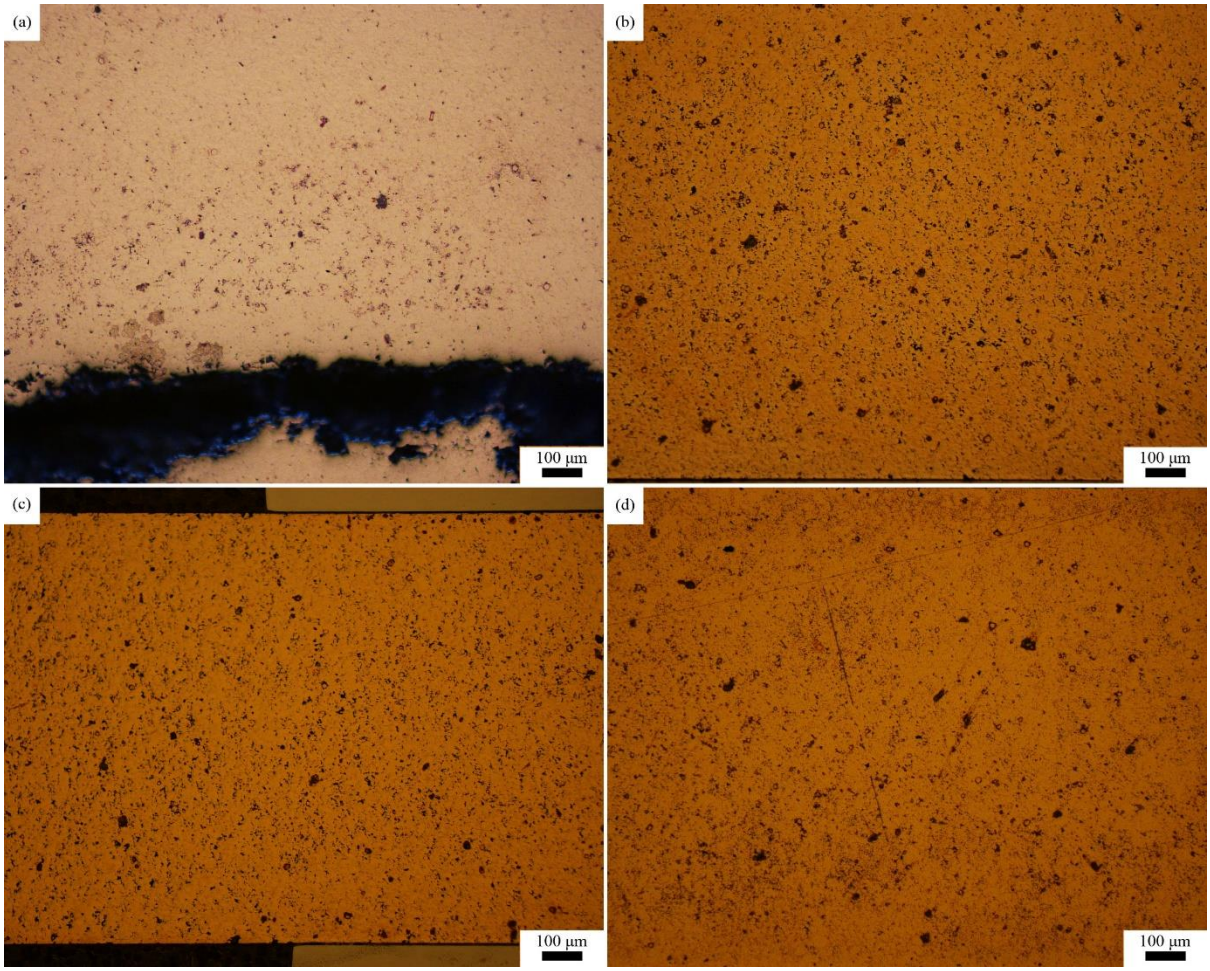

Figure 7-3 Cross-section of manual pressing and sintering Cu sample 1 (a), 2 (b), 3 (c), and 4 (d).

7.1.3 Pressure-assisted sintering (Spark plasma sintering)

The optical images of the SPS Cu samples under 60 MPa at different temperatures are displayed in Figure *7-4*. Obvious voids still can be found on the cross-section of the Cu pellet, which was obtained at 600°C for 5 min (Figure *7-4*a). This result is consistent with the data from Table *7-2* that 95.4% of the relative density was obtained. With the pressing temperature reaching 700°C and above, there is a significant increase in density, and the relative density reaches as high as around 99%. The optical images of both samples at 700 and 800°C (Figure *7-4* b and c) show far fewer voids, indicating the perfect densification of the reduced Cu micron powders through SPS. Combining the Archimedes principle data with the cross-section optical images of the Cu pellets, it can be found that dense Cu pellets were successfully obtained, and fewer voids

could be detected when the pressing temperature reaches 700°C. Therefore, the thermal conduction performances of these dense Cu pellets produced through SPS could be measured later, and the optimal SPS parameters to prepare dense pellets could be adopted further in the composites' preparation section.

Table 7-2 Density of the SPS Cu pellets under different conditions.

Sample	Consolidation condition	Density (g cm^{-3})	Relative density (%)
1	600°C, 50 MPa, 5min	8.49	94.7
2	700°C, 50 MPa, 5min	8.79	98.1
3	800°C, 50 MPa, 5min	8.85	98.8
4	600°C, 60 MPa, 5min	8.55	95.4
5	700°C, 60 MPa, 5min	8.85	98.8
6	800°C, 60 MPa, 5min	8.88	99.1

The optical images of the SPS Cu samples under 60 MPa at different temperatures are displayed in Figure *7-4*. Obvious voids still can be found on the cross-section of the Cu pellet, which was obtained at 600°C for 5 min (Figure *7-4*a). This result is consistent with the data from Table *7-2* that 95.4% of the relative density was obtained. With the pressing temperature reaching 700°C and above, there is a significant increase in density, and the relative density reaches as high as around 99%. The optical images of both samples at 700 and 800°C (Figure *7-4* b and c) display that much fewer voids could be observed among the cross-section, indicating the perfect densification of the reduce Cu micron powders through SPS. Combining the Archimedes principle data with the cross-section optical images of the Cu pellets, it can be found that the dense Cu pellets were successfully obtained, and no obvious voids could be detected when the pressing temperature reaches 700°C. Therefore, the dense Cu pellets through SPS could be applied in thermal conduction measurement, and the optimal SPS parameter to prepare dense pellets could be adopted in the further composites' preparation section.

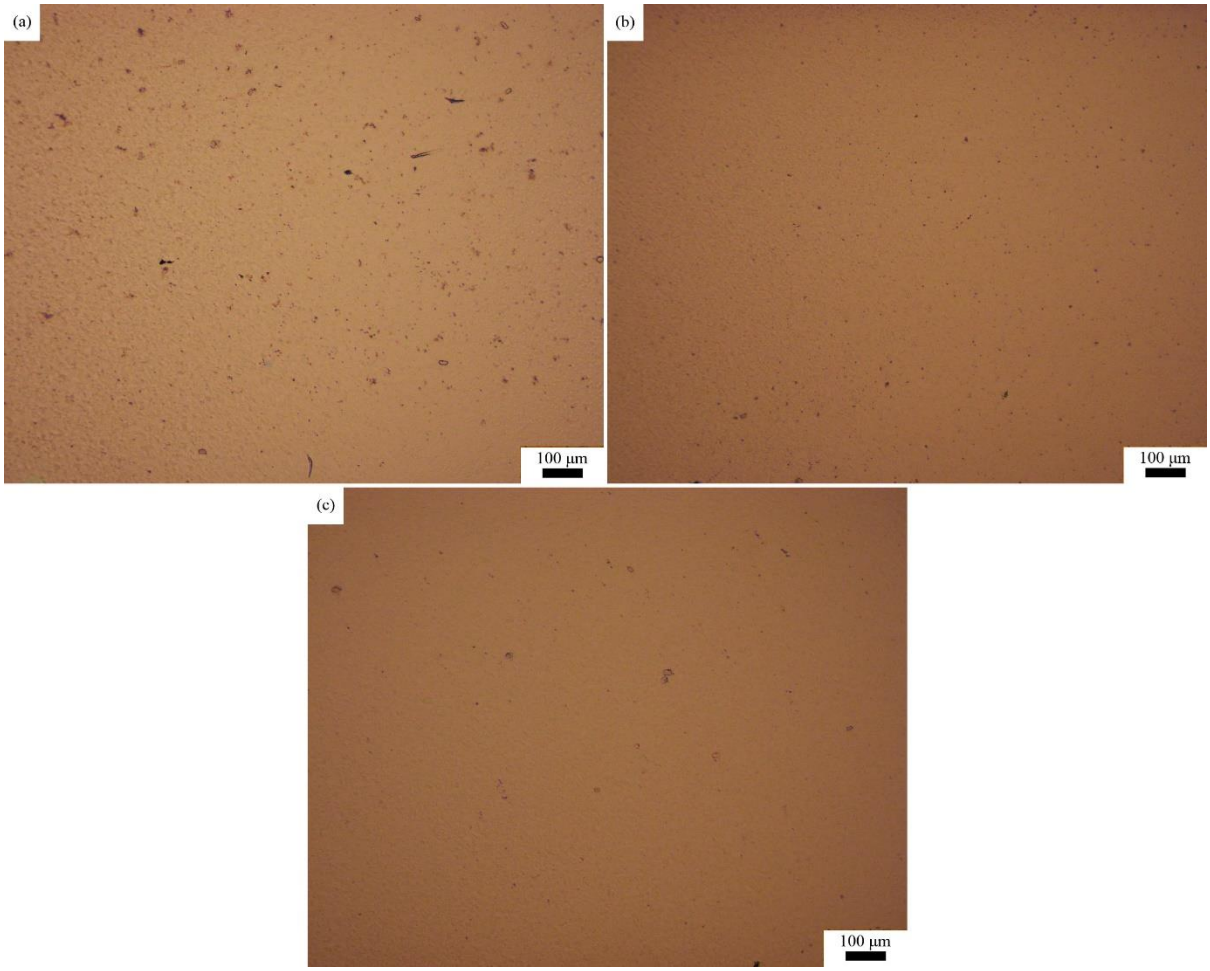

Figure 7-4 Cross-section of SPS Cu sample under 60 MPa at 600°C (a), 700°C(b), and 800°C (c).

7.1.4 Thermal conductivity of the Cu pellets through different sintering methods

After the density measurements, the thermal diffusivities of the as-prepared Cu pellets through manual pressing and sintering were then measured, and the results are shown in Figure *7-5*a. It can be noticed that the thermal diffusivity of the manual pressing and sintered Cu pellet grows with increasing density. This value increases from 29.7 mm^2 s^{-1} in sample 1, which was pressed without annealing, to 77.1 mm^2 s^{-1} in sample 4, whose density reaches 8.46 g cm^{-3} (94.4%). Since thermal diffusivity is closely connected with density, a denser structure and fewer voids would lead to better diffusivity. The obtained thermal conductivities of all samples calculated with the equation $K = \alpha \times \rho \times C_p$ are shown in Figure *7-5*b. A similar trend can also be

witnessed in the manual pressing and sintering Cu samples. The value grows from 89.4 W m^{-1} K^{-1} of sample 1 to 240.6 W m^{-1} K^{-1} of sample 5. Although thermal conductivity triples from sample 1 to sample 4, it is still far lower than the theoretical value of pure Cu (around 370 W m^{-1} K^{-1}). Therefore, manual pressing and sintering should not be applied to prepare dense Cu pellets under the current condition.

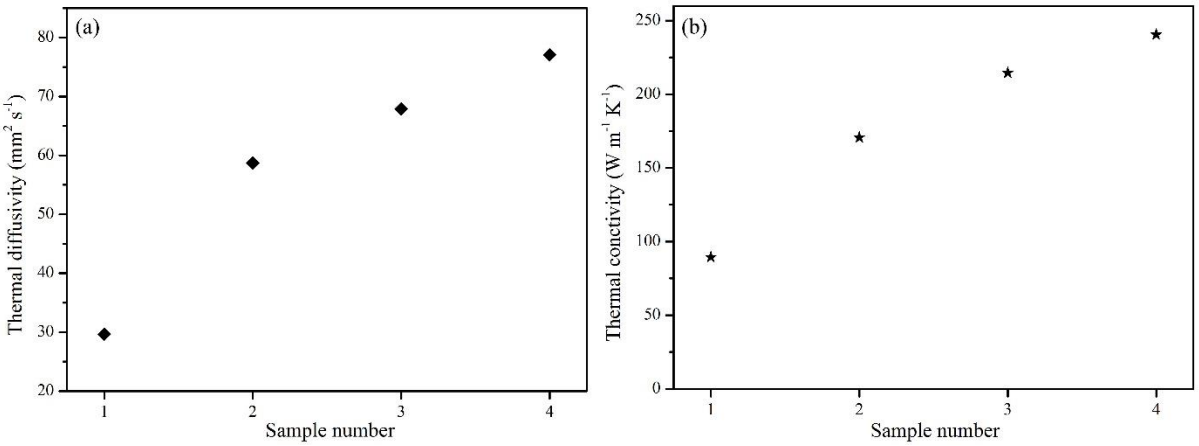

Figure 7-5 Thermal diffusivity (a) and thermal conductivity (b) of manual pressing and sintering of pure micron Cu pellets at different parameters.

The thermal conductivity of the SPS sintered Cu pellets has also been investigated and the results are displayed in Figure 7-6. Figure 7-6a illustrates the increasing thermal diffusivity of the SPS Cu pellets with increasing sintering temperature. This thermal diffusivity increases from 98.8 mm^2 s^{-1} for the Cu pellet, which was sintered at 600°C for 5min to finally around 104.2 mm^2 s^{-1} for the Cu pellet obtained at 800°C. According to the previous results, denser pellets should show better thermal diffusivity. By using the equation $K = \alpha \times \rho \times C_p$, the calculated thermal conductivities of these SPS sintered Cu pellets are displayed in Figure 7-6b. Like the density and thermal diffusivity trend, the SPS sintering pellet's thermal conductivity grows with increasing sintering temperature, especially when the sintering temperature reaches above 700°C (the relative density reaches around 99%) that the thermal conductivity reaches over 350 W m^{-1} K^{-1}. The highest obtained thermal conductivity of these SPS sintered Cu pellets appears in sample 3 (around 365 W m^{-1} K^{-1}), close to the commercial Cu's theoretic value. This

proves that the SPS prepared Cu pellets to show both similar density and thermal conductivity to pure Cu, and such parameters will be useful for further composites preparation.

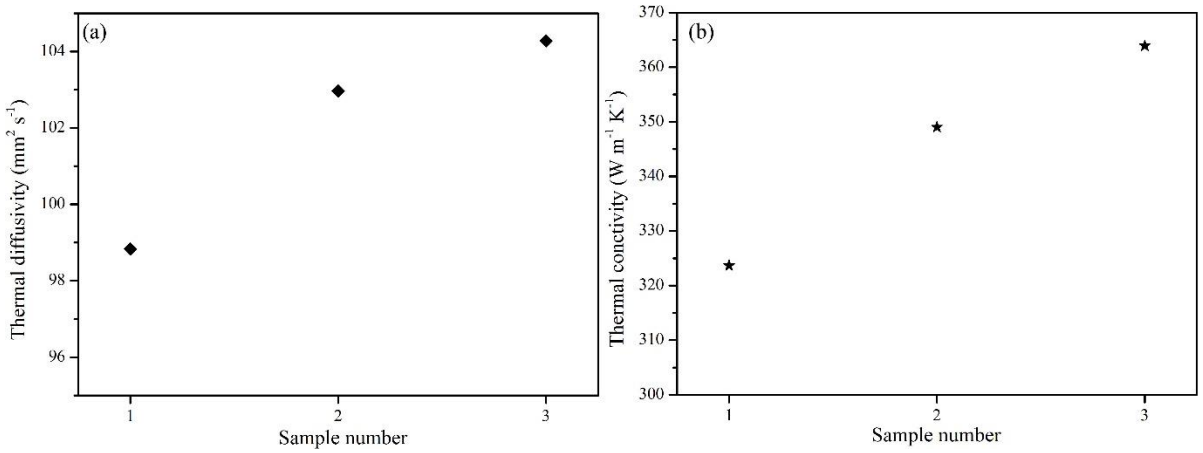

Figure 7-6 Thermal diffusivities (a) and thermal conductivities (b) of SPS consolidated pure micron Cu pellets at different parameters.

7.2 Preparation of FGCu nanostructure and micro Cu mixed powders

7.2.1 Filtration method to prepare FGCu-Cu mixed powders

The Cu nanoparticles decorated GNT (FGCu) nanostructures have been successfully prepared in chapter 4 and then been adopted as fillers to enhance the thermal performance of the SPS sintered Cu matrix. To prepare uniform mixed FGCu+Cu powders, the FGCu samples and Cu micron powders were dispersed in water and then vacuum filtrated. Before sintering, the obtained mixed powders were reduced in Ar/H_2 atmosphere at 450°C for 2 h to remove the surface oxidation, and the XRD and TGA results are displayed in Figure 7-7. In Figure 7-7a, the XRD patterns show the three strongest peaks, which correspond to the pure Cu phase, and the broad peak ascribed to the GNT component located at around 30° still can be observed. Thus, the XRD results confirm the constitution of the Cu and GNT components in the mixed powders, and no obvious signals generated grom impurities can be found. In the TGA results

(Figure *7-7*b), there is an obvious weight increase with temperature under the Air atmosphere. The final weight is around 123.23% after 800°C. The calculated weight percentage of the carbon part (GNT) is around 1.42 wt.%, which corresponds to 6.03 vol.%.

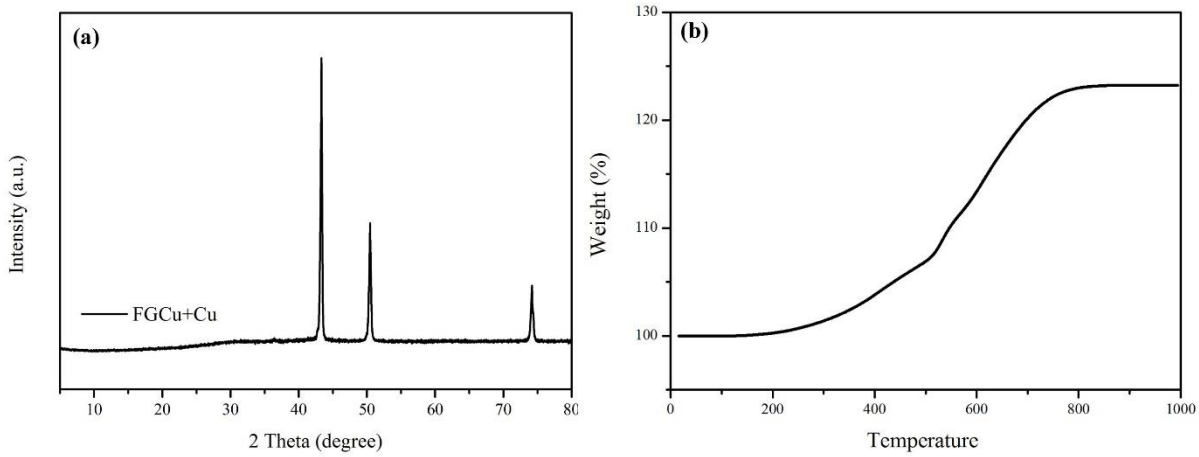

Figure 7-7 XRD (a)and (b) result of mixed FGCu+Cu mixed powders.

The SEM results of the FGCu nanostructures (a and b) and their mixed powders with micron Cu powders (c-f) are displayed in Figure *7-8*. Figure *7-8* a and b display the FGCu nanostructures, similar to the previous results (Figure *4-13*), the uniform decoration of Cu nanoparticles, which are 20-50 nm can be found on the surface of GNT nanostructures. The samples also keep the graphene layer like structure with no obvious agglomerations. After been mixed with Cu micron powders through the stirring and filtration process, the Cu micron powders can be observed and the graphene-layer structure of FGCu samples could be found attaching onto the surface of Cu micron particles (Figure *7-8*d). Meanwhile, some FGCu samples with large graphene layers can also be found covering Cu micron particles (Figure *7-8*e). In the high-resolution image (Figure *7-8*f), the FGCu nanostructures which are observed attaching onto the surface of the Cu micron particle still show the uniform Cu nanoparticle decoration on GNT morphology. No obvious agglomeration or aggregation of FGCu samples can be found, which indicates that the FGCu+Cu mixed powders with 1.42 wt.% of GNT component are uniformly mixed through the filtration mixing process.

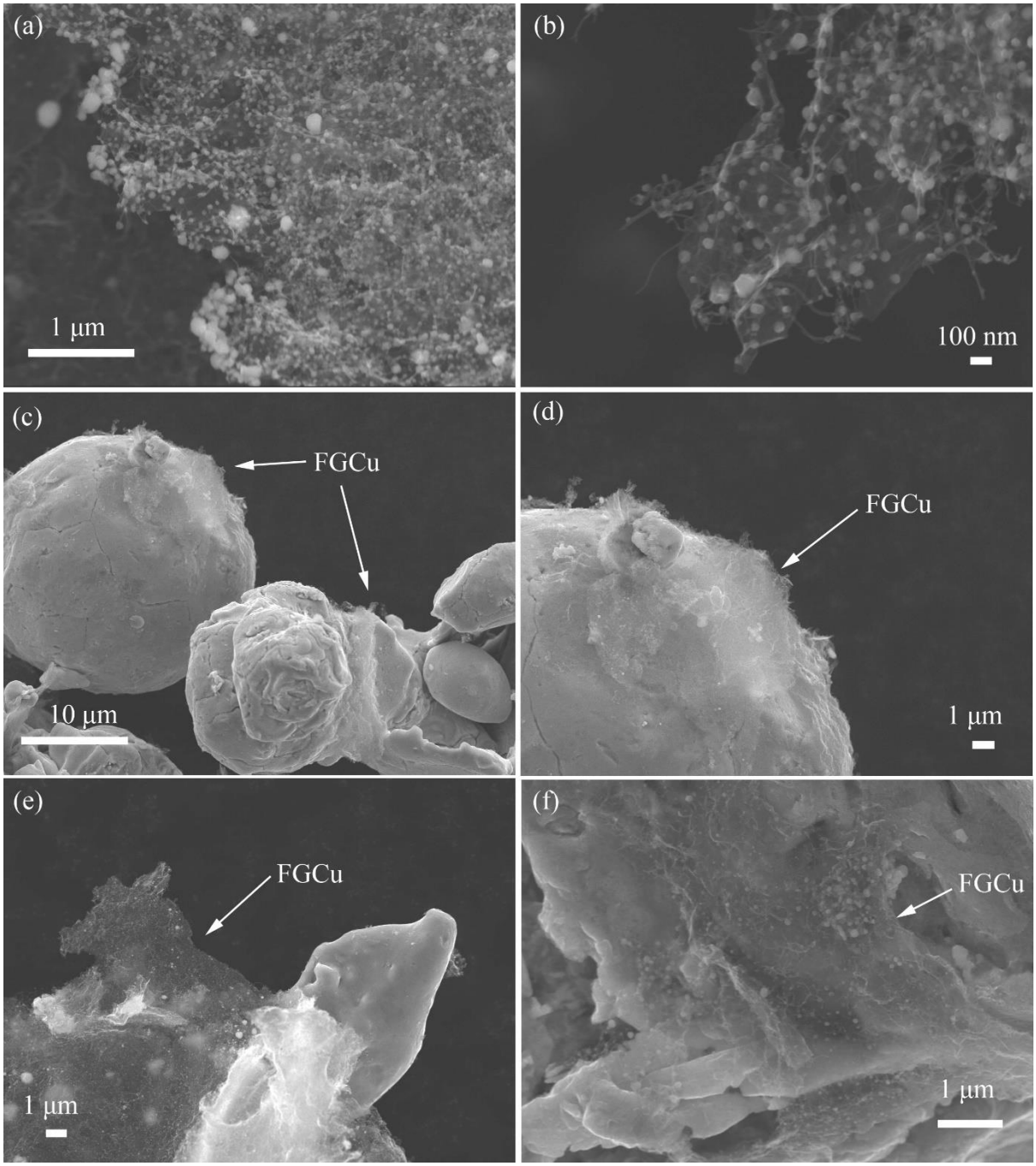

Figure 7-8 SEM images of FGCu nanostructures (a and b) and FGCu+Cu mixed powders (c-f) at different magnifications.

7.2.2 Consolidation of obtained mixed powders and the thermal performance

After been mixed through the filtration process, the obtained FGCu+Cu mixed powders were then consolidated through SPS at 800°C 50 MPa for 5min, which resulted in the best thermal

conductivity for pure Cu micron powder. Figure *7-9* displays the cross-section image of the obtained FGCu+Cu pellet obtained through SPS under 600°C 50 MPa for 5min. From the higher resolution images (Figure *7-9* b and c), the graphene layer like structure can be found to be anisotropic vertical to the pressing direction. This obvious alignment could be ascribed to the SPS process, which facilitates the self-alignment of FGCu nanostructures in the perpendicular direction to the pressure axis as well as the vacuum filtration process, which provides laminated powder structure of FGCu samples in the mixed powders. Meanwhile, Figure *7-9*d shows the SPS consolidated pure Cu pellet. Different from the FGCu+Cu pellet, the cross-section of pure Cu pellet displays a smooth surface, which is consistent with the result that the relative density is over 99% (Table *7-2*).

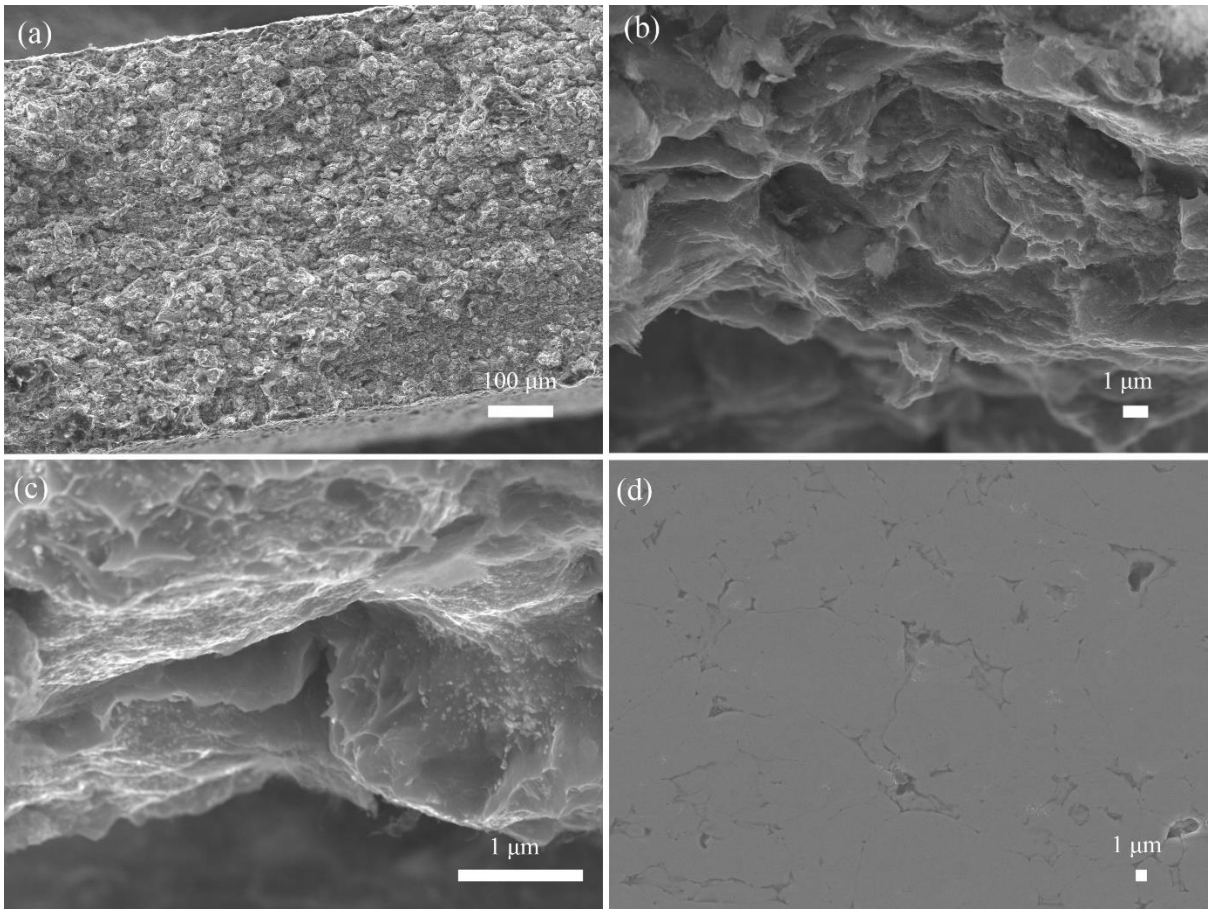

Figure 7-9 SEM images of the cross-section of SPS consolidated FGCu+Cu pellet at different magnification under low (a) and high (b and c) magnifications, and SPS consolidated pure Cu pellet (d).

After being SPS consolidated, the density and thermal performance of the as-prepared FGCu+Cu pellet has then been measured and the relevant results are displayed in Table *7-3*. According to the previous TGA results, the calculated percentage of the mixed powders is 1.42 wt.% (6.03 vol.%), and the measured density of the obtained pellet is 8.21 g cm^{-3}, which is around 96% of the relative density. Meanwhile, the thermal measurement of the FGCu+Cu pellet has also been carried out and the measured direction is vertical to the alignment direction of FGCu samples as shown in Figure *7-9*. The measured thermal diffusivity and conductivity are 75.61 mm^2 s^{-1} and 237.78 W m^{-1} K^{-1}, respectively, which is lower than the theoretic value of pure commercial Cu and the obtained SPS consolidated Cu.

Table 7-3 Measured density and thermal conduction results of the FGCu+Cu pellet.

Sample	Consolidation condition	Density (g cm^{-3})	Relative density (%)	Thermal diffusivity (mm^2 s^{-1})	Thermal conductivity (W m^{-1} K^{-1})
FGCu+ Cu	FGCu+Cu powders 800°C, 60 MPa, 5min	8.21	96.14	75.62	237.78

7.3 Discussion

7.3.1 Effect of press parameters to the density of pure Cu pellets

For the purchased Cu micron powders, the XRD and XPS results (Figure *7-1*) have confirmed a minor oxidised part in the obtained Cu micron powders, this may generate before receiving or during storage in the labs as copper is easily oxidised when exposing in the open air. Such oxidised Cu should be ascribed to the surface oxidation as copper is easily oxidised when exposing in the open air. Without further treatment, this oxidised surface would act as a gap during the consolidation process and hence resulting in the un-dense pellet. After been reduced under Ar/H_2 atmosphere at 450°C for 2 h, the results (Figure *7-1*b) show no more obvious

oxidisation signals. Therefore, it is suggested that the pre-reduction process is necessary for all the purchased Cu micron powders and their composites in case of the side effects of the oxidised surface.

The manual pressing and sintering process was investigated first due to its simplicity and convenience. As the name implies, the as-prepared pellets were initially pressed through manual pressing and then directly sintered without pressure. In this case, the pressing and sintering are separated, according to the measured density results (Table *7-1*), the obtained density of the sintered pellets slightly increased from 8.06 to 8.46 g cm^{-3} even after several cycles of pressing and sintering. The final density of 8.46 g cm^{-3} equals 94.4 % of the density of pure copper, which is still far lower than the requirement. The optical images (Figure *7-3*) also display obvious voids among the cross-section of all the manual pressing and sintering pellets. Such voids and low relative density of the as-prepared pellets mean that they cannot be applied as further thermal management materials, as these voids should hinder the transfer of heat. Comparing to manual pressing and sintering, the SPS provides a more advanced and faster procedure to prepare pellets. The measured results (Table *7-2*) also show that denser pellets have been obtained in a short time (only 5 min) under certain conditions. Obviously, there is an intense improvement in density when the sintering temperature above 700°C, which can reach as high as around 99% compared with pure commercial Cu. Meanwhile, the optical images of SPS consolidated pellets (Figure *7-4*) also reveal a clear cross-section surface without obvious voids compared to manual pressed and sintered pellets (Figure *7-3*).

7.3.2 Effect of press parameters to the thermal conductivities of pure Cu and FGCu+Cu pellets

After the consolidation process through different methods, the thermal conductivities of all the

obtained pellets were then measured and compared. In the measured data of manual pressing and sintering pellets (Figure *7-5*), it can be found that the Cu pellets show poor thermal conduction performance even after several cycles of pressing and sintering. Combining with the fact that a large number of voids have been observed in the manual pressing and sintering sample, this poor thermal conduction performance could be ascribed to the low density, which results from these large numbers of voids in the pellets that hindered the thermal conduction. However, it also can be found that both the thermal diffusivity and conductivity value of the manual pressing and sintering pellets increase with density, which further confirms that the denser the pellet the better thermal conduction performance. When it comes to the SPS consolidated pellets, the as-prepared pellets display much better thermal performances due to their better densities. From Figure 7-6, both the obtained thermal diffusivities and conductivities of SPS sintered Cu pellets are much higher than the manual pressing and sintering ones, especially the pellets obtained at above 700°C with 60 MPa for 5 min, which shows a thermal conductivity of over 350 W m^{-1} K^{-1}. The best result appears in the SPS sintered sample at 800°C and 60 MPa for 5 min whose relative density is above 99.1%, the obtained thermal conductivity is over 365 W m^{-1} K^{-1}, which is close to the commercial copper. Therefore, it can be concluded that the introduction of SPS is a good choice to prepare dense Cu pellets, especially when the pressure is above 60 MPa for 5 min and sintering temperature is above 700°C.

The as-prepared FGCu nanostructures have been introduced into the pure Cu matrix through SPS for better thermal conduction performance with the best consolidation parameters in pure Cu samples (800°C and 60 MPa for 5 min). As the uniform Cu nanoparticles have successfully decorated on GNT nanostructures, shown through the relevant XRD and SEM characterisation, the FGCu nanostructures have been regarded as a potential reinforcement among the Cu matrix. During the investigation, the FGCu samples were firstly mixed with Cu micron powders

through stirring in water and vacuum filtration. The SEM images (Figure *7-8*) show that the FGCu nanostructures were uniformly mixed with the Cu micron particles and there is no obvious agglomeration between FGCu samples after mixing. Before SPS, the mixed powders were also pre-reduced under Ar/H_2 atmosphere in case of oxidised surface, which has been observed previously. Meanwhile, the cross-section SEM images of the FGCu+Cu pellet (Figure *7-9* a-c) show that the FGCu graphene-layer structures became anisotropic vertical to the pressing direction, and such alignment of the FGCu structures can be ascribed to the SPS itself, which facilitates the distribution during sintering. Comparing with the SEM image of pure Cu pellet (Figure *7-9*d), the FGCu+Cu pellet (Figure *7-9* a-c) still shows obvious voids among the cross-section which may result in poor thermal conductivity. The measured data (Table *7-3*) of SPS sintered FGCu+Cu pellet shows that the obtained density is 8.21 g cm^{-3}. Taking the TGA result (Figure *7-7*) into account, the obtained relative density of FGCu+Cu pellet is around 96% as the calculated weight percentage of carbon content (GNT) is around 1.42 wt.% (6.03 vol.%). However, the thermal performance of the FGCu+Cu pellet shown in Table *7-3* demonstrates that both the thermal diffusivity and conductivity are not as good as predicted, which are 75.61 mm^2 s^{-1} and 237.78 W m^{-1} K^{-1}, respectively. The obtained thermal performance is much lower than the SPS sintered pure Cu pellet. Thus, such a relatively low density of the FGCu+ Cu pellet may this poor thermal conduction performance and a further improvement to make the FGCu+Cu pellet denser is still needed. Another possible reason for such unsatisfactory thermal performance could be ascribed to the horizontal distribution of FGCu structure in the Cu Matrix. As shown in Figure *7-10*, the measurement of heat conduction is from bottom to top (as can be seen in the schematic Figure 3-8), and such horizontal direction distribution of the FGCu nanostructures could hinder the heat conduction through the vertical direction. According to the TGA result of FGCu+Cu powders (Figure *7-7*), even the 93.97 vol.% Cu without any reinforcement could show a thermal conductivity of around 342 W m^{-1} K^{-1}.

Therefore, it can be concluded that the horizontal distribution of the FGCu nanostructures has a negative effect on the Cu matrix. However, it would be interesting to have a measurement of the thermal conduction in the horizontal direction and this horizontal alignment of FGCu nanostructures leaves room for potential improvement in the FGCu+Cu system.

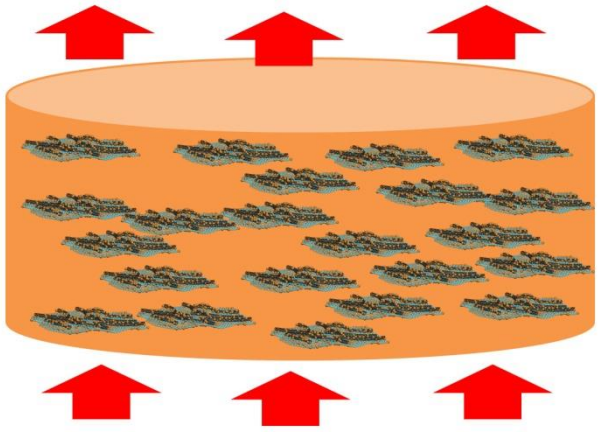

Figure 7-10 Schematic of the thermal conduction of the FGCu+Cu pellet during measurement.

Figure *7-11* a and b displays the copper matrix reinforced by graphene nanoplatelets (GNP) from literature [97]. The graphene and copper were mixed and then consolidated by SPS, Figure *7-11*a shows the SEM images of the fracture surface of the composite pellet. It can be found that the copper matrix between graphene became a thin-layer structure. This result is consistent with ours: the aligned distribution of fillers has been obtained during sintering (Figure *7-9*). The thermal performance of the products, shown in Figure *7-11*b, demonstrated obvious deterioration with the addition of graphene. However, the horizontal direction still performed better than the vertical direction, especially when the graphene content is over 0.8 vol.%. This is consistent with our prediction that the distribution of fillers that are parallel to the measurement direction would show better conduction performance to the ones vertical to the measurement direction. Figure *7-11* c-f show another graphene/copper composites by Chu [48]. The SEM images (Figure *7-11* c and d) display a long-range and highly aligned graphene

network established in the Cu matrix. The authors then compared the thermal conduction performances with and without aligned graphene structures, as well as in different directions. As shown in Figure *7-11* e and f, it can be found that the pellets with aligned graphene structures (V-GNP/Cu) illustrated improved thermal conductivities than non-aligned ones. In most cases, the measured thermal conductivities decreased with the increase of graphene amount, except the ones in in-plane direction. The authors ascribed this significant enhancement to the long-range and highly aligned graphene network that dramatically suppressed both GNP plane-Cu and GNP edge-Cu thermal resistances. However, there were obvious voids between filler layers among the cross-section of their composites (Figure *7-11* c and d), we also doubt that such obvious voids in the composites would prevent the thermal conduction or not. Thus, investigating the thermal conduction performance of the composites with different filler directions becomes an interesting topic, and these literature results also inspired us to continue our FGCu+Cu composites, especially their thermal performance in the horizontal direction.

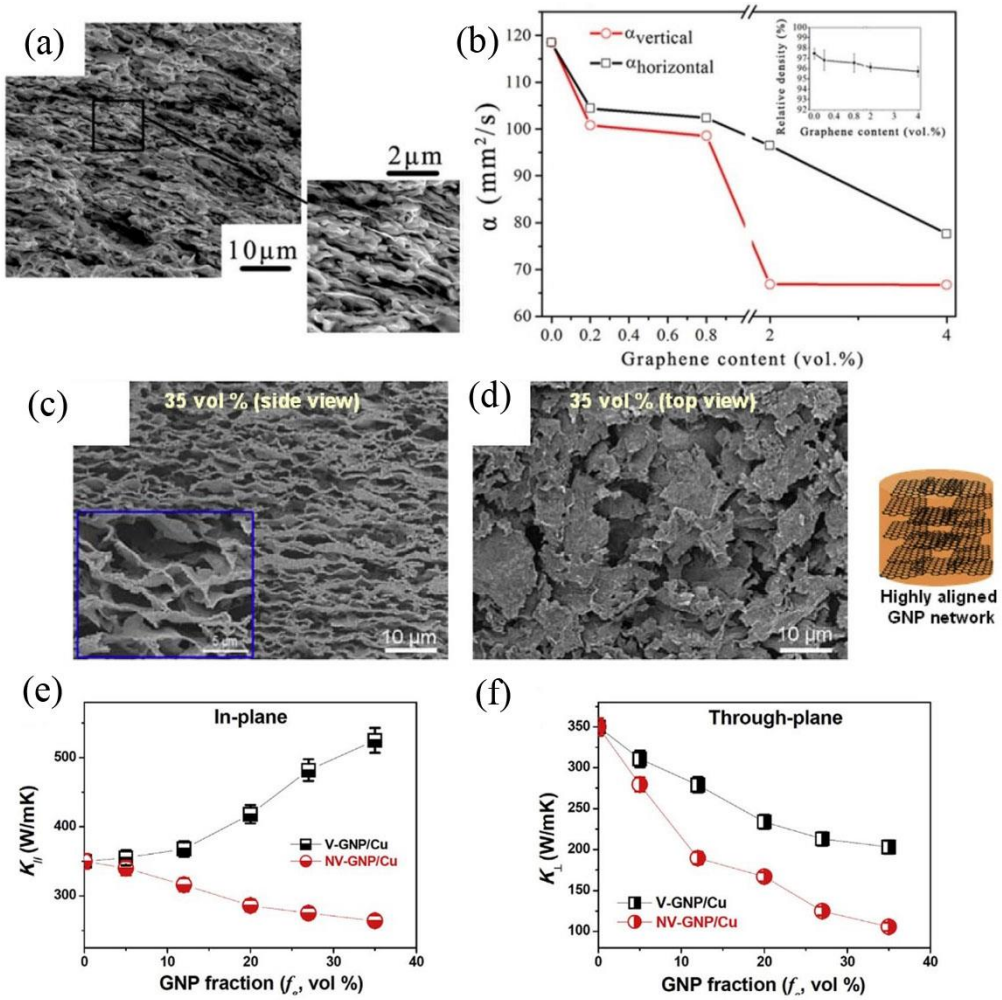

Figure 7-11 (a)SEM images and (b) thermal diffusivity of Cu/GNPs composites [97], (c and d) SEM images of V-GNP/Cu composites, and (e) in-plane and (f) through-plane thermal conductivity of V-GNP/Cu and NV-GNP/Cu composites [48].

7.4 Summary

In this chapter, the commercial pure Cu micron powders have been introduced to investigate the thermal conduction performance. Firstly, the pure Cu pellets obtained through manual pressing and sintering displayed poor density, as well as thermal conductivity even after several cycles of pressing and sintering. Such poor performance could be ascribed to the low density of Cu pellets which is a result of many voids that hinder the thermal conduction. After adopting SPS, the as-prepared Cu pellets became much denser with the relative density reaching above 99% under certain conditions, and the measured thermal conduction performance also reaches

close to pure Cu (above 370 W m^{-1} K^{-1}). Meanwhile, the FGCu+Cu mixed powders have been prepared through stirring and vacuum filtration and then consolidated through SPS. The cross-section SEM images of the FGCu+Cu pellet demonstrated that the graphene-layer structure of FGCu samples became distributed horizontally. However, the measured thermal conduction results of FGCu+Cu pellets were even lower than pure Cu pellets (75.61 mm^2 s^{-1} and 237.78 W m^{-1} K^{-1}), which can be ascribed to such horizontal distribution of FGCu graphene layer like structure. It can be predicted that there is a great potential for thermal conduction performance in the horizontal direction.

8 Conclusions and future works

8.1 Conclusions

The research work in this thesis is focused on: (a) preparing well-dispersed GO-CNT (GNT) nanostructures to prevent the natural agglomeration of carbon materials; (b) decorating different metal nanoparticles (Cu, Ag, and Ni) on GNTs to obtain uniformly metal nanoparticles decorated GNT nanostructures; (c) structure and morphology feature characterisation of these obtained samples; and (d) exploration of potential applications for prepared GNT and Metal-GNT nanostructures, including thermal and electrical conductivity, as well as the organic dye removal property.

The well-dispersed GNT nanostructures were successfully prepared through the freeze-drying method after ultrasonic dispersion. Firstly, a GO-CNT mixed suspension was homogenously dispersed under ultrasonication. The LN fast-frozen process was used to prevent the agglomeration, which largely kept the well-dispersed mixture. The subsequent freeze-drying method effectively removed the solution (ice) in the system and did not destroy the well-dispersed structure. Finally, the obtained powders displayed a well-dispersed graphene-like structure with the CNTs that were attached on the surface of GO layers.

Based on the GNT nanostructures, the Cu nanoparticle decorated GNT (FGCu) nanostructures have been prepared through MLM mixing process combined with the freeze-drying and subsequent reduction process. The relevant research showed that heating at 300°C for 3 h under Ar/H_2 atmosphere is optimal for preparing the uniformly Cu nanoparticles coated GNT nanostructures. Like the FGCu system, the Ni and Ag nanoparticles decorated GNT (FGNi and FGAg) nanostructures were also successfully obtained via this MLM mixing, freeze-drying

and reduction process, respectively. The subsequent characterisation demonstrates that the optimised reduction parameter for FGNi samples is at 400°C under pure Ar atmosphere for 1 h combined with Ar/H_2 atmosphere for another 2 h. In comparison, this parameter for Ag nanoparticles decorated GNT (FGAg) nanostructures is 200°C for 3 h under Ar/H_2 atmosphere. Therefore, although there are slight differences in the preparation parameters of each product, the uniform decoration of metal nanoparticles (including Cu, Ag, and Ni) on these 3D nanostructures have been obtained through the MLM and subsequent reduction methods.

To explore the potential application of these prepared samples, the FGAg nanostructures were applied as a promising filler in the PEEK matrix. The structure characterisation displays that the FGAg nanostructures formed a 3D network in the PEEK matrix. Because of this 3D network and the instinct properties of Ag and GNT, FGAg-PEEK composites showed enhanced thermal conductivity (around 1.62 times to pure PEEK) and significant improvement of electrical conductivity (form around 10^{-10} Ω m^{-1} of pure PEEK to 10^{-1} Ω m^{-1} of FGAg -PEEK composites). In addition, thanks to the unique morphology of the AgGNT nanostructures, which uniformly dispersed in the PEEK matrix and formed a 3D network structure, the AgGNT-PEEK composites showed perfect thermal durability. The obtained pellet structure remained integrity even above the melting temperature of pure PEEK. Thus, the AgGNT-PEEK composites have shown great potentials in the application as structures, high temperature electrical, aerospace as well as automotive.

Meanwhile, the FGNi nanostructures have been explored as reinforcements in the epoxy matrix with a magnetic field's assistance. The morphology and structure characterisation results showed that the FGNi samples were uniformly distributed in the epoxy matrix without obvious agglomeration, especially the sample in the magnetic field, which distributed alignment in the direction of the magnetic field. The property measurements demonstrated the improved thermal

and electrical conduction performance, especially the magnetic field assisted sample. In the FGNi-epoxy-M composites, the alignment of FGNi fillers has been proven to generate straight 3D pathways that could effectively conduct heat and electrons and prevent the thermal expansion of the epoxy matrix. The 30-FGNi-epoxy-M composites displayed a thermal conductivity of 0.462 W $m^{-1}K^{-1,}$ which is 2.67 times than that of pure epoxy (0.107 W $m^{-1}K^{-1}$). Meanwhile, the CTE of FGNi-epoxy also improved in the alignment direction of FGNi samples. Thus, the results show that the enhancement of FGNi nanostructures will play important roles in reinforcing the epoxy matrix and make them great potential candidates in fields like aerospace, automobile, and electronics.

Besides using as reinforcements in the polymer matrices, the prepared GNT and FGNi nanostructures have also been explored for water purification. For the pure GNT nanostructure, the well-dispersed 3D structure without obvious agglomeration showed high surface area according to the N_2 sorption measurement. The results indicated that the GNT nanostructures have a mesoporous structural feature with a high surface area, especially the GNT 1-5 sample with the surface area of 257.56 m^2 g^{-1}. It showed excellent dye removal performance with both cationic (RhB) and anionic (MO) dyes. The GNT 1-5 sample displayed the best adsorption performance with an adsorption capacity of 248.48 mg g^{-1} for RhB and 66.96 mg g^{-1} for MO. Because of the different charges of the dyes in solution, the GNT nanostructure with negative charge functional groups could adsorb more cationic dyes.

To further improve the dye removal property of the as-prepared samples, the Ni nanoparticle decorated GNT nanostructures have been introduced. The RhB removal test indicated a synergistic effect of physical adsorption and photo-degradation under UV irradiation. The FG30Ni70 samples displayed a removal capacity of 41.5 mg g^{-1} in 5 ppm RhB solution, which outperformed the most reported Ni/C products. Using the ferromagnetism of Ni nanoparticles,

the FGNi nanostructures are easily collected after reaction with dyes by magnetic separation technology. Therefore, novel FGNi nanostructures showed better removal performance than pure GNT samples and greater potentials as an efficient organic dye removal material.

Lastly, the FGCu nanostructures have been investigated as a reinforcement in the Cu matrix. At first, manually pressed and sintered pure Cu pellets displayed poor density and thermal conduction performance even after several cycles of pressing and sintering. This poor performance could be ascribed to the low-density Cu pellet containing a large number of voids that hindered the thermal conduction. Secondly, when the SPS method was introduced, the as-prepared Cu pellets become much denser with the relative density above 99% under certain conditions, and the measured thermal conduction performance reaches that of pure Cu standard (above 370 W m^{-1} K^{-1}). Thirdly, FGCu+Cu mixed powders were prepared through stirring and vacuum filtration process. The cross-section SEM images of the FGCu+Cu pellet demonstrated that the graphene-layer like structures of the FGCu samples were horizontally distributed. Although the measured thermal conductivities of FGCu+Cu pellets were even lower than pure Cu pellets due to the horizontal distribution of the FGCu layers (75.61 mm^2 s^{-1} and 237.78 W m^{-1} K^{-1}), it also showed that there is a great potential for the thermal conduction performance in the horizontal direction.

8.2 Future work

This research work has shown several positive results, and there are also some suggestions based on the results obtained for future work. Such recommendations have not been done or accomplished in this thesis because of the lack of material, time, or facilities.

- The well-dispersed metal nanoparticles decorated GNT nanostructures have been successfully prepared in the thesis. Although the production of these samples is suitable

for lab usage, the quantity of the produced is far lower than required for industrial applications. A method to scale up production is needed if more samples are needed for both the preparation and reduction equipment.

- The metal nanoparticles decorated GNT composites, especially the Ag and Ni, have been used to improve both PEEK and epoxy matrix. The enhancement is still far lower than predicted as both CNT and graphene materials have exhibited much greater thermal and electrical conduction performance in previous research. Therefore, more in-depth investigations are required to utilise GNT samples' advantages, such as the interface between filler and matrix and the size of graphene and CNTs.
- Although the FGCu nanostructures did not show a positive result as reinforcement in the Cu matrix currently, it is believed that better results can be obtained for the following reasons. Firstly, the SEM results illustrated that the FGCu layer structures aligned in the XY direction. Thus, more equipment, such as the sample holder for the thermal conduction measurement in XY direction and the similar holders for SPS sample preparation, are needed. Secondly, the density results suggested that the FGCu+Cu pellets are not as dense as the pure Cu pellet. Thus, further work could be done and focus on the preparation of the denser FGCu+Cu pellet.
- The dye removal performances of GNT and FGNi products have displayed the potentials of these samples as dye removal materials. However, the removal efficiency is not good enough. Therefore, based on the results obtained in the thesis, several further works could be done. For example, as the GNT 1-5 nanostructures showed the best adsorption performance with both dyes, they can be used as the basic structure for coating with Ni nanoparticles, which may exhibit improved performance compared with current results. In addition, the recycling performance of FGNi sample can be also explored as it is an important index to evaluate its possibility in our daily application.

- In-depth investigations of GNT and metal nanoparticles decorated GNT reinforced composites will be interesting. As the enhancement of either thermal or electrical performance is not as good as predicted in current results, some further investigations can be done, such as changing the size of graphene and CNT materials. As is known, previous research showed that larger sized of graphene structures lead to better thermal and mechanical properties. Therefore, the investigation of different carbon material sizes is of great importance. Meanwhile, the number and distribution of metal nanoparticles coated on the GNTs may lead to different results.
- Another potential area for future research would be the electromagnetic shielding property of GNT based nanostructures. Some important results have been presented in this thesis, i.e., the aligned distribution of GNT based structures and the magnetic property of the Ni decorated GNT nanostructures. By combining such results with literature, it is proposed that such structures could be explored as electromagnetic wave shielding materials, which may effectively adsorb and reflect the electromagnetic waves.

References

1. Novoselov, K.S., et al., *Electric field effect in atomically thin carbon films.* Science, 2004. **306**(5696): p. 666-669.
2. Iijima, S., *Helical microtubules of graphitic carbon.* Nature, 1991. **354**(6348): p. 56.
3. Yang, S.-Y., et al., *Design and tailoring of a hierarchical graphene-carbon nanotube architecture for supercapacitors.* Journal of Materials Chemistry, 2011. **21**(7): p. 2374-2380.
4. Lee, C., et al., *Measurement of the elastic properties and intrinsic strength of monolayer graphene.* Science, 2008. **321**(5887): p. 385-388.
5. Ghosh, S., et al., *Dimensional crossover of thermal transport in few-layer graphene.* Nature materials, 2010. **9**(7): p. 555.
6. Yu, M.-F., et al., *Strength and breaking mechanism of multiwalled carbon nanotubes under tensile load.* Science, 2000. **287**(5453): p. 637-640.
7. Pop, E., et al., *Thermal conductance of an individual single-wall carbon nanotube above room temperature.* Nano letters, 2006. **6**(1): p. 96-100.
8. Tombros, N., et al., *Electronic spin transport and spin precession in single graphene layers at room temperature.* Nature, 2007. **448**(7153): p. 571-574.
9. Xu, X., et al., *Length-dependent thermal conductivity in suspended single-layer graphene.* Nature communications, 2014. **5**(1): p. 1-6.
10. Bonaccorso, F., et al., *Graphene, related two-dimensional crystals, and hybrid systems for energy conversion and storage.* Science, 2015. **347**(6217).
11. Marinho, B., et al., *Electrical conductivity of compacts of graphene, multi-wall carbon nanotubes, carbon black, and graphite powder.* Powder Technology, 2012. **221**: p. 351-358.
12. Tong, X.C., *Advanced materials for thermal management of electronic packaging*. Vol. 30. 2011: Springer Science & Business Media.
13. Grady, B.P., *Carbon nanotube-polymer composites: manufacture, properties, and applications*. 2011: John Wiley & Sons.
14. Ghosh, d., et al., *Extremely high thermal conductivity of graphene: Prospects for thermal management applications in nanoelectronic circuits.* Applied Physics Letters, 2008. **92**(15): p. 151911.
15. Balandin, A.A., et al., *Superior thermal conductivity of single-layer graphene.* Nano letters, 2008. **8**(3): p. 902-907.
16. Li, D., et al., *Processable aqueous dispersions of graphene nanosheets.* Nature nanotechnology, 2008. **3**(2): p. 101.
17. Kim, P., et al., *Thermal transport measurements of individual multiwalled nanotubes.* Physical review letters, 2001. **87**(21): p. 215502.
18. Rastogi, R., et al., *Comparative study of carbon nanotube dispersion using surfactants.* Journal of colloid and interface science, 2008. **328**(2): p. 421-428.
19. Krause, B., et al., *Correlation of carbon nanotube dispersability in aqueous surfactant solutions and polymers.* Carbon, 2009. **47**(3): p. 602-612.
20. Tian, Z.Q., et al., *Synthesis and characterization of platinum catalysts on multiwalled carbon nanotubes by intermittent microwave irradiation for fuel cell applications.* The Journal of Physical Chemistry B, 2006. **110**(11): p. 5343-5350.
21. Chen, X., et al., *Electrodeposited nickel composites containing carbon nanotubes.* Surface and Coatings Technology, 2002. **155**(2-3): p. 274-278.

22. Guo, C., et al., *The effects of pulse–reverse parameters on the properties of Ni–carbon nanotubes composite coatings.* Surface and Coatings Technology, 2007. **201**(24): p. 9491-9496.
23. Chen, X., et al., *Dry friction and wear characteristics of nickel/carbon nanotube electroless composite deposits.* Tribology international, 2006. **39**(1): p. 22-28.
24. Dai, P.-Q., W.-C. Xu, and Q.-Y. Huang, *Mechanical properties and microstructure of nanocrystalline nickel-carbon nanotube composites produced by electrodeposition.* Materials Science and Engineering: A, 2008. **483**: p. 172-174.
25. Jeon, Y., J. Byun, and T. Oh, *Electrodeposition and mechanical properties of Ni–carbon nanotube nanocomposite coatings.* Journal of Physics and Chemistry of Solids, 2008. **69**(5-6): p. 1391-1394.
26. Arai, S., et al., *Excellent solid lubrication of electrodeposited nickel-multiwalled carbon nanotube composite films.* Materials Letters, 2008. **62**(20): p. 3545-3548.
27. Firkowska, I., et al., *Effect of carbon nanotube surface modification on thermal properties of copper–CNT composites.* Journal of Materials Chemistry, 2011. **21**(43): p. 17541-17546.
28. Zhang, C., et al., *Graphene oxide-assisted dispersion of pristine multiwalled carbon nanotubes in aqueous media.* The Journal of Physical Chemistry C, 2010. **114**(26): p. 11435-11440.
29. Gong, X., et al., *Surfactant-assisted processing of carbon nanotube/polymer composites.* Chemistry of materials, 2000. **12**(4): p. 1049-1052.
30. Garg, P., et al., *Effect of dispersion conditions on the mechanical properties of multi-walled carbon nanotubes based epoxy resin composites.* Journal of Polymer Research, 2011. **18**(6): p. 1397-1407.
31. Yen, M.-Y., et al., *Preparation of graphene/multi-walled carbon nanotube hybrid and its use as photoanodes of dye-sensitized solar cells.* Carbon, 2011. **49**(11): p. 3597-3606.
32. Sun, H., Z. Xu, and C. Gao, *Multifunctional, ultra‐flyweight, synergistically assembled carbon aerogels.* Advanced Materials, 2013. **25**(18): p. 2554-2560.
33. Jia, H., et al., *3D graphene/carbon nanotubes/polydimethylsiloxane composites as high-performance electromagnetic shielding material in X-band.* Composites Part A: Applied Science and Manufacturing, 2020. **129**: p. 105712.
34. Liang, C., et al., *Highly oriented three-dimensional structures of Fe3O4 decorated CNTs/reduced graphene oxide foam/epoxy nanocomposites against electromagnetic pollution.* Composites Science and Technology, 2019. **181**: p. 107683.
35. Liu, T., et al., *Highly compressible anisotropic graphene aerogels fabricated by directional freezing for efficient absorption of organic liquids.* Carbon, 2016. **100**: p. 456-464.
36. Im, H. and J. Kim, *Thermal conductivity of a graphene oxide–carbon nanotube hybrid/epoxy composite.* Carbon, 2012. **50**(15): p. 5429-5440.
37. Agarwal, A., S.R. Bakshi, and D. Lahiri, *Carbon nanotubes: reinforced metal matrix composites*. 2018: CRC press.
38. Wang, L., et al., *Mechanical alloying of multi-walled carbon nanotubes and aluminium powders for the preparation of carbon/metal composites.* Carbon, 2009. **47**(15): p. 3427-3433.
39. Goh, C., et al., *Development of novel carbon nanotube reinforced magnesium nanocomposites using the powder metallurgy technique.* Nanotechnology, 2005. **17**(1): p. 7.
40. Taylor, G.F., *Apparatus for making hard metal compositions*. 1933, Google Patents.
41. Xu, C., et al., *Fabrication of aluminum–carbon nanotube composites and their*

electrical properties. Carbon, 1999. **37**(5): p. 855-858.
42. Kim, C., et al., *Strengthening of copper matrix composites by nickel-coated single-walled carbon nanotube reinforcements.* Synthetic Metals, 2009. **159**(5-6): p. 424-429.
43. Yue, H., et al., *Effect of ball-milling and graphene contents on the mechanical properties and fracture mechanisms of graphene nanosheets reinforced copper matrix composites.* Journal of Alloys and Compounds, 2017. **691**: p. 755-762.
44. Luo, H., et al., *Mechanical enhancement of copper matrix composites with homogeneously dispersed graphene modified by silver nanoparticles.* Journal of Alloys and Compounds, 2017. **729**: p. 293-302.
45. Chu, K., et al., *Fabrication and effective thermal conductivity of multi-walled carbon nanotubes reinforced Cu matrix composites for heat sink applications.* Composites Science and Technology, 2010. **70**(2): p. 298-304.
46. Wu, J., et al., *Mechanical and thermal properties of carbon nanotube/aluminum composites consolidated by spark plasma sintering.* Materials & Design, 2012. **41**: p. 344-348.
47. Jiang, R., et al., *Copper–graphene bulk composites with homogeneous graphene dispersion and enhanced mechanical properties.* Materials Science and Engineering: A, 2016. **654**: p. 124-130.
48. Chu, K., et al., *Largely enhanced thermal conductivity of graphene/copper composites with highly aligned graphene network.* Carbon, 2018. **127**: p. 102-112.
49. Ci, L., et al., *Investigation of the interfacial reaction between multi-walled carbon nanotubes and aluminum.* Acta Materialia, 2006. **54**(20): p. 5367-5375.
50. Huang, W., H. Chen, and J.M. Zuo, *One‐Dimensional Self‐Assembly of Metallic Nanostructures on Single‐Walled Carbon‐Nanotube Bundles.* Small, 2006. **2**(12): p. 1418-1421.
51. Zhang, Y., et al., *Coating of carbon nanotubes with tungsten by physical vapor deposition.* Solid state communications, 2000. **115**(1): p. 51-55.
52. Shu, J., et al., *Cage-like carbon nanotubes/Si composite as anode material for lithium ion batteries.* Electrochemistry Communications, 2006. **8**(1): p. 51-54.
53. Wang, Y., et al., *Microstructure and thermal characteristic of Si-coated multi-walled carbon nanotubes.* Nanotechnology, 2006. **17**(15): p. 3817.
54. Kamat, P.V., *Photochemistry on nonreactive and reactive (semiconductor) surfaces.* Chemical Reviews, 1993. **93**(1): p. 267-300.
55. Cha, S.I., et al., *Extraordinary strengthening effect of carbon nanotubes in metal‐matrix nanocomposites processed by molecular‐level mixing.* Advanced Materials, 2005. **17**(11): p. 1377-1381.
56. Hwang, J., et al., *Enhanced mechanical properties of graphene/copper nanocomposites using a molecular‐level mixing process.* Advanced materials, 2013. **25**(46): p. 6724-6729.
57. Zhang, X., et al., *In-situ space-confined synthesis of well-dispersed three-dimensional graphene/carbon nanotube hybrid reinforced copper nanocomposites with balanced strength and ductility.* Composites Part A: Applied Science and Manufacturing, 2017. **103**: p. 178-187.
58. Sadasivuni, K.K., et al., *Graphene-based polymer nanocomposites in electronics*. 2015: Springer.
59. Mittal, V., *Polymer-graphene nanocomposites*. Vol. 26. 2012: Royal Society of Chemistry.
60. Sahoo, N.G., et al., *Effect of carbon nanotubes and processing methods on the properties of carbon nanotube/polypropylene composites.* Journal of nanoscience and

nanotechnology, 2009. **9**(10): p. 5910-5919.
61. Wunderlich, B., *Reversible crystallization and the rigid–amorphous phase in semicrystalline macromolecules.* Progress in polymer science, 2003. **28**(3): p. 383-450.
62. Tzavalas, S., et al., *Effect of Carboxy-Functionalized Multiwall Nanotubes (MWNT− COOH) on the Crystallization and Chain Conformations of Poly (ethylene terephthalate) PET in PET− MWNT Nanocomposites.* Macromolecules, 2006. **39**(26): p. 9150-9156.
63. Grady, B.P., *Review and critical analysis of the morphology of random ionomers across many length scales.* Polymer Engineering & Science, 2008. **48**(6): p. 1029-1051.
64. Pujari, S., et al., *Preparation and characterization of multiwalled carbon nanotube dispersions in polypropylene: Melt mixing versus solid‐state shear pulverization.* Journal of Polymer Science Part B: Polymer Physics, 2009. **47**(14): p. 1426-1436.
65. Iervolino, R., et al., *The role of multi-walled carbon nanotubes in shear enhanced crystallization of isotactic poly (1-butene).* Journal of thermal analysis and calorimetry, 2009. **98**(3): p. 611-622.
66. Choi, H.J., K. Zhang, and J.Y. Lim, *Multi-Walled Carbon Nanotube/Polystyrene Composites Prepared by in-situ BulkSonochemical Polymerization.* Journal of nanoscience and nanotechnology, 2007. **7**(10): p. 3400-3403.
67. Liu, P., *Facile graft polystyrene onto multi-walled carbon nanotubes via in situ thermo-induced radical polymerization.* Journal of Nanoparticle Research, 2009. **11**(4): p. 1011-1016.
68. Kwon, S.M., et al., *Poly (methyl methacrylate)/multiwalled carbon nanotube microspheres fabricated via in‐situ dispersion polymerization.* Journal of Polymer Science Part B: Polymer Physics, 2008. **46**(2): p. 182-189.
69. Xia, H., G. Qiu, and Q. Wang, *Polymer/carbon nanotube composite emulsion prepared through ultrasonically assisted in situ emulsion polymerization.* Journal of applied polymer science, 2006. **100**(4): p. 3123-3130.
70. Blond, D., et al., *Enhancement of modulus, strength, and toughness in poly (methyl methacrylate)‐based composites by the incorporation of poly (methyl methacrylate)‐functionalized nanotubes.* Advanced Functional Materials, 2006. **16**(12): p. 1608-1614.
71. Geng, Y., et al., *Effects of surfactant treatment on mechanical and electrical properties of CNT/epoxy nanocomposites.* Composites Part A: Applied Science and Manufacturing, 2008. **39**(12): p. 1876-1883.
72. Liu, L., et al., *Comparison of covalently and noncovalently functionalized carbon nanotubes in epoxy.* Macromolecular rapid communications, 2009. **30**(8): p. 627-632.
73. Bergin, S.D., et al., *Towards solutions of single‐walled carbon nanotubes in common solvents.* Advanced Materials, 2008. **20**(10): p. 1876-1881.
74. Martin, C., et al., *Formation of percolating networks in multi-wall carbon-nanotube–epoxy composites.* Composites Science and Technology, 2004. **64**(15): p. 2309-2316.
75. Du, F., J.E. Fischer, and K.I. Winey, *Coagulation method for preparing single‐walled carbon nanotube/poly (methyl methacrylate) composites and their modulus, electrical conductivity, and thermal stability.* Journal of Polymer Science Part B: Polymer Physics, 2003. **41**(24): p. 3333-3338.
76. Ramanathan, T., H. Liu, and L.C. Brinson, *Functionalized SWNT/polymer nanocomposites for dramatic property improvement.* Journal of Polymer Science Part B: Polymer Physics, 2005. **43**(17): p. 2269-2279.
77. Pham, J.Q., et al., *Glass transition of polymer/single‐walled carbon nanotube composite films.* Journal of Polymer Science Part B: Polymer Physics, 2003. **41**(24): p. 3339-3345.

78. Grady, B.P., et al., *Nucleation of polypropylene crystallization by single-walled carbon nanotubes.* The Journal of Physical Chemistry B, 2002. **106**(23): p. 5852-5858.
79. Liu, J., T. Liu, and S. Kumar, *Effect of solvent solubility parameter on SWNT dispersion in PMMA.* Polymer, 2005. **46**(10): p. 3419-3424.
80. Gao, J., Y. He, and X. Gong, *Effect of electric field induced alignment and dispersion of functionalized carbon nanotubes on properties of natural rubber.* Results in Physics, 2018. **9**: p. 493-499.
81. Zhang, K., et al., *Carboxylic Acid Functionalized Multi-Walled Carbon Nanotube-Adsorption onto Poly (methyl methacrylate) Microspheres.* Journal of nanoscience and nanotechnology, 2009. **9**(2): p. 1058-1061.
82. Grunlan, J.C., et al., *Water‐based single‐walled‐nanotube‐filled polymer composite with an exceptionally low percolation threshold.* Advanced Materials, 2004. **16**(2): p. 150-153.
83. Regev, O., et al., *Preparation of conductive nanotube–polymer composites using latex technology.* Advanced Materials, 2004. **16**(3): p. 248-251.
84. Cao, Z., et al., *The surface modifications of multi-walled carbon nanotubes for multi-walled carbon nanotube/poly (ether ether ketone) composites.* Applied Surface Science, 2015. **353**: p. 873-881.
85. Martínez-Gómez, A., et al., *Searching for effective compatibilizing agents for the preparation of poly (ether ether ketone)/graphene nanocomposites with enhanced properties.* Composites Part A: Applied Science and Manufacturing, 2018. **113**: p. 180-188.
86. Hwang, Y., M. Kim, and J. Kim, *Improvement of the mechanical properties and thermal conductivity of poly (ether-ether-ketone) with the addition of graphene oxide-carbon nanotube hybrid fillers.* Composites Part A: Applied Science and Manufacturing, 2013. **55**: p. 195-202.
87. Jiang, G., L. Diao, and K. Kuang, *Advanced thermal management materials*. 2012: Springer Science & Business Media.
88. Wei, L., et al., *Thermal conductivity of isotopically modified single crystal diamond.* Physical Review Letters, 1993. **70**(24): p. 3764.
89. Sukhadolau, A., et al., *Thermal conductivity of CVD diamond at elevated temperatures.* Diamond and related materials, 2005. **14**(3-7): p. 589-593.
90. Stankovich, S., et al., *Graphene-based composite materials.* Nature, 2006. **442**(7100): p. 282.
91. Balandin, A.A., *Thermal properties of graphene and nanostructured carbon materials.* Nature materials, 2011. **10**(8): p. 569.
92. Klemens, P., *Theory of the a-Plane Thermal Conductivity of Graphite.* Thermal Conductivity, 1993. **22**: p. 365-365.
93. Pierson, H.O., *Handbook of carbon, graphite, diamonds and fullerenes: processing, properties and applications*. 2012: William Andrew.
94. Moradi, Z., M. Vaezzadeh, and M. Saeidi, *Temperature-dependent thermal expansion of graphene.* Physica A: Statistical Mechanics and its Applications, 2018. **512**: p. 981-985.
95. Chu, K., C.-c. Jia, and W.-s. Li, *Thermal conductivity enhancement in carbon nanotube/Cu–Ti composites.* Applied physics A, 2013. **110**(2): p. 269-273.
96. Nan, C.-W. and R. Birringer, *Determining the Kapitza resistance and the thermal conductivity of polycrystals: A simple model.* Physical Review B, 1998. **57**(14): p. 8264.
97. Chen, F., et al., *Effects of graphene content on the microstructure and properties of copper matrix composites.* Carbon, 2016. **96**: p. 836-842.

98. Goli, P., et al., *Thermal properties of graphene–copper–graphene heterogeneous films.* Nano letters, 2014. **14**(3): p. 1497-1503.
99. Nan, C.-W., et al., *Effective thermal conductivity of particulate composites with interfacial thermal resistance.* Journal of Applied Physics, 1997. **81**(10): p. 6692-6699.
100. Liu, L., et al., *Improvement of the thermal conductivity and friction performance of poly (ether ether ketone)/carbon fiber laminates by addition of graphene.* RSC advances, 2015. **5**(71): p. 57853-57859.
101. Saleem, A., L. Frormann, and A. Iqbal, *High performance thermoplastic composites: Study on the mechanical, thermal, and electrical resistivity properties of carbon fiber‐reinforced polyetheretherketone and polyethersulphone.* Polymer Composites, 2007. **28**(6): p. 785-796.
102. Rivière, L., et al., *Specific heat capacity and thermal conductivity of PEEK/Ag nanoparticles composites determined by Modulated-Temperature Differential Scanning Calorimetry.* Polymer Degradation and Stability, 2016. **127**: p. 98-104.
103. Wu, S., et al., *Aligning multilayer graphene flakes with an external electric field to improve multifunctional properties of epoxy nanocomposites.* Carbon, 2015. **94**: p. 607-618.
104. Yagub, M.T., et al., *Dye and its removal from aqueous solution by adsorption: a review.* Advances in colloid and interface science, 2014. **209**: p. 172-184.
105. Ai, L. and J. Jiang, *Removal of methylene blue from aqueous solution with self-assembled cylindrical graphene–carbon nanotube hybrid.* Chemical Engineering Journal, 2012. **192**: p. 156-163.
106. Chen, L., et al., *Three-dimensional graphene-based adsorbents in sewage disposal: a review.* Environmental Science and Pollution Research, 2018. **25**(26): p. 25840-25861.
107. Salleh, M.A.M., et al., *Cationic and anionic dye adsorption by agricultural solid wastes: A comprehensive review.* Desalination, 2011. **280**(1-3): p. 1-13.
108. Purkait, M., S. DasGupta, and S. De, *Adsorption of eosin dye on activated carbon and its surfactant based desorption.* Journal of environmental management, 2005. **76**(2): p. 135-142.
109. Thines, R., et al., *Application potential of carbon nanomaterials in water and wastewater treatment: a review.* Journal of the Taiwan Institute of Chemical Engineers, 2017. **72**: p. 116-133.
110. Thein, M.T., et al., *Highly UV light driven WOx@ ZnO nanocomposites synthesized by liquid impregnation method.* Journal of Industrial and Engineering Chemistry, 2017. **46**: p. 119-129.
111. Ma, C., et al., *Rapid large-scale preparation of ZnO nanowires for photocatalytic application.* Nanoscale research letters, 2011. **6**(1): p. 536.
112. Gupta, V.K., et al., *Adsorptive removal of dyes from aqueous solution onto carbon nanotubes: a review.* Advances in colloid and interface science, 2013. **193**: p. 24-34.
113. Natarajan, S., H.C. Bajaj, and R.J. Tayade, *Recent advances based on the synergetic effect of adsorption for removal of dyes from waste water using photocatalytic process.* Journal of Environmental Sciences, 2018. **65**: p. 201-222.
114. Tiwari, J.N., et al., *Reduced graphene oxide-based hydrogels for the efficient capture of dye pollutants from aqueous solutions.* Carbon, 2013. **56**: p. 173-182.
115. Mohammed, M.I. and S. Baytak, *Synthesis of bentonite–carbon nanotube nanocomposite and its adsorption of rhodamine dye from water.* Arabian Journal for Science and Engineering, 2016. **41**(12): p. 4775-4785.
116. Zhao, D., et al., *Adsorption of methyl orange dye onto multiwalled carbon nanotubes.* Procedia Environmental Sciences, 2013. **18**: p. 890-895.

117. Zhu, H., et al., *Preparation, characterization, adsorption kinetics and thermodynamics of novel magnetic chitosan enwrapping nanosized γ-Fe_2O_3 and multi-walled carbon nanotubes with enhanced adsorption properties for methyl orange.* Bioresource technology, 2010. **101**(14): p. 5063-5069.
118. Liang, L., et al., *The efficient removal of dyes over magnetic Ni embedded on mesoporous graphitic carbon material.* Journal of Porous Materials, 2014. **21**(6): p. 985-991.
119. Zeng, D., et al., *Synthesis of Ni–Au–ZnO ternary magnetic hybrid nanocrystals with enhanced photocatalytic activity.* Nanoscale, 2015. **7**(26): p. 11371-11378.
120. Aarthi, T. and G. Madras, *Photocatalytic degradation of rhodamine dyes with nano-TiO_2.* Industrial & engineering chemistry research, 2007. **46**(1): p. 7-14.
121. Mishra, M. and D.-M. Chun, *α-Fe_2O_3 as a photocatalytic material: A review.* Applied Catalysis A: General, 2015. **498**: p. 126-141.
122. Yu, H., et al., *Enhanced photoinduced-stability and photocatalytic activity of CdS by dual amorphous cocatalysts: synergistic effect of Ti (IV)-hole cocatalyst and Ni (II)-electron cocatalyst.* The Journal of Physical Chemistry C, 2016. **120**(7): p. 3722-3730.
123. Kar, A., et al., *Facile synthesis of SnO_2–PbS nanocomposites with controlled structure for applications in photocatalysis.* Nanoscale, 2016. **8**(5): p. 2727-2739.
124. Li, X., et al., *In situ preparation of magnetic Ni-Au/graphene nanocomposites with electron-enhanced catalytic performance.* Journal of Alloys and Compounds, 2017. **706**: p. 377-386.
125. Qusti, A., R. Mohamed, and M.A. Salam, *Photocatalytic synthesis of aniline from nitrobenzene using Ag-reduced graphene oxide nanocomposite.* Ceramics International, 2014. **40**(4): p. 5539-5546.
126. Zhao, C., et al., *Preparation of magnetic Ni@ graphene nanocomposites and efficient removal organic dye under assistance of ultrasound.* Applied Surface Science, 2015. **357**: p. 22-30.
127. Bai, S., et al., *One-pot solvothermal preparation of magnetic reduced graphene oxide-ferrite hybrids for organic dye removal.* Carbon, 2012. **50**(6): p. 2337-2346.
128. Xiao, Z.H., et al., *Magnetically recoverable Ni@ carbon nanocomposites: solid-state synthesis and the application as excellent adsorbents for heavy metal ions.* Applied Surface Science, 2012. **263**: p. 795-803.
129. Wu, X., et al., *Magnetically recoverable Ni@C composites: The synthesis by carbonization and adsorption for Fe3+.* Journal of Alloys and Compounds, 2017. **718**: p. 15-21.
130. Dąbrowski, A., *Adsorption-from theory to practice.* Advances in colloid and interface science, 2001. **93**(1-3): p. 135-224.
131. Allen, S. and B. Koumanova, *Decolourisation of water/wastewater using adsorption.* Journal of the University of Chemical Technology and Metallurgy, 2005. **40**(3): p. 175-192.
132. Nandi, B., A. Goswami, and M. Purkait, *Removal of cationic dyes from aqueous solutions by kaolin: kinetic and equilibrium studies.* Applied Clay Science, 2009. **42**(3-4): p. 583-590.
133. Ho, Y.-S. and G. McKay, *Pseudo-second order model for sorption processes.* Process biochemistry, 1999. **34**(5): p. 451-465.
134. Weber, W.J. and J.C. Morris, *Kinetics of adsorption on carbon from solution.* Journal of the Sanitary Engineering Division, 1963. **89**(2): p. 31-60.
135. Langmuir, I., *The adsorption of gases on plane surfaces of glass, mica and platinum.* Journal of the American Chemical society, 1918. **40**(9): p. 1361-1403.

136. Freundlich, H., *Über die adsorption in lösungen.* Zeitschrift für physikalische Chemie, 1907. **57**(1): p. 385-470.
137. Pérez, M.H., et al., *Degradation of pesticides in water using solar advanced oxidation processes.* Applied Catalysis B: Environmental, 2006. **64**(3-4): p. 272-281.
138. Petala, M., et al., *Wastewater reclamation by advanced treatment of secondary effluents.* Desalination, 2006. **195**(1-3): p. 109-118.
139. Chen, C., et al., *Comparison of seven kinds of drinking water treatment processes to enhance organic material removal: a pilot test.* Science of the Total Environment, 2007. **382**(1): p. 93-102.
140. Masarwa, A., et al., *Oxidation of organic substrates in aerated aqueous solutions by the Fenton reagent.* Coordination Chemistry Reviews, 2005. **249**(17-18): p. 1937-1943.
141. Chamarro, E., A. Marco, and S. Esplugas, *Use of Fenton reagent to improve organic chemical biodegradability.* Water research, 2001. **35**(4): p. 1047-1051.
142. Torres, R., et al., *A comparative study of ultrasonic cavitation and Fenton's reagent for bisphenol A degradation in deionised and natural waters.* Journal of Hazardous Materials, 2007. **146**(3): p. 546-551.
143. Rauf, M., et al., *The effect of operational parameters on the photoinduced decoloration of dyes using a hybrid catalyst V_2O_5/TiO_2.* Chemical Engineering Journal, 2007. **129**(1-3): p. 167-172.
144. Mahmoodi, N.M., et al., *Kinetics of heterogeneous photocatalytic degradation of reactive dyes in an immobilized TiO_2 photocatalytic reactor.* Journal of colloid and interface Science, 2006. **295**(1): p. 159-164.
145. Rauf, M. and S.S. Ashraf, *Fundamental principles and application of heterogeneous photocatalytic degradation of dyes in solution.* Chemical engineering journal, 2009. **151**(1-3): p. 10-18.
146. Zhang, L.L., Z. Xiong, and X. Zhao, *Pillaring chemically exfoliated graphene oxide with carbon nanotubes for photocatalytic degradation of dyes under visible light irradiation.* Acs Nano, 2010. **4**(11): p. 7030-7036.
147. Xiong, Z., et al., *Photocatalytic degradation of dyes over graphene–gold nanocomposites under visible light irradiation.* Chemical Communications, 2010. **46**(33): p. 6099-6101.
148. Brunauer, S., P.H. Emmett, and E. Teller, *Adsorption of gases in multimolecular layers.* Journal of the American chemical society, 1938. **60**(2): p. 309-319.
149. Commons, W., *Electron Interaction with Matter.* 2019, September 22.
150. Everhart, T.E. and R. Thornley, *Wide-band detector for micro-microampere low-energy electron currents.* Journal of scientific instruments, 1960. **37**(7): p. 246.
151. Thein, M.T., et al., *Effect of Ni coupling on the photoluminescence property and photocatalytic activity of ZnO nanorods.* Journal of the Taiwan Institute of Chemical Engineers, 2016. **61**: p. 156-165.
152. Dong, L., et al., *Microstructure and properties characterization of tungsten-copper composite materials doped with graphene.* Journal of Alloys and Compounds, 2017. **695**: p. 1637-1646.
153. Li, F., et al., *Fabrication of Pt–Cu/RGO hybrids and their electrochemical performance for the oxidation of methanol and formic acid in acid media.* Carbon, 2013. **64**: p. 11-19.
154. Yu, J., T. Ma, and S. Liu, *Enhanced photocatalytic activity of mesoporous TiO_2 aggregates by embedding carbon nanotubes as electron-transfer channel.* Physical Chemistry Chemical Physics, 2011. **13**(8): p. 3491-3501.
155. Li, J., et al., *Preparation of nanocomposites of metals, metal oxides, and carbon*

nanotubes via self-assembly. Journal of the American Chemical Society, 2007. **129**(30): p. 9401-9409.
156. Ghijsen, J., et al., *Electronic structure of Cu_2O and CuO.* Physical Review B, 1988. **38**(16): p. 11322.
157. Kumar-Krishnan, S., et al., *Chitosan/silver nanocomposites: Synergistic antibacterial action of silver nanoparticles and silver ions.* European Polymer Journal, 2015. **67**: p. 242-251.
158. de Jesús Ruíz-Baltazar, Á., et al., *Biosynthesis of Ag nanoparticles using Cynara cardunculus leaf extract: Evaluation of their antibacterial and electrochemical activity.* Results in Physics, 2018. **11**: p. 1142-1149.
159. Gong, J., et al., *Structural and magnetic properties of hcp and fcc Ni nanoparticles.* Journal of Alloys and Compounds, 2008. **457**(1-2): p. 6-9.
160. Jeon, Y.T., et al., *Comparison of the magnetic properties of metastable hexagonal close-packed Ni nanoparticles with those of the stable face-centered cubic Ni nanoparticles.* The Journal of Physical Chemistry B, 2006. **110**(3): p. 1187-1191.
161. Zhou, X., et al., *Design of magnetic core–shell Ni@graphene composites as a novel electrochemical sensing platform.* Sensors and Actuators B: Chemical, 2018. **255**: p. 2959-2962.
162. Ji, Z., et al., *One-step thermal synthesis of nickel nanoparticles modified graphene sheets for enzymeless glucose detection.* Journal of colloid and interface science, 2017. **506**: p. 678-684.
163. Lee, D., et al., *Enhanced electrical conductivity and hardness of silver-nickel composites by silver-coated multi-walled carbon nanotubes.* Nanotechnology, 2015. **26**(29): p. 295705.
164. Zhang, Y., et al., *In situ growth of Ag-reduced graphene oxide-carbon nanotube on indium tin oxide and its application for electrochemical sensing.* Materials Research Bulletin, 2016. **84**: p. 355-362.
165. Khan, A., et al., *Green synthesis of thermally stable Ag-rGO-CNT nano composite with high sensing activity.* Composites Part B: Engineering, 2016. **86**: p. 27-35.
166. Zhang, Y., et al., *Synthesis of Ag nanoparticle–carbon nanotube–reduced graphene oxide hybrids for highly sensitive non-enzymatic hydrogen peroxide detection.* RSC Advances, 2015. **5**(49): p. 39037-39041.
167. Díez-Pascual, A.M., et al., *High performance PEEK/carbon nanotube composites compatibilized with polysulfones-I. Structure and thermal properties.* Carbon, 2010. **48**(12): p. 3485-3499.
168. Wang, X., et al., *Flame retardancy and thermal degradation mechanism of epoxy resin composites based on a DOPO substituted organophosphorus oligomer.* Polymer, 2010. **51**(11): p. 2435-2445.
169. Moosa, A.A., et al., *Mechanical and thermal properties of graphene nanoplates and functionalized carbon-nanotubes hybrid epoxy nanocomposites.* Am. J. Mater. Sci., 2016. **6**(5): p. 125-134.
170. Rivière, L., et al., *Silver fillers aspect ratio influence on electrical and thermal conductivity in PEEK/Ag nanocomposites.* European Polymer Journal, 2016. **85**: p. 115-125.
171. Mohiuddin, M. and S. Hoa, *Temperature dependent electrical conductivity of CNT–PEEK composites.* Composites science and technology, 2011. **72**(1): p. 21-27.
172. Mohiuddin, M. and S.V. Hoa, *Estimation of contact resistance and its effect on electrical conductivity of CNT/PEEK composites.* Composites Science and Technology, 2013. **79**: p. 42-48.

173. Lin, Y.J., et al., *Preparation of poly (ether ether ketone)-based composite with high electrical conductivity, good mechanical properties and thermal stability.* High Performance Polymers, 2017. **29**(2): p. 205-210.
174. Li, S., et al., *Synergistic effect of graphene nanoplate and carbonized loofah fiber on the electromagnetic shielding effectiveness of PEEK-based composites.* Carbon, 2019. **143**: p. 154-161.
175. Wu, S., et al., *A novel route for tethering graphene with iron oxide and its magnetic field alignment in polymer nanocomposites.* Polymer, 2016. **97**: p. 273-284.
176. Wu, S., et al., *Epoxy nanocomposites containing magnetite-carbon nanofibers aligned using a weak magnetic field.* Polymer, 2015. **68**: p. 25-34.
177. Johnsen, G., et al., *Conductivity enhancement of silver filled polymer composites through electric field alignment.* Composites science and technology, 2012. **72**(15): p. 1841-1847.
178. Zhang, Y., et al., *One-dimensional graphene nanoribbons hybridized with carbon nanotubes as cathode and anode interfacial layers for high performance solar cells.* RSC Advances, 2015. **5**(61): p. 49614-49622.
179. Kruk, M. and M. Jaroniec, *Gas adsorption characterization of ordered organic-inorganic nanocomposite materials.* Chemistry of materials, 2001. **13**(10): p. 3169-3183.
180. Thommes, M., et al., *Physisorption of gases, with special reference to the evaluation of surface area and pore size distribution (IUPAC Technical Report).* Pure and Applied Chemistry, 2015. **87**(9-10): p. 1051-1069.
181. Wang, H., et al., *Efficient and scalable high-quality graphene nanodot fabrication through confined lattice plane electrochemical exfoliation.* Chemical Communications, 2019. **55**(41): p. 5805-5808.
182. Bulut, Y. and H. Aydın, *A kinetics and thermodynamics study of methylene blue adsorption on wheat shells.* Desalination, 2006. **194**(1-3): p. 259-267.
183. Langmuir, I., *The constitution and fundamental properties of solids and liquids. Part I. Solids.* Journal of the American chemical society, 1916. **38**(11): p. 2221-2295.
184. Gupta, V., et al., *Removal of rhodamine B, fast green, and methylene blue from wastewater using red mud, an aluminum industry waste.* Industrial & engineering chemistry research, 2004. **43**(7): p. 1740-1747.
185. Chen, D., et al., *Characterization of anion–cationic surfactants modified montmorillonite and its application for the removal of methyl orange.* Chemical engineering journal, 2011. **171**(3): p. 1150-1158.
186. Shariati-Rad, M., et al., *Magnetic solid phase adsorption, preconcentration and determination of methyl orange in water samples using silica coated magnetic nanoparticles and central composite design.* International Nano Letters, 2014. **4**(4): p. 91-101.
187. Wu, T., et al., *Photoassisted degradation of dye pollutants. V. Self-photosensitized oxidative transformation of rhodamine B under visible light irradiation in aqueous TiO2 dispersions.* The Journal of Physical Chemistry B, 1998. **102**(30): p. 5845-5851.
188. Song, Y., et al., *Metal organic framework derived magnetically separable 3-dimensional hierarchical Ni@C nanocomposites: Synthesis and adsorption properties.* Applied Surface Science, 2015. **359**: p. 834-840.
189. Du, H., et al., *Anchoring superparamagnetic core–shells onto reduced graphene oxide: fabrication of Ni–carbon–rGO nanocomposite for effective adsorption and separation.* RSC Advances, 2015. **5**(13): p. 10033-10039.

Appendix 1

2 Theta information for Cu (ICDD PDF No. 00-04-0836)

PDF#04-0836: QM=Common(+); d=Diffractometer; I=(Unknown)												PDF Card
Copper, syn Cu												
Radiation=CuKa1 Calibration= Ref: Level-1 PDF				Lambda=1.5406 2T=43.297-144.714			Filter= I/Ic(RIR)=					
Cubic, Fm-3m(225) CELL: 3.615 x 3.615 x 3.615 <90.0 x 90.0 x 90.0> Density(c)=8.95 Density(m)= Mwt= Vol=47.2 Ref: Ibid.						Z=4 P.S=	mp=					
Strong Lines: 2.09/X 1.81/5 1.28/2 1.09/2 0.83/1 0.81/1 1.04/1												
8 Lines, Wavelength to Compute Theta = 1.54056?(Cu), I%-Type = (Unknown)												
#	d(?)	I(f)	(h k l)	2-Theta	Theta	1/(2d)	#	d(?)	I(f)	(h k l)	2-Theta	Theta	1/(2d)
1	2.0880	100.0	(1 1 1)	43.297	21.648	0.2395	5	1.0436	5.0	(2 2 2)	95.139	47.570	0.4791
2	1.8080	46.0	(2 0 0)	50.433	25.216	0.2765	6	0.9038	3.0	(4 0 0)	116.918	58.459	0.5532
3	1.2780	20.0	(2 2 0)	74.130	37.065	0.3912	7	0.8293	9.0	(3 3 1)	136.507	68.253	0.6029
4	1.0900	17.0	(3 1 1)	89.931	44.965	0.4587	8	0.8083	8.0	(4 2 0)	144.714	72.357	0.6186

2 Theta information for Cu_2O (ICDD PDF No. 00-05-0667)

PDF#05-0667: QM=Common(+); d=Diffractometer; I=(Unknown)												PDF Card
Cuprite, syn Cu2+1O												
Radiation=CuKa1 Calibration= Ref: Level-1 PDF				Lambda=1.5406 2T=29.554-139.284			Filter= I/Ic(RIR)=					
Cubic, Pn-3m(224) CELL: 4.2696 x 4.2696 x 4.2696 <90.0 x 90.0 x 90.0> Density(c)=6.1 Density(m)= Mwt= Vol=77.8 Ref: Ibid.						Z=2 P.S=	mp=					
Strong Lines: 2.46/X 2.13/4 1.51/3 1.29/2 3.02/1												
13 Lines, Wavelength to Compute Theta = 1.54056?(Cu), I%-Type = (Unknown)												
#	d(?)	I(f)	(h k l)	2-Theta	Theta	1/(2d)	#	d(?)	I(f)	(h k l)	2-Theta	Theta	1/(2d)
1	3.0200	9.0	(1 1 0)	29.554	14.777	0.1656	8	1.2330	4.0	(2 2 2)	77.323	38.662	0.4055
2	2.4650	100.0	(1 1 1)	36.418	18.209	0.2028	9	1.0674	2.0	(4 0 0)	92.380	46.190	0.4684
3	2.1350	37.0	(2 0 0)	42.297	21.149	0.2342	10	0.9795	4.0	(3 3 1)	103.701	51.850	0.5105
4	1.7430	1.0	(2 1 1)	52.454	26.227	0.2869	11	0.9548	3.0	(4 2 0)	107.558	53.779	0.5237
5	1.5100	27.0	(2 2 0)	61.344	30.672	0.3311	12	0.8715	3.0	(4 2 2)	124.222	62.111	0.5737
6	1.3502	1.0	(3 1 0)	69.569	34.785	0.3703	13	0.8216	3.0	(5 1 1)	139.284	69.642	0.6086
7	1.2870	17.0	(3 1 1)	73.526	36.763	0.3885							

2 Theta information for $Cu(CH_3COO)_2$ (ICDD PDF No. 00-27-1126)

PDF#27-1126: QM=Intermediate; d=Film/Visual; I=(Unknown)												PDF Card
Copper Acetate C4H6CuO4												
Radiation=CuKa1 Calibration= Ref: Level-1 PDF				Lambda=1.5406 2T=11.191-38.957			Filter= I/Ic(RIR)=					
Tetragonal(Unknown), CELL: 13.36 x 13.36 x 15.08 <90.0 x 90.0 x 90.0> Density(c)=0.112 Density(m)= Mwt= Vol=2691.6 Ref: Ibid.							Z= P.S=		mp=			
Strong Lines: 7.40/X 7.90/X 3.76/8 6.00/8 3.33/5 3.05/5 2.71/5 2.49/5												
17 Lines, Wavelength to Compute Theta = 1.54056?(Cu), I%-Type = (Unknown)												
#	d(?)	I(f)	(h k l)	2-Theta	Theta	1/(2d)	#	d(?)	I(f)	(h k l)	2-Theta	Theta	1/(2d)
1	7.9000	100.0	(1 1 1)	11.191	5.595	0.0633	10	3.0500	50.0	(4 0 2)	29.257	14.629	0.1639
2	7.4000	100.0	(0 0 2)	11.950	5.975	0.0676	11	2.7100	50.0	(4 1 3)	33.026	16.513	0.1845
3	6.0000	80.0	(2 1 0)	14.752	7.376	0.0833	12	2.6400	30.0	(3 2 4)	33.928	16.964	0.1894
4	4.9600	40.0	(2 0 2)	17.868	8.934	0.1008	13	2.6000	10.0	(5 1 1)	34.466	17.233	0.1923
5	4.7300	30.0	(2 2 0)	18.745	9.372	0.1057	14	2.4900	50.0	(3 0 5)	36.040	18.020	0.2008
6	4.2300	10.0	(3 1 0)	20.984	10.492	0.1182	15	2.3900	30.0	(3 3 4)	37.603	18.802	0.2092
7	3.7600	80.0	(0 0 4)	23.643	11.821	0.1330	16	2.3600	40.0	(5 0 3)	38.100	19.050	0.2119
8	3.3300	50.0	(3 0 3)	26.749	13.375	0.1502	17	2.3100	30.0	(2 1 6)	38.957	19.479	0.2165
9	3.1500	30.0	(3 3 0)	28.309	14.154	0.1587							

2 Theta information for $Cu(CH_3COO)$ (ICDD PDF No. 00-28-0392)

PDF#27-0145: QM=Common(+); d=Densitometer; I=(Unknown)													PDF Card
Hoganite, syn C4H6CuO4!H2O													
Radiation=CuKa1			Lambda=1.5406			Filter=							
Calibration=			2T=12.800-68.253			I/Ic(RIR)=1.45							
Ref: Level-1 PDF													
Monoclinic, A2/a(15)					Z=8	mp=							
CELL: 13.863 x 8.558 x 13.171 <90.0 x 117.02 x 90.0>					P.S=								
Density(c)=1.882	Density(m)=	Mwt=	Vol=1392.0										
Ref: Ibid.													
Strong Lines: 6.91/X 6.17/4 5.38/3 5.87/3 3.53/2 5.75/2 3.59/1 2.29/1													
74 Lines, Wavelength to Compute Theta = 1.54056?(Cu), I%-Type = (Unknown)													
#	d(?)	I(f)	(h k l)	2-Theta	Theta	1/(2d)	#	d(?)	I(f)	(h k l)	2-Theta	Theta	1/(2d)
1	6.9100	100.0	(0 1 1)	12.800	6.400	0.0724	38	2.1370	2.0	(-6 1 1)	42.256	21.128	0.2340
2	6.1700	35.0	(2 0 0)	14.343	7.172	0.0810	39	2.0350	2.0	(-1 4 2)	44.484	22.242	0.2457
3	5.8700	25.0	(0 0 2)	15.081	7.540	0.0852	40	2.0270	4.0	(-6 1 5)	44.669	22.334	0.2467
4	5.7500	16.0	(-2 0 2)	15.397	7.699	0.0870	41	1.9760	1.0	(-6 2 4)	45.886	22.943	0.2530
5	5.3800	25.0	(-2 1 1)	16.463	8.232	0.0929	42	1.9630	4.0	(4 1 3)	46.208	23.104	0.2547
6	4.2800	2.0	(0 2 0)	20.736	10.368	0.1168	43	1.9520	2.0	(-3 2 6)	46.483	23.242	0.2561
7	4.0900	4.0	(2 1 1)	21.711	10.855	0.1222	44	1.9280	2.0	(-3 4 2)	47.097	23.548	0.2593
8	4.0500	2.0	(-3 1 1)	21.928	10.964	0.1235	45	1.8910	2.0	(-1 3 5)	48.076	24.038	0.2644
9	3.5880	12.0	(-1 2 2)	24.794	12.397	0.1394	46	1.8740	2.0	(-1 2 6)	48.540	24.270	0.2668
10	3.5270	20.0	(2 0 2)	25.230	12.615	0.1418	47	1.8300	2.0	(2 4 2)	49.785	24.893	0.2732
11	3.4550	4.0	(-4 0 2)	25.764	12.882	0.1447	48	1.8020	1.0	(-2 1 7)	50.613	25.306	0.2775
12	3.4340	4.0	(-2 2 2)	25.925	12.962	0.1456	49	1.7940	1.0	(-2 4 4)	50.854	25.427	0.2787
13	3.2920	4.0	(-2 0 4)	27.064	13.532	0.1519	50	1.7740	2.0	(-7 2 2)	51.469	25.735	0.2818
14	3.0870	4.0	(4 0 0)	28.899	14.449	0.1620	51	1.7630	4.0	(4 0 4)	51.814	25.907	0.2836
15	3.0330	2.0	(-4 1 3)	29.425	14.712	0.1649	52	1.7530	1.0	(5 3 1)	52.132	26.066	0.2852
16	2.9670	2.0	(3 2 0)	30.095	15.047	0.1685	53	1.7180	1.0	(-4 4 4)	53.277	26.638	0.2910
17	2.8750	2.0	(-4 0 4)	31.081	15.541	0.1739	54	1.7100	2.0	(-6 1 7)	53.546	26.773	0.2924
18	2.7730	2.0	(0 3 1)	32.255	16.128	0.1803	55	1.6950	2.0	(-8 1 3)	54.058	27.029	0.2950
19	2.7230	2.0	(2 2 2)	32.864	16.432	0.1836	56	1.6660	2.0	(1 2 6)	55.078	27.539	0.3001
20	2.6880	2.0	(-4 2 2)	33.305	16.652	0.1860	57	1.6320	1.0	(7 2 0)	56.326	28.163	0.3064
21	2.6450	2.0	(1 3 1)	33.862	16.931	0.1890	58	1.6160	1.0	(5 4 0)	56.935	28.467	0.3094
22	2.6090	2.0	(-2 2 4)	34.344	17.172	0.1916	59	1.6000	1.0	(-2 0 8)	57.557	28.779	0.3125
23	2.5920	2.0	(-5 1 3)	34.576	17.288	0.1929	60	1.5670	2.0	(-7 3 1)	58.887	29.443	0.3191
24	2.5760	1.0	(4 1 1)	34.798	17.399	0.1941	61	1.5440	1.0	(8 0 0)	59.853	29.926	0.3238
25	2.5430	4.0	(-3 2 4)	35.264	17.632	0.1966	62	1.5130	1.0	(-4 5 3)	61.209	30.604	0.3305
26	2.5100	2.0	(-2 1 5)	35.743	17.872	0.1992	63	1.5110	1.0	(-8 1 7)	61.299	30.649	0.3309
27	2.4950	2.0	(-3 1 5)	35.965	17.983	0.2004	64	1.5050	1.0	(-1 3 7)	61.569	30.785	0.3322
28	2.4250	2.0	(-3 3 1)	37.041	18.520	0.2062	65	1.4830	1.0	(-6 2 8)	62.585	31.292	0.3372
29	2.3930	4.0	(-4 1 5)	37.554	18.777	0.2089	66	1.4520	1.0	(8 2 0)	64.078	32.039	0.3444
30	2.3870	4.0	(-4 2 4)	37.652	18.826	0.2095	67	1.4280	2.0	(-6 4 6)	65.287	32.644	0.3501
31	2.3300	8.0	(4 0 2)	38.609	19.305	0.2146	68	1.4210	1.0	(7 3 1)	65.649	32.825	0.3519
32	2.2900	10.0	(-3 3 3)	39.311	19.656	0.2183	69	1.4110	1.0	(-4 5 5)	66.174	33.087	0.3544
33	2.2790	4.0	(2 0 4)	39.509	19.754	0.2194	70	1.4100	1.0	(6 0 4)	66.227	33.113	0.3546
34	2.2260	4.0	(-6 0 4)	40.490	20.245	0.2246	71	1.3920	2.0	(5 1 5)	67.196	33.598	0.3592
35	2.2220	4.0	(1 2 4)	40.566	20.283	0.2250	72	1.3870	1.0	(0 2 8)	67.471	33.735	0.3605
36	2.1860	2.0	(-5 2 4)	41.265	20.632	0.2287	73	1.3810	1.0	(1 4 6)	67.803	33.902	0.3621
37	2.1490	1.0	(5 1 1)	42.008	21.004	0.2327	74	1.3730	2.0	(-5 5 5)	68.253	34.126	0.3642

2 Theta information for $Cu(CH_3COO)_2 \cdot H_2O$ (ICDD PDF No. 00-27-0145)

PDF#27-0145: QM=Common(+); d=Densitometer; I=(Unknown) **PDF Card**

Hoganite, syn
C4H6CuO4!H2O

Radiation=CuKa1 Lambda=1.5406 Filter=
Calibration= 2T=12.800-68.253 I/Ic(RIR)=1.45
Ref: Level-1 PDF

Monoclinic, A2/a(15) Z=8 mp=
CELL: 13.863 x 8.558 x 13.171 <90.0 x 117.02 x 90.0> P.S=
Density(c)=1.882 Density(m)= Mwt= Vol=1392.0
Ref: Ibid.

Strong Lines: 6.91/X 6.17/4 5.38/3 5.87/3 3.53/2 5.75/2 3.59/1 2.29/1

74 Lines, Wavelength to Compute Theta = 1.54056?(Cu), I%-Type = (Unknown)

#	d(?)	I(f)	(h k l)	2-Theta	Theta	1/(2d)	#	d(?)	I(f)	(h k l)	2-Theta	Theta	1/(2d)
1	6.9100	100.0	(0 1 1)	12.800	6.400	0.0724	38	2.1370	2.0	(-6 1 1)	42.256	21.128	0.2340
2	6.1700	35.0	(2 0 0)	14.343	7.172	0.0810	39	2.0350	2.0	(-1 4 2)	44.484	22.242	0.2457
3	5.8700	25.0	(0 0 2)	15.081	7.540	0.0852	40	2.0270	4.0	(-6 1 5)	44.669	22.334	0.2467
4	5.7500	16.0	(-2 0 2)	15.397	7.699	0.0870	41	1.9760	1.0	(-6 2 4)	45.886	22.943	0.2530
5	5.3800	25.0	(-2 1 1)	16.463	8.232	0.0929	42	1.9630	4.0	(4 1 3)	46.208	23.104	0.2547
6	4.2800	2.0	(0 2 0)	20.736	10.368	0.1168	43	1.9520	2.0	(-3 2 6)	46.483	23.242	0.2561
7	4.0900	4.0	(2 1 1)	21.711	10.855	0.1222	44	1.9280	2.0	(-3 4 2)	47.097	23.548	0.2593
8	4.0500	2.0	(-3 1 1)	21.928	10.964	0.1235	45	1.8910	2.0	(-1 3 5)	48.076	24.038	0.2644
9	3.5880	12.0	(-1 2 2)	24.794	12.397	0.1394	46	1.8740	2.0	(-1 2 6)	48.540	24.270	0.2668
10	3.5270	20.0	(2 0 2)	25.230	12.615	0.1418	47	1.8300	2.0	(2 4 2)	49.785	24.893	0.2732
11	3.4550	4.0	(-4 0 2)	25.764	12.882	0.1447	48	1.8020	1.0	(-2 1 7)	50.613	25.306	0.2775
12	3.4340	4.0	(-2 2 2)	25.925	12.962	0.1456	49	1.7940	1.0	(-2 4 4)	50.854	25.427	0.2787
13	3.2920	4.0	(-2 0 4)	27.064	13.532	0.1519	50	1.7740	2.0	(-7 2 2)	51.469	25.735	0.2818
14	3.0870	4.0	(4 0 0)	28.899	14.449	0.1620	51	1.7630	4.0	(4 0 4)	51.814	25.907	0.2836
15	3.0330	2.0	(-4 1 3)	29.425	14.712	0.1649	52	1.7530	1.0	(5 3 1)	52.132	26.066	0.2852
16	2.9670	2.0	(3 2 0)	30.095	15.047	0.1685	53	1.7180	1.0	(-4 4 4)	53.277	26.638	0.2910
17	2.8750	2.0	(-4 0 4)	31.081	15.541	0.1739	54	1.7100	2.0	(-6 1 7)	53.546	26.773	0.2924
18	2.7730	2.0	(0 3 1)	32.255	16.128	0.1803	55	1.6950	2.0	(-8 1 3)	54.058	27.029	0.2950
19	2.7230	2.0	(2 2 2)	32.864	16.432	0.1836	56	1.6660	2.0	(1 2 6)	55.078	27.539	0.3001
20	2.6880	2.0	(-4 2 2)	33.305	16.652	0.1860	57	1.6320	1.0	(7 2 0)	56.326	28.163	0.3064
21	2.6450	2.0	(1 3 1)	33.862	16.931	0.1890	58	1.6160	1.0	(5 4 0)	56.935	28.467	0.3094
22	2.6090	2.0	(-2 2 4)	34.344	17.172	0.1916	59	1.6000	1.0	(-2 0 8)	57.557	28.779	0.3125
23	2.5920	2.0	(-5 1 3)	34.576	17.288	0.1929	60	1.5670	2.0	(-7 3 1)	58.887	29.443	0.3191
24	2.5760	1.0	(4 1 1)	34.798	17.399	0.1941	61	1.5440	1.0	(8 0 0)	59.853	29.926	0.3238
25	2.5430	4.0	(-3 2 4)	35.264	17.632	0.1966	62	1.5130	1.0	(-4 5 3)	61.209	30.604	0.3305
26	2.5100	2.0	(-2 1 5)	35.743	17.872	0.1992	63	1.5110	1.0	(-8 1 7)	61.299	30.649	0.3309
27	2.4950	2.0	(-3 1 5)	35.965	17.983	0.2004	64	1.5050	1.0	(-1 3 7)	61.569	30.785	0.3322
28	2.4250	2.0	(-3 3 1)	37.041	18.520	0.2062	65	1.4830	1.0	(-6 2 8)	62.585	31.292	0.3372
29	2.3930	4.0	(-4 1 5)	37.554	18.777	0.2089	66	1.4520	1.0	(8 2 0)	64.078	32.039	0.3444
30	2.3870	4.0	(-4 2 4)	37.652	18.826	0.2095	67	1.4280	2.0	(-6 4 6)	65.287	32.644	0.3501
31	2.3300	8.0	(4 0 2)	38.609	19.305	0.2146	68	1.4210	1.0	(7 3 1)	65.649	32.825	0.3519
32	2.2900	10.0	(-3 3 3)	39.311	19.656	0.2183	69	1.4110	1.0	(-4 5 5)	66.174	33.087	0.3544
33	2.2790	4.0	(2 0 4)	39.509	19.754	0.2194	70	1.4100	1.0	(6 0 4)	66.227	33.113	0.3546
34	2.2260	4.0	(-6 0 4)	40.490	20.245	0.2246	71	1.3920	2.0	(5 1 5)	67.196	33.598	0.3592
35	2.2220	4.0	(1 2 4)	40.566	20.283	0.2250	72	1.3870	1.0	(0 2 8)	67.471	33.735	0.3605
36	2.1860	2.0	(-5 2 4)	41.265	20.632	0.2287	73	1.3810	1.0	(1 4 6)	67.803	33.902	0.3621
37	2.1490	1.0	(5 1 1)	42.008	21.004	0.2327	74	1.3730	2.0	(-5 5 5)	68.253	34.126	0.3642

2 Theta information for fcc Ni (ICDD PDF No. 00-04-0850)

PDF#04-0850: QM=Common(+); d=Diffractometer; I=(Unknown)												PDF Card
Nickel, syn Ni												
Radiation=CuKa1 Calibration= Ref: Level-1 PDF				Lambda=1.5406 2T=44.507-155.653			Filter= I/Ic(RIR)=					
Cubic, Fm-3m(225) CELL: 3.5238 x 3.5238 x 3.5238 <90.0 x 90.0 x 90.0> Density(c)=8.907 Density(m)= Mwt= Vol=43.8 Ref: Ibid.						Z=4 P.S=	mp=					
Strong Lines: 2.03/X 1.76/4 1.25/2 1.06/2 0.79/2 0.81/1 1.02/1												
8 Lines, Wavelength to Compute Theta = 1.54056?(Cu), I%-Type = (Unknown)												
#	d(?)	I(f)	(h k l)	2-Theta	Theta	1/(2d)	#	d(?)	I(f)	(h k l)	2-Theta	Theta	1/(2d)
1	2.0340	100.0	(1 1 1)	44.507	22.253	0.2458	5	1.0172	7.0	(2 2 2)	98.446	49.223	0.4915
2	1.7620	42.0	(2 0 0)	51.846	25.923	0.2838	6	0.8810	4.0	(4 0 0)	121.930	60.965	0.5675
3	1.2460	21.0	(2 2 0)	76.370	38.185	0.4013	7	0.8084	14.0	(3 3 1)	144.669	72.335	0.6185
4	1.0624	20.0	(3 1 1)	92.944	46.472	0.4706	8	0.7880	15.0	(4 2 0)	155.653	77.826	0.6345

2 Theta information for hcp Ni (ICDD PDF No. 00-45-1027)

PDF#45-1027: QM=Intermediate; d=Diffractometer; I=(Unknown)												PDF Card
Nickel Ni												
Radiation=CuKa1 Calibration= Ref: Level-1 PDF				Lambda=1.5406 2T=39.100-133.300			Filter= I/Ic(RIR)=					
Hexagonal, P63/mmc(194) CELL: 2.6515 x 2.6515 x 4.343 <90.0 x 90.0 x 120.0> Density(c)=7.372 Density(m)= Mwt= Vol=26.4 Ref: Ibid.						Z=2 P.S=	mp=					
Strong Lines: 2.03/X 2.17/3 2.30/2 1.58/1 1.33/1 1.22/1 1.13/1 1.11/1												
16 Lines, Wavelength to Compute Theta = 1.54056?(Cu), I%-Type = (Unknown)												
#	d(?)	I(f)	(h k l)	2-Theta	Theta	1/(2d)	#	d(?)	I(f)	(h k l)	2-Theta	Theta	1/(2d)
1	2.3019	22.0	(0 1 0)	39.100	19.550	0.2172	9	1.1104	5.0	(2 0 1)	87.850	43.925	0.4503
2	2.1726	30.0	(0 0 2)	41.530	20.765	0.2301	10	1.0843	2.0	(0 0 4)	90.530	45.265	0.4611
3	2.0334	100.0	(0 1 1)	44.520	22.260	0.2459	11	1.0150	2.0	(2 0 2)	98.730	49.365	0.4926
4	1.5784	13.0	(0 1 2)	58.420	29.210	0.3168	12	0.9804	1.0	(0 1 4)	103.570	51.785	0.5100
5	1.3268	10.0	(1 1 0)	70.980	35.490	0.3768	13	0.8990	2.0	(2 0 3)	117.930	58.965	0.5562
6	1.2240	8.0	(1 0 3)	78.000	39.000	0.4085	14	0.8678	1.0	(2 1 0)	125.160	62.580	0.5762
7	1.1485	1.0	(2 0 0)	84.240	42.120	0.4354	15	0.8509	4.0	(2 1 1)	129.720	64.860	0.5876
8	1.1317	7.0	(1 1 2)	85.790	42.895	0.4418	16	0.8390	3.0	(1 1 4)	133.300	66.650	0.5960

2 Theta information for NiO (ICDD PDF No. 00-44-1159)

PDF#44-1159: QM=Common(+); d=Diffractometer; I=(Unknown)													PDF Card
Nickel Oxide NiO													
Radiation=CuKa1 Calibration= Ref: Level-1 PDF				Lambda=1.5406 2T=37.248-129.437						Filter= I/Ic(RIR)=2.1			
Hexagonal, R-3m(166) CELL: 2.9552 x 2.9552 x 7.2275 <90.0 x 90.0 x 120.0> Density(c)=6.809 Density(m)= Mwt= Vol=54.7 Ref: Ibid.									Z=3 P.S=			mp=	
Strong Lines: 2.09/X 2.41/6 1.48/3 1.48/3 1.26/1 1.21/1 0.93/1 0.93/1													
15 Lines, Wavelength to Compute Theta = 1.54056?(Cu), I%-Type = (Unknown)													
#	d(?)	I(f)	(h k l)	2-Theta	Theta	1/(2d)	#	d(?)	I(f)	(h k l)	2-Theta	Theta	1/(2d)
1	2.4120	60.0	(1 0 1)	37.248	18.624	0.2073	9	0.9588	4.0	(2 1 1)	106.905	53.453	0.5215
2	2.0885	100.0	(0 1 2)	43.286	21.643	0.2394	10	0.9582	2.0	(2 0 5)	107.009	53.505	0.5218
3	1.4773	30.0	(1 1 0)	62.852	31.426	0.3384	11	0.9576	2.0	(1 0 7)	107.100	53.550	0.5221
4	1.4761	25.0	(1 0 4)	62.912	31.456	0.3387	12	0.9344	7.0	(1 2 2)	111.053	55.526	0.5351
5	1.2595	14.0	(1 1 3)	75.404	37.702	0.3970	13	0.9336	7.0	(1 1 6)	111.184	55.592	0.5355
6	1.2062	9.0	(2 0 2)	79.372	39.686	0.4145	14	0.8528	7.0	(2 1 4)	129.168	64.584	0.5863
7	1.2046	4.0	(0 0 6)	79.501	39.751	0.4151	15	0.8519	3.0	(0 1 8)	129.437	64.718	0.5869
8	1.0443	6.0	(0 2 4)	95.052	47.526	0.4788							

2 Theta information for Ag (ICDD PDF No. 00-04-0783)

PDF#04-0783: QM=Common(+); d=Diffractometer; I=(Unknown)													PDF Card
Silver-3C, syn Ag													
Radiation=CuKa1 Calibration= Ref: Level-1 PDF				Lambda=1.5406 2T=38.116-134.882						Filter= I/Ic(RIR)=5.2			
Cubic, Fm-3m(225) CELL: 4.0862 x 4.0862 x 4.0862 <90.0 x 90.0 x 90.0> Density(c)=10.5 Density(m)= Mwt= Vol=68.2 Ref: Ibid.									Z=4 P.S=			mp=	
Strong Lines: 2.36/X 2.04/4 1.23/3 1.45/3 0.94/2 0.83/1 0.91/1 1.18/1													
9 Lines, Wavelength to Compute Theta = 1.54056?(Cu), I%-Type = (Unknown)													
#	d(?)	I(f)	(h k l)	2-Theta	Theta	1/(2d)	#	d(?)	I(f)	(h k l)	2-Theta	Theta	1/(2d)
1	2.3590	100.0	(1 1 1)	38.116	19.058	0.2120	6	1.0215	4.0	(4 0 0)	97.888	48.944	0.4895
2	2.0440	40.0	(2 0 0)	44.277	22.139	0.2446	7	0.9375	15.0	(3 3 1)	110.497	55.248	0.5333
3	1.4450	25.0	(2 2 0)	64.426	32.213	0.3460	8	0.9137	12.0	(4 2 0)	114.924	57.462	0.5472
4	1.2310	26.0	(3 1 1)	77.472	38.736	0.4062	9	0.8341	13.0	(4 2 2)	134.882	67.441	0.5994
5	1.1796	12.0	(2 2 2)	81.536	40.768	0.4239							

2 Theta information for $Ag(CH_3COO)$ (ICDD PDF No. 00-04-0096)

PDF#04-0096: QM=Uncommon(?); d=Other/Unknown; I=(Unknown)												PDF Card
Silver Acetate C2H3AgO2												
Radiation=CuKa1 Calibration= Ref: Level-1 PDF				Lambda=1.5406 2T=8.970-73.995			Filter= I/Ic(RIR)=					
, Density(c)= Density(m)= Mwt= Vol= Ref: Ibid.						Z= P.S=	mp=					
Strong Lines: 9.85/X 3.05/5 2.46/4 2.92/4 2.21/4 1.97/4 2.03/3 1.64/3												
25 Lines, Wavelength to Compute Theta = 1.54056?(Cu), I%-Type = (Unknown)												
#	d(?)	I(f)	(h k l)	2-Theta	Theta	1/(2d)	#	d(?)	I(f)	(h k l)	2-Theta	Theta	1/(2d)
1	9.8500	100.0		8.970	4.485	0.0508	14	2.0300	30.0		44.599	22.300	0.2463
2	5.0000	2.0		17.724	8.862	0.1000	15	1.9700	40.0		46.034	23.017	0.2538
3	3.9500	2.0		22.490	11.245	0.1266	16	1.8500	2.0		49.211	24.605	0.2703
4	3.8000	2.0		23.390	11.695	0.1316	17	1.8000	2.0		50.673	25.336	0.2778
5	3.3000	4.0		26.997	13.498	0.1515	18	1.7100	6.0		53.546	26.773	0.2924
6	3.0500	50.0		29.257	14.629	0.1639	19	1.6400	30.0		56.027	28.014	0.3049
7	2.9200	40.0		30.591	15.295	0.1712	20	1.5800	2.0		58.355	29.178	0.3165
8	2.7600	2.0		32.411	16.206	0.1812	21	1.5300	2.0		60.457	30.229	0.3268
9	2.6800	10.0		33.407	16.703	0.1866	22	1.4800	2.0		62.726	31.363	0.3378
10	2.5700	6.0		34.882	17.441	0.1946	23	1.4500	4.0		64.177	32.088	0.3448
11	2.4600	40.0		36.495	18.247	0.2033	24	1.4100	6.0		66.227	33.113	0.3546
12	2.3200	2.0		38.783	19.391	0.2155	25	1.2800	2.0		73.995	36.998	0.3906
13	2.2100	40.0		40.796	20.398	0.2262							

Appendix 2

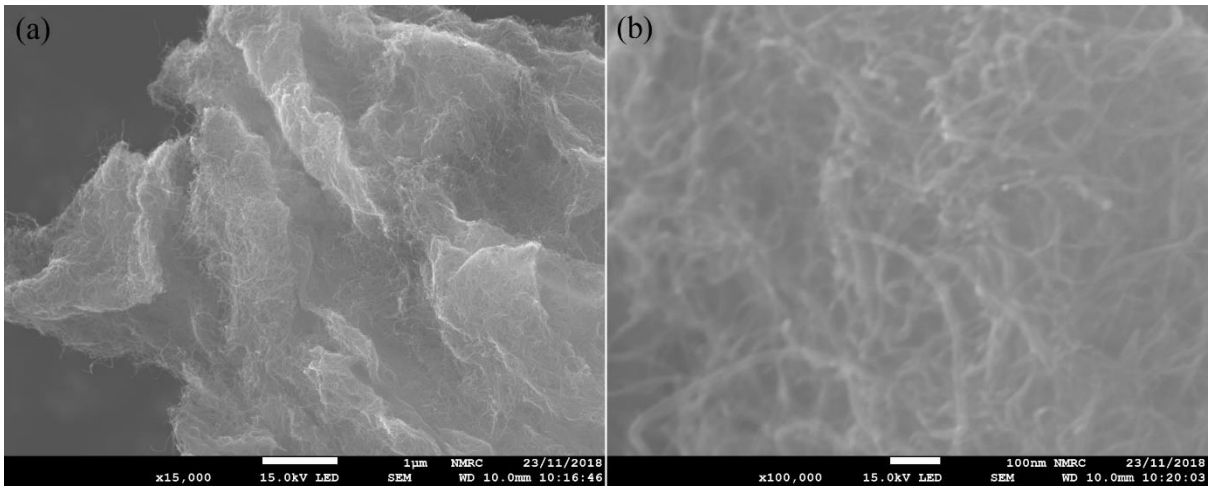

Figure 1 SEM images of GNT nanostructures after 120 min water purification experiment in water.

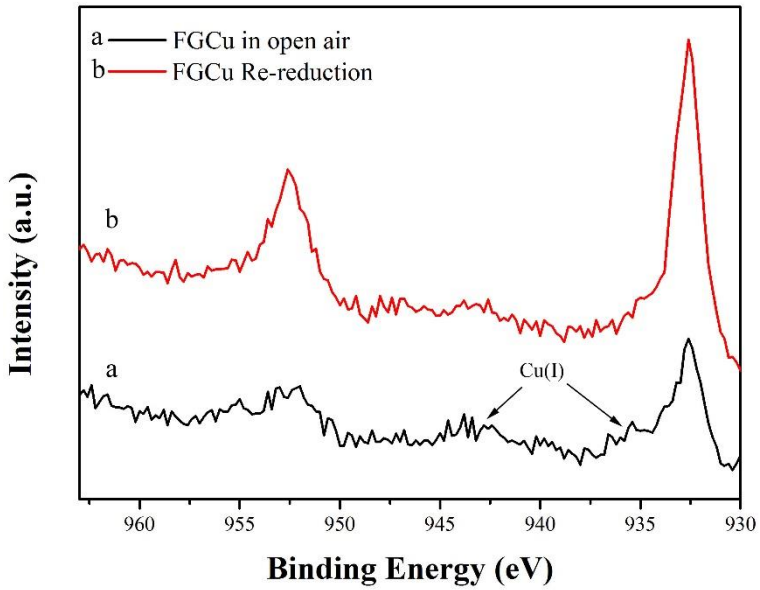

Figure 2 High-resolution Cu 2p XPS spectrum of FGCu samples (a) stored in the open air and (b) after re-reduction.